

Fabricating and Characterizing Metal-Organic Framework Thin Films for Optoelectronic and Sensing Applications

Zur Erlangung des akademischen Grades eines

DOKTORS DER INGENIEURWISSENSCHAFTEN (Dr.-Ing.)

von der KIT-Fakultät für Elektrotechnik und Informationstechnik des
Karlsruher Instituts für Technologie (KIT)

angenommene

DISSERTATION

von

M.Sc., Fischer, Jan Christoph

geboren am 30.01.1995 in Pforzheim

Tag der mündlichen Prüfung:

11.02.2025

Hauptreferent:

Prof. Dr. Bryce S. Richards

Korreferent:

Prof. Dr. techn. Roland Resel

Kurzfassung

Metallorganische Gerüste (engl. „metal-organic frameworks“, kurz MOFs) haben seit den wegweisenden Arbeiten von Robson,^{1,2} Yaghi,³ Kitagawa,⁴ und Ferey,⁵ in den 1990er Jahren großes Interesse erweckt. Insbesondere in Form von Dünnschichten haben MOFs das Potenzial für Einsatz in integrierten funktionellen Bauteilen mit verschiedensten Anwendungsbereichen von der Gastrennung bis hin zu Sensorik und Optoelektronik. Eine große Herausforderung, die die schnelle Entwicklung neuer MOF-Materialien behindert, ist die detaillierte Bestimmung ihrer Struktur. Gerade bei Dünnschichten macht die sehr begrenzte Stoffmenge eine Charakterisierung mit Methoden wie Kernspinresonanzspektroskopie unmöglich. Stattdessen üblich sind eindimensionale Röntgenbeugungstechniken (engl. „X-ray diffraction“, kurz XRD), die z. B. die horizontale und vertikale Periodizität der Struktur untersuchen. Die begrenzten Strukturinformationen, die mit solchen Methoden erzielt werden können reichen jedoch nicht aus, um die Kristallstruktur dünner Schichten zuverlässig zu überprüfen oder Details über die Textur des gewachsenen Materials zu liefern. Diese Informationen sind jedoch sehr wichtig für die eindeutige Materialbestimmung und für spätere Anwendungen.

In dieser Arbeit wird gezeigt, wie mithilfe von Weitwinkelröntgenstreuung unter streifendem Einfallswinkel (engl. „grazing-incidence wide-angle X-ray scattering“, kurz GIWAXS) im Labormaßstab hochwertige Daten über Dünnschichtstrukturen gewonnen werden können, die es ermöglichen theoretische Strukturmodelle durch experimentellen Daten zu verifizieren und die Textur multikristalliner Dünnschichten zu quantifizieren. Darüber hinaus kann die Veränderung der Struktur und Textur mit der Probertiefe erfasst werden, was dazu befähigt Heterostrukturen

Kurzfassung

detailliert zu beschreiben. Außerdem wird gezeigt, wie diese strukturellen Daten genutzt werden können, um eine akkurate und direkte Rückmeldung zu verwendeten Synthesemethoden zu erlangen, sodass angestrebte Morphologien, Heterostrukturen und Texturen von MOF-Dünnschichten erreicht werden können, die für optoelektronische und sensorische Anwendungen wichtig sind. Eine vollständige strukturelle Rückmeldung in der direkten Laborumgebung bietet einen umfassenden Einblick in die Auswirkungen der Syntheseparameter und sollte zu einem wichtigen Grundpfeiler der zukünftigen MOF-Dünnschichtentwicklung werden.

Für die Integration in optoelektronische Bauteile ist die Fähigkeit zur Herstellung von MOF-Dünnschichtarchitekturen mit hochgradig orientierten Kristalliten auf einer Substratoberfläche ein wichtiges Ziel. Im ersten Ergebniskapitel wird gezeigt, wie mit einer etablierten dampfunterstützten Umwandlungsmethode zur Herstellung von texturierten Dünnschichten der wichtigen MOF-Klasse UiO (norw. Abkürzung für „Universitet i Oslo“) erzeugt werden können. Diese MOFs eignen sich aufgrund ihrer reichhaltigen zweidimensionalen Beugungsmuster ideal für die Demonstration einer GIWAXS-basierten Strukturanalyse. Auf dieser Grundlage wird gezeigt, dass eine Abfolge von GIWAXS-Messung und Auswertung, die speziell für Diffraktometer im Labormaßstab entwickelt wurde, quantitative Informationen über orientierte und nicht-orientierte Kristallitanteile von MOF-Dünnschichten mit Tiefeninformation liefern kann. Mithilfe der gewonnenen strukturellen Erkenntnisse wird die homogene Keimbildung bei der Kristallisation als ein Hauptfaktor identifiziert, der zu nicht-orientiertem Kristallwachstum führt, und durch Anpassung der Synthesebedingungen minimiert. Dies führt zu einer deutlichen Verbesserung des Anteils der orientierten Kristallanteile in UiO-66-Dünnschichten von 4 % auf über 95 %. Darüber hinaus wird die Herstellung von UiO-Heterostrukturen mit hohen Anteilen von Kristalliten in der angestrebten zweidimensionalen Pulvertextur in der

unteren UiO-66-Schicht (83 %) und der oberen UiO-67-Schicht (über 94 %) erreicht. Texturierte UiO-Heterostrukturen bieten eine vielseitige Plattform für zukünftige optoelektronische Anwendungen mit steuerbarer Funktionalität. Die beispielhafte Demonstration einer GIWAXS-basierten Syntheseoptimierung, die durch Diffraktometrie im Labormaßstab gewonnen wurde, wird die beschleunigte Entwicklung neuer MOF-Dünnschichtarchitekturen fördern.

Nachdem die Nützlichkeit von GIWAXS-basierter Strukturanalyse von UiO-Dünnschichten nachgewiesen wurde, richtet sich der Fokus auf MOF-Dünnschichten bestehend aus zweidimensionalen, gestapelten Schichten. Solche Architekturen sind besonders für Anwendungen auf der Basis von Photolumineszenz (PL) von großer Bedeutung, da sie Fluorophoren auf sehr engen Abständen beinhalten können, was eine präzise Kontrolle von intermolekularen Wechselwirkungen ermöglicht. Gegenüber den etabliertesten zweidimensionalen MOF-Strukturen basierend auf Kupfer, wie etwa dem oberflächenverankerten MOF-2 (engl. „surface-anchored MOF-2“, kurz SURMOF-2), sind Materialien auf Zinkbasis vorzuziehen um ein Löschen der PL durch Einfluss der Metallknoten zu vermeiden. Im zweiten Ergebniskapitel wird gezeigt, dass die kristallinen Strukturen, die durch in der Literatur beschriebene Methoden schichtweiser Rotationsbeschichtung unter Verwendung von Zinkacetat-Dihydrat mit Dicarbonsäuren wie Benzol-1,4-dicarbonsäure (BDC) und Biphenyl-4,4'-dicarbonsäure (BPDC) also Vorläuferstoffe entstehen, oft nicht die angestrebten MOF-Stapelschichtstrukturen aufweisen. Die methodische Analyse mittels GIWAXS enthüllt, dass das molare Verhältnis von Zinkionen zu Dicarbonsäuren ein kritischer Parameter bei der Herstellung ist, der einen signifikanten Einfluss auf die erzeugten kristallinen Strukturen hat. Bei stöchiometrisch ausgeglichenen Vorläuferverhältnissen formt BPDC die erwartete Stapelschichtstruktur vom Typ SURMOF-2. BDC hingegen führt zur Entstehung eines metallhydroxidorganisches Gerüsts mit deutlich

Kurzfassung

anderer Struktur, die jedoch bei eindimensional-vertikalen Standard-XRD-Messungen sehr ähnlich wie SURMOF-2 erscheinen kann. Wird für die schichtweise Synthese ein Überschuss an Zn^{2+} -Ionen verwendet, entstehen wiederum ganz andere Zinkhydroxid-Schichtstrukturen. Es wird gezeigt, dass sich die Bildung solcher Zinkhydroxid-Schichtstrukturen bei einem Überschuss von Zn^{2+} -Ionen als ein allgemeines strukturelles Motiv erweist für diverse Dicarbonsäuren. Auf Grundlage dieser Entdeckungen wird ein Mechanismus für die Bildung der Kristallstruktur während der schichtweisen Rotationsbeschichtung vorgeschlagen, der sich von der herkömmlichen Vorstellung einer schrittweisen Zugabe von molekularen Bausteinen in ein anwachsendes Gitter unterscheidet. Im Gegensatz dazu wird vorgeschlagen, dass Ablagerung des Metallvorläufers bei der Rotationsbeschichtung zur Bildung von Zinkhydroxyacetat-Schichtstrukturen führt, die nach und nach umgewandelt werden während der Zuführung von Dicarbonsäuren. Die großen strukturellen Unterschiede der zuvor genannten Materialien, die aus denselben Vorläufern gewonnen werden, wirken sich auf die lokale Umgebung der eingebauten Fluorophoren aus, was ihre photolumineszenten Eigenschaften in den verschiedenen Strukturen deutlich verändert. Die resultierenden, unterschiedlichen Dünnschichtemissionen können sogar mit bloßem Auge unterschieden werden und zeigen sich daher als leicht zugänglicher Indikator für die verschiedenen hergestellten Strukturen.

Ein interessanter Weg um Funktionalität in MOFs zu erzeugen ist die Schaffung von ausreichend freien Räumen in der porösen Struktur und somit eine zumindest begrenzte Rotation der molekularen Bausteine zu ermöglichen. Interessanterweise kann eine solche Molekülrotation durch externe Faktoren wie Gastmoleküle im Porennetzwerk beeinflusst werden. Dies eröffnet ganz neue Anwendungsmöglichkeiten im Bereich der Sensorik. Im letzten Ergebniskapitel wird ein einfaches Tropf-Depositionsverfahren

entwickelt, mit dem orientierte säulen-gestützte Schicht-MOF-Dünnschichten hergestellt werden, die Fluorophoren mit der Fähigkeit zur Rotation in offenen Räumen innerhalb des Kristallgitters enthalten. Mithilfe einer GIWAXS-basierten Strukturbewertung werden die Syntheseparameter so eingestellt, dass die Winkelabweichung der Kristallite von der angestrebten Orientierungsrichtung minimiert wird. In diesen MOF-Dünnschichten bestehend aus Zink, 9,10-Anthracendicarbonsäure (ADC) und 1,4-Diazabicyclo[2.2.2]octan, wird der Einfluss der Aufnahme und Abgabe von Lösungsmitteln auf die Lumineszenz untersucht. Bemerkenswerterweise wird während der Verdampfung von Methanol oder Ethanol aus den MOF-Poren ein Anstieg der Lumineszenz um einen Faktor von etwa 50 beobachtet. Es wird gezeigt, dass die Emissionsverstärkung durch die kollektive Rotation von ADC-Molekülen infolge der Aufwärtsbewegung der aus der Struktur verdampfenden Lösungsmittelmoleküle verursacht wird. Die bemerkenswerte Veränderung der optischen Eigenschaften des MOF-Dünnschichtfilms in diesem Zustand wird auf die Versteifung der Fluorophoren in der nach oben geneigten Ausrichtung zurückgeführt. Auf diese Weise wird ein lumineszierender Indikator für die Anzeige der Bewegung von Lösungsmittelmolekülen innerhalb der MOF-Hohlräume in Echtzeit realisiert. Die Arbeit schließt mit einer prototypischen Demonstration, die die Entwicklung neuartiger molekularer Bauteile zur Überwachung von Flüssigkeitstransports auf der Nanometerskala anregt.

Zusammengefasst beinhaltet diese Arbeit die Entwicklung eines GIWAXS-Mess- und Analyse-Prozess im Labormaßstab, der darauf zugeschnitten ist die Produktion von MOF-Dünnschichten zu verstehen und zu optimieren. Eingesetzt in den spezifischen Anwendungsfällen von UiO- und Zn-basierten Stapelschicht-MOFs wird ein besseres Verständnis der synthetischen Verfahren erreicht. Schließlich wird eine Struktur, die die Rotation von organischen Chromophoren ermöglicht, durch ein einfaches Herstellungs-

Kurzfassung

verfahren realisiert und ein neuartiger Sensoreffekt für den Lösungsmittelfluss in ihren Poren entdeckt.

Abstract

Metal-organic frameworks (MOFs) have gathered significant interest since the first pioneering works by Robson,^{1,2} Yaghi,³ Kitagawa,⁴ and Ferey,⁵ in the 1990s. Particularly in the form of thin films, MOFs have the potential to impact integrated functional devices in various fields of application from gas separation to sensing and optoelectronics. A major challenge hampering the development of new MOF materials, is the detailed determination of their structure. Especially in the form of thin films, due to the limited amount of material, characterization by methods such as nuclear magnetic resonance is not possible. One-dimensional X-ray diffraction (XRD) techniques are commonly used, such as those probing the out-of-plane and in-plane periodicity of the structure. However, this very limited projection of the full structural information is not sufficient to robustly check the crystal structure of thin films, or provide detail about the texture of the grown material that is also important in terms of application.

This thesis demonstrates how laboratory-scale grazing-incidence wide-angle X-ray scattering (GIWAXS) can be used to provide high quality structural data that allows simulated structures to be meaningfully compared with experimental data, and the texture of multi-crystalline thin films to be quantified. Furthermore, the change in texture with depth, and the structure and texture of different layers in a heterostructure can be determined. It is demonstrated how these structural data can be used to provide accurate and direct feedback to the synthetic methods, allowing targeted morphologies, heterostructures and textures to be achieved. important for optoelectronic and sensing applications. Complete structural feedback in a laboratory environment provides vital insight into the impact of synthesis parameters and should become a keystone of MOF thin film development.

Abstract

For integration into optoelectronic devices, the ability to produce thin film architectures with highly oriented crystallites relative to a substrate's surface represents a major objective. In the first results chapter, a well-established vapor-assisted conversion method is shown to create thin films of the important UiO (Norwegian abbreviation for Universitet i Oslo) MOF class that are ideal to demonstrate GIWAXS-based analysis due to their rich two-dimensional diffraction patterns. On the basis of the UiO MOF system, a GIWAXS measurement and analysis tool chain developed for laboratory-scale measurement devices is shown to provide quantitative information about oriented and non-oriented crystallite fractions of a thin film as function of depth. Guided by the obtained structural insights, homogeneous nucleation as a major factor leading to non-oriented crystal growth is identified and minimized by adaptation of synthetic conditions. This leads to a major improvement of the oriented crystallite fraction in a UiO-66 MOF from 4 % to over 95 %. Moreover, the fabrication of UiO heterostructures is achieved with high percentages of crystallites in the desired 2D powder texture in the UiO-66 bottom layer (83 % 2D powder texture) and UiO-67 top layer (over 94 %). Textured UiO heterostructures provide for a versatile platform for future optoelectronic applications with tunable functionality. The exemplary demonstration of GIWAXS-guided synthesis optimization gained from direct feedback in a laboratory-scale environment will stimulate the accelerated development of new MOF thin film architectures.

Having established the utility of GIWAXS-based analysis on UiO structures, the focus is turned towards stacked layer MOF thin films. Such architectures are highly relevant for photoluminescence (PL)-based functional devices, as they can hold fluorophore linkers at close distances providing precise control over inter-molecular interactions. In order to avoid PL quenching by the metal cluster, materials based on zinc are favorable over the most established two-dimensional MOF

structural analogs based on copper such as the surface-anchored MOF-2 (SURMOF-2). In the second results chapter, the crystalline structures that emerge from layer-by-layer spin-coating of zinc acetate dihydrate with dicarboxylic acid linkers such as benzene-1,4-dicarboxylic acid (BDC) and biphenyl-4,4'-dicarboxylic acid (BPDC) following methods found in the literature are shown to often not exhibit the targeted stacked layer MOF structures. Methodical analysis by GIWAXS uncovers the zinc ion-to-linker molar ratio utilized for the production as a critical parameter that has significant impact on the created morphologies. At stoichiometrically balanced precursor ratios, BPDC generates the expected SURMOF-2 type structure. BDC, in contrast, creates a metal-hydroxide organic framework with a distinctly different morphology but that can appear very similar to SURMOF-2 in standard out-of-plane XRD measurements. If an excess of Zn^{2+} ions is used for the layer-by-layer synthesis, entirely different layered zinc hydroxide structures emerge. The formation of layered zinc hydroxide structures in the excess of Zn^{2+} ions is shown to be a general theme for various dicarboxylic linkers. Based on these discoveries, a mechanism for the crystal structure formation during layer-by-layer spin-coating is suggested that differs from conventional understanding of incremental addition of molecular building blocks into a growing lattice. Instead, zinc hydroxy acetate layers are proposed to be formed after the deposition of the metal precursor and successively converted when the dicarboxylic linker is presented. The vast structural differences of the materials mentioned above and obtained from the same precursors affect the local environment of the fluorophores incorporated, meaning that they notably change their photoluminescent properties in the different structures. Thereby, differences in photoluminescence, that can even be apparent by eye, are shown to serve as an easily accessible indicator of the different fabricated structures.

Abstract

An interesting way to introduce functionality in MOFs is the creation of sufficient free volumes in the structure for at least limited rotation of the molecular building blocks. Interestingly, such molecular rotation can be influenced by external factors such as guest molecules in the porous network. This opens up a whole new domain of sensing applications. In the final results chapter, a simple drop-casting method is developed that produces oriented layer-pillar MOF thin films that contain luminescent linkers with the ability to rotate within open spaces inside the crystal lattice. By means of a GIWAXS-based structural evaluation, synthetic parameters are tuned to minimize the angular deviation of crystallites from the targeted orientation direction. In these thin films built from zinc, 9,10-anthracene-dicarboxylic acid (ADC) and 1,4-diazabicyclo[2.2.2]octane, the influence of the sorption and release of solvents on the MOF luminescence is studied. Remarkably, during the evaporation of methanol or ethanol from the MOF pores, a luminescence turn-on by a factor of ~50 is observed. The emission enhancement is shown to be caused by collective rotation of ADC linker due to the upwards streaming motion of solvent molecules leaving the structure. The notable changes of the optical properties of the MOF thin film in this state is ascribed to the rigidification of fluorophore rotors being locked in an upwards tilted configuration. Therewith, a luminescent indicator is realized that reports solvent motion inside of MOF cavities in real-time. The thesis concludes with a prototypical demonstration stimulating the development of novel molecular devices to monitor fluid transport at a nanoscale.

In summary, this work comprises the development of a lab-scale GIWAXS measurement and analysis workflow tailored to understand and optimize MOF thin film production. Applied to the specific use cases of UiO and Zn-based stacked layer MOFs, an improved understanding of synthetic procedures is obtained. Lastly, a structure supporting rotation of organic chromophores is realized by a facile

Abstract

fabrication procedure and in which a highly novel sensing effect for solvent flow inside its pores is discovered.

Acknowledgements

I would like to express my deep gratitude to Dr. Ian Howard. His vast knowledge, creativity and kindness were a constant source for motivation and he always continued to support me throughout my journey. In the same manner, I would like to thank Prof. Dr. Bryce Richards for giving me the chance to pursue a PhD in the “Advanced Materials and Optical Spectroscopy” research group. I am very grateful for his scientific guidance as well as the creation of an always productive and pleasant working environment.

Special thanks, I would like to express towards the Karlsruhe School of Optics and Photonics for their many events including summer schools, symposiums and seminars to connect with other amazing scientists and always expand the personal horizon. For funding of my work through the priority program SPP 1928 COORNETS, I gratefully acknowledge the Deutsche Forschungsgemeinschaft.

Furthermore, I would like to thank all my great colleagues at the Institute of Microstructure Technology and Light Technology Institute Dr. Milian Kaiser, Dr. Marius Jakoby, Dr. Dmitry Busko, Dr. Ngei Katumo, Vinay Kumar, Fernando Arteaga-Cardona, Dr. Damien Hudry, Dr. Andrey Turshatov, Leon Geiger, Dr. Tonghan Zhao, Dr. Dejing Meng, Dr. Eduard Madirov, Dr. Arzu Ergene, Dr. Justine Nyarige, Dr. David Ritzer, Dr. Nils Rosemann, Dr. Yang Li, Dr. Isabel Allegro and Felix Laufer with whom I not only enjoyed amazing science but also a lot of friendly conversations.

My publications would not have been possible without the support of collaborators from other institutes at KIT and from other universities. I am very grateful for the support I received from the Institute for Functional Interfaces, especially from Prof. Dr. Christof Wöll, Dr. Peter Weidler, Dr. Chun Li, Priv.-Doz. Dr. Lars Heinke, Dr. Zhiyun Xu, Dr.

Acknowledgements

Dong-Hui Chen and Reader-F Dr. Ritesh Haldar, providing access to various laboratories and very helpful scientific advice. Furthermore, I want to thank Prof. Dr. Egbert Zojer, Prof. Dr. Roland Resel, Robbin Steentjes and Mario Fratschko from the Graz University of Technology for the interesting scientific discussions and fruitful collaborative work. Finally, I want to express my gratitude to Prof. Dr. Ross Forgan for the very kind support of a short research stay at the University of Glasgow and especially Joe Schofield Holyoake who was a great guide not only in the chemistry lab but also around Scotland.

Abschließend geht mein besonderer Dank an meine ganze Familie, insbesondere an meine Eltern und an meine Verlobte Melina, die mich immer bedingungslos unterstützt haben und mir auch durch schwierige Phasen hinweg immer Halt gegeben haben.

Content

<i>Kurzfassung</i>	i
<i>Abstract</i>	vii
<i>Acknowledgements</i>	xiii
Content	1
List of Publications	5
1. Introduction	9
1.1. Gas Storage	10
1.2. Membranes	11
1.3. Catalysis	12
1.4. Electric Energy Storage	13
1.5. Optoelectronics	13
1.6. Challenges and Opportunities for Application of MOF Thin Films	14
2. Theoretical Background	19
2.1. X-ray Diffraction	19
2.1.1. Principle of X-ray Diffraction	19
2.1.2. XRD Measurement Techniques	23
2.1.3. GIWAXS: Scattering Geometry	25
2.1.4. GIWAXS: Crystallite Orientations	31
2.1.5. GIWAXS: Depth Dependence	33
2.2. Electronic States in Organic Molecules	35
2.2.1. Molecular Orbitals	35

Content

2.2.2.	Molecular Excited States and Electronic Transitions	38
2.2.3.	Excited State Relaxation	43
2.2.4.	Molecular and Environmental Effects on Fluorescence	46
2.2.5.	Exciton Transport	49
2.3.	Metal-organic Frameworks	51
2.3.1.	MOF Basics	52
2.3.2.	MOF Thin Films	55
2.3.3.	Photoluminescence in MOFs	58
2.3.4.	Molecular Motion in MOFs	60
3.	Fabrication and Characterization Methods	63
3.1.	Thin Film Fabrication	63
3.1.1.	Overview of Organic Molecules	63
3.1.2.	Substrate Preparation	64
3.1.3.	Layer-by-layer Spin-coating	65
3.1.4.	Drop-casting on Hot Plate	66
3.1.5.	Vapor-assisted Conversion	68
3.2.	Structural Characterization	69
3.2.1.	Grazing-incidence Wide-angle X-ray Scattering (GIWAXS)	69
3.2.2.	Powder X-ray Diffraction (PXRD)	72
3.2.3.	Infrared Reflection-absorption Spectroscopy (IRRAS)	72
3.2.4.	Scanning Electron Microscope (SEM)	74
3.3.	Photophysical Characterization	74

3.3.1.	Excitation Sources	75
3.3.2.	Spectrometers	77
3.3.3.	Time-integrated PL Spectroscopy	79
3.3.4.	Time-resolved PL Spectroscopy	80
3.3.5.	PL Quantum Yield	81
3.3.6.	Absorption Spectroscopy	84
4.	Insight into Oriented Growth of UiO Thin Films by Lab-scale GIWAXS	87
4.1.	Motivation	87
4.2.	Overview	89
4.3.	GIWAXS Image Projection and Diffractogram Analysis	90
4.4.	Orientational Analysis of UiO Thin Films from VAC	96
4.5.	Optimization of Oriented Thin Film Growth	103
4.6.	Depth Profiling of Oriented Thin Film Fraction	107
4.7.	UiO Heterostructures	112
4.8.	Conclusion	120
5.	Structure Determination of Zn-based Metal-organic Thin Films	121
5.1.	Motivation	121
5.2.	Overview	124
5.3.	Structures Obtained from Layer-by-layer Spin-coating	125
5.4.	Layered Zinc Hydroxide (LZH) Intercalated with Dicarboxylates	129
5.5.	Metal-hydroxide-organic Framework (MHOF) from Zn and BDC	140
5.6.	Mixed Phases of LZH and MHOF from Zn and BDC	146

Content

5.7.	Plausible Structure Formation Mechanism	152
5.8.	Thin film PL	158
5.9.	Conclusion	161
6.	PL Turn-on by Flow-mediated Chromophore Realignment in MOFs	165
6.1.	Motivation	165
6.2.	Overview	167
6.3.	<001>-oriented Thin Films by Drop-casting	168
6.4.	Luminescence Turn-on During Solvent Evaporation	187
6.5.	Molecular Rotor Realignment	197
6.6.	Proof-of-concept Demonstrator	206
6.7.	Conclusion	208
7.	Conclusion and Outlook	211
7.1.	Conclusion	211
7.2.	Outlook	215
8.	References	221

List of Publications

During my work, three first-author publications have been created. Two of them have already been published in peer-reviewed scientific journals and one of them is currently in submission. Additionally, I contributed as a co-author to seven other publications, one of which has been submitted lately.

First-author publications and manuscript in submission:

Fischer, J. C., Ji, H., Busko, D., Li, Y., Duan, P., Richards, B. S., Howard, I. A. & Zhao, T. Nanoscale Flow Indicator: Molecular Rotor Realignment Modulates Luminescence in Metal-Organic Framework Thin Films. – *in submission*

Fischer, J. C., Steentjes, R., Chen, D.-H., Richards, B. S., Zojer, E., Wöll, C. & Howard, I. A. Determining Structures of Layer-by-Layer Spin-Coated Zinc Dicarboxylate-Based Metal-Organic Thin Films. *Chem. – A Eur. J.* **202400565**, 26–29 (2024).

Fischer, J. C., Li, C., Hamer, S., Heinke, L., Herges, R., Richards, B. S. & Howard, I. A. GIWAXS Characterization of Metal–Organic Framework Thin Films and Heterostructures: Quantifying Structure and Orientation. *Adv. Mater. Interfaces* **10**, (2023).

Co-author publications and manuscript in submission:

Fratschko, M., Strasser, N., Taghizade, N., Linares-Moreau, M., **Fischer, J. C.**, Zhao, T., Howard, I. A., Falcaro, P., Zojer, E. & Resel, R. Identifying Structure and Texture of Metal-Organic Frameworks Thin Films by Combining X-ray Diffraction and Quantum Mechanical Modelling. – *in submission*

List of Publications

Fratschko, M., Zhao, T., **Fischer, J. C.**, Werzer, O., Gasser, F., Howard, I. A. & Resel, R. Thin Film Formation Based on a Nanoporous Metal-Organic Framework by Layer-By-Layer Deposition. *ACS Appl. Nano Mater.* (2024).

Zhao, T., Taghizade, N., **Fischer, J. C.**, Richards, B. S. & Howard, I. A. [001]-Oriented heteroepitaxy for fabricating emissive surface mounted metal-organic frameworks. *J. Mater. Chem. C* **12**, 5496–5505 (2024).

Chen, H., Martín-Gomis, L., Xu, Z., **Fischer, J. C.**, Howard, I. A., Herrero, D., Sobrino-Bastán, V., Sastre-Santos, Á., Haldar, R. & Wöll, C. Tunable J-type aggregation of silicon phthalocyanines in a surface-anchored metal-organic framework thin film. *Phys. Chem. Chem. Phys.* **25**, 19626–19632 (2023).

Li, Y., Roger, J., Allegro, I., **Fischer, J. C.**, Jin, Q., Lemmer, U., Howard, I. A. & Paetzold, U. W. Lasing from Laminated Quasi-2D/3D Perovskite Planar Heterostructures. *Adv. Funct. Mater.* **32**, 1–8 (2022).

Hu, H., Moghadamzadeh, S., Azmi, R., Li, Y., Kaiser, M., **Fischer, J. C.**, Jin, Q., Maibach, J., Hossain, I. M., Paetzold, U. W. & Abdollahi Nejand, B. Sn-Pb Mixed Perovskites with Fullerene-Derivative Interlayers for Efficient Four-Terminal All-Perovskite Tandem Solar Cells. *Adv. Funct. Mater.* **32**, (2022).

Kiseleva, N., Filatov, M. A., **Fischer, J. C.**, Kaiser, M., Jakoby, M., Busko, D., Howard, I. A., Richards, B. S. & Turshatov, A. BODIPY-pyrene donor-acceptor sensitizers for triplet-triplet annihilation upconversion: The impact of the BODIPY-core on upconversion efficiency. *Phys. Chem. Chem. Phys.* **24**, 3568–3578 (2022).

Besides journal publications, I participated in the scientific exchange in the form of an international conference, summer schools and workshops as listed below.

International Conference:

Fischer, J. C., Chen D.-H., Wöll, C., Richards, B. S. & Howard, I. A. Structural Comparison of Cu- and Zn-based SURMOF-2. *8th International Conference on Metal-Organic Frameworks and Open Framework Compounds (Poster)*, 4th – 7th Sep, 2022, Dresden.

Summer Schools and Symposiums:

KSOP Summer School, 26th – 27th Sep, 2024, Bad Herrenalb (*"Metal-organic Framework (MOF) Thin Films for Photoluminescence Applications"*)

9th Karlsruhe Days of Optics and Photonics, 16th – 17th Nov, 2023 (*"Metal-organic framework (MOF) thin film structure identification"*)

KSOP Summer School, 29th – 30th Sep, 2022, Bad Herrenalb (*"Dipolar Molecular Rotors in Surface-Anchored Metal-Organic Frameworks (SURMOFs)"*)

8th Karlsruhe Days of Optics and Photonics, 10th – 12th Nov, 2021, online (*"Dipolar Molecular Rotors in Surface-anchored Metal-Organic Frameworks (SURMOFs)"*)

Conductive Metal-Organic Frameworks – From Synthesis To Functions, 6th – 8th Sep, 2021, online (*"Molecular Dipolar Rotors in Surface-anchored MOFs (SURMOFs)"*)

List of Publications

1. Introduction

In recent decades, the desire for artificial materials with tailored properties at the molecular level has sparked substantial research across many different research areas. One of the most promising developments following this goal are metal-organic frameworks (MOFs). These are hybrid crystalline materials formed by the coordination of metal ions and organic ligands. The sheer amount of combinations between different molecular building blocks provides these materials with a remarkable level of tunability allowing for precise control of structure and functionality. The opportunity of engineering at a molecular level has established MOFs at the forefront of advanced materials research with the potential to revolutionize a wide palette of applications such as gas storage, separation, catalysis, optoelectronics, sensing, and so on. Following the seminal work of Yaghi *et al.* in 1995 that coined the term “metal-organic framework”,³ showing microporous structures from metal-organic compounds for the selective binding of aromatic guest molecules, MOF research has experienced an ever-increasing expansion (**Figure 1.1**) with currently

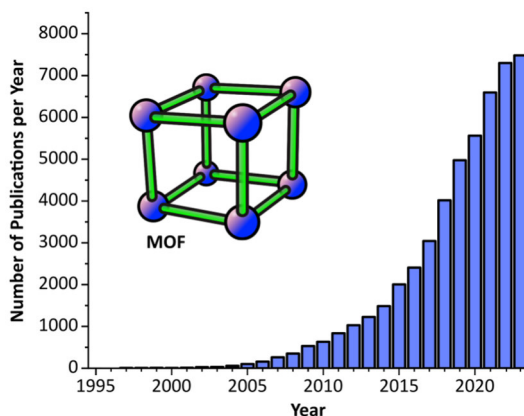


Figure 1.1. Publications per year containing the term “metal-organic framework” according to Web of Science (accessed 26.08.24). The inset shows an illustration of a generic MOF consisting of metal clusters (purple) connected by organic linkers (green).

over 7000 publications per year and over 120000 individual structures registered in the Cambridge Crystallographic Data Centre.⁶ The main versatility of this material class stems from the modular nature of MOFs. By independent selection of metal nodes and organic linkers, three-dimensional molecular networks can be created with controlled pore size, geometry, and specific functionality. This level of control has led to wide-spread interest in MOFs and enables disruptive technological advances across various research domains.

1.1. Gas Storage

One of the most interesting features of MOFs is their extremely large internal surface area. MOFs are, besides substances like activated carbon or zeolites,⁷ among the materials with the highest measured specific surface areas, surpassing $7000 \text{ m}^2\text{g}^{-1}$.^{8,9} Ultrahigh porosity combined with tailored adsorption sites make MOFs ideal candidates for gas storage. For example, MOFs can play a key role in the current endeavor to find suitable materials for hydrogen storage,^{10,11} and CO_2 capturing,^{12,13} both of which are critical for the development of clean future energy technologies. Although high pressure or liquid storage of H_2 is already possible with currently available technologies, these have limited practical use in terms of energy efficiency and safety.¹¹ Targeted MOF design strategies are actively pursued to reach the major milestone of ambient temperature H_2 sorption and release with government-specified storage performance (*e.g.* 50 g L^{-1} in the United States).¹⁴ A promising step towards this goal has recently been achieved, for example, with the Cu-based NU-2100 (NU, Northwestern University) MOF.¹⁵ The material displays good air-stability and deliverable H_2 storage capacity of 10.4 g L^{-1} with a realistic potential for scaled-up synthesis. With regards to reducing global CO_2 atmospheric release, a primary strategy is to capture the climate-active gas. One attractive approach is capturing the gas post-combustion as it could be a retro-fitting technology to improve already existing CO_2 -producing systems.¹⁶ Great effort has been

undertaken in recent years to optimize CO₂ adsorption capacity and selectivity in MOFs.¹⁷ To this end, structures have been designed, for example, with pore dimensions specifically adjusted for the CO₂ molecule kinetic diameter,¹⁸ or that incorporate improved adsorption sites such as open metal sites,¹⁹ or linkers with polar functional groups.²⁰ A recent achievement was the commercial demonstration CO₂ capturing using the Zn-based MOF CALF-20 (CALF, Calgary Framework).²¹

A specialized gas storage application utilizing the ultrahigh porosity and selective adsorption capabilities of MOFs is direct water harvesting from the atmosphere.²² Currently majorly promoted by Yaghi and co-workers, this technology has the potential to play a major role in countries suffering from acute groundwater scarcity. MOF water harvester rely on cyclic water sorption from air followed by pressure- or temperature-initiated release in the vapor-phase. Liquid water is then produced by condensation.²² Such a system was demonstrated, for example, by Kim *et al.* based on MOF-801, a Zr-containing 12-connected metal clusters and fumaric acid linkers, and using solar irradiance as a heating source for the desorption step.²³ Fuchs *et al.* recently revealed that a maximum of ~3.8 L of water could be extracted per hour and kilogram of MOF-801 if single crystals are used for harvesting, eliminating inter-particle condensation that leads to permanently trapped water.²⁴ This report highlights the importance of a high-quality monocrystalline MOF material.

1.2. Membranes

MOFs acting as a membrane can be used for the treatment of bypassing gases or liquids.²⁵ Liu *et al.*, for example, have presented a UiO-66 Zr-MOF thin film membrane with remarkable stability and multivalent ion rejection capabilities that make it a promising candidate for pressure-driven water desalination in the future.²⁶ MOF nanoparticles can be embedded into polymeric membranes as shown

by Sorribas *et al.* who filled different MOFs with pores sizes from 50 to 150 nm into a polyamide layer to achieve MOF-based nanofiltration of particulates in different solvents.²⁷ Li *et al.* showcased that an oriented ZIF-7 (ZIF, zeolitic imidazolate framework) membrane with a large-scale anisotropic pore structure exhibits notably different permeance properties than a membrane of the same type with randomly oriented crystallites, underlining the significance of crystallite orientation.²⁸

MOF membranes are one example of application for which the use of textured thin layers can provide significant benefit over MOF bulk powder. Crystallites with a uniform orientation enable the formation of extended channels through the material to allow for controlled gas or liquid flow through the pore network. Rather than fabricating MOFs in the form of powder, MOFs already grown as thin films are a development that combined the inherent material properties with the unique advantages of reduced dimensionality and surface effects. Using dedicated synthetic procedures that are able to yield thin films with controlled thickness and crystallite orientation provides the possibility of seamless integration into a multitude of functional devices.

1.3. Catalysis

One important example for beneficial usage of MOF thin films are catalytic applications, where a thin layer provides significant benefits over a bulk structure such as improved accessibility to large number of catalyst sites within extended channels inside the pore network and reduced diffusion path lengths for reactants.²⁹ MOF thin film-based catalysis has been utilized, for example, in the context of water splitting or the reduction of CO₂.^{29,30} Zhang *et al.*, for example, demonstrated the catalytic performance of a nanocomposite photoanode formed by TiO₂ core and a Ti-based (MIL-125) MOF thin film shell for photoelectrochemical water splitting.³¹ Ye *et al.* have

presented an example of an electrocatalytic MOF thin film device for the reduction of CO₂ to CO, showing that highly oriented crystallites lead to improved conversion efficiency.³²

1.4. Electric Energy Storage

MOF thin films have been demonstrated in devices for electric energy storage. Recent advances have been made proposing MOF thin films as an electrode material in batteries or supercapacitors.^{33–36} Research on supercapacitors aims at increasing the density of stored electric potential energy. To achieve that MOFs are in the focus as new electrode materials due to their massive internal surface area, good conductivity and adjustable pore sizes.³⁵ A pioneering demonstration of a MOF-based supercapacitor forming Ni-based electrodes with high conductivity and large channels allowing for electrolyte motion was made by Sheberla *et al.*³⁷ Similar to supercapacitors, batteries in general can benefit from highly porous electrode materials that enable cyclic insertion and extraction ions, for example in established Li-ion batteries.³⁶ A current development drawing considerable interest are aqueous zinc batteries, appealing because of their low toxicity, high safety and high theoretical capacity, for which MOF thin films are considered promising cathode materials.^{34,38}

1.5. Optoelectronics

Finally, the wide field of optoelectronics presents a very important research domain with a plethora of highly specialized applications for MOF thin films, a few of which are highlighted here. Owing to their tunable structure and electronic configurations, MOFs have garnered significant interest for usage in photovoltaic devices.³⁹ MOF thin film layers have been demonstrated as suitable charge transport layers aiding in electronic band alignment and improving charge extraction,^{40,41} as interface modifiers to enhance crystallinity throughout a device stack and suppress interfacial charge carrier recombination,^{42–44} and as scaffolds to guide growth of perovskite

absorber materials.^{44,45} MOFs have also been utilized as photodetectors, as for example presented by Arora *et al.*, in the form of a Fe-based two-dimensional MOF thin film covering a broad absorption range from visible to near-infrared radiation.⁴⁶ Another example is given by Tian *et al.* who created an indium-porphyrin MOF thin film that showed exceptional responsivity due to long-range one-dimensional alignment of the photo-active ligands.⁴⁷ In the context of white light-emitting diodes (LEDs), MOF thin films are explored for use as luminescent phosphor films,⁴⁸ using different strategies such as incorporation of luminescent guest molecules,⁴⁹ or dedicated engineering of photo-active linker molecules.⁵⁰ Lastly, there is a wide range of highly specific photoluminescent sensing use cases for MOF thin films,^{51,52} including biomedical applications,⁵³ chemical and explosives detection,⁵⁴ and gas monitoring.⁵⁵ Using luminescent MOFs as sensing materials presents several benefits owing to the natural porosity readily allowing for adsorption and concentration of guest molecules inside the molecular matrix. Furthermore, the linkers and metal centers can be tuned to adjust the photophysical material properties, for example by varying the size of the metal cluster or changing the level of conjugation of the linker. Finally, the possibilities to either immobilize linkers or allow for their unrestricted movement inside a MOF lattice provide valuable levers to steer the default emission intensity by altering non-radiative excited state relaxation pathways.⁵⁴

1.6. Challenges and Opportunities for Application of MOF Thin Films

All of these examples for very diverse applications highlight the significance of MOFs and their promising potential for breakthrough technologies across different research areas. However, despite the remarkable progress in synthesizing new components for MOFs with unique properties and expanding the library of MOF structures, several challenges remain that hinder the widespread

implementation of resulting the thin film materials in practical applications. These challenges are rooted in current limitations of fabrication processes and the generated film properties.

Targeted development of functional MOF thin films for novel applications is only possible with the ability to produce high-quality structures with tailored material properties. This requires refined synthetic protocols that reliably yield the desired MOF thin film structures. A prerequisite for the optimization of any synthetic approach, especially with regards to eventual industrial implementation, is a certain understanding of the formation process, which is, however, not often addressed in the literature. Valuable insight into such processes can be granted by a thorough investigation of the structural properties of fabricated materials. To harness the full potential of MOFs, for optoelectronic applications in particular, even not only the crystal structure is of vital importance but also the orientation of the installed crystallites plays a crucial role *e.g.* when utilizing anisotropic optical and electronic properties.^{56–59} Thus, the crystallite orientation needs to be controlled as well. To study both of these structural properties of MOF thin films in depth, there is a major potential for improvement by utilizing 2D X-ray diffraction (XRD) methods over 1D out-of-plane XRD which is still the dominating characterization technique. Finally, unambiguous structure determination and refinement of synthetic protocols go hand in hand and can form a cyclic process at the end of which, high-quality materials with highly specific functional properties emerge.

Instead of fully MOF-based optoelectronic devices, which might be a possibility in the more distant future, there are specialized applications that present very promising opportunities for the short-term future. Two such especially interesting possibilities are modular sensing platforms and auxiliary materials in the molecular engineering of integrated optoelectronic devices. With the extremely high number of functionalized linkers that can be incorporated into a MOF

architecture, the first major opportunity provides the potential to create a common thin film sensor archetype which could be adjusted to different requirements by choosing a suitable ligand. Exploiting MOF heterostructures, multiple sensing layers designed to interact with different analytes could be achieved. This could give rise to a modular “standard” sensing platform with very high versatility and the opportunity of shared optimization across multiple research groups. Modular sensing platforms are very interesting, for example, for point of care analysis in lab-on-chip applications.^{60–63} The second great opportunity lies in expanding the direct and indirect usage of MOFs as auxiliary materials for optoelectronic thin film components. In this way, MOF thin films can be used to boost other already existing technologies and enhance their performance. The first example of using MOFs for interfacial engineering or templating layers to guide growth in perovskite solar cell architectures was already mentioned above.^{42–45} Another prominent achievement using an auxiliary MOF material was the stabilization of perovskite nanocrystals as emitters in LEDs.⁶⁴ The key protection mechanism increasing the perovskite lifetime in this application was preventing the perovskite nanocrystals from merging inside the MOF matrix. Apart from a combination with perovskites, MOFs can also serve as highly structured template layers for entirely different scenarios such as to create organized polymers with bioactive functionality.⁶⁵ To conclude, there is a great wealth of opportunities for applications of MOFs that can serve an impactful purpose almost within reach.

This work contributes to key cornerstones for a rapid developmental progress in MOF thin film research, in terms of detailed structural investigations of different MOF thin films emerging from various synthesis strategies *via* two-dimensional X-ray diffraction analysis and concluding with the demonstration of a novel luminescent sensing mechanism inside a MOF with controlled structure and texture to indicate liquid flow at a nanoscale through the porous material.

The thesis is organized according to the following outline:

Chapter 2: Introduction of i) important theoretical concepts of X-ray diffraction for the structural characterization of thin films, ii) theoretical framework for photophysical properties of organic molecules, and iii) metal-organic frameworks.

Chapter 3: Explanation of the techniques used for fabrication of thin film samples and experimental methods and instruments employed for their characterization.

Chapter 4: Structural analysis of oriented UiO MOF thin films based on two-dimensional GIWAXS diffractometry providing quantitative insight into oriented crystallite fractions in mono- and multilayer systems.

Chapter 5: Determination of metal-organic thin film structures obtained from layer-by-layer spin-coating based on Zn and various dicarboxylic acid linkers utilizing GIWAXS analysis in combination with density functional theory-derived models.

Chapter 6: Synthesis of MOF thin film by drop-casting on a hot plate that yields oriented layer-pillar structures incorporating molecular rotors and experimental demonstration of a luminescence-based solvent flow indication by passive molecular rotation in these materials.

Chapter 7: Concluding summary of the findings presented in this work and outlook to future developments.

2. Theoretical Background

This chapter introduces theoretical concepts behind three major topics of this thesis. These are MOFs, structural characterization by means of X-ray diffraction (XRD), in particular by grazing-incidence wide-angle X-ray scattering (GIWAXS), and optical properties of organic chromophores in MOFs. The following three sections shall provide compact summaries of each of these topics to understand the most important aspects.

2.1. X-ray Diffraction

Structural characterization of crystalline structures by means of X-ray diffraction is a widely established technique. Especially the surface sensitive grazing-incidence methods have become state-of-the-art for the examination of thin films. This section summarizes the fundamental principles of the X-ray diffraction phenomenon and then focusses on grazing-incidence wide-angle X-ray scattering in particular as primary structural characterization method used throughout this thesis. The content is mainly based on the textbooks *Thin Film Analysis by X-ray Scattering* by Birkholz,⁶⁶ *Two-dimensional X-ray Diffraction* by He,⁶⁷ and *Elements of Modern X-ray Physics* by Als-Nielsen and McMorrow.⁶⁸

2.1.1. Principle of X-ray Diffraction

When electromagnetic radiation interacts with periodic structures that exhibit geometrical variations of the same order of magnitude as the photon wavelength, diffraction phenomena are observed. To probe a structure on the molecular level with interatomic distances in the range of *Ångstrom* (\AA , 10^{-10} m), X-ray photons with energies of keV are necessary. There are two different types of interactions between such photons with matter: inelastic and elastic scattering. In the inelastic case, energy is transferred from the photon to an atom

Theoretical Background

resulting in rearrangement of its electron distribution (*Compton scattering*) or ionization. Elastic scattering does not involve energy transfer (*Thomson scattering*). In this process, the incident photon causes the electrons to oscillate like a Hertzian dipole. Thereby, the accelerated charges release the exact same amount of energy by emitting a spherical electromagnetic wave. This effect is the foundation of all structural investigations based on X-ray diffraction.

The scattering angle 2θ in the scattering event of an X-ray photon from a single atom, can be expressed by

$$2\theta = \cos^{-1} \frac{\langle \mathbf{k}_f, \mathbf{k}_i \rangle}{k_f k_i} \quad (2.1)$$

with the wavevectors \mathbf{k}_i and \mathbf{k}_f (vectoral quantities, labeled by bold font) of the incident and final electromagnetic waves. Calling the scattering angle 2θ instead of only θ is a convention specific to X-ray diffraction, the reason of which will become apparent in **Figure 2.1**. Further, the scattering vector \mathbf{q} can be defined as follows

$$\mathbf{q} = \mathbf{k}_f - \mathbf{k}_i \quad (2.2)$$

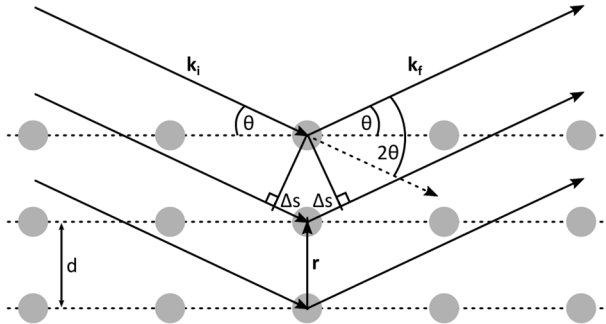


Figure 2.1. Scattering from periodically arranged atoms. Simple case of horizontally oriented atomic layers and equal angles towards incident and final wavevectors \mathbf{k}_i and \mathbf{k}_f . For constructive interference, the path difference $2\Delta s = 2d \sin \theta$ must be an integer multiple of the photon wavelength. Adapted from Birkholz.⁶⁶

with $|\mathbf{k}_i| = |\mathbf{k}_f| = \frac{2\pi}{\lambda}$ describing the momentum transfer of the propagating electromagnetic wave due to scattering.

Constructive interference (*i.e.*, the maximum amplitude of the scattered electromagnetic wave) is achieved when the path difference $2\Delta s = 2d \sin \theta$ equals an integer multiple m of the wavelength λ

$$m\lambda = 2d \sin \theta \quad (2.3)$$

which is also known as *Bragg's law*, illustrated in **Figure 2.1**. In the temporal domain, the phase difference $\Delta\varphi$ introduced by the longer paths is given by the scalar product of the scattering vector \mathbf{q} and the atomic positions inside the unit cell \mathbf{r}_n

$$\Delta\varphi_n = (\mathbf{k}_f - \mathbf{k}_i) \cdot \mathbf{r}_n = \mathbf{q} \cdot \mathbf{r}_n \quad (2.4)$$

For a more general consideration of interference during scattering from an arbitrary crystal lattice, the intensity of the resulting electromagnetic wave becomes important. The scattering intensity is proportional to the product of the *form factor* $S(\mathbf{q})$, which can be interpreted as the three-dimensional Fourier transform of the sample's crystal lattice reflecting on its macroscopic size and shape,⁶⁹ and the absolute square of the *unit cell structure factor* $F(\mathbf{q})$ that is given by

$$F(\mathbf{q}) = \sum_{n=1}^N f_n \exp(-i\mathbf{q}\mathbf{r}_n) = \sum_{n=1}^N f_n \exp(-i\Delta\varphi_n) \quad (2.5)$$

with the atomic form factor of the n -th atom f_n . Based on the form factor $S(\mathbf{q})$ that takes into account the phase differences from the sum of all lattice sites inside the crystal, the important condition for constructive interference from a three-dimensional crystal lattice results that is called the *Laue condition*:

$$\mathbf{q} = \mathbf{G}_{hkl} \quad (2.6)$$

in which \mathbf{G}_{hkl} is the general reciprocal lattice vector

$$\mathbf{G}_{hkl} = h\mathbf{c}_1^* + k\mathbf{c}_2^* + l\mathbf{c}_3^* \quad (2.7)$$

constructed by integer numbers h, k, l and the reciprocal lattice unit cell vectors $\mathbf{c}_1^*, \mathbf{c}_2^*, \mathbf{c}_3^*$. In other words, **Equation 2.6** and **2.7** mean that, if the scattering vector coincides with a specific vector of the reciprocal crystal lattice, a non-vanishing scattered wave is observable. This insight will become especially important later on for understanding two-dimensional diffraction patterns.

The reciprocal crystal lattice is the Fourier transform of the real crystal lattice and, therefore, is the representation of the crystal lattice in the reciprocal space. Based on the unit vectors $\mathbf{c}_1, \mathbf{c}_2, \mathbf{c}_3$ of the real space crystal lattice, the principle axes vectors in the reciprocal space ($\mathbf{c}_1^*, \mathbf{c}_2^*, \mathbf{c}_3^*$) can be described as follows:

$$\mathbf{c}_1^* = 2\pi \frac{\mathbf{c}_2 \times \mathbf{c}_3}{\mathbf{c}_1 \cdot (\mathbf{c}_2 \times \mathbf{c}_3)} \quad (2.8)$$

$$\mathbf{c}_2^* = 2\pi \frac{\mathbf{c}_3 \times \mathbf{c}_1}{\mathbf{c}_2 \cdot (\mathbf{c}_3 \times \mathbf{c}_1)} \quad (2.9)$$

$$\mathbf{c}_3^* = 2\pi \frac{\mathbf{c}_1 \times \mathbf{c}_2}{\mathbf{c}_3 \cdot (\mathbf{c}_1 \times \mathbf{c}_2)} \quad (2.10)$$

As a final note, it shall be added that the real scattered wave intensity depends on many more factors than the form factor and structure factor alone, such as: multiplicity (number of equivalent scattering planes leading to a common scattering angle), geometry factor (specific scaling of the intensity with the scattering angle), preferred orientation of crystallites (*texture*), X-ray polarization, and absorption.

2.1.2. XRD Measurement Techniques

With this fundamental understanding of the scattering phenomenon, we discuss two different XRD measurement geometries that are primarily used for MOF characterization. These are the θ - 2θ coupled scan (also called *Bragg-Brentano geometry*) and the grazing-incidence 2θ scan, which are sketched in **Figure 2.2**.

In a θ - 2θ measurement (**Figure 2.2a**), X-ray source and detector (usually a 1D strip detector) simultaneously move upwards on a goniometer with the sample in its center. This procedure keeps the scattering vector \mathbf{q} always pointed vertically upwards. In consequence, only crystallographic planes that are horizontally aligned can be probed by the measurement. This is why the measurement is also sometime called *out-of-plane* XRD. In an oriented thin film, this property is used as an indicator for its texture. If the crystallites exhibit a preferred orientation, only a subset of all possibly visible diffraction peaks will be recorded. If the crystal lattice of the measured material is precisely known, the obtained peaks can be identified to describe the film texture, by naming the crystal plane horizontally aligned to the substrate. In the context of powder XRD (PXRD) measurements, preferred orientation is not an issue since the

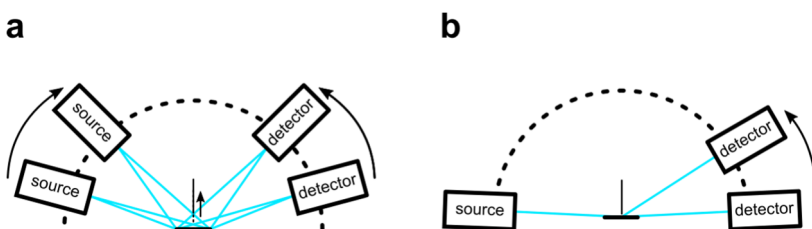


Figure 2.2. XRD measurement techniques. **a)** θ - 2θ coupled scan. **b)** 2θ scan. In the coupled scan, the source and the detector move synchronously upwards. A divergent beam is used in combination with a movable scattering shield in the center above the sample to keep the illuminated area constant. In the 2θ scan, the source is fixed for a low angle illumination of the sample with a collimated X-ray beam, while only the detector moves.

crystallites' spatial configurations are fully random (given a small enough grain size and totally filled sample holder). In this special case, θ - 2θ scans can also be used for phase identification. Examples of how such PXRD patterns can look like are given in **Figure 2.3** that are simulated based on face-centered cubic crystal structures (Si in **Figure 2.3a** and UiO-66 in **Figure 2.3b**) from the literature.^{70,71} The diffraction peaks are labeled with the Laue indices indicating crystal lattice planes that are responsible for the constructive interference. In consequence of the different unit cell dimensions, approximately 5.3 Å in the case of Si and 20.8 Å in the case of the UiO-66 MOF, the diffraction peaks appear anti-proportionally at larger or smaller diffraction angles.

In the second type of measurement, the 2θ scan (**Figure 2.2b**), only the detector moves on the goniometer while the source is fixed at a very low incidence angle (measured from the substrate plane). Due to the X-rays interacting with the sample under a grazing incidence angle, the technique is very surface-sensitive and ideally suited for thin films even with very small layer thicknesses in the nm range. Grazing-incidence 2θ scans can be performed with a 1D detector. Apart from an upwards movement of the detector, as shown in the sketch, the detector could also be moved within the sample plane. This allows access to scattering from differently oriented crystallographic planes and is, hence, called *in-plane* XRD. However, an even more convenient way to record the diffraction pattern is using a 2D detector. With an area detector many diffraction maxima can be measured at once. Depending on the distance between sample and 2D detector, two different measurement regimes are distinguished. These are called grazing-incidence small-angle X-ray scattering (GISAXS, probing distances in the order of ~100 nm) and grazing-incidence wide-angle X-ray scattering (GIWAXS, probing distances in the order of ~1 nm). In this work, GIWAXS is the major tool used for structural thin film characterization. Therefore, the next section introduces general principles for this technique specifically.

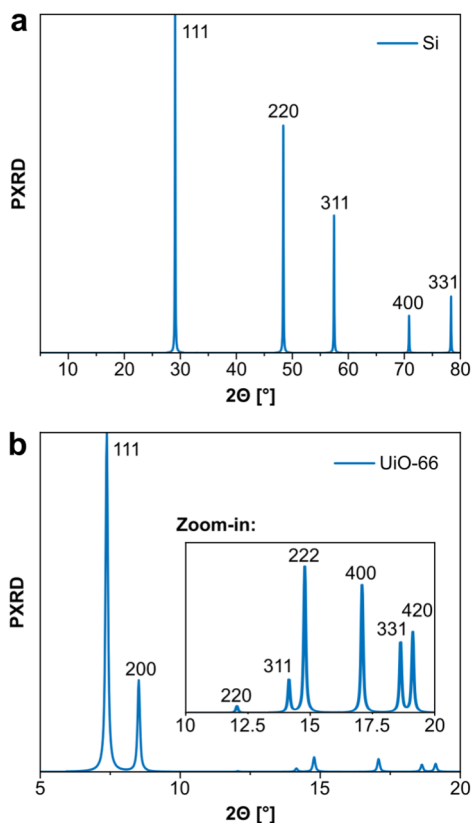


Figure 2.3. PXRD Examples. **a)** Silicon. **b)** UiO-66 MOF. Both unit cells exhibit a face-centered cubic crystal lattice according to space groups $Fd\bar{3}m$ (Si) and $Fm\bar{3}m$ (UiO-66). The diffraction peaks are labeled with their Laue indices indicating the crystallographic planes responsible for constructive interference. Since the unit cell dimensions of Si (5.3 Å) are much smaller than the ones of UiO-66 (20.8 Å), the peaks appear at higher diffraction angles than those of UiO-66. The shown PXRD patterns are simulated based on crystallographic data files from the literature.^{70,71}

2.1.3. GIWAXS: Scattering Geometry

Understanding a 2D diffractogram recorded with GIWAXS is significantly more complex than a pattern emerging from a coupled θ - 2θ scan. For this reason, first, we consider the 3D scattering under grazing-incidence irradiation in detail. Earlier we saw that for

constructive interference to occur in a crystal, the scattering vector \mathbf{q} needs to match the reciprocal lattice vector. In grazing-incidence scattering, a helpful visualization of this rule is given by the *Ewald Sphere*. This sphere is constructed by the incident and final wavevectors \mathbf{k}_i and \mathbf{k}_f whereby its surface signifies all possible scattering vectors realizations. This can be seen in the sketch in **Figure 2.4a**. As a consequence, the condition for constructive interference can be transferred to a graphical description by saying that the Ewald

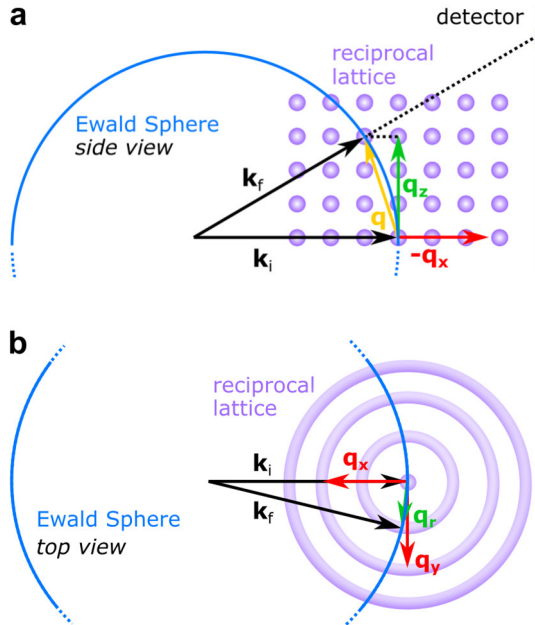


Figure 2.4. Elastic scattering described by Ewald Sphere. **a)** Side view. **b)** Top view. Incident and final wavevectors (black) form a three-dimensional sphere that determines all possible scattering vectors (yellow). If the scattering vector coincides with a reciprocal lattice vector (i.e. if the Ewald sphere intersects the reciprocal lattice), constructive interference is observed. If a mixture of crystallites is considered that have a common horizontal orientation but are randomly rotated about the vertical axis, the reciprocal lattice is smeared out to rings. This enables to describe an obtained scattering pattern in terms of the scattering vector components q_z and q_r . Adapted from Fischer et al. with permission (CC BY 4.0).⁷²

Sphere has to intersect the reciprocal lattice of the probed crystal structure. Each such instance is responsible for an individual scattering intensity maximum observable at a detector placed behind the sample. An important conclusion from this concept is that there are certain regions of the reciprocal space lattice that are inherently inaccessible in a GIWAXS measurement (every point that does not intersect with the Ewald sphere). The lattice along the real q_z axis, for example, cannot be probed as the deviation from the pure axis grows considerably with increasing scattering angle. This is why there will be certain areas in the resulting diffractogram where no data can be shown (the *missing wedge*). This can be observed in any GIWAXS diffractogram shown throughout **Chapters 4 – 6**. One might wonder what the chances are to see any diffraction peaks at all. In GIWAXS, a trick can be used to probe most of the reciprocal lattice. If a sample is measured that contains crystallites with a common horizontal alignment on the substrate but can be arbitrarily rotated about the vertical axis, this results in a combined reciprocal lattice that is smeared out into rings around the q_z axis. Such a crystallite configuration is called *2D powder* and applies for the majority of MOF thin films produced by liquid-phase deposition. This situation is shown by the top view in **Figure 2.4b**. Scattering from a 2D powder ensures that most types of reciprocal lattice points will intersect somewhere with the Ewald Sphere which greatly enhances the chances to observe a scattering pattern. If a thin film does not exhibit a 2D powder texture but a highly anisotropic structure, then sample rotation at a much faster rate than the image acquisition frequency can be used to achieve the same effect.⁶⁹ Since a distinction between q_x and q_y directions is not needed in such a case to describe the reciprocal lattice, a convenient measure is the combine these scattering vector components into one

$$q_r = \sqrt{q_x^2 + q_y^2}. \quad (2.11)$$

Theoretical Background

In **Figure 2.5**, simulated examples of GIWAXS diffractograms presented over q_r and q_z are given, based on 2D powders of the same

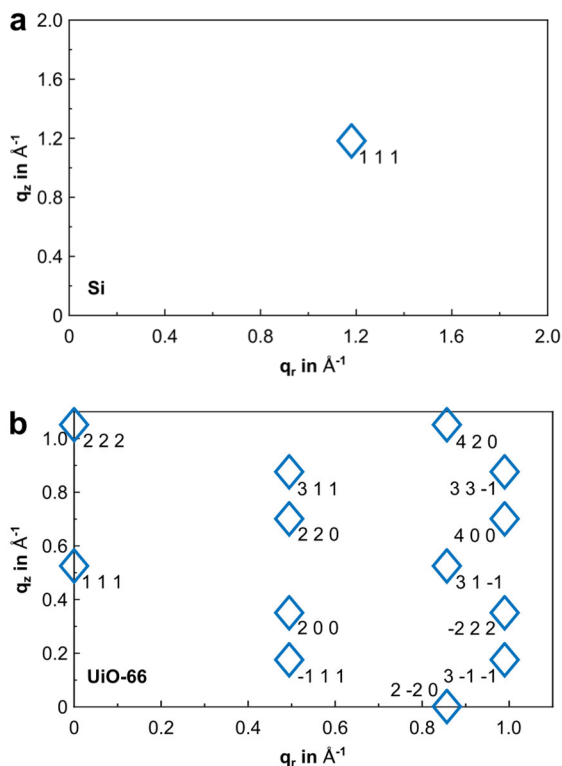


Figure 2.5. GIWAXS diffractogram examples of oriented crystals (2D powder). **a)** Silicon in $\langle 100 \rangle$ -orientation. **b)** UiO-66 MOF in $\langle 111 \rangle$ -orientation. The diffraction peaks are labeled with their Laue indices indicating the crystallographic planes responsible for constructive interference. The more tightly packed Si only shows one diffraction peak for the common $\langle 100 \rangle$ -orientation of Si substrates. In contrast, the UiO-66 MOF in $\langle 111 \rangle$ orientation shows much more diffraction peaks, even in a smaller scattering vector window. In case of the UiO-66, the $\langle 111 \rangle$ -orientation can be read-off the pattern by observing the $\{111\}$ and $\{222\}$ peaks along the q_z axis. This is different in the case of Si, because the first symmetry-allowed peak $\{400\}$ would only be observed at much higher scattering vector amplitudes along the q_z axis than would be probed by common measurement windows. The shown GIWAXS patterns are simulated based on crystallographic data files from the literature.^{70,71}

material systems as considered earlier for the PXRD in **Figure 2.3**, Si and UiO-66.^{70,71} The different unit cell dimensions are now reflected in higher or lower numbers of visible peaks within a given examination window. For $\langle 100 \rangle$ Si, only one peak is visible, indicated by a diamond symbol within in a 2 by 2 Å⁻¹ window. In contrast, for $\langle 111 \rangle$ UiO-66 with a roughly four times larger unit cell, much more diffraction peaks can be observed in an even smaller 1.2 by 1.2 Å⁻¹ window. The preferred crystallite orientation, here, can be seen by the $\{111\}$ peak (and its higher order $\{222\}$) appearing in the direction of the q_z axis. A more detailed discussion of the effect of crystallite orientation on the GIWAXS diffractogram will be given in **Section 2.1.4**.

All vectors and angles that are relevant to describe the X-ray scattering in grazing-incidence and to represent an obtained diffractogram over reciprocal space coordinates are illustrated in **Figure 2.6**. The three scattering vector components are then given by

$$q_z = \frac{2\pi}{\lambda} (\sin(\alpha_i) + \sin(\beta_\perp)) \quad (2.12)$$

$$q_y = \frac{2\pi}{\lambda} \sin(\beta_\parallel) \cos(\beta_\perp) \quad (2.13)$$

$$q_x = \frac{2\pi}{\lambda} (\cos(\beta_\parallel) \cos(\beta_\perp) - \cos(\alpha_i)) \quad (2.14)$$

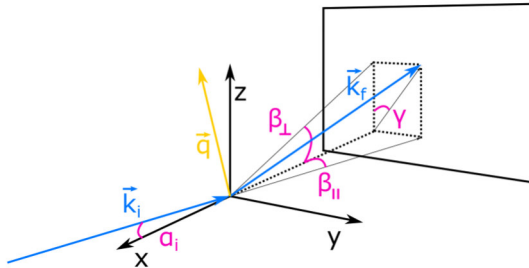


Figure 2.6. Important vectors and angles in grazing-incidence scattering. Adapted from Fischer et al. with permission (CC BY 4.0).⁷²

Theoretical Background

with the incidence angle α_i and the orthogonal scattering angle out-of-plane and in-plane components β_{\perp} and β_{\parallel} .^{73,74} Regarding the scattering angle, there is an important aspect to consider that is related to the reflection geometry in GIWAXS. Due to the possibility for X-rays to bounce off the substrate before or after a scattering event inside the thin film, four different cases arise (no reflection, reflection before scattering, reflection after scattering, reflection before and after scattering). The consideration of such multiple scattering effects is known as *Distorted Wave Born Approximation (DWBA)*.⁷³ As a result, scattering is observed under two slightly different angles that vary with the incidence angle. The out-of-plane component β_{\perp} is given by

$$\beta_{\perp} = \sin^{-1} \left(\left(\frac{q_z}{k} \right)^2 + (\sin(\alpha_i))^2 \mp \frac{2q_z}{k} \sqrt{n^2 - 1 + (\sin(\alpha_i))^2} \right)^{\frac{1}{2}} \quad (2.15)$$

and the in-plane component β_{\parallel} by

$$\beta_{\parallel} = \cos^{-1} \left(\frac{(\cos(\beta_{\perp}))^2 + (\cos(\alpha_i))^2 - \left(\frac{q_z}{k} \right)^2}{2 \cos(\beta_{\perp}) \cos(\alpha_i)} \right) \quad (2.16)$$

with k being the wavenumber of the incident X-ray photons.⁷³ The minus term in **Equation 2.15** corresponds to direct scattering (and potential reflection afterwards) and the plus term from indirect scattering after reflection from the substrate (and potential reflection afterwards again). The resulting two different diffraction peaks can be notably observed next to each other for a certain intermediate range of incidence angles that is dependent on the measured material and the X-ray wavelength. For smaller angles, the reflection beam almost perfectly coincides with the transmission beam and vanishes completely at higher incidence angles (see for a more detailed analysis of this phenomenon *e.g.* Savikhin *et al.*).⁷⁵ The GIWAXS

measurements presented throughout this work were taken at incidence angles where no double peaks are observable.

To summarize this section: What we see on the detector is not a direct reciprocal space representation of the crystal lattice but the interception of the reciprocal lattice with the Ewald sphere. This means that the image recorded by the 2D detector actually represents the surface of a sphere and, hence, the horizontal and vertical pixel axes of the detector do not correspond to orthogonal scattering vector components in the diffractogram.⁷³ In order to transform such an image into a physically meaningful presentation that allows to draw conclusions about the crystal lattice, it must be projected along the orthogonal scattering vector components q_z and q_r . This 2D image transformation of experimental data can be performed with readily available open-access software such as GIXSGUI,⁷³ or GIDVis,⁷⁶ among others.

2.1.4. GIWAXS: Crystallite Orientations

Now that X-ray scattering in grazing-incidence geometry has been established, we take a closer look at the features created in the diffractogram by different types of crystallite orientations (also known as thin film textures). At first, we imagine the already mentioned 2D powder in which crystallites have a common horizontal orientation but random vertical rotation. In simple terms, this can be expressed by: all crystallites lie with the same side on the substrate, as is depicted in **Figure 2.7a**. The reciprocal lattice of all these crystallites combined takes the shape of rings around the q_z axis (**Figure 2.7b**). With the GIWAXS measurement only a two-dimensional slice through the 3D reciprocal lattice is observed which corresponds to scattering from a small subset of crystallites with the correct vertical rotation to cause constructive interference.⁷⁷ In the case of a *3D powder*, all crystallites are fully randomly oriented, *i.e.* there is no

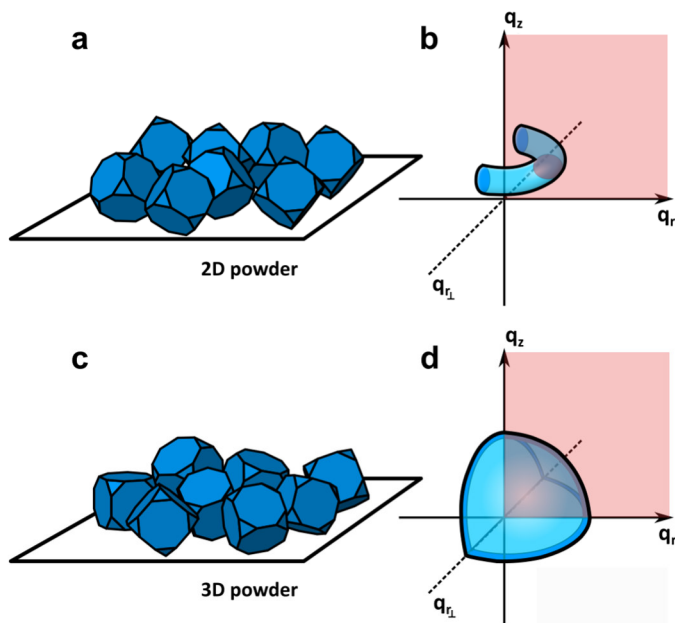


Figure 2.7. Crystallite orientations in real space and reciprocal space. **a)** Crystallites with common horizontal orientation but with random vertical rotation (2D powder texture). **b)** Representation of 2D powder crystallites in reciprocal space. **c)** Crystallites with fully random orientation (3D powder texture). **d)** Representation of 3D powder crystallites in reciprocal space. The random crystallite orientation in one or two dimensions translates to rotationally symmetric reciprocal space representations for the sum of all crystallites. Adapted from Fischer et al. with permission (CC BY 4.0).⁷²

common side on which they lie on the substrate. This is illustrated in **Figure 2.7c**. Following the same principle as above, the combined reciprocal space representation of these crystallites is equal to a sphere (**Figure 2.7d**). The 2D slice seen by the GIWAXS measurement projected onto the q_z - q_r plane, consequently, has the shape of a circle. In summary, if one observes individual spots in a 2D diffractogram, this points towards oriented crystallites; whereas, if rings are visible, the crystallites have no preferred orientation. Taking a step further, we can also consider an in-between case. In a real thin film, crystallites rarely possess a perfect texture throughout the whole sample.

Instead, there is a certain angular distribution around a specific preferred orientation that is also called *mosaicity*. The mosaicity is reflected by the azimuthal width of a diffraction peak.^{69,78} In the most extreme case of fully isotropic crystallites, a peak is smeared out into a ring. In a less extreme manifestation, this leads to an azimuthal elongation of the diffraction spot making it more ellipsoidal. Estimation of the azimuthal full width at half maximum (FWHM) can provide a measure for the average angular deviation of crystallites from a given perfect texture. In case of two different crystallite textures where one is a 2D powder and the other is a 3D powder, the respective crystallite fractions can be derived by evaluating an azimuthal line cut (also called *pole figure*). While the 3D powder constitutes a constant value scattering intensity across the azimuthal angle γ , the 2D powder creates a Gaussian peak at a specific location. The ratio of the respective area under these curves then gives the ratio of the two crystallite moieties.^{79–84} The implementation of this measure applied to crystallite fractions in UiO (Norwegian abbreviation for Universitet i Oslo)⁸⁵ MOF thin films is explained in detail **Chapter 4**. To obtain a quantitative comparison between the crystallite fractions with 2D and 3D powder texture from the azimuthal pole figure, a $\sin(\gamma)$ correction factor needs to be applied to the scattering intensity over angle $I(\gamma)$.^{81,83,84} As seen earlier from **Figure 2.7**, crystallites in thin films with 2D powder texture create smeared out toroidal shaped reciprocal lattices of which only a very small subset is actually probed. The $\sin(\gamma)$ term relates the measured intensity $I(\gamma)$ to the radius of reciprocal space torus and thereby scales the scattering intensity as if all crystallites with 2D and 3D powder would be observable.

2.1.5. GIWAXS: Depth Dependence

An interesting optical property of X-rays emerges from their refractive index. The general refractive index for X-rays is:

$$n = 1 - \delta - i\beta \quad (2.17)$$

Theoretical Background

with the real part $\delta = \rho_e r_e \frac{\lambda^2}{2\pi}$ (containing the sample's electron density ρ_e and electron radius r_e) and the imaginary part $\beta = \frac{\lambda}{4\pi} \mu$ (with the sample's linear attenuation coefficient). δ usually takes values of the order of 10^{-5} to 10^{-6} in solids and 10^{-8} in air. β is much smaller than δ with common values from 10^{-7} to 10^{-8} .⁶⁹ A peculiar consequence of the real part of the refractive index being negative is the observation of total external reflection for small incidence angles that are below the material-specific critical angle

$$\alpha_c = \sqrt{2\delta} \quad (2.18)$$

An important consequence of this phenomenon is the incidence-angle-dependent probing depth of X-rays. For angles smaller than the critical angle ($\alpha_i < \alpha_c$), there is an evanescent penetration of X-rays into the sample material. For small incidence angles close to the critical angle, the 1/e penetration depth of X-rays can be estimated by

$$d_{\frac{1}{e}} = \frac{\sqrt{2}}{4\pi} \frac{\lambda}{\sqrt{\sqrt{(\alpha_i^2 - \alpha_c^2)^2 + 4\beta^2} - (\alpha_i^2 - \alpha_c^2)}} \quad (2.19)$$

At this depth, the X-ray intensity has decreased to 1/e of its initial value. At $\alpha_i = \alpha_c$, an enhancement of the evanescent wave occurs created by constructive interference of incident and reflected waves, approximately doubling the electric field amplitude and quadrupling the intensity.⁶⁹ For $\alpha_i > \alpha_c$, X-rays are fully transmitted through the whole sample material. The dependence of the penetration depth from the incidence angle provides a certain control over the probed volume of a thin film sample enabling to additively scan through its volume from the surface onwards.

Another factor influencing the probed sample volume that should be mentioned is the beam footprint. Assuming a perfectly parallel beam

with a given width w_{beam} , the beam footprint on the sample along the X-ray propagation direction is given by

$$l_{Footprint} = \frac{w_{beam}}{\sin(\alpha_i)}. \quad (2.20)$$

Especially if samples with a large diameter of multiple centimeters are to be examined, the footprint notably decreases with the incidence angle changing the probed sample volume. In this work, only very small samples with a maximum length of approximately 1 cm were measured. Hence, the footprint size is of lesser importance (see Chapter 4).

2.2. Electronic States in Organic Molecules

The optical properties of organic constituents are determining factors for the functionality of MOFs. Deliberate choice of organic linkers can, for example, enable photoluminescent sensing.^{54,86,87} This section shall provide a concise overview of the main theoretical concepts to understand the phenomena of photon absorption and emission in organic molecules. The explanations are predominantly based on the textbooks *Electronic processes in Organic Semiconductors* by Köhler and Bässler,⁸⁸ and *Molecular Fluorescence: Principles and Applications* by Valeur and Berberan-Santos.⁸⁹

2.2.1. Molecular Orbitals

In order to describe optical properties of chromophores (*i.e.* the molecular parts determining a material's color), their electronic behavior needs to be understood first. Electronic states of organic molecules are described on the basis of electron orbitals. Since organic ligands always contain carbon atoms, we consider such an atom as an example. Carbon comprises 6 electrons that are in a $1s^2 2s^2 2p_x^1 2p_y^1$ configuration in its ground state. This terminology reads as two electrons being (in ascending energetic order) in the 1s orbital, two electrons in the 2s orbital. The two remaining electrons

Theoretical Background

are distributed over the three equal $2p_x$, $2p_y$ and $2p_z$ orbitals. When the carbon atom comes into the vicinity of a binding partner, for example hydrogen, the energetic differences between $2s$ and $2p$ atomic orbitals are compensated leading to a degenerate electronic state. This means that electrons have equal likelihood of being found in one of the two orbitals at the same time, thereby forming a new type of orbital, a *hybrid orbital*. Depending on the number of mixed $2s$ and $2p_{xyz}$ orbitals, different hybrid orbitals emerge. For example, mixing of all four atomic orbitals forms four equal $2sp^3$ hybrid orbitals, while mixing with only two or one $2p_{xyz}$ orbital(s) creates $2sp^2$ or $2sp$ hybrid orbitals. The process of orbital hybridization is the basis to understanding all following electronic states and the resulting optical properties. In the next step, the interaction between two carbon atoms with already hybridized orbitals shall be considered. As an educational example, a basic carbon-based molecule by the name ethene that consists of two CH_2 molecules is sketched in **Figure 2.8a** and **b**. Two hydrogen atoms per carbon atom give rise to three $2sp^2$ hybrid orbitals in the $2p_x$ - $2p_y$ plane with a remaining orthogonal $2p_z$ orbital. Electrons in the unpaired $2sp^2$ orbitals of each singular CH_2

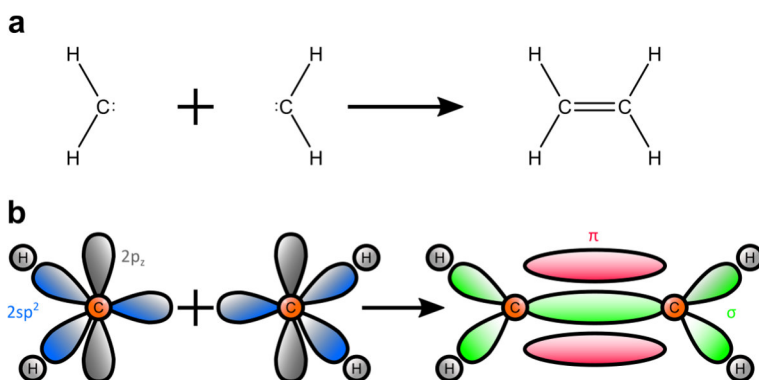


Figure 2.8. Molecular orbitals of ethene. **a)** Molecular structure of ethene. **b)** Colored illustration of the same structures as in a). Ethene is formed by two merged CH_2 molecules with $2sp^2$ hybridized orbitals. When bonded, these result in shared π - and σ -orbitals. Adapted from Köhler and Bässler.⁸⁸

molecule can form a bond which is called σ -bond and the corresponding orbital a σ -orbital (green in **Figure 2.8b**). In parallel, the respective $2p_z$ electrons form a π -bond. Consequently, these electrons will be encountered above or below the molecular axis, within the π -orbital (red in **Figure 2.8b**). As a result of the overlapping $2p_z$ and $2sp^2$ orbitals, the carbon atoms in the ethene molecule are paired by two bonds. Electrons in the thereby created *molecular orbitals* have equal probability to be found in either of the two atoms participating in the bond. A molecular orbital can be described by linear combinations of atomic orbitals and interpreted as a superposition of electron wavefunctions. Such superposition can give rise to *bonding orbitals* (constructive interference) with enhanced charge density and *anti-bonding orbitals* (destructive interference) with reduced charge density. The bonding or anti-bonding characters of these two cases can be understood as effective and less effective screening of the nuclei's positive charges, that either leads to attraction in bonding orbitals or repulsion in anti-bonding orbitals (labeled with a *). The splitting into bonding and anti-bonding electronic states can be illustrated by the energy diagram shown in **Figure 2.9**. The electrons initially occupying the non-bound $2p_z$ and $2sp^2$ atomic orbitals fill up

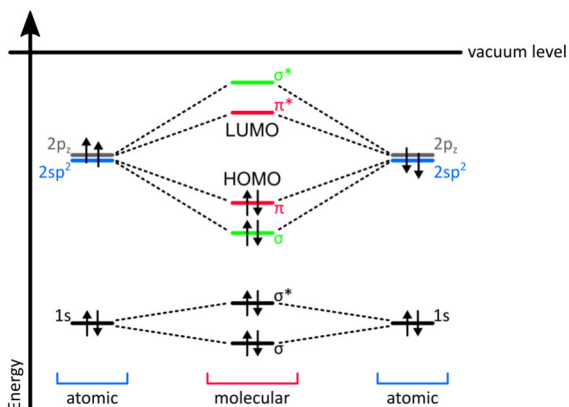


Figure 2.9. Splitting of energy levels in ethene molecule. Only energy states related to carbon-carbon bond are shown. Adapted from Köhler and Bässler.⁸⁸

the lower energy π - and σ -orbitals while leaving the higher energy anti-bonding π^* - and σ^* -orbitals empty. This makes the π -orbital the *highest occupied molecular orbital* (HOMO) and the π^* -orbital the *lowest unoccupied molecular orbital* (LUMO). These orbitals are decisive for the molecule's absorption and emission characteristics. The less pronounced energetic splitting of the π and π^* -orbital, in contrast to the σ - and σ^* -orbitals, is a consequence of the overlapping electron densities being located further away from the molecular axis. This also renders the π and π^* -orbitals less involved in the created attractive forces between the carbon atomic nuclei. As there is no overlap between π and σ orbitals, electrons in these two states can be considered independent. In this context, it should be noted that the further the π orbital is extended the smaller the energy gap between the π and π^* levels. A change of this energy gap directly influences the emission and absorption spectra of the organic molecules. An example of this based on different aromatic (*i.e.*, cyclic conjugated) molecules in which π electrons are delocalized across multiple carbon atoms will be discussed later.

2.2.2. Molecular Excited States and Electronic Transitions

After establishing different types of molecular orbitals, we discuss the electronic transitions between them. By absorbing a photon of sufficient energy, an electron can be promoted from the HOMO to the LUMO bringing the molecule into an *excited state*. If these are π - and π^* -orbitals, absorption of photons from the range of visible light (~ 2.5 eV) are suitable for such a transition. In case of σ - and σ^* -orbitals as HOMO and LUMO, the energetic difference would be higher, leading to absorption in the ultraviolet (UV, ~ 8 eV) range instead. This simple Gedankenexperiment only incorporated a single electron. In general, there are interactions between different electrons in a molecule which makes it more appropriate to regard an excited state as the superposition of multiple electron configurations. This is depicted by **Figure 2.10** showing the ground state (S_0) and first

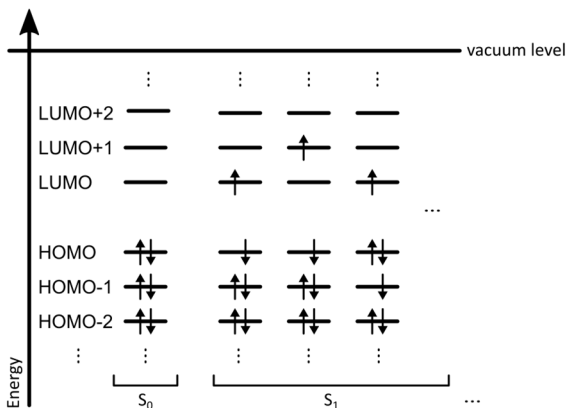


Figure 2.10. Molecular excited states. Due to interactions between multiple electrons inside a molecule, a simple excited state based on a single electron configuration is extremely unlikely to occur. A more suitable model of an excited state is, therefore, a superposition of multiple electron configurations. Adapted from Köhler and Bässler.⁸⁸

excited state (S_1). Based on this diagram, the excited state can be made up of electrons in the LUMO (or LUMO+1) and a missing electron, or hole, in the HOMO (or HOMO-1) state. If these electron-hole pairs are coulombically bound to each other, they can be regarded as a quasi-particle that is also referred to as an *exciton*. Based on the average distance between bound electron and hole, two types of excitons are generally distinguished. For large distances of the order ~ 100 nm, they are called Wannier-Mott exciton. In case of smaller distances of the order of ~ 1 nm they are referred to as Frenkel excitons. Since this work deals with MOFs that exhibit localized excitations within their linker molecules, excitons are of the Frenkel-type, here.

When an electron is promoted from the ground state into a higher energy state, its spin has to be considered as well. The total spin of a certain energy state is determined by the spins of all electrons across all orbitals. As the total spin of paired electrons (with anti-parallel spins) always adds up to zero, only the unpaired electrons are of

interest for this calculation. Excited states with unpaired electrons in HOMO and LUMO with antiparallel spin are referred to as *singlet* states, while those with parallel spin would be called *triplet* states. This terminology arises from the unpaired electrons building a two-particle system that can be in four different states. In three of these states, the total spin is one (triplet), in one state it is zero (singlet).⁹⁰ With the ground state assumed to always be a singlet state (S_0), optical excitation will always lead to an excited singlet state (S_1, S_2, \dots) as well. By a process called *inter-system-crossing*, the spin of the electron in the LUMO can flip which results in a triplet excited state T_1 (T_2, \dots) with vastly different optical properties as compared to singlet states. However, such states are not important for this work and are therefore only mentioned briefly here.

Experimentally, molecular transitions due to the absorption of light can be characterized by *transmittance* $T(\lambda)$ and *absorbance* $A(\lambda)$ that are both dependent on the photon wavelength λ , which is inversely proportional to the photon energy ($E_{ph} = \frac{hc}{\lambda}$, with h Planck's constant). The absorbance is a decadic, dimensionless quantity that determines the exponential decrease of an initial light intensity passing through a sample material (Lambert-Beer law):

$$I_s(\lambda) = I_0 10^{-A(\lambda)} \quad (2.21)$$

with $I_0(\lambda)$ and $I_s(\lambda)$ being the light intensities before and after passage through the sample. Another representation, especially useful when dealing with organic molecules in solutions, is:

$$I_s(\lambda) = I_0 10^{-\varepsilon(\lambda)cl} \quad (2.22)$$

with the decadic extinction coefficient $\varepsilon(\lambda)$, the concentration c and the optical path length l . When the transmittance is defined as

$$T(\lambda) = \frac{I_s(\lambda)}{I_0(\lambda)} \quad (2.23)$$

the absorbance can be readily obtained from a measured transmittance spectrum by:

$$A(\lambda) = \log\left(\frac{1}{T(\lambda)}\right) = -\log(T(\lambda)) \quad (2.24)$$

In classical theory, the transition between electronic states due to photon absorption, is described by regarding the molecule as a dipolar oscillator. Based on this model, the dimensionless quantity *oscillator strength* f can be derived

$$f = \frac{4 \ln(10) \varepsilon_0 m_e c^2}{N_a e^2 \lambda_{trans}^2} \int \varepsilon(\lambda) d\lambda \quad (2.25)$$

with the vacuum permittivity ε_0 , mass m_e and charge e of an electron, the vacuum light speed c , Avogadro's constant N_a , and the wavelength at which the transition occurs λ_{trans} . The oscillator strength is a measure for the probability of a transition to occur, exhibiting values close to one for strong molecular transitions and close to zero for weak molecular transitions. From quantum mechanical theory, another measure emerges that relates to the magnitude and direction of the transient displacement of charges taking place during a transition. The absolute value of the *transition moment* can be calculated by

$$|M_{12}| = \sqrt{\frac{3 \ln(10) h c \varepsilon_0}{2 \pi^2 N_a \lambda_{trans}}} \int \varepsilon(\lambda) d\lambda. \quad (2.26)$$

The transition moment corresponds to the spatial axis of a molecule along which absorption occurs and can be very important in case of organic molecules that are in predetermined three-dimensional configurations. An example for the transition moments in an extended organic molecule is given by anthracene in **Figure 2.11**. Two transition moments oriented along the long and short molecular axis

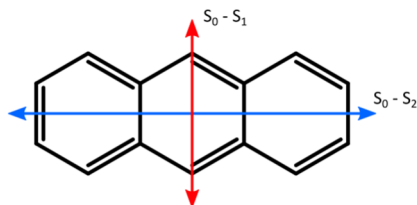


Figure 2.11. Absorption transition moments in anthracene. The moments along the short and long molecular axes correspond to lower and higher energy transitions from the ground state S_0 to S_1 and S_2 , respectively. Adapted from Valeur and Berberan-Santos.⁸⁹

correspond to higher energy ($S_0 \rightarrow S_2$) and lower energy transitions ($S_0 \rightarrow S_1$).

Due to the large difference in mass between the atomic nuclei and electron clouds, the latter are usually considered to respond instantaneously to a change of configuration by external forces, while the nuclei remain static. This is called the *Born-Oppenheimer approximation*. Nuclear vibrational motion can also be considered slow (on the time scale of 10^{-10} to 10^{-12} s) in comparison to a photon absorption event ($\sim 10^{-15}$ s). An interesting consequence arises when considering molecular vibration in this context. During photo-excitation, the electron cloud changes its configuration instantaneously while the atomic nuclei remain (initially) still. Therefore, transitions are most probable between states that have similar spatial configurations of the nuclei (*Franck-Condon principle*). This translates into vertical transitions from the ground state into vibrational levels in the excited state and also from the excited state to vibrational levels in the ground state (see energy diagram sketch in **Figure 2.12a**). The wavefunction overlap between initial and final quantum states, thereby, determines the transition probabilities and gives rise to the vibronic peaks visible in absorption and emission spectra of the molecule, as illustrated in **Figure 2.12b**. The photon emission phenomenon will be introduced in the next section. The

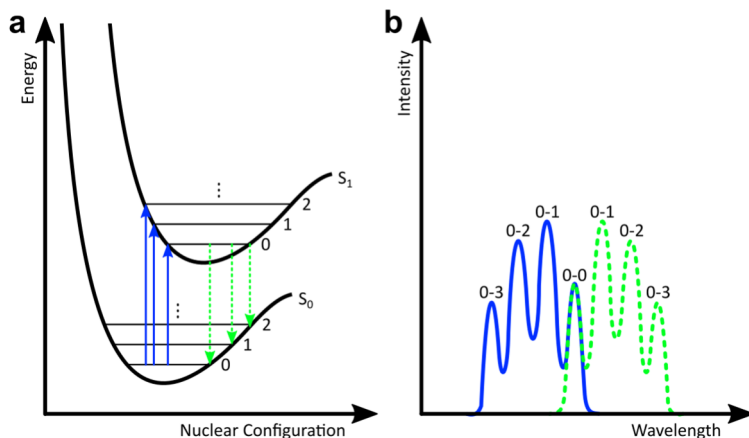


Figure 2.12. Franck-Condon principle sketch. **a)** Potential energy curves of ground state (S_0) and first excited state (S_1) with vibrational sublevels indicated by numbers. **b)** Absorption (blue) and emission (green) spectra resulting from vertical transitions in the energy diagram. The fused individual peaks in the spectra reflect transitions between different molecular vibrational states. Adapted from Köhler and Bässler, and Valeur and Berberan-Santos.^{88,89}

shifted potential energy curve of the excited state in **Figure 2.12a** can be understood when picturing the molecular orbitals electrons occupy in this state: a reduced number of electrons will be found in bonding orbitals and, instead, reside in an anti-bonding orbital. The reduced attractive forces between atomic nuclei increases their average mutual distance, which is reflected in the shift along the nuclear configuration axis. The integer numbers correspond to different vibrational sublevels of the respective energy state.

2.2.3. Excited State Relaxation

So far, we have discussed the electronic transitions in response to photon absorption. In the opposite direction, from an excited state back towards the ground state, there are multiple routes of molecular relaxation. The two main pathways can be distinguished as non-radiative and radiative processes that occur at rates $k_{non-rad}$ and

Theoretical Background

k_{rad} , respectively. The natural excited state lifetime τ , therefore, can be expressed by:

$$\tau_{nat} = \frac{1}{k_{rad} + k_{non-rad}} \quad (2.27)$$

Non-radiative transitions are termed *internal conversion* between electronic states with equal spin multiplicity (e.g. $S_2 \rightarrow S_1$), and inter-system crossing in case a spin flip is involved (e.g. $S_1 \rightarrow T_1$). Transition from a higher to a lower excited state is often followed by *thermal relaxation* from a higher vibrational state to the lowest vibrational state within the S_1 state. Thereby, the excess energy is released in the form of phonons. This relaxation cascade brings the molecule into the lowest vibrational level of the S_1 state very fast, usually within a time of $\sim 10^{-12}$ s.

Radiative transition from $S_1 \rightarrow S_0$ is called *fluorescence*. This process gives rise to the emission of photons whose energy corresponds to the energy gap between the first excited state and ground state. Since these radiative transitions happen rather slow compared to internal conversion and thermal relaxation, often on a time-scale of $\sim 10^{-9}$ s, photon emission usually – there are exceptions, for example azulene – happens from the lowest excited state of a spin configuration. This effect is also known as *Kasha's rule*. Therefore, fluorescence emission properties are largely independent of the excitation energy. Due to the energy lost after excitation by internal conversion and thermal relaxation, the fluorescence spectrum of a molecule is located at longer wavelengths (lower energy) than its absorption spectrum. Since, generally, the energy differences of vibrational sublevels in ground and excited state are similar, fluorescence spectra commonly are the mirror image of the (first band) absorption spectrum. Besides fluorescence, there is also a process called *phosphorescence* which originates from $T_1 \rightarrow S_0$ radiative transitions. Like the inter-system crossing mentioned before, this is actually a spin-forbidden

transitions. Still they can be experimentally observed. This is only possible in case the triplet state wavefunction acquires a contribution of a singlet state wavefunction, or the other way around. A perturbation that can cause this situation is called *spin-orbit coupling*. However, since triplet states and phosphorescence are not in focus of this work, this topic will not be expanded on.

Photoluminescence (PL) processes (including fluorescence and phosphorescence phenomena) are in most cases based on *spontaneous emission*. Therefore, after a short excitation pulse, the molecule resides in the first excited state for a random period of time before relaxing to the ground state and emitting a photon. This entails an exponential decay of the photoluminescence intensity whose time scale reflects the statistical average lifetime of the molecules' excited state. The resulting PL intensity profile can be modeled exponentially

$$I(t) = I_0 e^{-\frac{t}{\tau}} + c \quad (2.28)$$

where τ is the $1/e$ lifetime, and c is the level of the background noise. In some cases, an excited state can relax via two different decay channels. This would be reflected in a double-exponential profile

$$I(t) = I_1 e^{-\frac{t}{\tau_1}} + I_2 e^{-\frac{t}{\tau_2}} + c \quad (2.29)$$

Such exemplary PL decay profiles are shown in **Figure 2.13**. Typical fluorescence lifetimes range from picoseconds to nanoseconds, while phosphorescence lifetimes are much larger, commonly on the scale of microseconds up to seconds.

Besides the excited state lifetime, the photoluminescence quantum yield (PLQY) is an essential measure characterizing the emission of a molecule. The PLQY η is given by the ratio of radiative decay compared to all excited state decay processes:

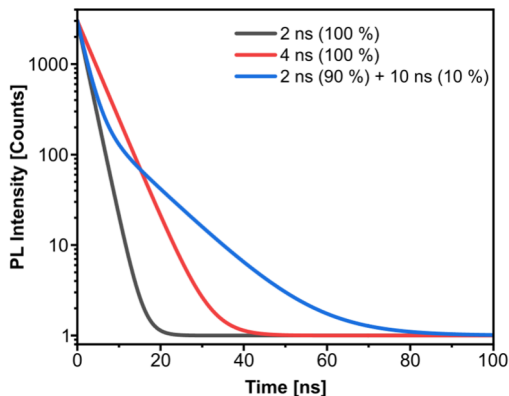


Figure 2.13. Excited state decay examples. Shown in semilogarithmic scale are two mono-exponential decay and one double-exponential decay with characteristic decay times as given in the legend. The offset of one mimics a low background noise level. Adapted from Köhler and Bässler.⁸⁸

$$\eta = \frac{k_{rad}}{k_{rad} + k_{nonrad}} = \tau_{nat} k_{rad} \quad (2.30)$$

which can also be interpreted as the likelihood of photon emission during the natural lifetime of the excited state, or the number of photons emitted per photons absorbed. The PLQY can be very different among common aromatic molecules dissolved in ethanol such as benzene (4 %), naphthalene (21 %), anthracene (30 %) or pyrene (65 %).^{89,91}

2.2.4. Molecular and Environmental Effects on Fluorescence

After gaining an understanding of the photophysical processes inside a single organic molecule, the influence of different external factors on its emission properties is discussed. Molecular orbitals and transitions can be altered by interactions with the environment, including other molecules or atoms. From the extremely broad palette of such effects, the ones relevant for this work shall be briefly summarized:

Conjugated π -networks: Most fluorescent chromophores (then also called *fluorophores*) are based on aromatic subgroups, *i.e.*, these molecules consist of ring-shaped molecular bonds with conjugated π systems. As a consequence of large-scale π -orbital coupling, electrons occupying these orbitals are delocalized across the whole aromatic group and the energy gap between the π^* - and π -orbitals is decreased. This effect gets more intense the larger the extent of the π -conjugated network which can be experimentally observed by an increase in absorption and emission wavelengths with the number of aromatic rings in the series of polycyclic hydrocarbons: naphthalene (2 rings, $S_1 \leftarrow S_0$: 310 nm, UV emission), anthracene (3 rings, $S_1 \leftarrow S_0$: 375 nm, blue emission), tetracene (4 rings, $S_1 \leftarrow S_0$: 470 nm, green emission).

Molecular aggregation and coupling: The impact of molecular aggregation on fluorescence properties is especially important in the context of densely packed chromophores inside MOFs. When organic molecules are situated in close proximity to each other, their excited states can couple (splitting of energy states) leading to changes in absorption and emission. The direction in which a spectral shift occurs depends on the mutual alignment of the transition moments. A side-by-side orientation (*H-aggregate*) leads to a forbidden lower energy transition causing a blue-shifted absorption and theoretically no photon emission (even though in real systems a weak emission might be observable due to slight misalignments or vibronic coupling). A head-to-tail configuration (*J-aggregate*) exhibits a forbidden higher energy transition that results in a red-shifted absorption and emission. Of particular importance in aromatic fluorophores is the π orbital coupling among aggregated molecules causing large-scale delocalization of excitons. Face-to-face alignment of anthracene-based molecules at a close distance has been shown to cause majorly red-shifted emission in comparison to the parent molecule.^{92–94} Besides influencing absorption and emission spectra, large π -orbital

overlap between adjacent aromatic molecules can often quench their fluorescence.^{94–96} Molecular coupling is an example for an interaction that can lead to more than one distinct excited state decay channel and can be responsible for a double-exponential PL decay, illustrated earlier in **Figure 2.13**.

Molecular rigidification: Emission from chromophores that are very flexible or whose subgroups can perform molecular rotations can be heavily influenced by surrounding molecules. In such chromophores internal conversion processes are dominated by relaxation *via* vibrational levels or different rotational modes which majorly contribute to energy being lost non-radiatively. This changes the excited state lifetime and leads to the counter-intuitive phenomenon of a much brighter fluorescence in highly aggregated molecules compared to largely isolated ones.^{97–99} Such molecular rigidification can be induced, for example, by steric effects due to close proximity of other bulky molecules preventing large-scale rotation. Another mechanism can be a coordinative immobilization enforced inside a MOF.^{100,101}

Solvent influence: Changes in the fluorescence (or absorption) of a molecule in response to being surrounded by solvent molecules are called *solvatochromic* shifts. The general reason for that is more or less improved stabilization of the ground and excited states of the solute due to interactions with the solvent molecules. Usually, the polarity of a molecule changes upon excitation as the electron cloud is redistributed. Hence, an especially strong interaction can occur with polar solvents, *i.e.* solvent molecules that carry a dipole moment.¹⁰² Furthermore, solvent molecules surrounding a solute molecule that performs internal rotations can have an influence on its emission comparable to the effect of rigidification by steric hindrance mentioned previously. An enhancement of solute radiative rates can be observed especially in highly viscous solvents. Consequently, if photoluminescent properties are determined for a molecule in

solution it is important to always state in which solvent it was dissolved.

2.2.5. Exciton Transport

Molecular excited states, *i.e.* excitons, can be transferred to another molecule, relaxing the original molecule to its ground state and promoting the other molecule into the excited state. The first straightforward manifestation of this process is emission of a photon by the first molecule which is then absorbed by the second molecule. This type of energy transfer is long-range, requires efficient absorption and emission and good overlap of the respective spectra. Over short ranges, energy can also be transferred non-radiatively *via* quantum chemical coupling. If the nature of the molecular coupling is an electromagnetic dipole-dipole interaction, the energy transfer is called *Förster transfer* or *Förster resonance energy transfer (FRET)*. In case of an electron exchange-type interaction, it is called *Dexter energy transfer (DET)*. Usually, FRET is the dominating transfer mechanism at distances greater than 1 nm, while DET prevails only at smaller length scales. From a quantum mechanical description of the two processes can be concluded that FRET requires both the molecules, in the excited state and in the ground state, to have the same spin multiplicity. For this reason, FRET can only take place between two molecules that respectively are in an S_1 and S_0 or in a $T_{>1}$ and T_1 state. The much more frequent option of the two is FRET between two singlet states. Further it can be seen that DET requires a strong wavefunction overlap between the quantum states of the two different molecules. As this is naturally the case in systems with efficient triplet state population, DET is most relevant among triplet states. In this work, only excited singlet states are important, so the FRET mechanism will be elucidated further.

A crucial quantity characterizing FRET, is the *Förster radius* R_0 . At this distance, energy transfer to a neighboring molecule is equally likely as

Theoretical Background

the spontaneous relaxation of the excited state, which is given by

$$R_0 = \sqrt[6]{\frac{9 \ln(10)}{N_A 128 \pi^5 n^4} \eta \kappa^2 f} \quad (2.31)$$

with the refractive index n , the orientation factor κ^2 , and the spectral overlap integral f . Depending on the mutual orientation of energy donor and acceptor molecules in space, κ^2 can take values 0 (perpendicular arrangement), $2/3$ (isotropic arrangement), 1 (parallel arrangement) or 4 (colinear arrangement). The spectral overlap between PL and extinction spectra is calculated by

$$f = \int I_{PL}(\lambda) \varepsilon(\lambda) \lambda^4 d\lambda \quad (2.32)$$

The energy transfer rate k_{FRET} across a distance r is then dependent of R_0 and the natural excited state lifetime τ_{nat} :

$$k_{FRET}(r) = \frac{1}{\tau_{nat}} \left(\frac{R_0}{r} \right)^6 \quad (2.33)$$

Thereby, efficient energy transfer usually occurs over distances of the order of the Förster radius, which commonly takes values from 1 to 4 nm. An energy transfer mechanism such as FRET provides excitons with a certain mobility (random hopping) inside a material containing organic chromophores. In regards to the temporal evolution of the excited state density n_{exc} after a given excitation pulse, this requires the consideration of mono- and bimolecular recombination processes. The relation is given by

$$\frac{\partial n_{exc}}{\partial t} = N_0 - k_{mono} n_{exc}(t) - k_{bi}(t) n_{exc}^2(t) \quad (2.34)$$

with the initial excited state density N_0 , the monomolecular recombination rate constant k_{mono} and the bimolecular rate constant k_{bi} . The monomolecular rate reflects all the transition

processes from the excited towards the ground state we already discussed above. In addition to that, the mobility of excited states can lead to collisions of excitons. This causes a very high excited state in one molecule, while the second molecule is relaxed to the ground state. The highly excited molecule quickly relaxes to the first excited state afterwards. This bimolecular process called *exciton-exciton annihilation* is a luminescence quenching mechanism that becomes more important as the exciton density in the material increases. In case of 3D exciton diffusion, the bimolecular rate constant can be regarded as time-independent.¹⁰³ This leads to the following solution for the exciton density:¹⁰³

$$n_{exc,3D}(t) = \frac{k_{mono}N_0}{e^{k_{mono}t}(k_{mono} + k_{bi}N_0) - k_{bi}N_0} \quad (2.35)$$

When spatially highly organized organic molecules are assumed, the exciton motion can become highly anisotropic. In the case of one-dimensional energy transfer, the bimolecular recombination rate constant needs to be treated as time-dependent variable,¹⁰⁴ which leads to the following exciton density over time:¹⁰³

$$n_{exc,1D}(t) = \frac{e^{-k_{mono}t}N_0}{2\pi L_{1D}R_0^2N_0 \operatorname{erf}(\sqrt{k_{mono}t}) + 1} \quad (2.36)$$

with the one-dimensional exciton diffusion length L_{1D} . Singlet exciton diffusion lengths usually range from 2 to 20 nm but can also majorly exceed these values up to an approximate maximum value of 230 nm in case of precisely aligned transition moments.^{56,105–107} The introduced concepts for singlet exciton transport will become important in **Chapter 6**.

2.3. Metal-organic Frameworks

Metal-organic frameworks (MOFs) are an extremely versatile class of artificial materials that has revolutionized the fields of materials science, chemistry and engineering. Precise choice of molecular

building blocks and their resulting functionality makes MOFs suitable across a multitude of very different applications such as gas sorption and separation,^{22,108–110} catalysis,^{111,112} optoelectronics,^{113,114} or light harvesting.^{115,116}

2.3.1. MOF Basics

In general, MOFs consist of metal clusters, commonly referred to as *secondary building units* (SBUs), that are connected by organic ligands (also referred to as *linkers*) to form extended networks. One of the most common types of coordination groups in MOFs are carboxylate anions that consist of two oxygen atoms bonded to a carbon atom.¹¹⁷ Depending on the possible oxidation states and the number of ligands attached to an SBU, different metal atoms can be incorporated. **Figure 2.14** shows three different exemplary realizations of SBUs. In **Figure 2.14a**, the Zn-based SBU of the IRMOF (isoreticular MOF) series first presented by Yaghi and co-workers is presented, with the most prominent member of this series being MOF-5.^{118,119} The cluster is formed by four Zn^{2+} ions coordinated with 6 carboxylate groups.

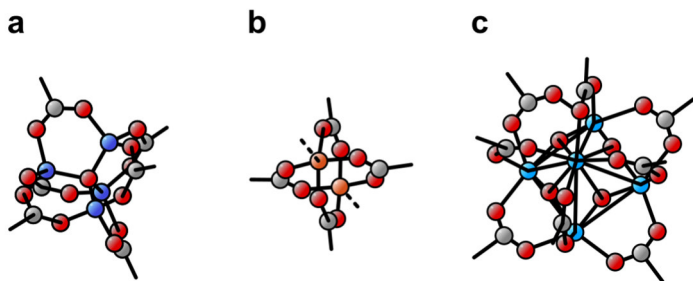


Figure 2.14. Different types of SBUs. **a)** Zn-based SBU of MOF-5. Six linkers surround a central cluster of four Zn atoms and one O atom. **b)** Cu-based paddle wheel SBU. Four linkers connect two Cu atoms in the same plane. At the apical sites, different types of linker or solvent molecules can attach. **c)** Zr-based UiO SBU. 12 linkers are coordinated with a central cluster of six Zr atoms and eight O atoms. For clarity, only the top half of the octahedral cluster is shown. C atoms are shown in grey, O atoms in red, Zn atoms in blue, Cu atoms in orange, Zr atoms in turquoise.

Illustrated in **Figure 2.14b** is a Cu-based paddle wheel cluster consisting of two Cu^{2+} ions surrounded by carboxylate anions. This type of SBUs, for example, occurs in MOF-2,¹²⁰ layer-pillar MOFs,^{121,122} or HKUST-1.¹²³ This cluster exhibits two additional coordination points at its apical sites orthogonal to the linker plane that can be occupied by solvent molecules of a different type than the layer linker. **Figure 2.14c** presents a Zr-based SBU that contains six Zr^{4+} ions that are held in an octahedral configuration by 12 carboxylate groups. The metal cluster is the basis of the isorecticular UiO MOF family that emerges from using different sorts of dicarboxylic ligands as linkers.⁸⁵ These MOFs are exceptionally stable structures still retaining their shape for temperatures up to 540 °C and pressures of the order of GPa.^{124,125} In all of these presented examples, the SBUs can be constructed with more than one type of metal atom.¹²⁶ Cu in paddle wheel clusters (**Figure 2.14b**) can be replaced by other transition metals such as Zn, Ni or Co,^{127,128} or the Zr in the UiO SBU can also be created based on Hf.^{129,130} The ability to deliberately choose the metal ions inside of a MOF allows for huge potential in engineering, for example, its optical properties.

Based on the example of the layer-pillar MOF mentioned in the context of the paddle wheel SBU in **Figure 2.14b**, different types of MOF geometries can be achieved based on the chosen linkers combined with the metal cluster. In general, the resulting MOFs can be categorized into 2D and 3D networks, sketched in **Figure 2.15a** and **b**. As alluded to earlier, the paddle wheel cluster offers two apical sites than can either be connected to surrounding solvent molecules (creating separate 2D MOF sheets), or to a second type of linker, then called *pillar linker* (and giving rise to a 3D pillar-layer MOF structure). A 2D MOF can be interesting due to the close proximity of neighboring linkers at a length scale below 1 nm to exploit resulting optical properties,^{56,131} or, for example, loading with intercalating molecules.¹³² The 3D type of MOF, on the other hand, provides full

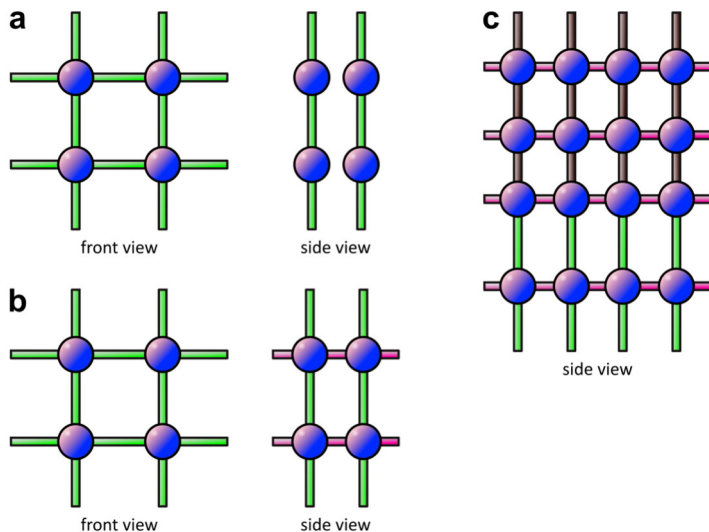


Figure 2.15. Generic types of MOFs. **a)** 2D MOF. **b)** 3D MOF. **c)** MOF-on-MOF heterostructure. Symbolized by purple spheres are the SBUs and the green, pink and red rods stand for different types of linkers that connect SBUs.

control of the pore volume and interlayer spacing by choice of linker molecules with different length. The different nature of the chemical bond between SBU and layer linkers vs. pillar linkers allows to independently tune pore dimensions along two crystal directions. This can go so far as to combine different MOFs to produce heterostructures fusing different properties and functionalities into one structure.^{133–135}

Based on the same simple model, a MOF-on-MOF heterostructure is illustrated in **Figure 2.15c**, where the upper part of the network consists of different pillar molecules connecting the SBUs in vertical orientation while the same layer linkers are used throughout the whole stack. A combined MOF system such as this one has the potential to be grown monolithically, *i.e.* grains from the bottom and top material are connected to each other on a molecular level preserving the crystal lattice. MOF heterostructures can also be

formed if the layer linkers are different in top and bottom part. This might lead to defects because of missing links between some of the metal clusters at the MOF boundary. However, due to the inherent elasticity of MOFs, templated heterostructures are possible to be formed even with significant differences of top and bottom layer unit cells.^{134,136,137} However, there can still be a templating effect that translates the crystal structure and orientation from the bottom layer towards the top layer. MOF-on-MOF heterostructures can be generated in the powder form,¹³⁴ but become even more interesting when grown in a controlled manner as MOF thin films. Oriented MOF heterostructure thin films, for example, can be especially appealing to control charge or exciton transport between different layers for optoelectronic applications.^{138–141} Thus, MOF heterostructures are highly desirable for future optoelectronic applications.

2.3.2. MOF Thin Films

For integration of MOFs into functional devices, fabrication of thin films with a uniform crystalline texture is highly desirable. Textured thin films are of special significance for multiple reasons. One reason is that common alignment of pores can result in extended channels controlling molecular diffusion inside the material that can be beneficial for gas storage, membrane, or catalytic applications.^{142–145} Another one is that large-scale anisotropy can have important consequences for optoelectronic properties such as directional exciton or charge transport.^{56,57,146–148} Ultimately, the ability to choose a specific crystallite orientation provides positioning control over organic ligands in three-dimensional space. In the literature, different techniques have been proposed for the controlled synthesis of oriented MOF thin films that can be divided into two groups that are sequential techniques and one-step techniques.

Common sequential MOF deposition methods to grow oriented thin films are based on the layer-by-layer technique.¹⁴⁹ The general

concept layer-by-layer growth is sketched in **Figure 2.16**. A substrate is treated in a step prior to the actual synthesis to make its surface suitable for the anchoring of MOF SBUs. This can be achieved, for example, by growing a functional self-assembled monolayer (SAM) on top of its surface, as indicated by the yellow octahedrons in the picture (1). The MOF deposition cycle starts with exposing the functionalized substrate to a solution containing the metal precursor (2). Such metal precursors commonly are metal salts such as nitrates or acetates.^{150,151} After an intermediate rinsing step with the pure solvent to remove any uncoordinated material, a second precursor solution is applied to the sample containing the linker molecules (3). After another rinsing step, the next cycle begins with the metal precursor again (4), and so forth. The synthesis always ends with a rinsing cycle. With such a protocol the thickness of the resulting thin films can be precisely controlled by the number of deposition cycles.^{151,152} The bottom-up direction of growth, initiated by metal SBUs in a controlled spatial configuration enables the formation of crystallites with preferred orientation.^{121,153,154} Alternate exposure of substrates to metal and linker precursor solutions can be realized in a variety of ways such as spin-casting,^{56,155} spraying,^{152,156} dipping,^{157,158} or pumping in and out of a static vessel,^{121,159} or by continuous flow in a fluidic cell.^{57,160} The layer-by-layer technique was utilized to create

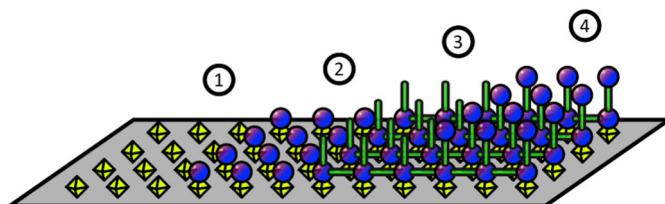


Figure 2.16. Concept of layer-by-layer MOF growth. On a surface with functional groups (yellow octahedrons) (1) allowing for metal clusters (purple spheres) to form at the beginning of the deposition procedure the MOF is grown in a step-wise manner, by sequential deposition (2-3-4) of metal and linker (green rods). Adapted from Halder *et al.*¹⁶¹

thin films studied in **Chapter 5**, where it will also be suggested that the general growth concept sketched in **Figure 2.16** might be too simplified.

An example for a one-step approach is the vapor-assisted conversion method for oriented UiO MOF thin films presented by Virmani *et al.*¹⁶² The schematic in **Figure 2.17** conveys the basic reaction concept, whereby a substrate loaded with precursor growth solution droplet is placed inside a heated, sealed reactor. The precursor solution contains, besides metal precursor and linker, also a modulator. This is a small monocarboxylic acid that can also lead to SBU formation but without connection to neighboring SBUs. It can, however, be replaced by a dicarboxylic linker molecule in a second step. As a result, the crystallization process is slowed down. The modulator is also present in another solution contained at the bottom of the reaction vessel and is distributed in the form of a vapor upon heating. This synthesis approach is used to create UiO-66- and UiO-67-based thin films discussed in **Chapter 4**. One-step fabrication protocols for oriented

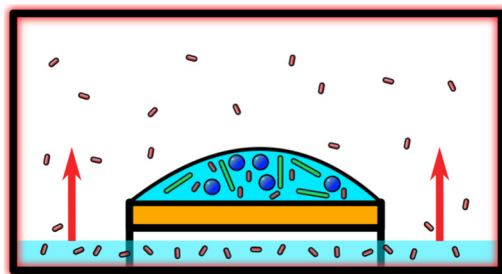


Figure 2.17. Vapor-assisted conversion method. A substrate with a precursor growth solution droplet on top is situated inside a heated and sealed reactor. Besides the necessary precursors to form the MOF, also a modulator is contained in the precursor solution and in the bath at the bottom of the vessel that slows down the crystallization process. Upon heating, the modulator is released as a vapor into the air surround the droplet on the substrate and establishes a precise balance of modulator inside the precursor solution throughout the whole MOF synthesis. Adapted from Virmani *et al.*¹⁶²

thin films also exist for other MOF systems, such as recently presented for large-scale textured ZIF-8 synthesis.¹⁶³ A special sub category of a one-step MOF fabrication approach is given by transformation methods as demonstrated for example by Kim *et al.*¹²² After creating a hydroxy double salt basis layer containing Cu and Zn, they showed that this precursor can be transformed into a layer-pillar MOF by exposure to solution containing two kinds of linker molecules; for certain combinations of linkers, also with preferred orientation. Comparable transformation strategies were demonstrated for example by Falcaro *et al.*,¹⁶⁴ and Stassin *et al.*¹⁶⁵ Conversion processes from a common basis layer will play a role later in the discussion in **Chapter 5**.

2.3.3. Photoluminescence in MOFs

MOF that exhibit emission can be used as versatile sensing elements by reacting to a variation of external factors with a change of their photoluminescent properties. In general, photon emission can occur in MOFs due to multiple mechanisms within their molecular components including the metal-containing SBUs, conjugated organic linkers or guest molecules inside the pores, which is schematically illustrated by **Figure 2.18**. Relevant interactions between these compounds include charge transfer between metal cluster and linker, sensitization of via the organic ligand, adsorption, *i.e.* capturing, of emissive guest species inside the pores, π - π orbital coupling between adjacent linkers.^{54,166,167}

Emission can become more linker-based, depending on the energy levels of HOMO and LUMO of the linker in comparison to the metal valence states. Increased conjugation within the linker molecule moves its HOMO and LUMO levels closer, decreasing the probability of energy transfer to a metal ion and enhancing the radiative transition rates within the linker.¹⁶⁶ This results in a MOF emission spectrum that bears close resemblance to the pure linker spectrum as

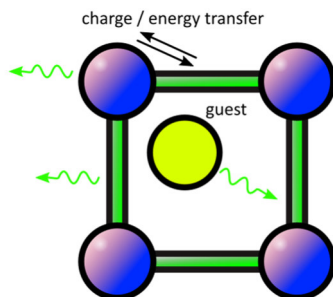


Figure 2.18. PL in MOFs. Photon emission can occur from any part of the MOF, including SBUs (purple), linkers (green) or guest molecules residing in the pores (yellow). Thereby, different types of interactions among these components can occur including, for example, linker-sensitization of the SBU or metal-to-ligand or ligand-to-metal charge transfer. Adapted from Allendorf et al.¹⁶⁶

is the case, for example, in pyrene-based IRMOF-11 and IRMOF-13.¹⁶⁶ Furthermore, the possibility of a ligand-to-metal charge transfer is influenced by the electronic structure of the metal ion. Zn^{2+} ions inside the structure, for example, are favorable to preserve linker-based emission because of their filled 3d atomic orbitals preventing charge transfer from linker to metal.¹⁶⁸ This is very different, for example, in the case of open-shell Cu^{2+} ions that cause luminescence quenching by rapid non-radiative ligand deactivation by charge or energy transfer.¹⁶⁹ For this reason, Zn-based structures are a primary target for applications exploiting linker luminescence. In summary, depending on a specific targeted PL sensing application, a suitable MOF can be chosen (or designed) considering factors such as: linker conjugation, rigidity, and orientation; quenching or non-quenching metal ions in the SBU; or pore volume in relation to guest molecule dimensions.¹⁶⁶

Luminescent MOF thin films, in comparison to MOF powder, are especially interesting for sensing devices due to faster analyte uptake and enhanced emission by reduction of self-quenching effects.¹⁷⁰ Furthermore, MOF thin films can present advantageous regarding

recyclability and portability and exhibit reduced cost due to a minimal amount of deposited material.¹⁷⁰ Thin film-based luminescent sensors have been demonstrated based on a variety of analyte-MOF interactions. For example, the luminescence quenching of lanthanide-based thin film material in response to binding of analyte ions within active sites in the MOF pores has been utilized as an indicator for the presence of heavy-metal pollutants in aqueous solutions.^{171,172} A UiO-67-derived MOF thin film with lanthanide-functionalized linkers has been shown to react to ammonia in ambient air with a significant luminescence enhancement by an alteration of the ligand triplet level that allows for more efficient energy transfer towards Eu^{3+} ions.¹⁷³ Another example is given by ZIF-8 (ZIF, Zeolitic Imidazolate Framework) thin films that cause a significant emission enhancement of adsorbed Nile red fluorescent dyes by improving photon extraction from the dye.¹⁷⁴ The dye-loaded ZIF-8 thin films were demonstrated as versatile sensing platform for organic vapors causing a further luminescence increase or emission spectral shift, depending on analyte concentration.¹⁷⁴

2.3.4. Molecular Motion in MOFs

Within recent years, an intriguing sub category of MOFs has emerged of structures that incorporate movable parts inside a stabile lattice. Molecular movement, schematically illustrated in **Figure 2.19** inside a MOF can take different forms such as rotation or shuttling,^{100,175–177} translation,^{178,179} or switching.^{180–185} The precise tuning of cavities inside of MOFs can be used to modify molecular mechanics and allows for specific interaction with chemicals entering the pores.^{186–190} Some molecular movements can be actively triggered by external influences such as temperature,¹⁸⁹ illumination with light,^{191,192} electric fields,¹⁹³ etc. One way to achieve actively controllable molecular switches (**Figure 2.19a**), for example, is to exploit photoisomerization of MOF linkers. This been demonstrated, for example, based on visible-light induced switching between *cis*- and *trans*-configuration of linker side

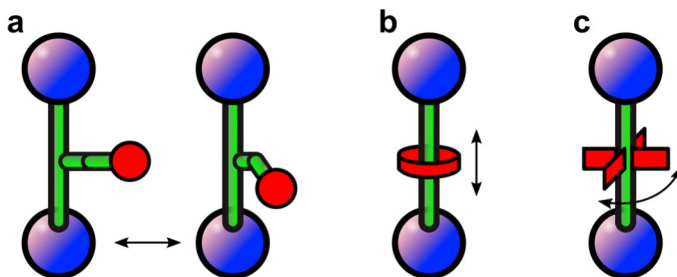


Figure 2.19. Molecular motion in MOFs. **a)** Molecular switch. **b)** Molecular shuttle. **c)** Molecular rotor. SBUs are illustrated as purple spheres and linkers as green rods and movable parts indicated in red. Adapted from Martinez-Bulit *et al.*¹⁹⁴

groups in layer-pillar MOFs,¹⁹¹ or using direct or indirect photoisomerization (*via* porphyrin-sensitization) of a bispyridyl molecular motor strut.^{180,182} Recent progress has been made by Thaggard *et al.*, presenting adjustable photoisomerization switching rates from 10^{-4} to 10^1 s⁻¹ in a spiropyran-based MOF material.¹⁹⁵ Molecular shuttle translation (**Figure 2.19b**) has been presented, *e.g.* by Zhu *et al.*, constructing a cyclophane macrocycle that can move back and forth on a MOF linker,¹⁷⁹ or by Feng *et al.* who realized active pumping based on molecular shuttles.¹⁷⁸

Especially MOFs containing linkers acting as molecular rotors (**Figure 2.19c**) have gathered notable interest owing to their ability to pair low potential energy barriers to full rotation with rotor-rotor or rotor-guest interactions in designer three-dimensional configurations.^{196–199} For example, the influence of flowing solvent on molecular rotors of different shapes has been demonstrated by Garcia-Garibay and co-workers,¹⁹⁷ where the size of the rotor blades either led to a “slip” or “stick” interaction with the surrounding solvent molecules. A possibility to create coupled rotary motion is to equip rotor linkers with a constant dipole moment that can allow for collective switching behavior upon external stimuli such as electric fields.^{177,200}

Rotary motion can also be coupled with luminescent sensing approaches in MOFs. Using the mechanism of aggregation-induced emission, for example, provides a sensing strategy for guest molecules that enter MOF pores.^{101,201}

The choice of specific molecular bonds as rotor axles can be used to adjust the rotational speed.²⁰² A common interest is fast molecular rotation in MOFs, which has been demonstrated by rotary axles based on hybridized molecular bonds such as sp^3 - sp^2 , sp^2 - sp , sp^3 - sp .^{175,202} However, also rotor systems are possible with higher rotational barriers based on sp^2 - sp^2 bonds, as are present in standard dicarboxylic acids such as benzene or naphthalene dicarboxylic acids.²⁰² In contrast to fast moving rotary systems, the higher potential energy barriers to full rotation of such linkers lead to a more confined range of motion. This relative stability allows for switching between two different linkers states and can be utilized for specialized luminescent sensing applications, as will be demonstrated with an anthracene dicarboxylic acid-based MOF thin film in **Chapter 6**.

3. Fabrication and Characterization Methods

In this chapter, the experimental methods used for MOF thin film fabrication and characterization throughout this work are presented. In order to provide the reader with an understanding of each method, the working principles of those techniques not already introduced in detail in **Chapter 2** will be briefly explained as well.

3.1. Thin Film Fabrication

The fabrication of MOF thin films, especially with a defined crystallite orientation is very challenging. The synthetic procedure of a MOF thin film strongly depends on its molecular building blocks and on the specific target crystal structure. Since different MOF systems were investigated in this work, a variety of thin film synthesis methods was employed, including layer-by-layer and one-step deposition approaches. The utilized methods are partially according to reports in the literature and partially self-developed.

3.1.1. Overview of Organic Molecules

In order to provide the reader with a visual impression of the organic molecules used to fabricate metal-organic thin films in this work, an overview of all utilized these molecules is presented in **Figure 3.1**. The displayed ligands belong to the two groups of “linkers” (**Figure 3.1a to e**) and “pillars” (**Figure 3.1f and g**). The linkers used are based on carboxylate groups on both ends that were used to coordinate with different types of metal including zinc, copper and zirconium. The pillar molecules were used as a special type of linker that is capable of orthogonally connecting two-dimensional substructures based on metal clusters and linkers in 3D layer-pillar MOFs (see **Section 2.3.1** for more details on basic MOF components).

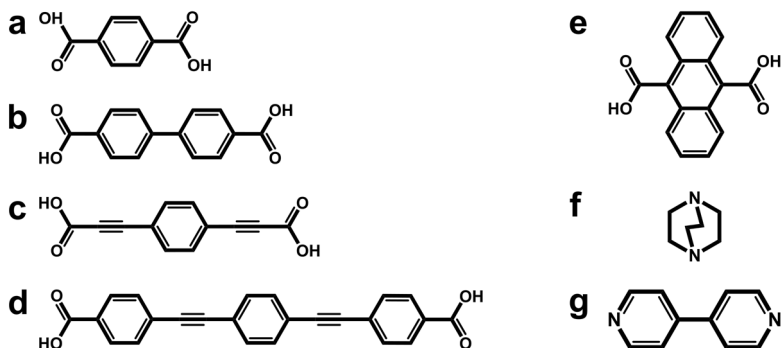


Figure 3.1. Overview of organic molecules used for MOF fabrication. **a)** Benzene-1,4-dicarboxylic acid (BDC). **b)** biphenyl-4,4'-dicarboxylic acid (BPDC). **c)** 3,3'-(1,4-phenylene)bis(2-propynoic acid). **d)** 4,4'-(1,4-phenylenebis(ethyne-2,1-diyl))dibenzoic acid. **e)** 9,10-anthracene-dicarboxylic acid (ADC). **f)** 1,4-diazabicyclo[2.2.2]octan (DABCO). **g)** 4,4'-bipyridine (BPy).

3.1.2. Substrate Preparation

As substrates, predominantly Si or Au were used and prepared for thin film synthesis in specific ways depending on the synthesis procedure. All substrates were cut by hand from standard circular wafers into conveniently usable pieces, typically 0.5 – 1 cm by 1 cm. To remove any dust particles from the surface, afterwards, they were thoroughly rinsed multiple times with ethanol followed by drying with pressurized nitrogen. Depending on the synthesis method used for MOF thin film fabrication and type of substrate, further preparation of the surface prior to the synthesis was conducted. For layer-by-layer spin-coating, two types of substrates were utilized: <100> Si substrates with a thin native SiO₂ layer, and Au-coated Si substrates with a functional self-assembled monolayer (SAM) on top. After rinsing with ethanol, the Si substrates were additionally cleaned by a UV-ozone plasma for at least 15 mins in order to remove any remaining organic compounds and activate the surface by creating hydroxy groups on the surface that can serve as binding sites for subsequent MOF growth. The Au substrates, on the other hand, were

immersed in 16-mercaptohexadecanoic acid (MHDA)-containing 0.02 mM ethanol solution for two days to create a functional top layer with carboxylic binding sites. After extraction, the remaining liquid was very gently rinsed off with ethanol and the coated substrate subsequently dried with nitrogen. Both types of substrates were used for synthesis immediately after the respectively last preparation step. For vapor-assisted conversion (VAC) and drop-casting on a hot plate, <100> Si substrates with a thin native SiO₂ layer and Au-coated Si substrates were used without further modification except ethanol rinsing and nitrogen drying.

3.1.3. Layer-by-layer Spin-coating

Layer-by-layer spin-coating is a technique that enables fabrication of thin layers with controlled thickness, based on the number of cycles of sequentially applying ethanol-based metal and linker precursor solutions onto the substrate.^{56,155,203} A deposition cycle, depicted in **Figure 3.2a** comprises application of the 1) metal precursor solution (at concentrations ranging from 0.1 to 1 mM), 2) pure ethanol to remove any non-attached precursor molecules, 3) linker solution (at concentrations ranging from 0.01 to 1 mM), and 4) again pure ethanol. All of these solutions were prepared by adding the solid precursors in their powder form to an appropriate volume of ethanol and dissolving them by means of ultrasonication until clear liquids were obtained. The substrate was located on a vacuum chuck inside the spin-coater in ambient atmosphere, held in place by a continuously applied under-pressure at its backside. The sequential application of the liquids involved drop-casting onto the still-standing substrate with a micro pipette and followed by a rotation for 10 s with a maximum speed of 2000 rpm and an acceleration of 500 rpm s⁻¹, as illustrated by **Figure 3.2b**. This procedure was conducted according to Haldar *et al.*⁵⁶ A typical synthesis comprises 40 deposition cycles is 40, however even much fewer (< 10) cycles can already lead to thin films characterizable with GIWAXS. Utilizing this method, metal-organic

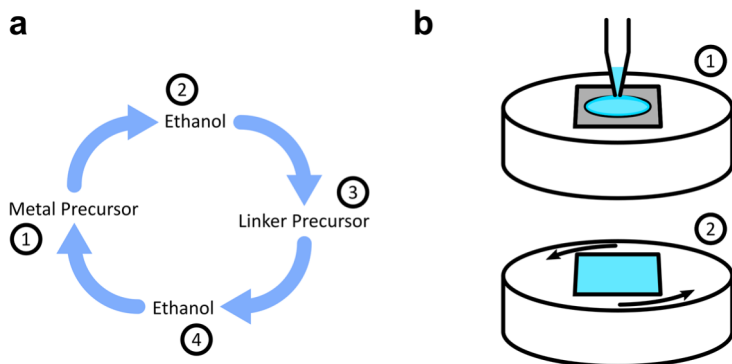


Figure 3.2. Layer-by-layer spin-coating. **a)** Precursor solution application sequence. Metal and linker solution are alternately deposited onto the substrate with intermediate pure ethanol rinsing cycles. The procedure always starts with the metal solution and ends with ethanol rinsing after a linker solution has been drop-cast. **b)** Alternate solution deposition and substrate spinning. Precursor solution is applied when the substrate is standing still. After its surface has been fully covered by the liquid, it is spun for 10 s with a maximum speed of 2000 rpm. Throughout the whole procedure, the substrate is tightly held in place by the vacuum chuck underneath.

framework as well as layered Zn hydroxide thin films with structure-specific preferred orientations were generated (see **Chapter 5**).

3.1.4. Drop-casting on Hot Plate

Drop-casting on a hot plate allows for a one-step MOF synthesis that is time-efficient and without the need for advanced equipment. To achieve that, an ethanol-based precursor solution containing all MOF precursors was deposited on a substrate preheated to 50°C, in ambient environment (**Figure 3.3a**). The precursors for the herein fabricated layered-pillared MOF thin films of the form $(\text{ZnADC})_2\text{DABCO}$ (and $(\text{ZnADC})_2\text{BPy}$) comprised Zn acetate dihydrate at 0.15 mM (0.20 mM), hydrochloric acid at 0.15 mM (0.20 mM), ADC at 0.15 mM (0.20 mM) and DABCO at 0.15 mM (BPy 0.05 mM). After all ethanol had evaporated, the sample was removed from the hot plate and washed by immersion and gentle shaking inside an ethanol bath to eliminate unreacted molecular components (**Figure 3.3b**). This procedure is considered one synthesis cycle. The thickness of the

resulting film could be controlled by the number of successive cycles. The drop-casting synthesis yields $\langle 001 \rangle$ -oriented MOF thin films, *i.e.* their pillar molecules (DABCO or BPy) vertically aligned to the substrate surface. Studies on the MOF coatings produced by this method are presented in **Chapter 6**.

The precursors were dissolved in ethanol by aid of ultrasonication. However, since there were more components involved in creating the solution here, the order of their addition becomes important. While the linker and pillar molecules were added at once to one ethanol solution, the Zn precursor was mixed with HCl in another ethanol solution in a different flask. These stock solutions could be kept for multiple days. Only directly before the drop-casting synthesis, both premixed solutions were combined in the appropriate ratio to obtain the final growth solution. This aspect is very important as Zn and linker reacted with each other also on their own. A final precursor solution left in a flask at room temperature for one day could be observed to form MOF powder which only resulted in randomly oriented crystallites, when drop-cast on a substrate afterwards.

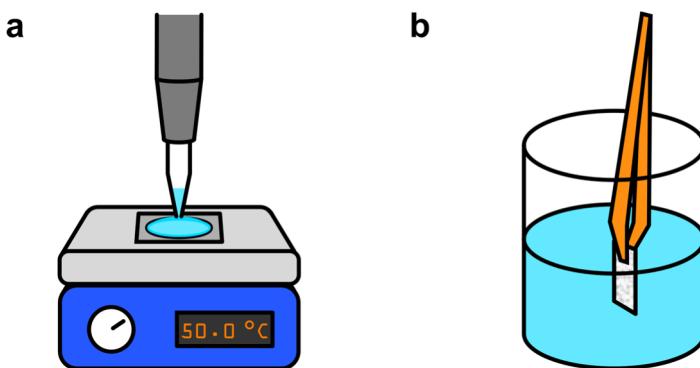


Figure 3.3. Drop-casting on a hot plate. **a)** Ethanol-based growth solution deposition on pre-heated substrate. **b)** Sample washing in an ethanol bath after drop-casting. This cleaning step follows after application of every single droplet to avoid residual unreacted components in the thin film.

3.1.5. Vapor-assisted Conversion

Like the drop-casting method described above, the vapor-assisted conversion (VAC) is a one-step fabrication process that yields UiO-type MOF oriented thin films. However, this technique is much more involved, as it takes place in a specifically prepared, sealed reaction vessel, and requires a longer synthesis time. The VAC synthesis procedure was based on Virmani *et al.*¹⁶² As in the case of drop-casting, a one pot growth solution was prepared containing all MOF precursors in N,N-Dimethylformamide (DMF). These are in the case of UiO-66 (and UiO-67) the metal precursor $\text{ZrOCl}_2 \cdot 8\text{H}_2\text{O}$ at 2.9 mM (2.2 mM), modulator acetic acid 232 mM (427 mM), and linker BDC 2.9 mM (BPDC 2.2 mM). The components were added in the presented order to an appropriate volume of DMF upon ultrasonication immediately prior to the synthesis in order to prevent pre-nucleation of crystals in solution. The bottom of the reaction vessel was covered with Raschig rings and afterwards filled with a mixture of 4.2 ml DMF and 0.8 ml acetic acid. On top of the Raschig rings, a substrate was placed and filled with a droplet of the growth solution, as depicted in **Figure 3.4**. The mixture of DMF and acetic acid serves as a liquid source to create a vapor in the followingly sealed and heated bottle.

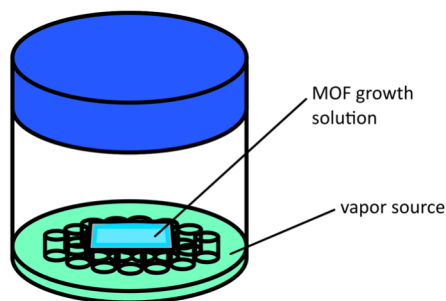


Figure 3.4. Vapor-assisted conversion. Inside a sealed vessel, a substrate fully covered by the MOF growth solution made from DMF, Zr precursor, acetic acid and linker is situated elevated above a vapor source bath consisting of DMF and acetic acid. Heating the container to 100°C for three hours creates a MOF thin film on the substrate.

While originally the usage of a 100 mL Duran glass bottle GL45 as reaction vessel with a droplet volume of $\sim 40 \mu\text{L cm}^{-2}$ was proposed,¹⁶² here, improved results were achieved using a 250 mL wide-mouth Duran GLS80 bottle and $\sim 80 \mu\text{L cm}^{-2}$. The synthesis took place over 3 h in an oven preheated to 100 °C. After cooling down, the samples were taken out, rinsed with acetone and activated over night at a reduced pressure at room temperature overnight, to remove any remaining DMF from the MOF pores. By applying this synthesis procedure twice consecutively, with the first MOF thin film serving as the substrate for the fabrication of the next one, UiO-67-66 heterostructures could be achieved with a preferred crystallite orientation in both layers. More information on these investigations is given in **Chapter 4**.

3.2. Structural Characterization

In order to determine the structure of the produced thin films, different techniques were utilized throughout this work, each one dedicated to reveal specific material traits. X-ray diffraction (XRD) methods were used to analyze the periodic arrangement of heavy elements thereby elucidating the crystalline structure and orientation. The presence of certain chemical groups and bonds within a thin film could be assessed by analyzing characteristic peaks in its infrared reflection-absorption (IRRA) spectra. More macroscopic features such as crystallite size and surface roughness could be visually determined by scanning electron microscopy (SEM). All these characterization approaches used are explained in the following.

3.2.1. Grazing-incidence Wide-angle X-ray Scattering (GIWAXS)

To allow for a clear structure determination of the fabricated MOF thin films, GIWAXS was used as primary method throughout this thesis. Since the fundamental principles were already introduced earlier in the **Chapter 2**, the focus now lies on the experimental

implementation of the measurements. GIWAXS was conducted on a laboratory-scale *Bruker D8 Advance* diffractometer, shown in **Figure 3.5** with all important parts labeled. The system contains a Cu-anode X-ray source producing Cu $k_{\alpha 1,2}$ and k_{β} radiation. In a basic X-ray tube, a Tungsten filament is heated by an electric current such that it releases electrons that are then accelerated by an electric field towards the anode. Inside the atoms of the anode material, two types of interactions with incoming electrons can take place. The first one, Bremsstrahlung, caused by a deflection of electron trajectories by the positively charged nucleus creates a continuous emission spectrum. The second type of radiation is produced by collisions between anode atoms and incident accelerated electrons. Thereby ejected inner-orbital electrons create vacancies that are replaced by atomic electrons relaxing from higher-lying orbitals. This process leads to material-specific discrete emission lines, orders of magnitude more intense than the Bremsstrahlung, which are the ones used for the diffraction experiment (e.g. k_{α} and k_{β} radiation).^{66,68} The generated X-ray beam is collimated and monochromatized afterwards by a Göbel mirror which is a parabolically shaped interference mirror optimized for $K_{\alpha 1,2}$ radiation (thereby suppressing K_{β} radiation). Afterwards the beam passes through a 0.5 mm micro mask and 0.3 mm snout, further improving beam collimation. A molybdenum knife-edge is placed directly above the sample and can be manually height adjusted to decrease noise from air scattering recorded by the detector. Mounted on the right side of the sample stage, a metallic beam stop is attached that shields the detector from specular reflection of X-rays off the sample surface during the measurement. On the opposite side of the X-ray source, a *Dectris Eiger2 R 500 2D* detector with a pixel size of 75 μm is mounted at a distance of 118.1 mm from the sample. Both, the primary track containing the source and the secondary track with the detector, are mounted on motorized goniometer arms with the sample on the stage situated in the center.

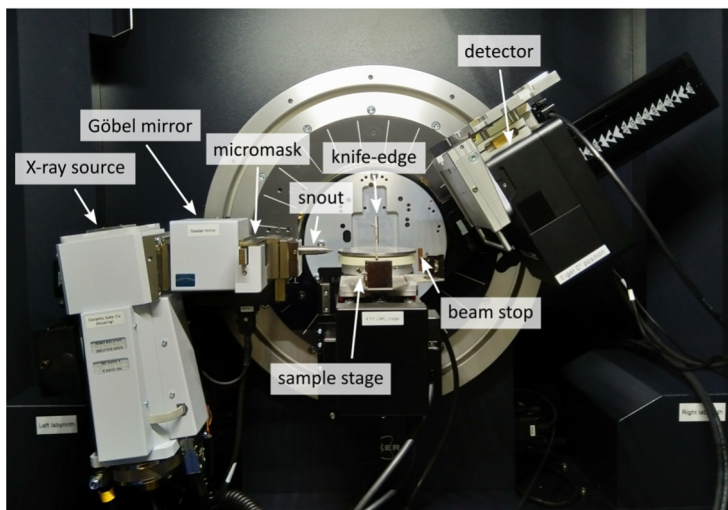


Figure 3.5. GIWAXS measurement setup with all major parts components indicated.

Prior to each measurement, the system needed to be aligned in several steps aiming to achieve a horizontal sample alignment including height adjustment, sample tilt correction (θ calibration) and reflection correction (2θ calibration). For this alignment procedure, the beam stop was manually lowered and reset afterwards. Due to the small dimensions of the X-ray detector area, multiple frames were recorded with the detector positioned at different azimuthal angles in the goniometer. In post-processing, the individual images were stitched together to form a complete picture which is explained in detail in **Chapter 4**. To obtain a clear diffractogram, the integration time per frame was chosen longer (up to 10 – 20 h per frame) or shorter (typically 0.5 – 1 h), depending on the thickness and quality of the sample. The incidence angle was chosen depending on the targeted probing volume of the thin film. Angles below the material-specific critical angle were used for surface characterization and supercritical angles (typically $>0.2^\circ$) for full depth characterization.

3.2.2. Powder X-ray Diffraction (PXRD)

Supplementary PXRD measurements were carried out on two different laboratory-scale diffractometers configured in Bragg-Brentano geometry. With this technique, only horizontally oriented crystallographic planes are probed. This allows all possible crystal planes to be revealed only in the case of randomly oriented crystallites (powder). In the case of oriented thin films only a small subset of the diffraction planes can be detected (see **Section 2.1.2**). This means that considering structures of oriented films from the few diffraction peaks visible in this technique is problematic and only limited agreement between a model structure and experimental data can be checked.

The first utilized diffractometer was a *Bruker D8 Advance* (primary track: Cu- $k_{\alpha 1,2}$ source, variable divergence slit; secondary track: (2.3°) equatorial Soller slit, LynxEye Si strip detector), and the second one a *Bruker D2 Phaser* (primary track: Cu- $k_{\alpha 1,2}$ source, equatorial Soller slit, horizontal 1 mm slit; secondary track: equatorial Soller slit, LynxEye Si strip detector). Both systems exhibited an automated stage that provides for a rotation of the sample during the measurement for spatial averaging of the entire coated area.

3.2.3. Infrared Reflection-absorption Spectroscopy (IRRAS)

IRRAS is a surface-sensitive technique to obtain information about molecules and, in particular, the chemical bonds of a material by using IR photons to excite vibrational modes. Distinct absorption peaks in the IR absorption spectrum point towards the presence of individual organic groups and bonds. An example based on the linkers utilized in this work, are the symmetric and antisymmetric stretching vibrations of the carboxylate group evoking pronounced absorption peaks around 1400 and 1600 cm^{-1} .^{204,205} Due to several benefits over dispersion-type spectroscopy such as improved accuracy, signal-to-noise ratio, and shorter measurement time, the established approach to record IR absorption spectra is the Fourier-transform (FT) IR

approach.^{206,207} The central part of an FTIR setup is a Michelson interferometer, sketched in **Figure 3.6**, in which an incoming broad band IR beam is divided in two parts that are then brought to interfere with each other. A variation in one of the beam path lengths creates destructive or constructive interference creating an interferogram probe that is led through the sample that absorbs certain wavelengths from the probe spectrum. The FT of the measured signal containing many superimposed oscillations at the detector reveals the spectral content of the interferogram and, therewith, about the sample's absorbance characteristic. To increase interaction of the incident light with the sample layer on the substrate surface, a grazing incidence is used in IRRAS.

In this work, the IRRAS spectra of MOF thin films were obtained with a *Bruker Vertex 80v* FTIR spectrometer comprising a liquid nitrogen-cooled detector made of mercury cadmium telluride, operated in the range from 400 to 4000 cm^{-1} with a spectral resolution of 2 cm^{-1} . The measurements were carried out with an incidence angle of 10°. In order to subtract the background signal created by the carboxylic SAM

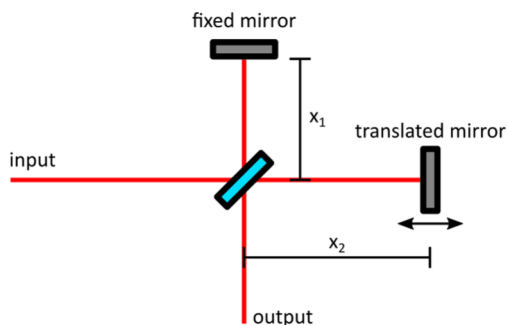


Figure 3.6. Michelson Interferometer. An incoming laser beam divided into two parts by a beam splitter into an arm of fixed path length x_1 and one with varying path length x_2 . The laser light at the output is modulated by successive constructive and destructive interference depending of the phase difference introduced by the moving mirror.

beneath the MOF thin films, reference measurements with perdeuterated hexadecanethiol SAMs on a gold surface were performed prior to the actual measurements.

3.2.4. Scanning Electron Microscope (SEM)

An SEM is an established device that overcomes the resolution limit set by diffraction of visible photons in light microscopy ($d = \lambda / 2NA$, with the wavelength λ and numerical aperture NA) by using accelerated electrons as a probe. The much higher achievable resolution is then majorly dependent on the kinetic energy of the accelerated electrons and the structural stability of the sample. In order to form a focused probe of electrons, beam shaping elements are used that are based on electric and magnetic fields rather than refractive elements. Many different types of interactions between the primary electron beam and the sample involve elastic and inelastic scattering processes. A surface image is created by detecting secondary electrons ejected from the sample's surface. To avoid distortions created by local charging of the sample material, a high electric conductivity is required at its surface. This is commonly achieved by deposition of a thin coating (of the order of a few nm) of noble metals such as silver, gold or platinum.

Here, a ZEISS Supra 60VP SEM was employed, using electron acceleration voltages from 3 to 10 kV at working distances from 5.6 to 10.7 mm. The MOF thin films were sputtered with a 5 nm layer of Pt or Ag prior to the measurement. To record cross-section images, the samples were broken in half at the center.

3.3. Photophysical Characterization

The photophysical characterization was based on absorption and photoluminescent properties of the MOF thin films. In order to assess these properties, many different specialized components were used, such as excitation sources, detectors and dedicated optical setups. In

the following, all of these parts are presented one by one and explained to provide a basic understanding of their function principle.

3.3.1. Excitation Sources

In order to observe photoluminescence of a MOF thin film, excited electronic states must be created inside the material. Optical excitation is a convenient way to create such excited states. Depending on the measurement pursued, different sources can be used to provide suitable photons for optical excitation. The devices used in this work include LEDs driven in continuous wave (CW) or pulsed mode, broadband lamps in combination with a monochromator, and pulsed lasers.

For steady-state PL measurements, **CW LEDs** are a convenient excitation source. A typical LED is based on the radiative recombination of charge carriers in a junction between a p-type (excess of holes, positive carriers) and n-type doped (excess of electron, negative carriers) semiconductor. If a forward voltage is applied to the junction, the higher potential being connected to the p-doped side, a current can be created that drives electrons from the n-type into the p-type semiconductor. The photons that are emitted during the recombination of electrons and holes can be harnessed to form a radiation source. Since many aromatic chromophores incorporated in the MOF thin films strongly absorb in the UV region, LEDs with center emission wavelengths between 300 and 400 nm were used, such as *Thorlabs* M300L4 and M365LP1. An alternative approach to an LED is a combination of **broadband light source and a monochromator**. The basic function principle of a monochromator is analogous to a Czerny-Turner spectrometer (that is explained in the next section) using a movable slit at the output port instead of a detector array. The benefit of such an excitation system can be a potentially narrower spectrum, depending on the quality of the monochromator. This type of excitation source was used inside an

Edinburgh Instruments FS5 spectrofluorometer. For excited state decay measurements, a certain type of LED was used that is capable of ultrashort-pulsed operation by specialized electronic drive circuits. Such external **picosecond pulsed LEDs** (EPLEDs) were employed for time-resolved PL measurements that are discussed in a later section.

To examine excited-state dynamics at varying exciton densities, excitation pulses with high fluences and ultrashort time durations were required. A CW excitation would be not suitable in this case, as it would hide the potential influence of migration of excitons within their lifetime on the measured PL. For this reason, a **Lightconversion fs-pulsed laser system** was used comprising a Pharos laser unit and HIRO harmonics generator. In the Pharos system, laser pulses are created in a Kerr lens mode-locked oscillator and intensified by means of chirped pulse amplification. In the laser resonator, many different modes can be supported with an intermodal spacing of $\Delta f_{mode} = c/2l$, with the speed of light c and the cavity length l . The process of phase-coupling all of these modes is called mode-locking and is used to create constructive interference.²⁰⁸ Passive mode-locking can be achieved utilizing the Kerr lens effect that describes a non-linear relationship of the refractive index of a medium with the electric field. This property is used to focus pulses with very high photon densities onto an aperture, while non-focused (low-intensity) light is kept within the resonator. To amplify the outcoupled pulses afterwards to highest intensities, they are chirped by a grating stretcher before amplification minimizing the peak optical power in the amplifying medium, and compressed again afterwards. With this technique, ultrashort pulses at 1028 nm were created in an ytterbium-doped potassium gadolinium tungstate active medium with a pulse duration in the range of hundreds of fs. To adjust the wavelength to the UV region suitable for excitation of the examined MOF thin films, the third harmonic at 343 nm was generated (illustrated in **Figure 3.7**).

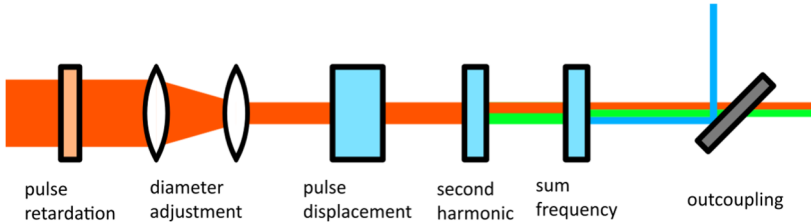


Figure 3.7. Third harmonic generation. An incident laser pulse passes a half-wave plate that splits into two cross-polarized components with different delay. To enable optimal conditions for the interaction in the nonlinear crystals, the pulse diameter is decreased by two lenses enhancing the peak intensity, and the temporal displacement is adjusted by passage through a birefringent crystal. In the nonlinear crystals, the second-order processes of second harmonic generation and sum frequency generation harnessed to create the second and third harmonic of the fundamental wavelength. Adapted from Lightconversion HIRO manual.

This was achieved by the HIRO system in which the laser pulses experience colinear type-1 interactions in non-linear optical crystals, schematically. A half-wave plate and a birefringent crystal retards the pulse and causes temporal displacement in two cross-polarized pulses created from the incident pulse. A combination of two lenses adjusts the beam diameter. In the first nonlinear crystal, by the process of second harmonic generation, laser light at 514 nm is created in addition to the fundamental wavelength. Both of these wavelengths interact in the second non-linear crystal via sum frequency generation to obtain the third harmonic of the fundamental wavelength that is then outcoupled.

3.3.2. Spectrometers

Spectrometers make use of a dispersive element to split an incident broad band light beam into its spectral components. A diffraction grating is commonly used as dispersive element as it enables a compact device design and high spectral resolution. The basic structure of a Czerny-Turner spectrometer configuration,²⁰⁹ is displayed in **Figure 3.8**. Through a narrow entrance slit, light is introduced into the spectrometer and guided onto a reflective diffrac-

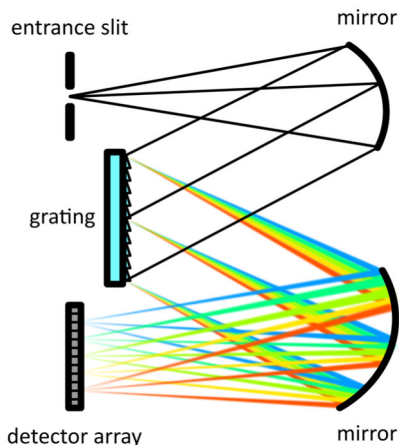


Figure 3.8. Czerny-Turner grating spectrometer. Light entering through an entrance slit is collimated by a concave mirror and led onto reflective optical grating. The dispersive effect of the grating leads to wavelength-dependent angular distribution of the light propagating to a second concave mirror that, consequently, focusses individual colors spatially distributed onto a detector array.

tion grating by a concave mirror. Depending on the grating period, small path differences are caused that result in wavelength-dependent paths of constructive interference for certain combinations of input and output angles. Thus, a color-dependent angular distribution is given off the grating which is then focused onto a detector array by a second concave mirror. Since each color hits the detector at a slightly different location, a certain pixel corresponds to a certain wavelength of the light and a spectrum is obtained.

To record time-integrated photoluminescence spectra in this work, fiber-coupled spectrometers from *Ocean Insight* (QEPro spectrometer with 100 μm entrance slit) and *Avantes* (AvaSpec-ULS2048x64TEC-EVO with 100 μm entrance slit) with optical fibers from *Thorlabs* (FP1000URT and BFY400MS02) have been used.

3.3.3. Time-integrated PL Spectroscopy

The basic setup to measure time-integrated PL spectra is depicted in **Figure 3.9**, where a suitable source illuminates the sample to optically excite the charge carriers. Its resulting emission is collected with optical elements imaging the probe spot on the sample's surface onto the entrance slit of a spectrometer. To guide the captured light, an optical fiber can be used as indicated in the sketch. To probe the material in a homogeneous state, the excited area of the sample usually is bigger than the probed spot from which emitted light is captured. Based on this principle, optical setups were built using different excitation sources suitable for the individual sample material with the already introduced fiber-coupled spectrometers as detectors. To introduce the maximum portion of the light collected by the imaging optics into the optical fiber, a secondary lens needs to be chosen with a focusing cone in accordance with the numerical aperture of the optical fiber. Another important experimental consideration is the introduction of a suitable excitation and emission filters (mainly from the *Thorlabs* FEL(H) and FES(H) series). These filters can be used to limit the excitation spectrum to a certain range or to reject any disturbing portion of light (*e.g.* scattered excitation) from the emission path. Alternatively to these self-built optical setups

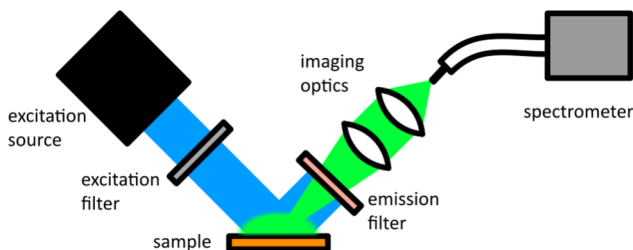


Figure 3.9. Basic setup to measure time-integrated PL. The sample is illuminated by an excitation source with appropriate wavelength. The emission is collected with a focal spot inside the excited sample area and imaged onto a fiber-coupled spectrometer.

also an *Edinburgh Instruments* FS5 fluorescence spectrophotometer was used. This fully automated device contains a xenon arc lamp as a light source, dual grating turret monochromators and filter wheels in excitation and emission monochromators. As a detector, a cooled photomultiplier tube is used. Contrary to a spectrometer-based setup, here, the PL spectrum is generated by slowly scanning the emitted light with a monochromator continuously recording the emission intensity within the moving window.

3.3.4. Time-resolved PL Spectroscopy

In order to examine the excited state decay behavior, it is possible to acquire time-dependent PL spectra. A common method, that is also utilized in this work, is time-correlated single-photon counting (TCSPC). This approach is based on a pulsed excitation with very high repetition rate but low pulse energy. In the flow chart in **Figure 3.10**, the signal processing involved in TCSPC is illustrated. In a nutshell, the technique resembles an elaborate stop watch: A reference pulse from the excitation source is used to create a start signal (top part of **Figure 3.10**) and with a certain time delay, a pulse emitted from the sample after a material-specific excited state lifetime creates a stop signal (bottom part of **Figure 3.10**). The measured time delay between start and stop signals is digitalized and saved in the form of a histogram, sorting the counting events by their time delay. By performing this experiment thousands of times, a fluorescence decay profile can be generated. For each start signal, only one stop signal can be counted, *i.e.* only one emission event from the sample is saved. Any additional emission events after the first one would be neglected which could result in a distortion of the measured decay profile. In order to avoid such pulse pile-up, the stop rate needs to be significantly lower than the start rate, reducing the probability of two emission events per pulse period to a negligible value. A good practical value for the maximum stop rate is 5 % of the start rate.

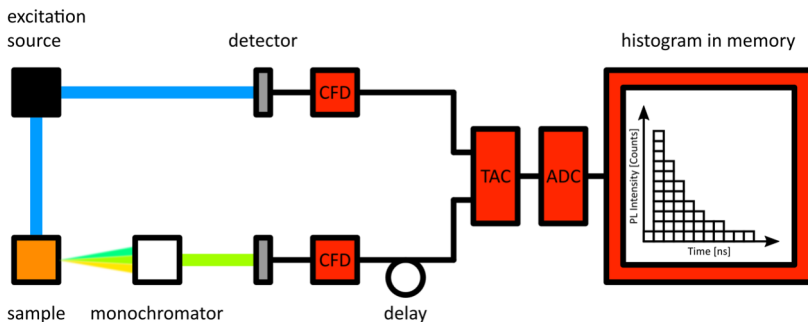


Figure 3.10. TCSPC flow chart. A pulsed source excites the sample and serves as a reference signal that starts a timer (upper arm). The emission from the sample is narrowed to a specified observation window by a monochromator and detected which creates a stop signal for the timer (lower arm). Signal processing in the TCSPC electronics part saves the timed detection events in a histogram, thereby creating a PL decay profile. Start and stop signal are generated by the constant fraction discriminator (CFD) if a certain threshold voltage is surpassed, distinguishing real signal from noise. An electronic delay can be added to the stop signal timing to position the acquired profile optimally within the measurement time window. Time-to-amplitude converter (TAC) and analog-to-digital converter (ADC) convert the measured delay time into a digital signal that can be stored in the memory in the form of a histogram. Adapted from <https://www.edinst.com/us/blog/what-is-tcspc/>.

TCSPC measurements, in this work, were carried out on an *Edinburgh Instruments* FS5 fluorescence spectrophotometer using EPLEDs at 260 and 365 nm center wavelengths and 900 ps pulse durations and repetition rates depending on the measured time window (one pulse per time window).

3.3.5. PL Quantum Yield

Besides the definition of the PLQY in **Equation 2.30**, it can also be expressed as the ratio between the number of emitted photons $n_{emitted}$ vs. absorbed photons $n_{absorbed}$:

$$\eta = \frac{n_{emitted}}{n_{absorbed}} \quad (3.1)$$

For this thesis, the 3M method to measure the PLQY according to de Mello *et al.* was used.²¹⁰ With this approach, the sample is placed in an integrating sphere (its inside coated with a highly diffusely reflecting white color) that isotropically redistributes all emitted light. This allows to conclude the total number of emitted photons N_{sum} from the number of photons N_{Ω} recorded from a certain solid angle Ω by:

$$N_{sum} = \frac{4\pi}{\Omega} N_{\Omega} \quad (3.2)$$

To obtain the PLQY, three measurements are needed and all of them are illustrated in **Figure 3.11**. Firstly, the response of the empty sphere is recorded when hit with the excitation beam (**Figure 3.11a**). Secondly, the sample is introduced into the middle of the sphere with the excitation directly aimed at it (**Figure 3.11b**); and, thirdly, a spectrum is recorded with the sample indirectly excited by scattered light from the sphere interior wall (**Figure 3.11c**). The recorded spectral radiance divided by the wavelength-dependent photon energy $E_{Ph} = \frac{hc}{\lambda}$ (with the Planck constant h) and integrated over the spectral range of interest provides a measure that is directly related to the number of photons. These integrated PL values obtained from each measurement are denoted L_a , L_b , and L_c for the excitation light and S_b , S_c for the sample emission. In the direct measurement (**Figure 3.11b**), A_{direct} describes the fraction of excitation light directly absorbed by the sample, and $(1 - A_{direct})$ the non-absorbed fraction getting transmitted or reflected. In the indirect measurement (**Figure 3.11c**), the $A_{indirect}$ describes the portion of excitation light scattered by the sphere and then absorbed by the sample. Based on these conventions, the following relations can be derived:

$$A_{direct} = 1 - \frac{L_b}{L_c} \quad (3.3)$$

$$L_b = L_a(1 - A_{direct})(1 - A_{indirect}) \quad (3.4)$$

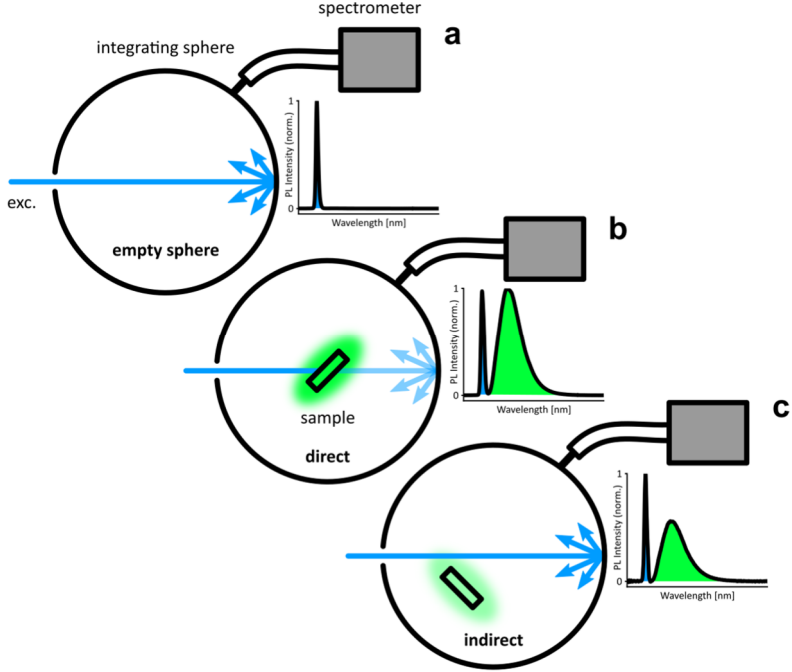


Figure 3.11. PLQY measurement procedure. To obtain the PLQY according to de Mello *et al.*,²¹⁰ three measurements are necessary including measurement of the **a)** empty sphere, **b)** directly excited sample, and **c)** indirectly excited sample. The insets illustrate the spectra measured in each case.

$$L_c = L_a(1 - A_{indirect}) \quad (3.5)$$

This leads to the full description of the direct measurement as follows:

$$L_b + S_b = (1 - A_{direct})(L_c + S_c) + \eta L_a A_{direct} \quad (3.6)$$

Solving this expression for the η enables to calculate the PLQY based on the measured spectra by:

$$\eta = \frac{S_b - (1 - A_{direct})S_c}{L_a A_{direct}} \quad (3.7)$$

The PLQY measurements were conducted using *Thorlabs* M300L4 and M365LP1 LEDs for excitation with the samples located in a 15 cm

diameter integrating sphere that was coupled *via* an optical fiber (Thorlabs BFY400MS02) to an intensity-calibrated spectrometer (Avantes AvaSpec-2048x64TEC and AvaSpec-ULS2048x64TEC-EVO).

3.3.6. Absorption Spectroscopy

In a typical absorbance measurement, a white light source is used to generate a broad band spectrum that is used to probe the absorption characteristic of a sample. There are two approaches to proceed with measuring the absorbance of a sample. The first one is depicted in **Figure 3.12a** and involves a monochromator and a photo detector. A small spectral window is created by the monochromator and used to probe the sample. This spectral window is scanned across a desired wavelength range to step-wise create a transmission spectrum by detecting the transmitted light in each step in the integrating sphere located behind the sample. The measurement time to acquire a UV-Vis spectrum depends on the utilized monochromator slit width and the dwell time (integration time per scanning step) which commonly takes up to several minutes. Therefore, this method is suitable to measure samples in a stable state. Another measurement option is to replace the photo diode as a detector by a spectrometer, as illustrated in **Figure 3.12b**. This enables recording a full transmission spectrum in one integration time step, speeding up the measurement with total acquisition times of the order of seconds. This allows to record spectra of samples in a more volatile state. A convenient way to guide the light transmitted by the sample into the spectrometer, in this case, is by use of an optical fiber that ends directly at its entrance slit, as already discussed earlier.

Both of these methods to measure absorbance were used in this thesis. The first approach was employed by using an *Agilent Cary 7000* universal measurement spectrophotometer that contains a double-monochromator and two parallel beam paths for sample and reference that are supplied with light by a rotating beam splitter at

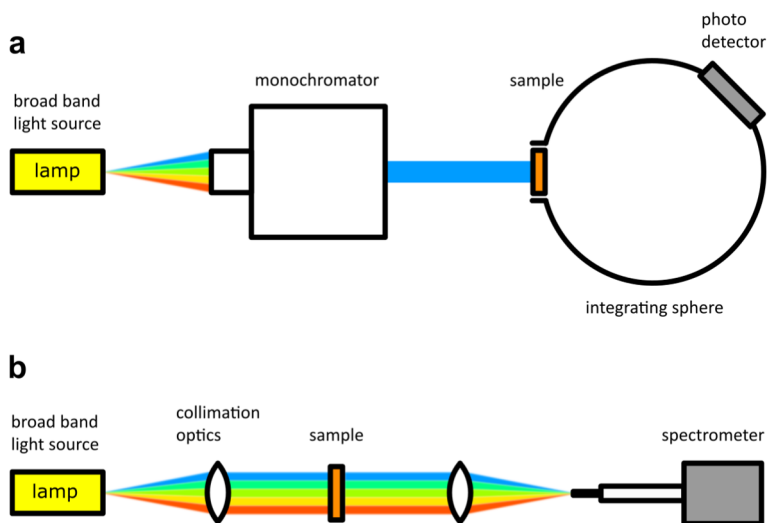


Figure 3.12. Absorbance measurement setups. **a)** Scanning spectrum acquisition. A white light source generates a broad band light spectrum from which only a narrow region is extracted by a monochromator led collimated through the sample. The transmitted portion is detected inside an integrating sphere. By step-wise scanning of the spectral region, an absorbance spectrum of the sample is constructed. **b)** Parallel spectrum acquisition. A broad band light spectrum is collimated, led through the sample and, successively, focused onto an optical fiber leading to a spectrometer. In contrast to the setup in a), here, the full spectrum is recorded in a single integration step.

30 Hz. For the UV-Vis measurements, a deuterium lamp was used as a light source and a photomultiplier tube as detector. The second approach was implemented in a self-assembled optical setup with a single beam path comprising a fiber-coupled (*Ocean Insight* QBIF600-UV-BX) *Ocean Optics* DH-2000-BAL deuterium-halogen lamp and an already mentioned above *Ocean Insight* QEPro spectrometer. In any case, the acquired transmission spectra need to be compared to a reference spectrum without the sample in order to be converted into absorbance values using **Equation 2.24**.

4. Insight into Oriented Growth of UiO Thin Films by Lab-scale GIWAXS

This chapter is based on my first-author research article “GIWAXS Characterization of Metal–Organic Framework Thin Films and Heterostructures: Quantifying Structure and Orientation” published in Advanced Materials Interfaces.⁷² Thin film synthesis, structural characterization measurements and analysis, development and implementation of MATLAB routines, data presentation and figure design were performed by J. C. Fischer (author). The co-author C. Li assisted in thin film synthesis. The co-authors B. S. Richards and I. A. Howard supervised the project and provided scientific guidance, intellectual input and proof-reading.

4.1. Motivation

For advanced application of MOF thin films in optoelectronic devices, for example as active component in LEDs,²¹¹ or biosensors,⁵³ or auxiliary component in organic photovoltaic cells,³⁹ high-quality crystalline architectures are needed that exhibit uniform crystallite orientation and phase purity. To reliably fabricate such devices, a detailed and unambiguous characterization of their structure is vitally important. It ensures, firstly, the correct morphology and texture of a MOF layer, and, secondly, can provide clues on how to improve synthetic protocols. Still, the most commonly used tool for MOF thin film structure characterization is out-of-plane XRD that, in fact, only allows for a very limited insight into crystalline properties by exclusively probing periodic structures along the substrate normal. While out-of-plane XRD is a powerful technique to assess crystalline structure MOF powder samples,²¹² it is not sufficient to reflect the full structure of oriented MOF thin films (see **Section 2.1** for more details). For thin films, a much more comprehensive alternative technique is given by 2D GIWAXS that can provide a much deeper

structural insight by assessing a multitude of crystallographic planes at once.

One main issue with two-dimensional grazing-incidence diffraction techniques is the low level of accessibility as such experiments are commonly conducted at synchrotron facilities. As a consequence, the measurements have to be planned and initiated a long time in advance, the thin films are only characterized much later than they were synthesized and the costly beamtime reduces the number of tested samples to a minimum. These are important downsides when it comes to development and optimization of synthetic protocols for MOF thin films in the laboratory, where researchers would much more benefit from direct feedback after the synthesis. In some cases, thin films might not even be stable for extended periods post-synthesis but require to be characterized immediately after production. This is why there is a strong need for structural characterization in smaller-scale laboratory-devices that can be readily accessed within a common research environment.

This work exemplarily demonstrates such a strategy to provide and refine insight into oriented UiO MOF thin film growth *via* GIWAXS analysis conducted on a compact laboratory-scale Bruker D8 Advance diffractometer. While there is a wide palette of sophisticated software to analyze 2D diffraction data acquired at a synchrotron,^{73,75,76} they are not readily usable for stitched image data from smaller-scale diffractometers that emerge from detector scanning on a goniometer. This work also provides a link to process a series of 2D images acquired on a goniometer in lab-scale thin film diffraction devices to be analyzed with common GIWAXS analysis software. Furthermore, an image processing tool chain was implemented in MATLAB to provide a quantitative measure for the oriented vs. non-oriented crystallite fractions in MOF thin films from their 2D diffractograms. The detailed GIWAXS analysis is used to gain an informative insight in the structural make-up of fabricated thin films

and allows to draw conclusions about processes happening during the synthesis by vapor-assisted conversion, recently reported to yield highly oriented UiO layers.¹⁶²

The UiO MOF was chosen as an exemplary system, since this class of MOFs is extremely versatile that is of interest for a large variety of different applications. UiOs are among the most stable MOF structures against environmental factors such as temperature,⁸⁵ pressure,^{124,125} or moisture.²¹³ Due to their structural variability allowing to incorporate different functional linkers or metal nodes, they can be applied in many very different fields including sensing,^{214–216} photovoltaics,^{217,218} catalysis,^{219,220} or memristors.^{221,222} Thus, advanced insight into the synthesis of UiO-based thin films and further development such as heterostructures are of high value for various research domains. Furthermore, oriented UiO thin films produce a very rich 2D scattering pattern with a high number of off-axis peaks which makes them well suited to test the GIWAXS analysis procedure.

4.2. Overview

In this chapter, a procedure implemented in MATLAB is presented to 1) accurately represent GIWAXS data obtained from a laboratory-scale diffractometer and to 2) extract quantitative information about oriented crystallite fractions of the measured thin film from the 2D images. This procedure is then used to analyze UiO-type MOF coatings made by a VAC fabrication technique from the literature (explained in **Section 3.1.5**),¹⁶² to create <111>-oriented structures. The GIWAXS analysis reveals that homogeneous nucleation of crystallites in the deposited mother liquor leads to 3D powder crystallites instead of a targeted 2D powder textured thin film. Fine-tuning of synthetic conditions to reduce homogeneous nucleation during the fabrication, such as change of the reactor geometry and minimization of the time duration between mixing and deposition of the precursor solution,

was shown to significantly improve oriented crystallite fractions in the produced films. UiO-66 and UiO-67 thin films could be obtained and determined to have reached >96 % and >95 % of <111>-oriented crystallites, respectively, with excellent long-range order. Moreover, it was demonstrated that heterostructures of UiO-67 and UiO-66 could be formed with both layers containing a high quality 2D powder texture (UiO-67: >94 %, UiO-66: 83 %). Details about the structural makeup of the obtained materials could be derived from depth-dependent GIWAXS analysis. In more general terms, the significant benefits of 2D GIWAXS analysis of MOF thin films were exemplified in terms of superior testing of theoretical structural models over 1D PXRD scans, providing quantitative estimates of 2D powder texture of a thin film very useful for process optimization and to allow for an approximation of this information across a films' thickness.

4.3. GIWAXS Image Projection and Diffractogram Analysis

Once experimental GIWAXS data has been acquired, it is necessary to represent the 2D image in reciprocal space spanned by the scattering vectors q_z and q_r that is independent of the measurement system (see **Section 2.1.3**). There is a great variety of open-access GIWAXS analysis software available, readily capable of performing such a transformation for images acquired at a synchrotron experiment. However, there is a significant difference between a synchrotron-based setup and a laboratory-scale 2D diffractometer. At a synchrotron, it is common to use a large-area, vertically-oriented detector situated behind the horizontally placed sample to probe a large region of the reciprocal space in a single shot. In a compact lab-scale system, such as a Bruker D8 Advance, a much smaller detector is used. In order to still retain a large portion of the scattering pattern the rectangular 2D detector is mounted on a goniometer on which a series of images is taken at multiple angles, instead of a single shot. In order to make these individually acquired images processable with

standard synchrotron analysis software, the image series is projected onto a new vertical plane of a virtual detector. This procedure is depicted in **Figure 4.1** and was implemented in MATLAB.⁷² Starting from the origin at the goniometer center, a pixel in the recorded image is projected onto the virtual detector array, resulting generally in a polygonal shape. Conserving the originally recorded energy per pixel, the overlap of each projected polygon with each virtual pixel is calculated and the intensity, then, proportionately distributed over the virtual detector array. Thereby, the virtual pixels were chosen to match their real detector counterparts. The pixel-wise implementation of the projection is illustrated in **Figure 4.2**.

Apart from taking images at multiple angles with a small detector, another experimental optimization to access a larger portion of the diffractogram is to avoid recording redundant diffraction data. Because of the point-symmetric nature of the MOF thin film scattering

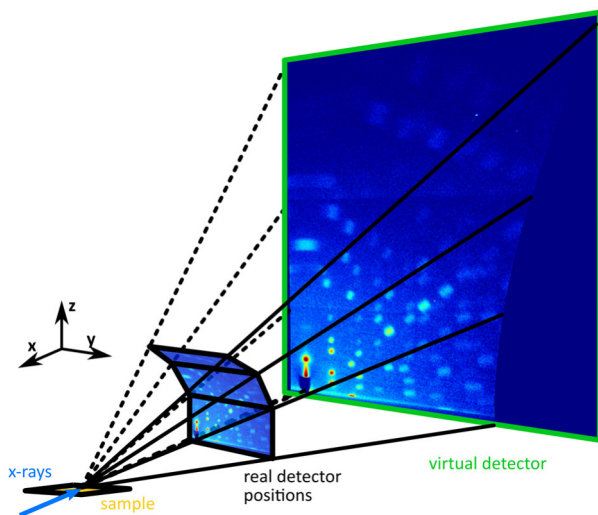


Figure 4.1. Projection of sequential 2D images taken with a small detector on a goniometer. Pixels from the individual images are projected onto a vertically oriented, virtual detector. Adapted from Fischer et al. with permission (CC BY 4.0).⁷²

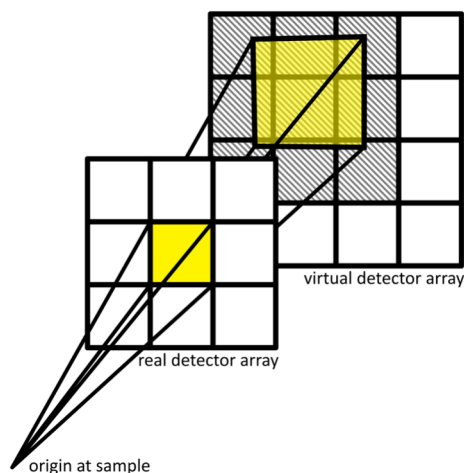


Figure 4.2. Pixel-wise projection during GIWAXS image processing. The area of the real detector pixel is transferred to the virtual detector (yellow) whereby the intensity value saved for this pixel is distributed over intersected virtual pixels (grey) according to the respective overlap area. The virtual detector array is set to have the same pixel size as the real detector. Adapted from Fischer et al. with permission (CC BY 4.0).⁷²

patterns resulting from its cubic crystal structure, it is sufficient to only consider one quadrant of the diffractogram. Hence, the relative position of the detector to the X-ray beam was chosen such that its direct reflection would hit the detector surface in the lower left corner. This can also be seen in **Figure 4.1** in which the detector images of a UiO-67 MOF with 2D powder texture are shown.

After the image has been projected onto the vertical virtual detector, it is reshaped for reciprocal space representation over \vec{q}_z and \vec{q}_r . For this step of image processing, the open-access MATLAB toolbox GIXSGUI was used.⁷³ In **Figure 4.3**, an example of such a reshaped image is given, showing the diffractogram of a highly oriented UiO-67 thin film with $\langle 111 \rangle$ -oriented crystallites. The color-coded GIWAXS intensity distribution, given in counts per second and on a logarithmic scale, reveals an extremely high number of strongly confined

diffraction maxima. Peaks instead of rings (see **Section 2.1.4**) indicate a 2D powder texture of the thin film, *i.e.*, crystallites were grown with a preferred orientation towards the substrate plane but with a random rotation about the substrate normal. In this case, the preferred orientation is such that the $\langle 111 \rangle$ direction of the MOF lattice is aligned parallel to the surface normal. This can be read off the scattering pattern as it shows a diffraction maximum exactly in q_z direction at a value of $q_z \approx 0.41 \text{ \AA}^{-1}$ which is created by the $\{111\}$ scattering plane family. An illustration of a UiO MOF unit cell in this orientation on a substrate is presented in **Figure 4.4**.

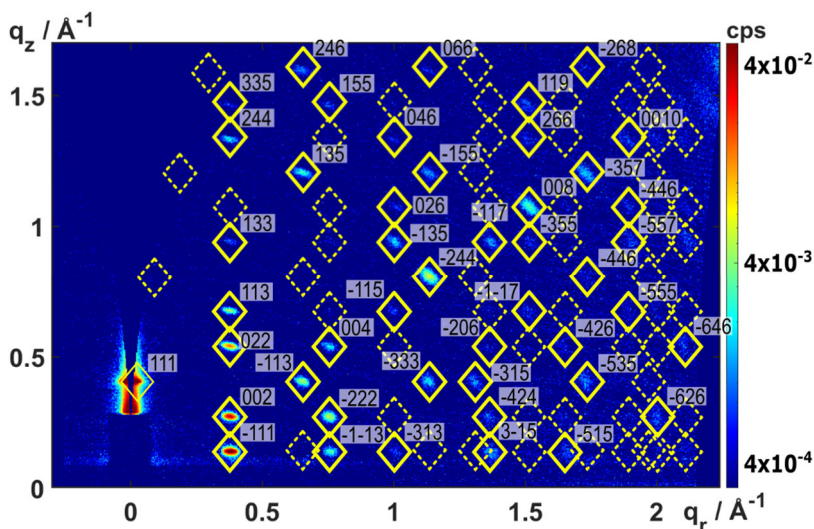


Figure 4.3. GIWAXS diffractogram of a $\langle 111 \rangle$ oriented UiO-67 thin film presented over scattering vectors q_z and q_r . The simulated diffraction pattern for a $\langle 111 \rangle$ texture (indicated by dashed-lined yellow diamonds, based on the expected crystal unit cells) was generated based on literature crystallographic data.^{134,223} Matching positions of experimental diffraction maxima and the expected, simulated ones confirm the MOF structure and preferred orientation of growth. Simulated diffraction maxima that coincide with experimental ones are highlighted by solid-lined diamonds and labeled with their Laue indices indicating the diffraction plane families responsible for the scattering signal. Adapted from Fischer et al. with permission (CC BY 4.0).⁷²

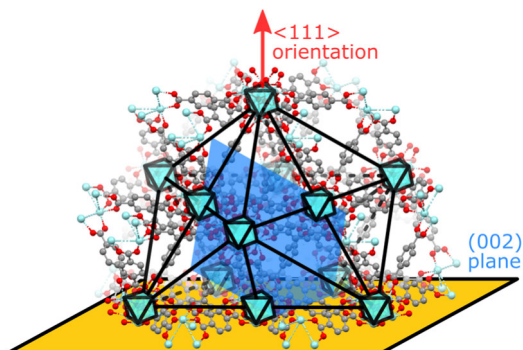


Figure 4.4. $\langle 111 \rangle$ -oriented UiO MOF with indication of (002) scattering plane on a substrate Adapted from Fischer et al. with permission (CC BY 4.0).⁷²

To verify that the observed pattern is the only orientation of crystallites occurring and not only a subset of many different ones, the expected diffraction peak positions for the UiO-67 MOF in $\langle 111 \rangle$ orientation were simulated and plotted as dashed-lined yellow diamonds onto the same image. The diamonds were made solid-lined everywhere experimental diffraction peaks coincide with the expected pattern and labeled with their respective Laue indices. The reference pattern was calculated based on the DWBA (see **Section 2.1.3**) using the GIXSGUI MATLAB toolbox.⁷³ The crystallographic parameters used for this calculation were based on crystal unit cell data ($a = b = c = 26.78 \text{ \AA}$, $\alpha = \beta = \gamma = 90^\circ$), chemical composition and density ($\text{C}_{84}\text{H}_{52}\text{O}_{32}\text{Zr}_6$, $\rho_{\text{UiO-67}} \approx 0.70 \text{ g cm}^{-3}$) from the literature which allowed for an estimation of values for attenuation $\mu_{\text{UiO-67}} \approx 27 \text{ cm}^{-1}$ and critical angle $\alpha_{c,\text{UiO-67}} \approx 0.12^\circ$.^{134,223–225} Comparing the experimental and simulated data, all observed scattering maxima are confirmed to coincide with a simulated diffraction peak. This points out the $\langle 111 \rangle$ -orientation as the only one present. All these peaks in **Figure 4.3** were labeled with their respective Laue indices, that indicate the scattering plane families responsible for the diffraction maximum.

To also quantitatively compare the relative positions of experimental and simulated diffraction peaks, the average relative deviation can be determined. For such an analysis, in order to reduce the recorded scattering maxima to single points, all experimental diffraction peaks are represented by their individual centers of mass. Because these are not trivially obtainable, their calculation is briefly delineated here.

For an accurate calculation of the center of mass of each peak, it is important which pixels in the GIWAXS image are considered to belong to a diffraction maximum and which are considered background, *i.e.* the image needs to be segmented. Different challenges need to be addressed to achieve that. Firstly, the background level originating from scattering of non-crystalline material is not uniform across the image and, moreover, can vary between each measured sample. Secondly, the height of the diffraction maxima can be orders of magnitude different across the image, *e.g.* dependent on the diffraction order and their azimuthal position. These aspects render common segmentation strategies, like the watershed algorithm, less efficient as very small peaks could easily be lost in the background with a constant threshold level. One approach to tackle this issue could be to remodel the background in each case to apply a position-dependent segmentation threshold to the image. However, depending on the shape and size of the diffraction peaks, the background could be largely masked by the actual thin film scattering maxima, potentially creating large undefined areas in the background model.

For this reason, a reverse strategy was chosen starting from the top of each peak, the local maximum, evaluating their immediate surroundings to determine the centers of mass of the diffraction peaks. As a first step the peaks of interest were manually chosen in the 2D image by cursor clicking any point close to a visible diffraction spot. From these initial starting points, iteratively, the next highest intensity nearest neighbor pixel was determined until each local

maximum was reached. This strategy allowed to easily find the highest points in a diffraction spot of arbitrary shape. This is beneficial since GIWAXS diffraction spots can exhibit many different shapes depending on distribution of crystallite orientations, crystallite sizes, strain, etc.

In the next step, the pixel segment defining the local peak is determined. Emerging outward from each local maximum, a closed area is formed by iteratively adding the next-highest intensity pixel. This was realized by performing image dilation on a binary image seed (initially only containing the starting pixel) and iteratively saving the highest pixel within the local neighborhood of the seed. This routine generates the peak segment from the top avoiding inclusion of low-level background pixels to define the area from which the center of mass will be calculated.

Comparing the single-point representations of the experimental diffraction spots in **Figure 4.3** with the simulated peak positions by means of the Euclidian distance, a very low average relative deviation of 0.45 % percent was found. For the calculation, the 30 brightest intensity diffraction peaks visible in the diffractogram were considered. In general, a discrepancy between experimental and simulated peak positions can indicate, for example, a difference of the unit cell size. However, there can also be more subtle factors influencing the peak position such as strain inside the thin film or non-uniform film flatness.^{226,227} Hence, to determine the exact cause for deviating peak positions in a specific case requires dedicated additional characterization of the thin film. This is, however, not indicated in this case of almost perfectly matching of experimental and simulated diffraction patterns.

4.4. Orientational Analysis of UiO Thin Films from VAC

In the previous section, a UiO-67 thin film was discussed that is in the desired 2D powder texture with a $\langle 111 \rangle$ orientation. To recall, this

means that the crystallites have their crystallographic $\langle 111 \rangle$ axis aligned with the substrate surface normal but can be rotated randomly about this axis. While highly oriented UiO-67 thin films could be created reasonably reproducibly, using the VAC method, this could not be achieved for the isorecticular UiO-66 system. Instead, the films repeatedly exhibited a 3D powder texture, *i.e.* fully randomly oriented crystallites, with a very minor portion of crystallites in the 2D powder form at best. **Figure 4.5** shows an example of such a UiO-66 thin film diffractogram with poor crystallite orientation.

Again, for comparison, an overlay of the expected peak positions of UiO-66 in $\langle 111 \rangle$ orientation was added by yellow diamonds as well. As for the UiO-67 before, this pattern was simulated with GIXSGUI and

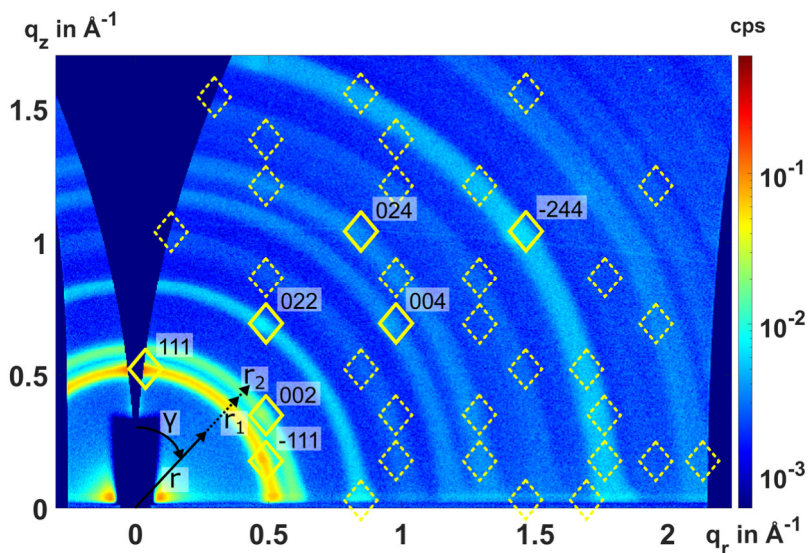


Figure 4.5. Poorly oriented UiO-66 thin film diffractogram. Dashed yellow diamonds indicate the expected diffraction pattern for a $\langle 111 \rangle$ orientation based on literature crystal data.^{134,223} They are depicted solid-lined and are labeled with their Laue indices where weak experimental peaks coincide. Radii r_1 and r_2 label the sector based on which an azimuthal line cut is calculated, *i.e.* a pole figure over the polar angle γ . Adapted from Fischer et al. with permission (CC BY 4.0).⁷²

the crystallographic parameters used for the calculation were based on literature values ($a = b = c = 20.80 \text{ \AA}$, $\alpha = \beta = \gamma = 90^\circ$, $\text{C}_{36}\text{H}_{25}\text{O}_{29}\text{Zr}_6$, $\rho_{\text{UiO}-66} \approx 0.92 \text{ g cm}^{-3}$) from which approximate values for the attenuation coefficient $\mu_{\text{UiO}-66} \approx 49 \text{ cm}^{-1}$ and critical angle $\alpha_{c,\text{UiO}-66} \approx 0.14^\circ$ could be derived.^{134,223–225}

We can clearly see that the simulated peak positions reside within the observed diffraction rings and, thereby, confirm a UiO-66 type crystal unit cell. Thereby, some rings diffraction rings are broader than others. This can be explained by diffraction rings from many different scattering planes with very similar spacing fusing and creating wider rings. Although these rings clearly dominate the GIWAXS image, occasionally, there are some spots of higher intensity surrounding the simulated peak positions. These spots indicate a certain fraction of crystallites that are, in fact, in the targeted $\langle 111 \rangle$ orientation. Interestingly, there are only two alternatives seen in the experiment: either totally random (isotropic) crystallite orientation or $\langle 111 \rangle$ -oriented crystallites, indicated by azimuthally highly confined diffraction spots close. This gives rise to the hypothesis that there are only two distinct routes of crystallite formation. This important insight will be of use later on as when attempting to improve the synthesis for better oriented crystallites.

From the GIWAXS image, we now know that there *is* a certain portion of crystallites in the $\langle 111 \rangle$ orientation mixed with randomly oriented crystallites. The next step is to determine *how much* of the thin film exhibits the $\langle 111 \rangle$ orientation in comparison to the isotropic fraction. This knowledge can be derived from the presented GIWAXS data by considering the azimuthal intensity distribution (along the angle γ indicated in the figure), the pole figure. The ratio of distinct areas under the curve then reflects the ratio between crystallites in 3D powder and 2D powder texture.^{79–84} This method has been used, for example, to characterize orientation in similar polymer-based thin

film systems,^{81,83,84} and is also an appropriate measure for the UiO thin films discussed in this work.

To arrive at a suitable pole figure for this analysis, a reporter diffraction ring and peak need to be chosen. For the UiO MOF in $\langle 111 \rangle$ orientation, the most convenient pole figure can be obtained for the $\{002\}$ diffraction plane family. One representative of this plane family, (002), is highlighted in blue in **Figure 4.4**. As a consequence of the fcc UiO unit cell symmetry, $\{002\}$ diffraction from 2D powder texture crystallites always results in one diffraction peak that is off-axis (neither in the q_z or q_r direction). This is very suitable for the pole figure analysis as it facilitates handling the inevitably missing portion of the pole figure (missing wedge) around a polar angle of $\gamma = 0^\circ$. Choosing an off-axis peak, consequently only a portion of the diffraction ring will be clipped around $\gamma = 0^\circ$. This missing part can be extrapolated by extending a fitted constant value towards the origin. It would be also possible to precisely reconstruct the missing wedge in the diffractogram by performing the GIWAXS experiment under local specular conditions.^{80,228,229} Thereby, the Ewald sphere is tilted such that intersection with reciprocal lattice point of interest is achieved. Experimentally this is realized by appropriate tuning of the incidence angle. This approach, however, would only be necessary if a diffraction peak should be evaluated that lies exactly on the q_z axis which is not the case using the $\{002\}$ as a reporter.

In order to extract the oriented crystallite fraction from GIWAXS data based on the $\{002\}$ pole figure, an image processing routine was implemented in MATLAB and its working principle shall be concisely explained in the following. At first, two ring-shaped sectors are defined in the GIWAXS image plotted over the reciprocal space coordinates q_z and q_r . The first sector defines the radial interval containing the reporter diffraction maxima in which the line integral for the pole figure shall be calculated. In our case, this is a ring around the $\{002\}$ diffraction maximum as indicated by the radii $r_1 = 0.57 \text{ \AA}^{-1}$

and $r_2 = 0.62 \text{ \AA}^{-1}$ in **Figure 4.5**. The second interval is chosen to serve as a reference containing only background noise. For the UiO diffractogram, the larger void space in the pattern between the $\{002\}$ and $\{022\}$ rings works well for that purpose ($r_1 = 0.67 \text{ \AA}^{-1}$ and $r_2 = 0.73 \text{ \AA}^{-1}$). The radial intervals can either be chosen by specific values or by graphical input in the program. For the diffraction signal interval, to find the exact center line of the reporter diffraction maximum, an auto-alignment was implemented. After the sector around the $\{002\}$ has been defined, the intensity profile is averaged over the polar angle and radially fitted with a Gaussian function. The center of this fitted function is then used as radius at which a narrow line cut is generated to achieve the pole figure.

In order to avoid overestimation of the constant offset of the diffraction ring (reflecting the unoriented crystallite fraction), the underlying background scattering needs to be accurately subtracted. To achieve that, first, the background sector is averaged in radial and azimuthal direction. This creates two curves that represent the background level over q and γ that are linearly modeled (see **Figure 4.6a** and **Figure 4.6b**). According to this model, the background level at the position of the $\{002\}$ is extrapolated (linearly extended from the background sector) and subtracted from the pole figure (**Figure 4.6c**). The background corrected reporter pole figure can then be modeled by a Gaussian peak with a constant offset to distinguish 2D powder and 3D powder contributions, with the respective areas under the curve highlighted in green and red in **Figure 4.7a**. The elevated area close to the horizon in the GIWAXS diffractogram at a polar angle close to 90° is a Yoneda peak and, hence, not considered for the orientational analysis.²³⁰

As discussed in **Section 2.1.4**, only a certain fraction of crystallites of a specific orientation can be seen in a GIWAXS experiment. To more precisely determine these crystallite fractions in the pole figure, the

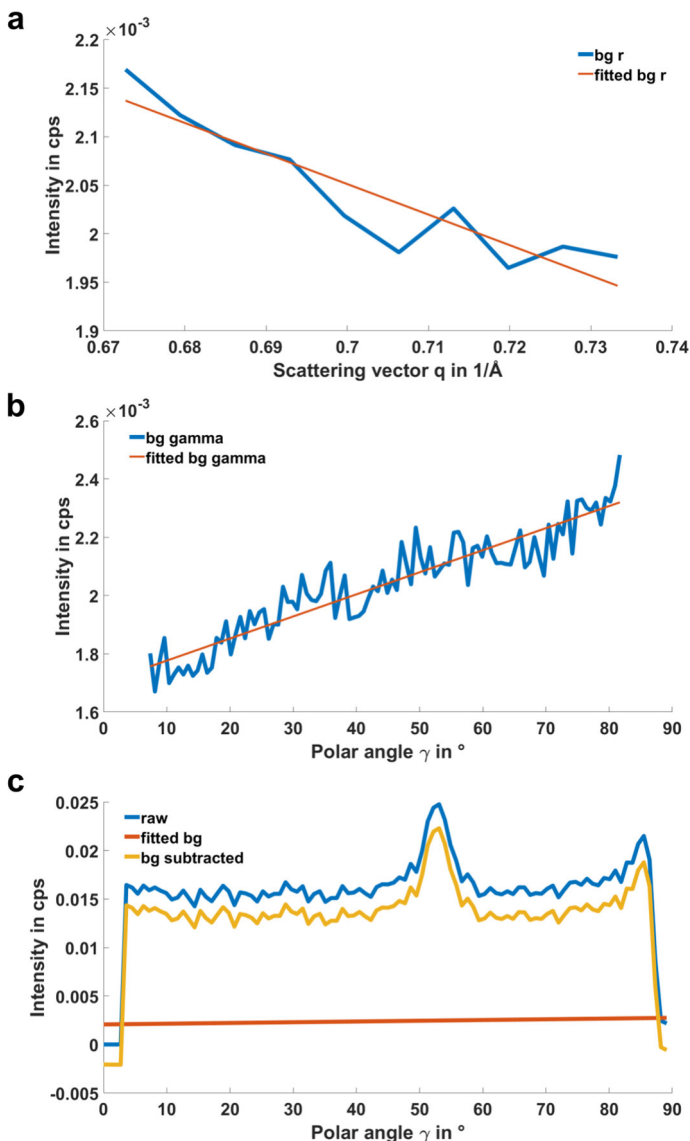


Figure 4.6. Background correction of pole figure. **a)** Averaged background noise in radial direction. **b)** Averaged background noise in azimuthal direction. **c)** {002} pole figure background correction based on radially and azimuthally modeled background level.

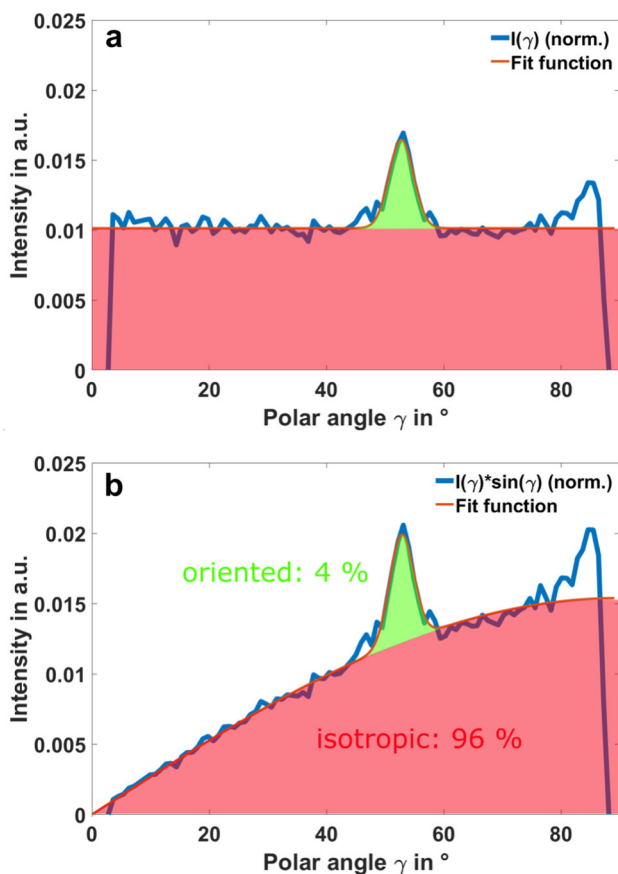


Figure 4.7. {002} pole figures from GIWAXS diffractogram of UiO-66 thin film. **a)** Pole figure without correction. **b)** Pole figure with $\sin(\gamma)$ correction. The green and red areas under the curves in b reflect the oriented and isotropic crystalline fractions of the thin film, indicating portions of 4 % oriented and 96 % non-oriented crystallites. Adapted from Fischer et al. with permission (CC BY 4.0).⁷²

intensity function needs to be multiplied by the $\sin(\gamma)$ correction term. So, the highlighted areas under the curve in this $\sin(\gamma)$ corrected pole figure (in **Figure 4.7b**) now correspond to the fractions of crystallites in 3D powder and 2D powder texture and reveal in this case a fraction of 4 % of crystallites in the $\langle 111 \rangle$ orientation.

As a final remark, in order for the method to reflect these crystallite fractions across the whole thin film, an important aspect to be considered is the probing depth during the data acquisition. As introduced in **Section 2.1.5**, the penetration of incident X-rays into the sample material is dependent of the incidence angle, where higher angles lead to increased penetration depth. The measurements presented in this and the following section, hence, are all taken at supercritical incidence angles. This ensures transmission of the X-rays into the thin film and in the consequence probing of the whole structure. If smaller incidence angles are chosen, the observed scattering only originates from a thin, evanescently probed layer at the top. This case is discussed later in **Section 4.6** when performing a depth-dependent analysis.

4.5. Optimization of Oriented Thin Film Growth

A high fraction of non-oriented UiO-66 crystallites is clearly not desired. In order to increase the portion of the thin film in the targeted 2D powder texture, the synthesis parameters were fine-tuned with the premise of homogeneous nucleation causing a high amount of unoriented crystallites. To test this hypothesis and reduce the formation of crystallites in solution that in the process land on the substrate with a random orientation, the rate at which the precursor concentration in the growth solution droplet rises after placement in the oven was reduced. This was implemented by using a broader base reaction vessel to more quickly increase the vapor pressure upon reactor heating, countering the droplet evaporation from the substrate surface. Additionally, in order to keep the concentration of precursors inside this droplet more uniform for a longer period of time (by lowering the impact of solvent evaporation at a certain rate on the relative droplet volume decrease), the total droplet volume was increased to the maximum amount still supported by the substrate. With this approach, the fraction of <111>-oriented crystallites in the UiO-66 thin film could be significantly improved to

40 %. The corresponding GIWAXS diffractogram and $\sin(\gamma)$ corrected pole figure are shown in **Figure 4.8a** and **Figure 4.9a**.

However, 40 % still suggests that there is a significant impact of unwanted homogeneous nucleation causing crystal formation not initiated at the substrate surface. Another aspect potentially driving formation in solution could be the gradual aggregation of clusters of precursors in the growth solution easing homogeneous crystal nucleation later on. Even though no obvious powder formation could be observed inside the growth solution this potential mechanism should be prevented. Therefore, the time between growth solution mixing and deposition on the substrates for the reaction was reduced to a minimum of less than 5 mins, from a time scale of several hours previously. This strategy yielded another notable improvement visible in the diffractogram and $\sin(\gamma)$ corrected pole figure in **Figure 4.8b** and **Figure 4.9b**. The extremely high number of confined diffraction peaks recorded readily explained by the Laue indices of the simulated pattern indicates a very high long-range order. The lack of a clear constant offset indicates that the synthesis could be majorly improved to yield a thin film with an at least 95 % fraction in the 2D powder texture. The lower limit was estimated by assessing the portion that could be hidden within the noise level and taking the standard deviation of that “baseline” as a reference. Looking back at the UiO-67 diffractogram in **Figure 4.3**, there is also no obvious ring visible superimposing the {002} reporter peak. The same estimation procedure, in this case, leads to a very similar lower limit of 96 % for the fraction of crystallites with the 2D powder texture.

In addition to this maximum fraction of crystallites in the 2D powder texture, the diffractogram of the best achieved UiO-66 thin film exhibits an extremely high number of confined diffraction peaks visible in **Figure 4.8b**, indicates a large average coherence length of the thin film (*i.e.* large crystallites). The observed diffraction maxima match the peak positions of the simulated pattern equally well as in

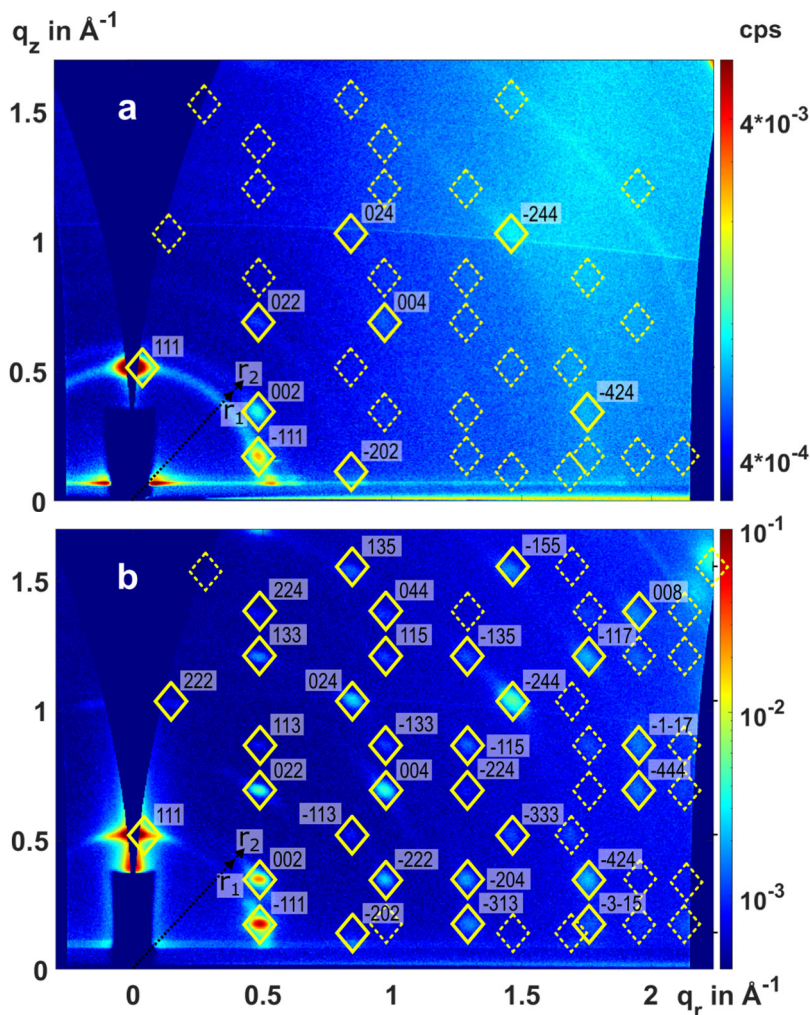


Figure 4.8. 2D GIWAXS diffractograms after fine-tuning UiO-66 synthesis with GIWAXS-based orientational analysis. **a)** UiO-66 thin film with synthesis procedure improved for mitigating growth solution droplet evaporation effects. **b)** UiO-66 thin film with minimized time between growth solution mixing and reaction start. The radii r_1 and r_2 indicate the q sector for the pole figures given next. The simulated pattern based on literature structure data,^{134,223} is shown by dashed yellow diamonds that are solid-lined and labeled when experimental peaks coincide. Adapted from Fischer et al. with permission (CC BY 4.0).⁷²

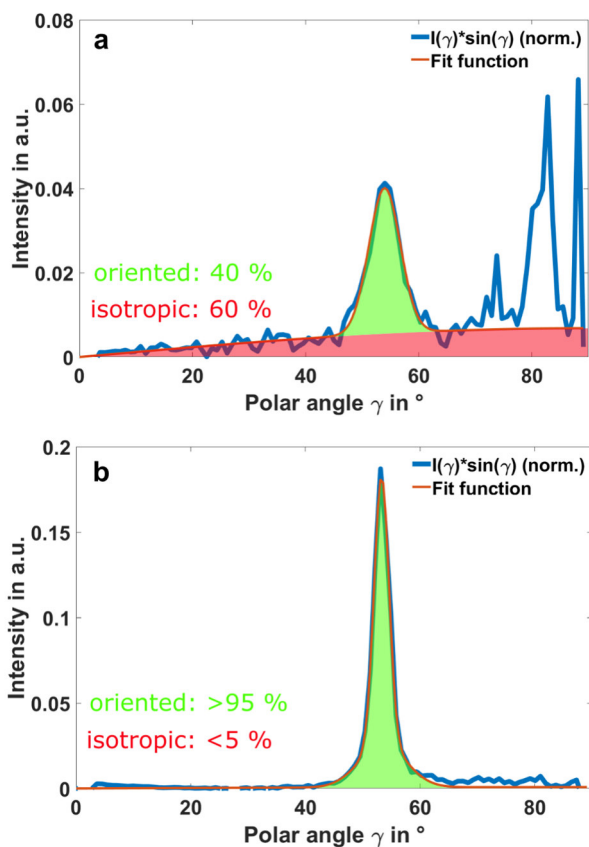


Figure 4.9. Pole figures after fine-tuning UiO-66 synthesis with GIWAXS-based orientational analysis. **a)** $\sin(\gamma)$ corrected pole figure of UiO-66 thin film with synthesis procedure improved for mitigating growth solution droplet evaporation effects. **b)** $\sin(\gamma)$ corrected pole figure of UiO-66 thin film with minimized time between growth solution mixing and reaction start. Adapted from Fischer et al. with permission (CC BY 4.0).⁷²

the case of UiO-67 in **Figure 4.3**, the average relative deviation only amounting to a value of 0.49 % (again evaluating the positions of the 30 brightest diffraction peaks).

4.6. Depth Profiling of Oriented Thin Film Fraction

As briefly mentioned previously, one interesting property of the GIWAXS measurement is the relation between probing depth and angle of incidence. This property in conjunction with the ability to assess oriented and unoriented crystallite fractions, allows for an informative insight into a thin film's vertical composition (although with certain caveats which will be discussed as well).

As an example, in **Figure 4.10a**, the diffractogram of a UiO-67 thin film is shown. In contrast to the one in **Figure 4.3**, here, diffraction rings are clearly visible in addition to some confined diffraction spots. The UiO-67 thin film corresponding to this diffractogram was made before the time duration between mixing and deposition of the growth solution was minimized, which is an honest indicator for the need of more robust synthesis protocols against minor variations. However, now this thin film can be used to learn more about its vertical makeup. Interestingly, the ratio of 2D powder vs. 3D powder crystallites significantly changes across measurements with increasing angles of incidence. This is observable in **Figure 4.10a – c** showing the GIWAXS diffractograms at incidence angles 0.05° , 0.10° and 1.00° and in **Figure 4.11a – c** with the corresponding $\sin(\gamma)$ corrected pole figures.

The X-ray penetration depth over incidence angle for a smooth UiO-67 thin film can be calculated based on **Equation 2.19**, using material properties from the literature,^{66,134,223,224} and is displayed in **Figure 4.12**. The strongly non-linear dependence between probing depth and incidence angle in a homogenous film provides for a very sensitive control of the evanescent X-ray penetration depth at incidence angles below the critical angle (in this case $\alpha_{c,UiO-67} \approx 0.12^\circ$). At higher angles, the much-enhanced penetration depth results in full thin film probing for structures with up to μm thickness. In the case of the presented measurement, these used incidence angles would lead to

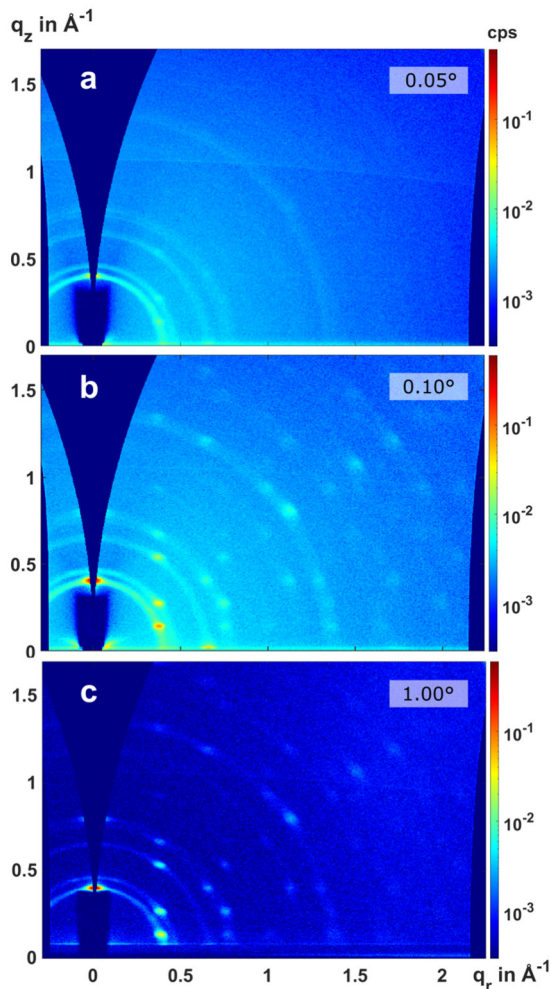


Figure 4.10. Depth-dependent GIWAXS measurements of UiO-67 thin film. **a) – c)** GIWAXS diffractograms acquired at different angles of incidence (indicated in the top right). Adapted from Fischer et al. with permission (CC BY 4.0).⁷²

penetration depths of 6 nm, 10 nm and 26.8 μm (whereby the last one, by far exceeding the thin film thickness, corresponds to full film probing). The GIWAXS pattern in **Figure 4.10a** relates to a material

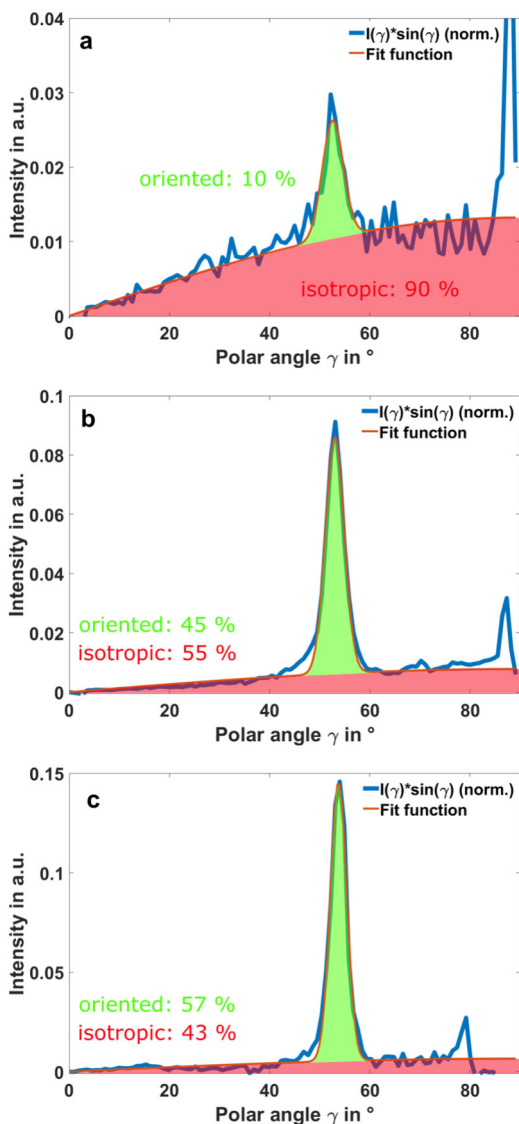


Figure 4.11. Depth-dependent orientational analysis with GIWAXS on UiO-67 thin film. **a) – c)** $\sin(\gamma)$ corrected pole figures, corresponding to the GIWAXS measurements shown in Figure 4.10 revealing a growing fraction of $\langle 111 \rangle$ -oriented crystallites with increasing probing depth. Adapted from Fischer et al. with permission (CC BY 4.0).⁷²

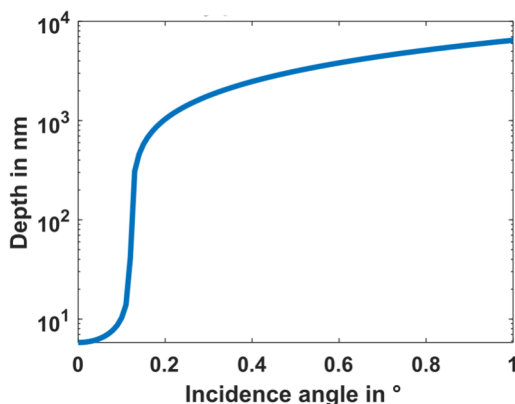


Figure 4.12. X-ray penetration depth in a perfect UiO-67 thin film. The model is based on crystallographic data from the literature and assuming a homogeneous MOF thin film.^{66,134,223,224} While the penetration depth (depicted on a logarithmic scale) can be very sensitively controlled for incidence angles below the critical angle ($\alpha_{c,UiO-67} \approx 0.12^\circ$), this changes dramatically at higher incidence angles. Adapted from Fischer et al. with permission (CC BY 4.0).⁷²

volume at the top of the thin film with a significantly smaller 2D powder crystallite fraction than the pattern in **Figure 4.10c** relating to the bulk of the sample. This tendency to show a reduced fraction of crystallites in the 2D powder texture for subcritical angles of incidence could also be observed in case of UiO-66 thin films.⁷² Interestingly, the $\sin(\gamma)$ corrected pole figure in **Figure 4.10b** that reflects the crystallite fractions from the $\alpha_i = 0.10^\circ$ measurement, already indicates a much higher portion of material in the 2D powder texture.

While the incidence angle scanning method in principle allows for the approximate reconstruction of the oriented crystallite fraction profile of a thin film depth, the accuracy is dependent of the crystallite size distribution. If the thin film is composed of homogenously sized crystallites, the estimation can be very accurate due to the high sensitivity of X-ray penetration depth with the incidence angle. However, in case of very large crystallite size differences, potential

layer boundaries will be significantly smeared out and large crystals could even protrude the thin film surface. The two extreme forms of these possible scenarios are illustrated in **Figure 4.13**.

Experimentally, in the case of the UiO synthesis, they would have different implications. In the first case, nucleation in solution could become the more prevalent the more the growth solution droplet on the substrate evaporates. A growing number of crystallites formed in solution towards the end of the synthesis would lead to a topping layer of 3D powder material. This scenario is depicted in **Figure 4.13a**. The second case would be given if crystals continuously form in solution, in parallel to the thin film growth from the surface. These crystals over time grow to significantly larger sizes such that, after falling down onto the substrate, they protrude from the surrounding

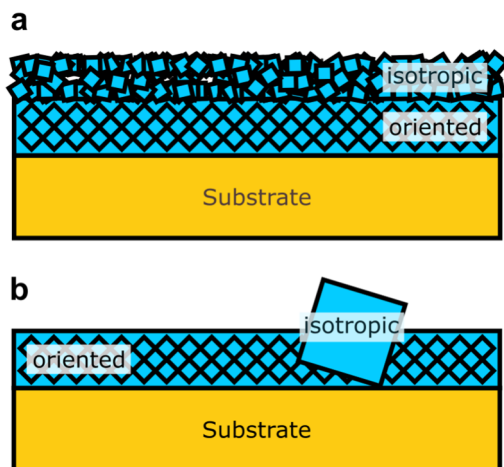


Figure 4.13. Possible interpretations of the depth-dependent orientational analysis of UiO thin films. **a)** Homogeneous thin film structure with clearly distinguished unoriented top and oriented bottom layer. The determined crystallite fractions in an incidence angle scan will more directly relate to the real depth profile. **b)** Oriented thin film with large isotropic crystal sticking out from its surface. The protruding crystal volume gets penetrated by X-rays even at small incidence angles, when the remaining thin film is only evanescently probed and, therefore, distort a depth profile derived from the GIWAXS scan. Adapted from Fischer et al. with permission (CC BY 4.0).⁷²

structures and increase surface roughness, as sketched in **Figure 4.13b**. The material volume sticking out can be penetrated by X-rays even in case of very low incidence angles that would only lead to evanescent probing of the remaining thin film. The strong difference of the 2D powder fraction between the measurements at $\alpha_i = 0.05^\circ$ and $\alpha_i = 0.10^\circ$ (corresponding to only a 4 nm difference in probing depth in a smooth thin film) could, in fact, be an indication for the presence of larger crystallites distorting the derived thin film profile. The other explanation would be an extremely thin and smooth unoriented top layer. Both of these structural hypotheses will be taken into account when examining the vertical buildup of MOF heterostructures in the next section. Both possible explanations for the GIWAXS depth scanning data, point out nucleation in solution as major cause for high unoriented crystallite fractions and, thereby, confirm the hypotheses in the previous section about promoting oriented growth. When changing the X-ray angle of incidence, also the beam projection on the surface changes. For the measurements depicted in **Figure 4.10**, the approximate footprint lengths dependent of the incidence angle α_i with a beam width of 0.3 mm (snout diameter) according to **Equation 2.20** are 344 mm (for $\alpha_i = 0.05^\circ$), 172 mm (for $\alpha_i = 0.10^\circ$), and 17 mm (for $\alpha_i = 1.00^\circ$). So, even in the case of the largest incidence angle, the footprint length exceeds the sample length of 1 cm. However, since the aperture used in the D8 Advance diffractometer is round and not rectangular, there is still a slightly varying lateral beam footprint shape at different incidence angles, changing from an almost straight line for low angles and increasingly ellipse-shaped for higher angles. In general, these footprint changes could have an influence and need to be considered in the context of potential spatial inhomogeneities of a thin film.

4.7. UiO Heterostructures

Multilayer MOF structures are of interest for various advanced optoelectronic applications. For this reason, as a final step, the VAC

method was tested as a measure to generate UiO-66/67 MOF heterostructures. This was realized in a straight-forward fashion, by conducting the fabrication procedure twice whereby the produced thin film of the first run will be used as a substrate in the second synthesis. Earlier it was found that the oriented fraction of crystallites could be majorly enhanced by reducing nucleation of crystallites in solution. With the first instance of a heterostructure, it should be investigated whether a highly $\langle 111 \rangle$ -oriented basis layer of MOF UiO-67 can have a templating effect during the synthesis of a UiO-66 top layer, that would promote oriented thin film growth even without careful control of precursor mixing time minimization prior to synthesis. To analyze the vertical makeup of the resulting heterostructure, the now familiar depth-dependent GIWAXS probing technique was used again. The characterization is presented in **Figure 4.14a** to **Figure 4.14f**, showing the GIWAXS diffractograms taken at subcritical incidence angle starting at $\alpha_i = 0.01^\circ$ and ending at a supercritical incidence angle $\alpha_i = 0.16^\circ$. In the lowest-angle GIWAXS measurement (**Figure 4.14a**), two aspects are immediately apparent. Firstly, the crystalline structure detected exhibits no preferred orientation whatsoever, showing only diffraction rings. Secondly, the position of the rings indicates that the unoriented top layer is made up of UiO-66. Probing deeper ($\alpha_i = 0.04^\circ$ to 0.07°) distinct diffraction peaks start to show at positions that are expected for the UiO-67 in $\langle 111 \rangle$ orientation, while the 3D powder UiO-66 rings still dominate the diffractogram. The different radial diffraction maxima positions indicating two different unit cell sizes are directly notable. The ring radii corresponding to scattering planes responsible for the scattering in UiO-66 are highlighted in orange and the confined peaks belonging to UiO-67 in pink in **Figure 4.14c**. Further increase of the incidence angle leading up to full film probing at $\alpha = 0.16^\circ$ reveals a strong increase of the UiO-67 with strongly growing number of diffraction spots appearing. In **Figure 4.14f**, the simulated diffraction peaks expected for UiO-67 in $\langle 111 \rangle$ orientation added as pink crosses clearly

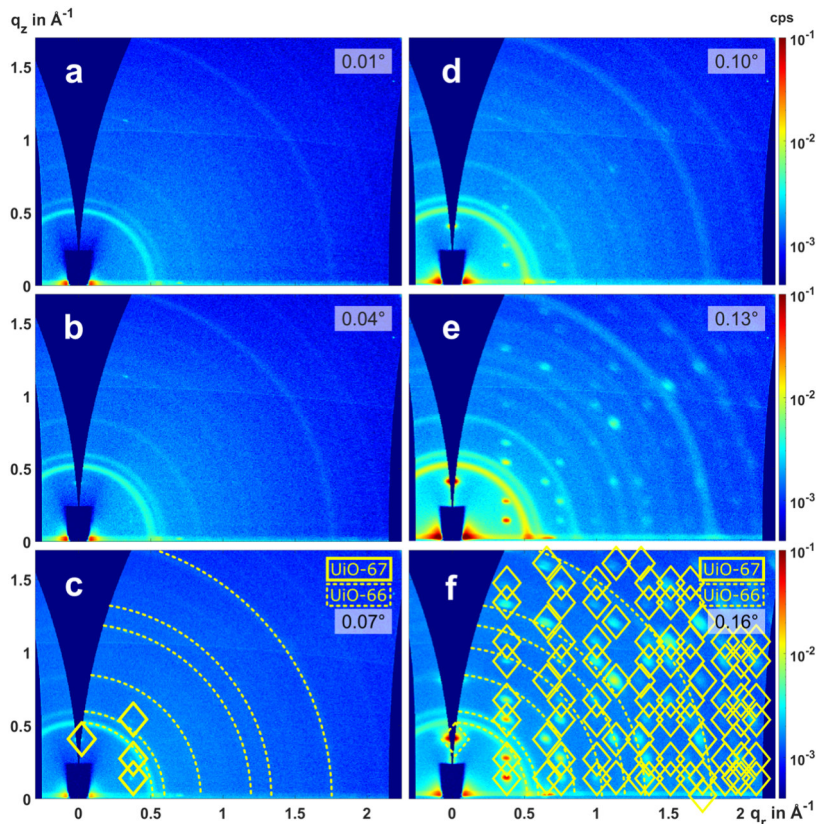


Figure 4.14. GIWAXS depth scan of UiO-66-67 (UiO-66 on top of UiO-67) heterostructure. **a) - f)** GIWAXS diffractograms acquired at different incidence angles as indicated in the top right of each image. With increasing angle, the X-rays reach deeper into the material until full film probing is achieved at the supercritical angle $\alpha_i = 0.16^\circ$. While only rings are visible at positions that are indicative of an unoriented UiO-66 phase at the lowest incidence angle, a $\langle 111 \rangle$ -oriented UiO-67 phase becomes increasingly visible the higher the incidence angle gets. In panels c and f, the respective diffraction maxima of UiO-66 (dashed) and UiO-67 (solid) are highlighted in yellow based on literature crystal data.^{134,223} Adapted from Fischer et al. with permission (CC BY 4.0).⁷²

identify all visible diffraction spots as UiO-67. In contrast, the UiO-66 scattering only apparent in the form of rings is again labeled in orange. In order to confirm this visual observation also quantitatively, the $\sin(\gamma)$

corrected $\{002\}$ pole figures are generated from the full film dataset at $\alpha = 0.16^\circ$ and shown in **Figure 4.15a** and **Figure 4.15b**. The pole figures show a >95 % oriented fraction in the UiO-67 bottom layer

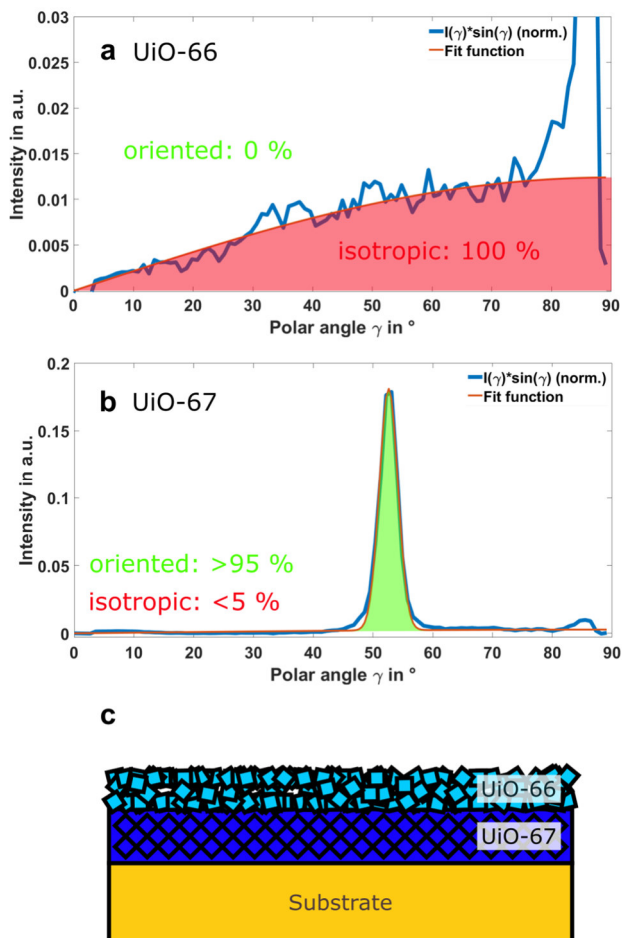


Figure 4.15. $\sin(\gamma)$ corrected pole figures and structural interpretation of UiO-66 on UiO-67 heterostructure derived from GIWAXS analysis in the previous figure. **a) – b)** $\sin(\gamma)$ corrected pole figures of UiO-66 and UiO-67 of the diffractogram with $\alpha_i = 0.16^\circ$. **c)** Structural interpretation of UiO-66-67 film with an oriented bottom and unoriented top layer. Adapted from Fischer et al. with permission (CC BY 4.0).⁷²

and a negligible orientation in the UiO-66 top layer. In conclusion, the GIWAXS analysis leads to the schematic graphical description of the heterostructure in **Figure 4.15c**.

In the second instance of a heterostructure, UiO-67 is grown on top of a UiO-66 ground layer using the fully optimized synthesis procedure to avoid crystal growth in solution. Aiming to achieve a high orientation in both layers this time, the more robustly growing UiO-67 was chosen as the more critical top layer. The depth-dependent GIWAXS characterization of the fabricated heterostructure is presented, in an analogous manner as previously, in **Figure 4.16a** to **Figure 4.16h**. In this case, the lowest-angle measurement, surprisingly, shows diffraction rings related to a UiO-66 3D powder texture instead of the actually intended UiO-67 top layer. However, UiO-67 peaks indicating a highly oriented $\langle 111 \rangle$ phase appear at higher incidence angles, while the UiO-66 rings still remain visible. This trend continues until the critical angle of $\alpha_{c,UiO-67} \approx 0.12^\circ$ is reached. From this angle onwards, now also probing the bottom structure, a small oriented fraction of UiO-66 is indicated by confined diffraction peaks superimposing the diffraction rings. In the measurement with an incidence angle of $\alpha_i = 0.16^\circ$, reflecting the whole thin film, strongly visible UiO-66 peaks are present along with the UiO-67 peaks. This is highlighted by orange (UiO-66) and pink (UiO-67) crosses that show the simulated, expected scattering peak positions for both MOFs. The $\sin(\gamma)$ corrected $\{002\}$ pole figures corresponding to the $\alpha_i = 0.16^\circ$ diffractogram in **Figure 4.17a** and **Figure 4.17b** quantitatively confirm a satisfyingly high fraction of crystallites in the 2D powder texture for both UiO-67 (>94 %) and UiO-66 (83 %). However, the non-oriented UiO-66 portion at the very top of the heterostructure, visible at subcritical incidence angles, still requires an explanation. As a plausible answer, a scenario as schematically illustrated in **Figure 4.17c** is suggested. A small number of UiO-66 crystals still form in the solution and grow to considerable

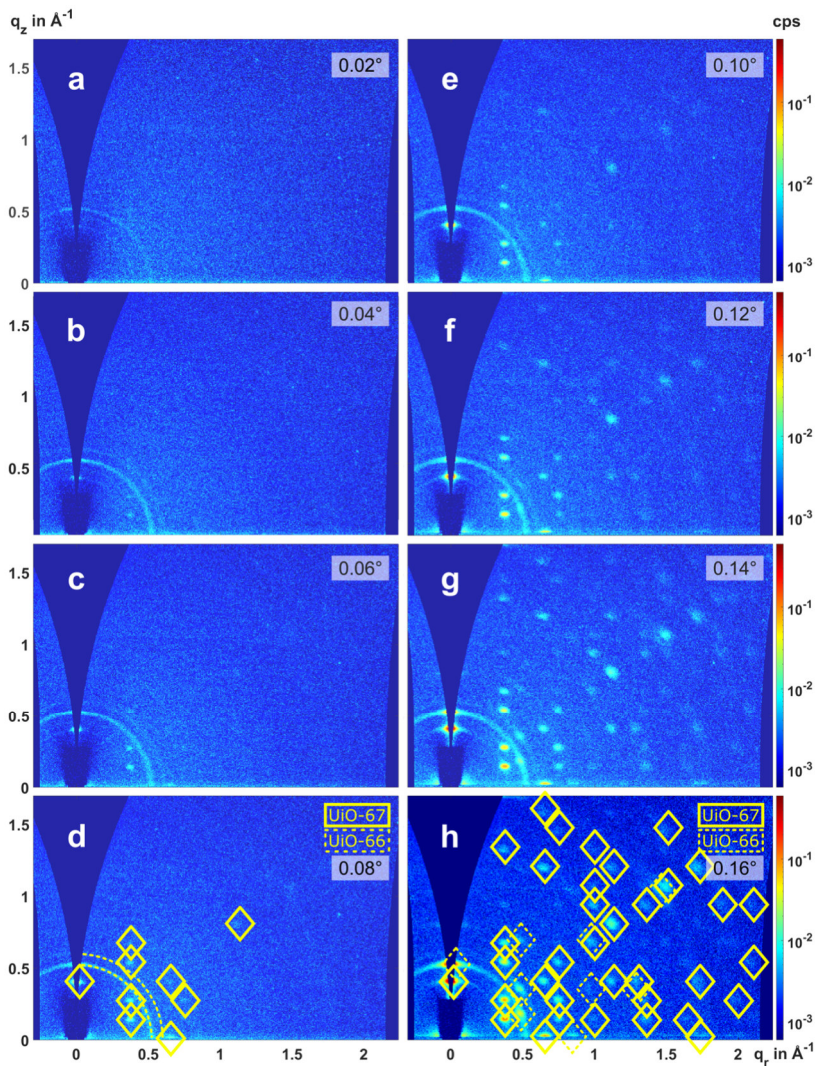


Figure 4.16. GIWAXS depth scan of UiO-67 on top of UiO-66. **a) - h)** 2D diffractograms from incidence angles as indicated. At low angles (**a) - d)**), distinct UiO-67 diffraction peaks are observed signaling a textured top layer. However, weak UiO-66 rings can be seen as well that suggest some larger, isotropic UiO-66 crystals protruding the surface. At higher angles, confined UiO-66 peaks confirm a textured bottom layer. Diffraction is highlighted in yellow (UiO-66: dashed, UiO-67: solid) based on literature structures.^{134,223}. Adapted from Fischer et al. with permission (CC BY 4.0).⁷²

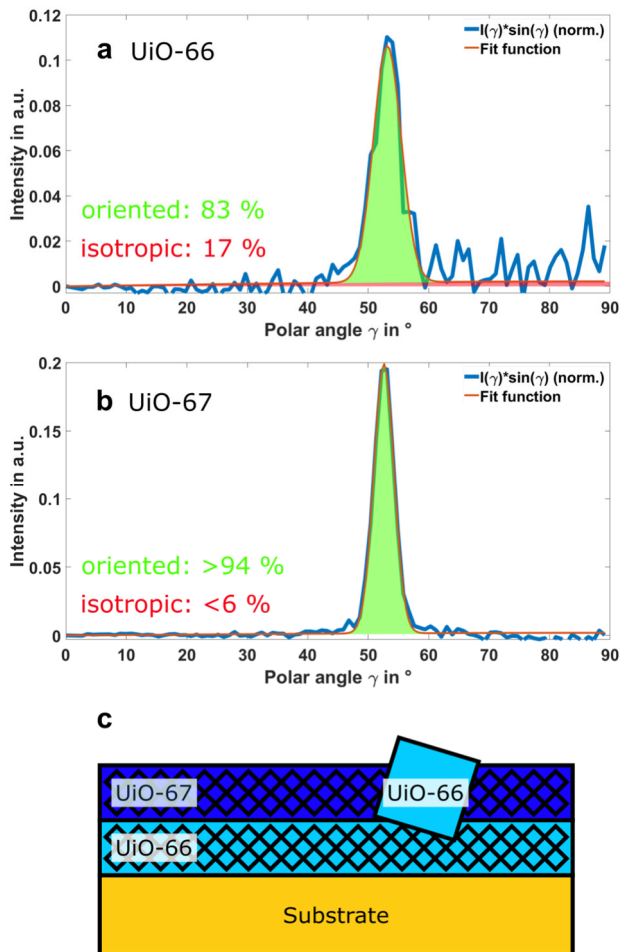


Figure 4.17. $\sin(\gamma)$ corrected pole figures and structural interpretation of UiO-67 on UiO-66 heterostructure derived from GIWAXS analysis. **a) – b)** $\sin(\gamma)$ corrected pole figures of UiO-66 and UiO-67 extracted from the full thickness probing of UiO-67-66 heterostructure at $\alpha_i = 0.16^{\circ}$. **c)** GIWAXS-based structural interpretation of UiO-67-66 film with oriented top and bottom layer with larger, unoriented UiO-66 crystals protruding. Adapted from Fischer et al. with permission (CC BY 4.0).⁷²

sizes of the order of ~ 100 nm. In the process, these crystals fall down onto the UiO-66 film in 2D powder texture and create protrusions

from the thin film's surface, that are still noticeable after the subsequent UiO-67 deposition. These crystals occasionally sticking out from the heterostructure experience are measured under a different effective incidence angle than the remaining film. Thereby, the crystals create a disproportionately larger signal at low incidence angles while the rest of the structure is only evanescently probed. To back-up the structural hypotheses made based on GIWAXS depth scans, cross-sectional SEM was performed additionally. The acquired images of both heterostructures are given in **Figure 4.18a** (UiO-66 on UiO-67) and **Figure 4.18b** (UiO-67 on UiO-66). In the first case, a multilayer structure can be seen with a denser phase at the bottom and a more granular phase at the top, with layer thicknesses of approximately 100 nm. In conjunction with the conclusions from the GIWAXS depth scan, we can readily identify the top part as the unoriented UiO-66 layer and the bottom part as the oriented UiO-67 layer. In the second case, the image was taken from slightly tilted viewing angle to simultaneously evaluate the thin film from the top. In full correspondence with the GIWAXS analysis, an oriented UiO-66

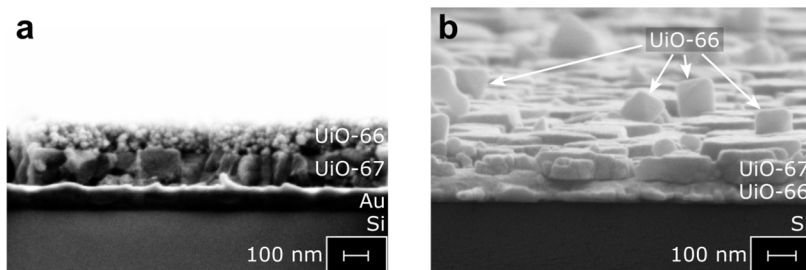


Figure 4.18. Cross-section SEM images of UiO heterostructures. **a)** UiO-66 on UiO-67. A multilayer structure can be seen composed of oriented crystallites at the bottom and isotropic crystallites at the top. Together with the GIWAXS depth-scanning, these layers can be readily identified as UiO-67 and UiO-66. **b)** UiO-67 on UiO-66. Here a multilayer structure of only oriented crystallites is visible with a few larger single crystals that protrude from the film. These crystallites confirm the earlier structure interpretation based on the diffraction rings visible at very small incidence angles. Adapted from Fischer et al. with permission (CC BY 4.0).⁷²

underlayer can be seen with an oriented UiO-67 layer on top and a lateral grain size of the order of ~100 nm. Furthermore, octahedral crystals of over 100 nm length occasionally stick out of the top layer. Together with the earlier GIWAXS based considerations, these large crystals are identified as UiO-66.

4.8. Conclusion

In conclusion of this chapter, a method to determine the fraction of MOF crystallites in a 2D powder texture vs. 3D powder texture based on 2D GIWAXS data was implemented in MATLAB, as well as to stitch and project images obtained from a laboratory-scale 2D diffractometer for usage in standard synchrotron analysis software. This method was tested on the basis of UiO-type MOF thin films made by vapor-assisted conversion. With help of such direct quantitative feedback on the sample structure, the synthesis process could be better understood and thus tuned to reduce homogeneous nucleation during the production of UiO-66 thin films to yield highly <111>-oriented MOF coatings with >95 % of crystallites in the 2D powder texture. Moreover, it was shown that heterostructures can be fabricated by a two-step synthesis process with a high fraction of 2D powder crystallites in both layers (>94 % in UiO-67 top layer and 83 % in UiO-66 bottom layer), using the thin film from the first fabrication iteration as a substrate for the second one. Thereby, it was found that there is no templating effect of the bottom layer promoting a preferred orientation in the top layer. Instead, optimal synthesis conditions for each individual layer have a much larger impact. The exemplary demonstration of the benefits of GIWAXS analysis of MOF thin films in a laboratory environment contributes to an accelerated future development of any type of MOF thin film.

5. Structure Determination of Zn-based Metal-organic Thin Films

The chapter is based on my first-author research article “Determining Structures of Layer-by-Layer Spin-Coated Zinc Dicarboxylate-Based Metal-Organic Thin Films” published in Chemistry – A European Journal [10.1002/chem.202400565].²³¹ Thin film synthesis, XRD and spectroscopic measurements and analysis thereof, figure design and data presentation were performed by J. C. Fischer (author) and the conception of the idea that structures from an excess of Zn form layered zinc hydroxides as well as the potential growth mechanism. The co-author R. Steentjes created the structural models based on density functional theory calculations and initially identified the Zn-BDC metal-hydroxide-organic framework structure. The co-author D. Chen provided guidance during IRRAS measurements and intellectual input. D. Busko built the setup that was used to measure the PLQY. E. Sauter performed the FTIR spectroscopy measurements in ultrahigh vacuum. The co-authors B. S. Richards and I. A. Howard supervised the project and provided scientific guidance, intellectual input and proof-reading.

5.1. Motivation

For photoluminescent device applications, stacked layered MOFs are a very interesting material class since they allow to arrange organic chromophores in close proximity and thereby favor intermolecular interactions influencing their photo-responsive properties.^{56,131,138,232,233} An example of such a targeted MOF is the surface-anchored MOF-2 (SURMOF-2) that has been first proposed with Cu-based metal nodes that form paddle wheel SBUs when coordinated with dicarboxylic ligands.²³⁴ This leads to extended square networks that form two-dimensional sheets as schematically illustrated in **Figure 5.1**.

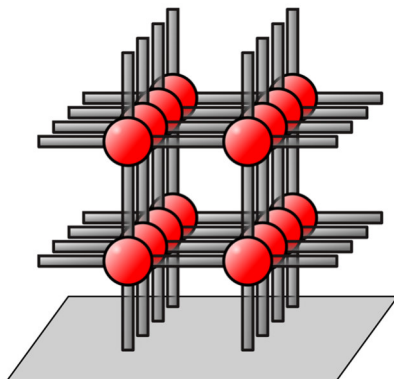


Figure 5.1. SURMOF-2 schematic. Metal clusters (red) are connected by dicarboxylic linkers (grey) forming sheet-like structures. While the intra-sheet distance between the SBUs depends on the incorporated linker length (~ 10.61 to 11.19 Å for BDC), the inter-sheet distance is independent of the linker (5.80 to 5.90 Å).^{164,234,235} The thin films created by layer-by-layer spin-coating grow in the form with standing sheets as depicted in the sketch.

Fabrication of thin films with this type of structure have been demonstrated utilizing different carboxylic linkers and synthesized by layer-by-layer or conversion methods, for example by Falcaro *et al.*,¹⁶⁴ Friedländer *et al.*,²³⁵ or Haldar *et al.*⁵⁶ For photoluminescent applications, however, Cu-based structures are obstructive due to rapid non-radiative deactivation of fluorophores by the Cu atoms (see **Section 2.3.3** for more details).¹⁶⁹ Instead, using Zn-based SBUs is much more desirable, as these preserve the linker luminescence.¹⁶⁸

However, MOFs are not the only material that can be grown from metal salts and carboxylic acids. A different group of structures is presented by layered metal hydroxides (LMHs) that exhibits versatile material properties as well. In LMHs multiple dense layers containing metal and oxygen atoms in octahedral and tetrahedral form are stacked over each other. At their interstitial sites, small acidic molecules can bond, connecting adjacent metal hydroxide layers. A well-studied example is basic layered zinc hydroxide (LZH) that is

often synthesized with intercalated acetic acid molecules.^{236–238} A long-known property of LZHS (and LMHS in general) is their ability to exchange intercalated molecules post-synthesis.^{239–242} Utilizing this property has led to LMHS being used as slow-release systems for drug or chemical delivery.^{243–245} LZH materials have also been demonstrated as a scaffold to hold organic fluorophores.^{246–248} Moreover, in the form of thin films, LZHS have found application, for example, as precursor layers for highly oriented ZnO crystals,^{249–251} or template layer and sensitizer for organic photovoltaic devices.^{250,252,253}

In this work, Zn-based thin film structures are investigated made from layer-by-layer spin-coating that is a deposition technique that is commonly used targeting SURMOF-2. Detailed GIWAXS analysis of the thin films obtained at different molar ratios of precursor concentrations in the growth solution, uncovered vastly different morphologies that are in part strongly deviating from the expected SURMOF-2 structure. With the support of density functional theory (DFT) calculations to obtain structural models, unambiguous determination of the previously thin film structures could be achieved. The profound differences among the obtained thin film morphologies were additionally verified by infrared spectroscopy and photoluminescence investigations, reflecting the chromophores situated in different structural environments.

This work provides a prototypical example of how detailed GIWAXS analysis, in conjunction with theoretical simulation, present a very powerful tool to determine previously unknown structures and to provide a more comprehensive understanding of a synthesis method to create MOF thin films. In the context of the development of Zn-based metal-organic thin films this work demonstrates the wide variety of structures that can be produced with facile spin-coating approaches, with a large palette of coordination modes of organic chromophores.

5.2. Overview

In this chapter, previously unknown structures of Zn-based metal-organic thin films made from layer-by-layer spin-coating are unraveled. Using dicarboxylic acids, such as BDC and BPDC, in different molar ratios with respect to the Zn precursor, different structures are obtained. For equimolar ratios, BPDC and Zn form a structure that strongly resembles its Cu-based analog and that agrees with literature data for SURMOF-2. BDC and Zn, however, grow in a different metal-hydroxide organic framework (MHOF) morphology. Using a Zn precursor solution with much higher concentration than the linker solutions, in both cases leads to growth of layered Zn hydroxides (LZHs) that contain the dicarboxylic linkers as vertically intercalated pillars between ZnOH sheets. This shows to be a general motif, also using additional, longer linker molecules. Testing a wide variety of Zn^{2+} -to- BDC^{2-} ratios revealed that MHOF and LZH structures can grow in parallel for a mild excess of the Zn precursor. Detailed structural knowledge is obtained by GIWAXS analysis based on experimental data in comparison to simulated diffraction patterns gained from *ab initio* DFT simulated models. The differences of the produced thin film structures are also confirmed by IRRAS and PL investigations. After establishing an overview of all obtained types of structures, all of them are examined in detail one by one, starting with the LZHs. Concluding the structural investigation, a growth mechanism is proposed that underlies thin film formation in layer-by-layer spin-coating. For ease of readability, throughout this chapter, structures *e.g.* made from Zn and BDC (or BPDC), are referred to as Zn-BDC (or Zn-BPDC).

As a preliminary remark, the author is aware that the detailed atomic arrangement of SURMOF-2 still being under an ongoing debate. While a sheet-like structure as indicated in the rough schematic is evident from the diffraction data, a detailed investigation of the precise atomic arrangement inside the metal SBUs was beyond the scope of

this work. Instead the focus was laid on the determination of the Zn-based structures, which proved to be far from trivial in itself. Research on the true nature of the SURMOF-2 structure is still ongoing and will be discussed elsewhere in the future.

5.3. Structures Obtained from Layer-by-layer Spin-coating

The sequential spin-coating procedure to alternately expose a substrate with metal and linker precursor solution with an intermediate pure solvent rinsing cycle is based on common procedures in the literature^{56,155,203,254}. The specific protocol with fixed spinning time of 10 s and speed of 2000 rpm used to prepare the herein investigated thin films (detailed in **Section 3.1.3**) was adopted from Haldar *et al.*⁵⁶. With this procedure, thin films were produced from Zn acetate dihydrate as a metal precursor with BDC and BPDC as organic linkers on Si. Initially, a 1:1 metal ion-to-linker ratio was utilized, reflecting the assumed stoichiometry of the initially targeted SURMOF-2 type structure (from 0.1 mM ethanol solutions). In the literature, there are many reports about conducting synthesis with very high metal ion-to-linker molar ratios, such as 10:1 to 50:1.^{57,132,138,153,154,234,254–256} Furthermore, it has been suggested that the precursor concentrations in the growth solutions can have a significant impact on the obtained thin film structure.²⁵⁷ Therefore, synthesis was additionally tested with a high excess of Zn²⁺ over the linker (50:1 with the Zn solution at 1 mM). The obtained thin films were characterized by GIWAXS, using the projection method and image processing explained in **Section 4.3** to represent the data over q_z and q_r . **Figure 5.2** gives an overview of the different Zn-based structures created along with Cu-reference structures in terms of their 2D diffractograms. The figure shows the data from BDC-based thin films on the left and BPDC-based ones on the right. The Cu SBU-based thin films serve as an experimental comparison of SURMOF-2. For this type of structure, experimental PXRD data can be found in the

Structure Determination of Zn-based Metal-organic Thin Films

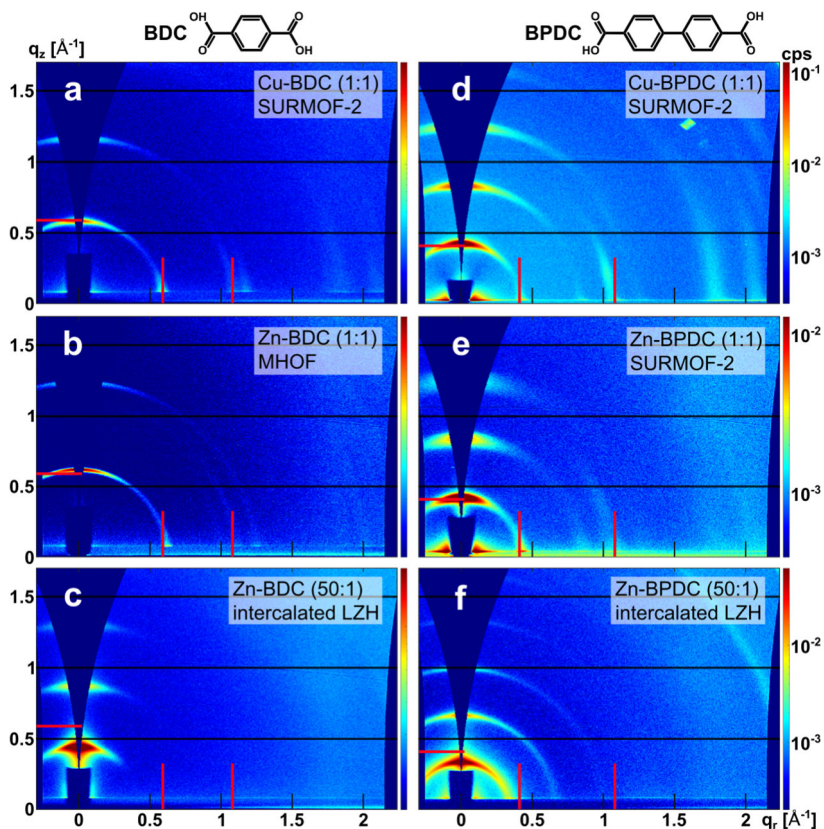


Figure 5.2. Overview of GIWAXS diffractograms from layer-by-layer spin-coated thin films indicating different structures obtained. **a) – c)** BDC-based structures. **d) – f)** BPDC-based structures. In each panel, the molar ratio of metal ion to linker used for the spin-coating precursor solution and resulting structure are indicated in the top right. In reference to the Zn-based thin films, Cu-based analogs (shown at the top) were fabricated in which metal clusters and linker are in a SURMOF-2 type configuration. Indicated by red bars are important scattering maxima expected for the SURMOF-2 structure in q_z and q_r direction based on literature data.²³⁵ Horizontal black lines were added to aid the visual comparison of the patterns. Adapted from Fischer et al. with permission (CC BY 4.0).²³¹

literature based on which linker-dependent intra-sheet SBU distances have been determined ranging from 10.61 – 11.19 Å for BDC as the ligand and 15.28 – 15.49 Å for BPDC, and linker-independent inter-

sheet separations of 5.80 – 5.90 Å.^{164,234,235} In the case of layer-by-layer spin-coating, the MOF sheets are found to be preferentially oriented vertically on the substrate (as shown in the sketch in **Figure 5.1**). This alignment can be identified immediately from a GIWAXS pattern by evaluating the positions at which inter- and intra-sheet diffraction maxima are observed: In the q_z direction, such an alignment would create diffraction maxima reflecting the intra sheet periodicity based on the length of the incorporated linker. In the q_r direction, one would expect the same diffraction maximum again (stemming from horizontal square edges of the MOF lattice), and another one originating from the small inter-sheet distance. Based on the unit cell dimensions from Friedländer *et al.* (10.71 Å, 15.28 Å and 5.80 Å),²³⁵ red bars were added in all panels of **Figure 5.2** indicating these expected scattering peak positions along the q_z and q_r axes. The bars line up with the detected diffraction maxima of the Cu-based structures in **Figure 5.2a** and **Figure 5.2d**, confirming the SURMOF-2 type structure in the vertical configuration.

With the now established expected diffraction patterns for the thin films, we continue by comparing the data on the structures fabricated from Zn. The diffractogram of the Zn-BPDC (1:1) thin film in **Figure 5.2e** matches well the Cu reference, pointing towards the same material structure and texture. However, in the case of Zn-BDC (1:1) (**Figure 5.2b**) we do not observe a match. Looking at the diffraction peak in the q_z direction, there is a small shift in relation to the Cu-BDC of $\sim 0.04 \text{ \AA}^{-1}$ (that translates to a difference of $\sim 0.6 \text{ \AA}$ in scattering plane separation). Furthermore, in the q_r direction, the recorded pattern appears clearly altered exhibiting an additional, faintly visible, diffraction maximum at $\sim 1.00 \text{ \AA}^{-1}$. This diffractogram can be explained by a metal-hydroxide organic framework (MHO) structure different from SURMOF-2 that will be discussed in detail in **Section 5.5**. The results on the Zn-based samples from a 50:1 Zn^{2+} -to-linker ratio (**Figure 5.2c** and **Figure 5.2f**) both, Zn-BDC and Zn-BPDC, appear

totally different than their reference patterns. These diffractograms, only exhibit diffraction maxima along the q_z axis which reveals horizontally ordered structures with a long-range periodicity normal to the substrate. Considering the distances between the diffraction peaks, layer separations of ~ 14.3 Å (Zn-BDC) and ~ 18.8 Å (Zn-BPDC) can be extracted. Such inter-atomic distances are far too large for a SURMOF-2 type structure. In the next section, it is derived in detail that these thin films made in high excess of the Zn precursor, both are actually layered zinc hydroxides.

It shall be added that, for a more convenient comparison of the acquired 2D GIWAXS diffractograms with literature PXRD data, pseudo-PXRD (pPXRD) patterns were generated by integration of the whole diffractogram and presenting the square root intensity values over the scattering angle 2θ , as is usually the case for PXRD data. The resulting curves corresponding to the diffractograms in **Figure 5.2** are shown in **Figure 5.3**. Added-in *via* green vertical bars are the ranges

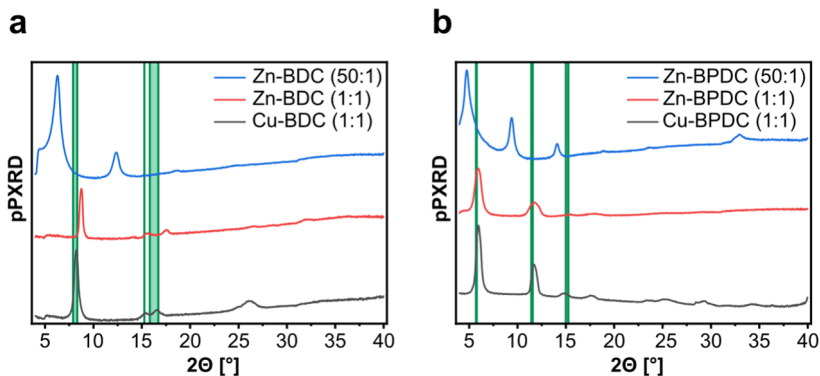


Figure 5.3. pPXRD generated from GIWAXS diffractograms in Figure 5.2. **a)** BDC-based structures. **b)** BPDC-based structures. In comparison to the experimental data, green bars indicate the expected ranges of peak positions for SURMOF-2 type structures based on the literature.^{164,235,258} Corresponding to the first and second order intra-sheet and first order inter-sheet diffraction peaks, the experimental maxima of the Cu-based structures and Zn-BPDC (1:1) resemble these literature values. In stark contrast, the remaining structures (Zn-BDC 50:1 and 1:1, and Zn-BPDC 50:1) exhibit strongly deviating pPXRD peaks. Adapted from Fischer et al. with permission (CC BY 4.0).²³¹

within which the peaks of the first- and second-order diffraction related to the intra-sheet SBU spacing, and first-order diffraction of the inter-sheet spacing of a SURMOF-2 type structure would be expected, according to the literature.^{164,234,235} From these comparisons, we can again see the agreement of the data reported on SURMOF-2 with the Cu-based references and Zn-BPDC (1:1) structures, and the disagreement with all other samples.

5.4. Layered Zinc Hydroxide (LZH) Intercalated with Dicarboxylates

The first part of the investigation of the initially unidentified thin films deals with the structures obtained from layer-by-layer spin-coating with the high Zn^{2+} -to-linker ratio. As representative structure for a more in-depth examination, Zn-BPDC was chosen. The reason for that can be understood when taking a second look upon **Figure 5.2c** and **Figure 5.2f**. For the structure determination with GIWAXS, it is desirable to capture as many different diffraction maxima as possible. The strong similarity in the appearance of the diffraction patterns in **Figure 5.2c** and **Figure 5.2f** gives rise to the idea that both films in fact relate to a common structural archetype. In addition to the clearly visible diffraction maxima lining up along the q_z axis, also a ring-like feature is visible at $q > 2 \text{ \AA}^{-1}$ (at the same position for both thin films). In the Zn-BDC diffractogram, it is only very faintly visible off-axis but seems to increase in intensity towards the q_r axis. This provides a pointer towards the actual diffraction maximum would be found on the q_r axis. Unfortunately, this region of the q_r axis lies just outside the accessible area dictated by the spatial extent of the detector in our GIWAXS setup. Fortunately, however, the Zn-BPDC thin film layers appear to be less preferentially oriented horizontally, evident by the much more ring-like appearance of the diffraction maxima. The more random crystallite orientation results in a much more prominent ring at $q > 2 \text{ \AA}^{-1}$. For this reason, the Zn-BPDC film diffractogram reveals the most structural insight and is used as a representing sample for

structure determination. Hoping to find even more diffraction rings at higher diffraction angles, an extended GIWAXS measurement was performed reaching up to a scattering vector absolute of just above 4 \AA^{-1} . The resulting 2D diffractogram is given in **Figure 5.4**. Indeed, at

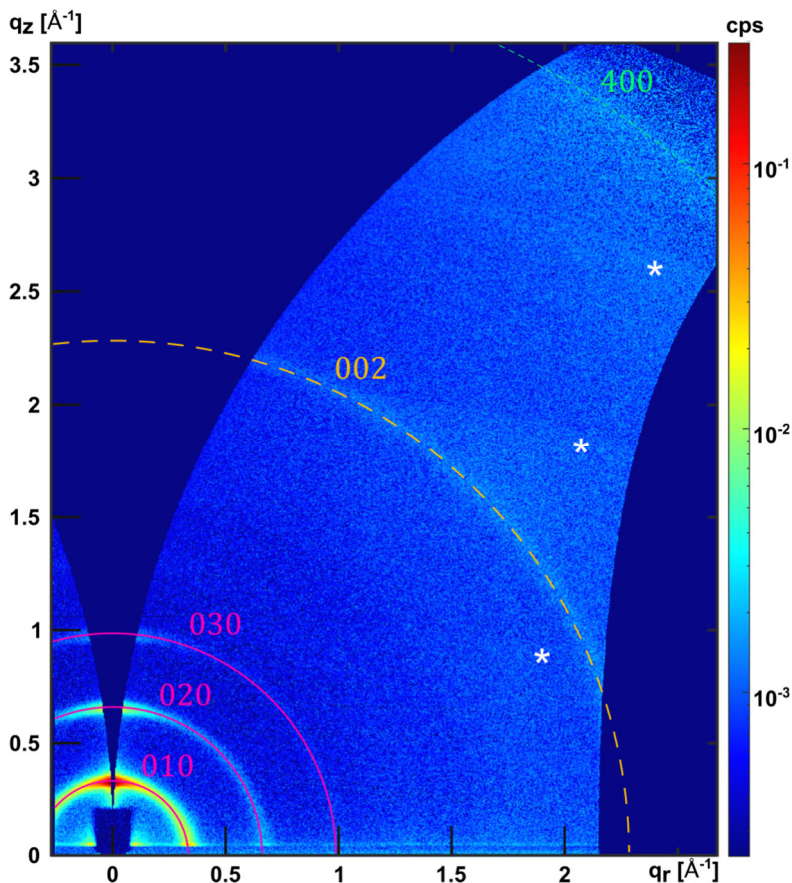


Figure 5.4. GIWAXS diffractogram of BPDC-LZH. Highlighted in the colors pink, orange and green are the observed GIWAXS intensity maxima that correspond to lattice planes on the basis of the model structure pointed out in the next figure. The abrupt changes in background scattering, labeled with white asterisks, stem from the composite nature of the stitched images taken at multiple detector angles. The large dark blue areas are inherently inaccessible regions by the GIWAXS measurement procedure. Adapted from Fischer et al. with permission (CC BY 4.0).²³¹

a very high scattering angle, in the top right of the diffractogram, an additional ring is detected. All of the visible intensity maxima are highlighted by differently colored rings. The main maximum at $q \approx 0.33 \text{ \AA}^{-1}$ (and higher orders at ~ 0.66 and ~ 0.99) labeled in pink, and the higher-up maxima at $q \approx 2.30 \text{ \AA}^{-1}$ and $q \approx 3.99 \text{ \AA}^{-1}$ in orange and green add up to a very distinct set of diffraction peaks. Such a diffraction “fingerprint” can usually be found in turbostratically disordered layered zinc hydroxides.^{236,238,242,259–261} The specific type of structural disorder presented by a rotation and/or translation of adjacent ZnOH layers that preserves their basal spacing causes only a small subset of diffraction maxima to be observable. This can be clearly seen, when comparing the experimental pPXRD (in blue) in **Figure 5.5a**. Based on this idea and similar models from the literature (in particular a Co(II) hydroxide structure intercalated with trans-1,4-cyclohexane dicarboxylic linkers by Kurmoo *et al.*),²⁶² a DFT-optimized structure for an LZH intercalated with BPDC was generated by collaboration partners from the TU Graz.²³¹ The achieved structural model is shown in **Figure 5.5b** to **Figure 5.5d** in different projections along the crystal lattice. In this framework, a substructure of ZnOH is orthogonally separated by the dicarboxylic linker. Distinct lattice planes are identified to be responsible for the observed diffraction maxima, {010} and its higher orders, {002} and {400}, which are indicated by the same color in the images of the structural model. The calculated basal layer spacing of 18.79 \AA , directly dependent of the intercalated dicarboxylate, would create diffraction peaks at 0.33 \AA^{-1} , 2.31 \AA^{-1} and 3.96 \AA^{-1} . These values are in excellent agreement with the experimental results, which is also highlighted in **Figure 5.5a**, comparing the calculated PXRD based on the structural model with the pPXRD. The high-angle {020} and {400} diffraction peaks, thereby, correspond to two specific diffraction planes inside the ZnOH layer (**Figure 5.5d**) that still create constructive interference in the turbostratic disorder.

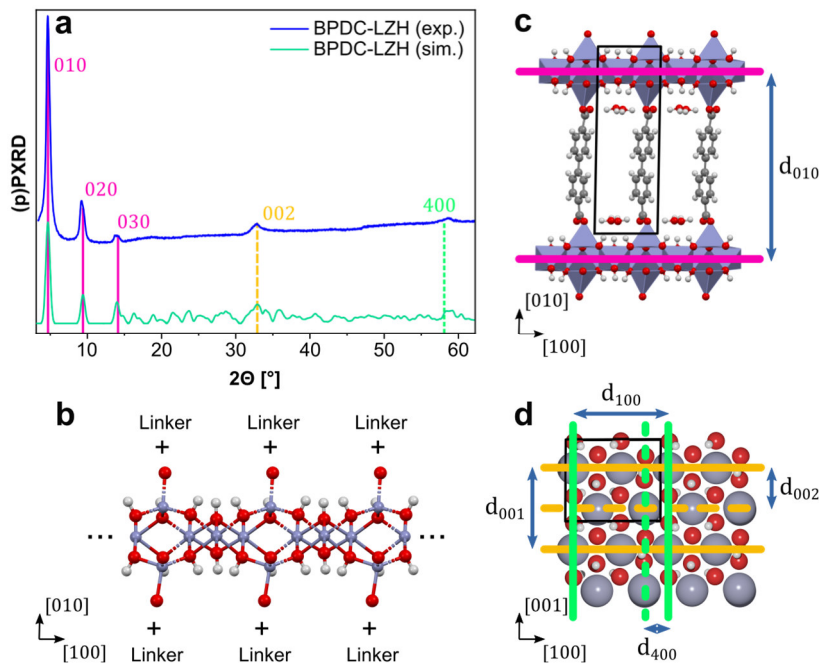


Figure 5.5. BPDC-intercalated LZH. **a)** pPXR D based on the experimental pattern in Figure 5.4 compared to the simulated PXR D derived from the DFT-based structural model. **b) – d)** Optimized structural model of BPDC-LZH in different viewing angles. Highlighted in the colors pink, orange and green are the observed diffraction maxima and the corresponding lattice planes responsible for the observed scattering. Adapted from Fischer et al. with permission (CC BY 4.0).²³¹

These diffraction maxima would, in a perfectly horizontally oriented thin film, exclusively be visible in the q_r direction. The BPDC-LZH, however, exhibits enough randomly oriented crystallites to show this diffraction signal also off-axis, in the form of rings. This allows for the verification of the small Zn-Zn inter-atomic model distances of 2.72 and 1.59 Å, which agree extremely well with the experimental values of ~ 2.73 and ~ 1.57 Å (and as well with other LZH structures in the literature).^{236,238,260,261,263}

To additionally check the structural make-up of the metal-organic thin films in terms of chemical bonds, IRRAS was employed as well. The IRRAS spectrum acquired of a BPDC-LZH thin film in ambient air is shown in **Figure 5.6a**. In this spectrum, two prominent absorption features attract immediate attention: The sharp carboxylate stretching peaks at ~ 1400 and $\sim 1600\text{ cm}^{-1}$, and the broad absorbance band, centered around $\sim 3350\text{ cm}^{-1}$. IR absorption in the range from 3200 and 3570 cm^{-1} usually is related to stretching of OH groups involved in hydrogen bonds and free water molecules, while the shoulder at around 3565 cm^{-1} would typically indicate OH stretching without H-bond involvement.^{237,264} Based on the LZH structural model containing a high number of OH groups and water molecules residing in the pores, all of these characteristics are expected to be present in the IRRAS spectrum.^{237,238,242,259,265,266} To more clearly resolve details in the OH vibration region, additionally, UHV-FTIR data was obtained with a specialized system in ultra-high vacuum ($\sim 1\text{e-}10$ mbar) with an InSb detector. The obtained spectrum, displayed in **Figure 5.6b**, reveals an interesting pattern around 3500 cm^{-1} . By considering the

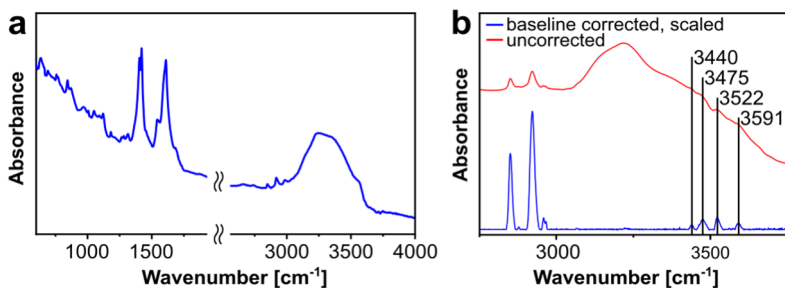


Figure 5.6. BPDC-LZH IRRAS spectra. **a)** Ambient environment IRRAS spectrum. Clearly visible carboxylate stretching vibration absorption at ~ 1400 and $\sim 1600\text{ cm}^{-1}$ indicate the presence of BPDC, while the broad peak around $\sim 3350\text{ cm}^{-1}$ points towards OH groups inside the structure. **b)** UHV-FTIR spectrum focusing on OH vibration region. The dedicated measurement reveals details in the absorbance band that can be assigned to hydroxyl groups,²⁶² further strengthening the structure hypothesis. Adapted from Fischer et al. with permission (CC BY 4.0).²³¹

modulation of the absorbance signal around a slowly changing baseline, a distinct set of absorption peaks (3440, 3475, 3522, 3591 cm^{-1}) is revealed. These peaks closely resemble the data reported by Kurmoo *et al.* and assigned to specific OH groups within the ZnOH layers.²⁶² Besides the metal hydroxide part of the structure, the presence of BPDC is indicated by 1) the absorption of symmetric ($\sim 1400 \text{ cm}^{-1}$) and antisymmetric ($\sim 1600 \text{ cm}^{-1}$) carboxylate stretching modes, 2) the set of peaks around $\sim 2900 \text{ cm}^{-1}$ that related to C-H stretching vibrations, and 3) the absorption peak at $\sim 830 \text{ cm}^{-1}$ stemming from vibration of benzene with 1,4-disubstitution.^{204,205,237,238,259,261,267} In the literature, there are reports of a shift of the carboxylate stretching modes due to different denticity of the coordination bonds, which could serve as an explanation for more than two distinguished peaks in the region around ~ 1400 and $\sim 1600 \text{ cm}^{-1}$ that is related to the turbostratic disorder in the material.^{262,268}

With the diffractogram observed for the high excess Zn^{2+} structure in **Figure 5.2f** now fully understood as BPDC-intercalated LZH structure, the Zn-BDC diffractogram from **Figure 5.2c** is re-examined. To check the LZH structural hypothesis also for this case, the experimentally determined basal layer spacing is compared with theoretical values from DFT-optimized structural model. From the Zn-BDC GIWAXS data, a ZnOH sheet spacing of $\sim 14.3 \text{ \AA}$ is extracted which fits very well the predicted value of 14.50 \AA based on the model. This is a first evidence that the inter-sheet separation of the layer-by-layer spin-coated LZH films can be tuned by choice of the pillaring linker. To further test this hypothesis for general applicability, besides BDC and BPDC, other types of linkers with increased length were tested as well: 3,3'-(1,4-phenylene)bis(2-propynoic acid) which is a non-polar version of linkers described by Hamer *et al.*,²⁶⁹ and 4,4'-(1,4-phenylenebis(ethyne-2,1-diyl))dibenzoic acid as synthesized by Marshall *et al.*²⁷⁰ In **Figure 5.7**, all layer separations vs. linker length

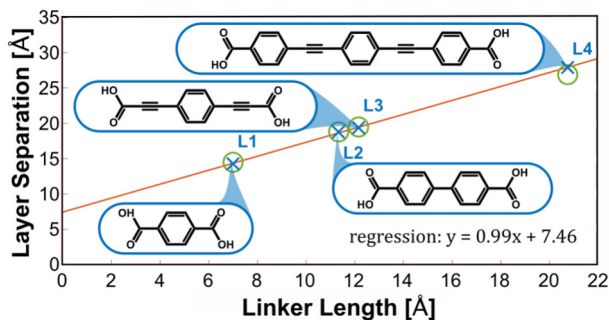


Figure 5.7. LZH basal layer spacing vs. linker length. The experimentally observed layer separation extracted from GIWAXS measurements with different intercalated linkers L1 to L4 (as drawn in the figure) are indicated by blue crosses. Comparison with the theoretical prediction based on the structural models, added-in by green circles, shows a very good match. Linear regression of the experimental data points reveals a slope of close to 1, and an offset of 7.46 Å that is reminiscent of the ZnOH sheet thickness. Adapted from Fischer et al. with permission (CC BY 4.0).²³¹

derived from the diffractograms of layer-by-layer spin-coated films (from a Zn^{2+} -to-linker ratio of 50:1) made with the above-mentioned ligands is presented. The linker length was defined as the distance between oxygen atoms in the carboxylate groups simulated for linkers relaxed in the gas phase. For the sake of readability, the linkers are referred to as L1 to L4 in this study. The GIWAXS diffractograms from which the layer separations were extracted, are shown in **Figure 5.8**. The comparison of experimental basal spacings (blue crosses) and simulated ones from 3D periodic, DFT-optimized structures (green circles) in each case agree very well. The measured layer spacings reveal a linear dependence with a fitted slope of 0.99, pointing towards a sheet-orthogonal linker inclusion, with an offset of 7.46 Å presenting an experimental estimate for the ZnOH sheet thickness separating the linkers.

An interesting side aspect that came up during the generation of the structural model for the intercalated LZHs is that small molecules, adsorbed within the material pores, are needed to enforce a vertical

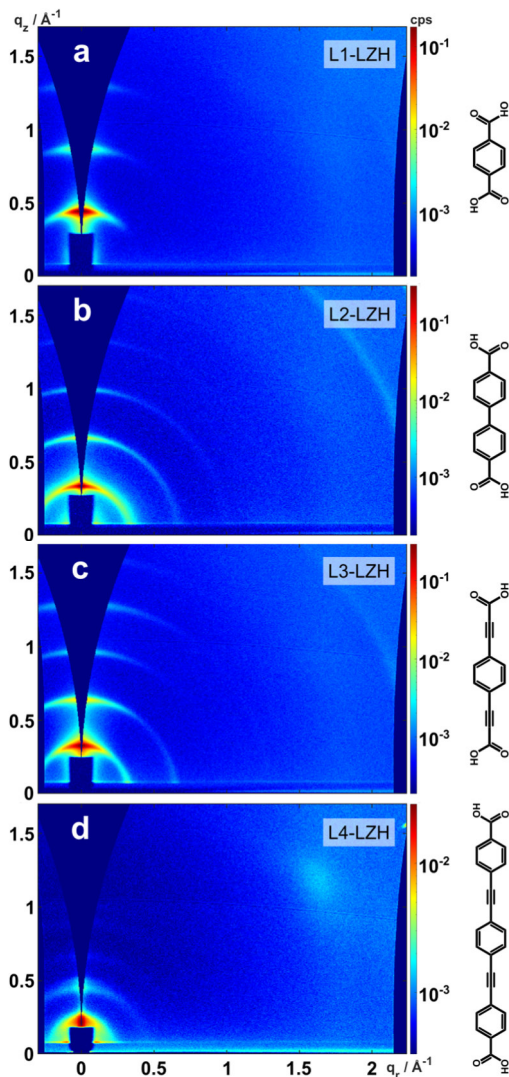


Figure 5.8. GIWAXS diffractograms of LZH intercalated with different dicarboxylates. **a)** L1-LZH. **b)** L2-LZH. **c)** L3-LZH. **d)** L4-LZH. The linkers L1 – L4 are sketched at the right-hand side of each panel. From the average distance between the different diffraction peak orders, layer separations of ~ 14.3 Å (L1), ~ 18.8 Å (L2), ~ 19.4 Å (L3), ~ 27.9 Å (L4) were extracted. Adapted from Fischer et al. with permission (CC BY 4.0).²³¹

orientation of the linkers. In the models, this stabilization was achieved with water molecules located in between neighboring linkers, as visible in **Figure 5.9** and also **Figure 5.5d**. Without any water in the pores, in the simulation, the unit cells were observed to contract significantly upon linker tilting. This is graphically shown in **Figure 5.9**, and quantitatively in terms of layer separation over the linker length in **Figure 5.10**. As a minor remark in this respect, it is noted that a second, weak set of diffraction peaks could be observed in the case of L4-LZH in **Figure 5.8d**, indicating another phase with a decreased layer spacing of ~ 24.8 Å. This, tentatively, is attributed to a structural configuration containing a different number of water molecules per unit cell within the pores as this spacing is situated in the middle of the simulated values for the cases of four and zero water molecules per unit cell, as shown in **Figure 5.10**. To experimentally

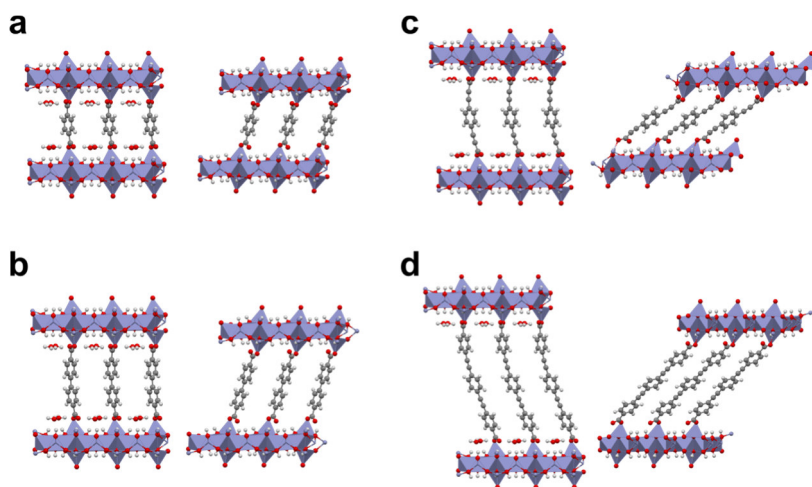


Figure 5.9. Structural models of LZH intercalated with different dicarboxylic linkers with and without water. **a) – d)** LZH structures with the linkers L1 – L4 optimized with water molecules next to the carboxylate groups and without water, which leads to a more contracted morphology with tilted linkers. The contraction, possibly caused by attractive forces between neighboring linkers, increases with ligand length. Adapted from Fischer et al. with permission (CC BY 4.0).²³¹

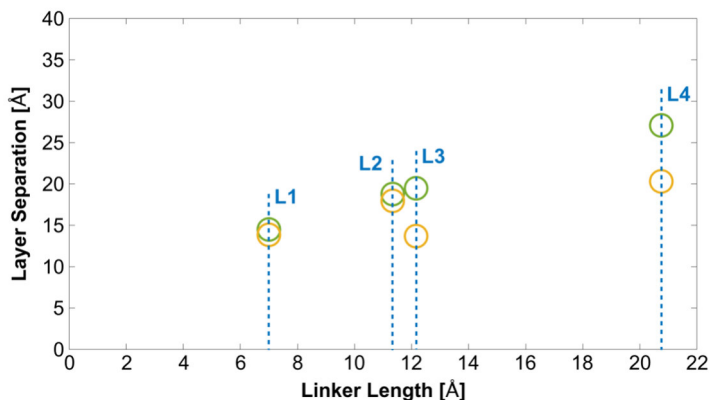


Figure 5.10. Calculated layer separation vs. linker length of LZH intercalated with different dicarboxylic linkers. The diagram indicates the calculated layer separations of the phases with water (green circles) and without water (orange circles), shown in Figure 5.9. Adapted from Fischer *et al.* with permission (CC BY 4.0).²³¹

test the stabilizing effect of water necessary for structural integrity, a BDC-LZH-containing thin film sample was dehydrated in a vacuum oven (120 °C, 15 h) and its structure evaluated by a short GIWAXS measurement (in ambient air) afterwards. In **Figure 5.11a** and **Figure 5.11b**, the comparison of the thin film's diffractograms after synthesis and dehydration are shown. Both resulting pPXRD patterns in **Figure 5.11c** show a peak shift after dehydration, indicating a layer contraction following the removal of water from the structure. The LZH diffraction peak visibly shifts from $2\theta \approx 6.18^\circ$ to $2\theta \approx 6.63^\circ$ which corresponds to a reduction of LZH layer spacing from ~ 14.3 to ~ 13.3 Å. This shift due to water removal confirms the structural contraction predicted by the simulation well (only deviating by ~ 4 % from the experimental value) and also agrees with observations in the literature on a similar structure by Kurmoo *et al.*²⁶² In anticipation to the next sections, the Zn-BDC sample examined in this experiment was a mixed thin film containing BDC-LZH and MHOH phases. Thereby, in a single run, the effect of dehydration on both structures could be tested. In correspondence to the theoretical model for Zn-BDC MHOH,

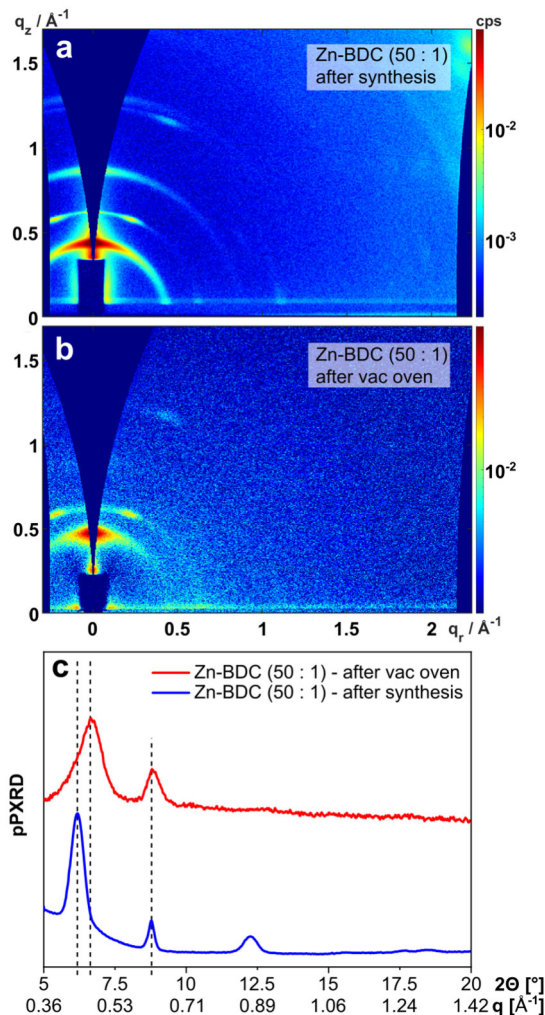


Figure 5.11. Zn-BDC thin film diffractograms before and after dehydration. GIWAXS diffractogram **a)** after synthesis and **b)** after vacuum oven treatment. **c)** pXRD patterns generated from the diffractograms in **a** and **b**. Dehydration shifts the LZH peak from $2\theta \approx 6.18^\circ$ to $2\theta \approx 6.63^\circ$ signaling a shrinkage of the LZH basal spacing from $\sim 14.3 \text{ \AA}$ to $\sim 13.3 \text{ \AA}$. The sample examined is a mixed-phase thin film of BDC-LZH and MHOF (the latter being the second type of structure observed for Zn-BDC). The MHOF structure, to be discussed in the next section, shows no contraction. Adapted from Fischer et al. with permission (CC BY 4.0).²³¹

water is not needed as a stabilizing factor and, hence, did not lead to change of diffraction peak positions as in the case of the LZH component. In the following section, this Zn-BDC MHOF structure will be fully disclosed.

To summarize the findings of this section, strong evidence could be provided for the formation of LZH hydroxides by layer-by-layer spin-coating of the Zn precursor and various linkers in high excess of Zn^{2+} . Thereby, the dicarboxylic linkers are preferentially oriented perpendicularly to the ZnOH sheets and majorly determine their layer separation.

5.5. Metal-hydroxide-organic Framework (MHOF) from Zn and BDC

After finding that the structures formed by using the Zn precursor solution with much higher molar concentration than the linker solution are not related to SURMOF-2 at all, the question arises whether also in the case of Zn-BDC (1:1) in **Figure 5.2b** an entirely different material is formed. The dissimilarity of the Zn-BDC (1:1) and (50:1) diffractograms excludes that this structure is as well an LZH. To perform a detailed analysis on the (1:1) diffractogram, a more clearly resolved version of the diffraction pattern would be desirable. In fact, this could be achieved by fabricating a thin film with slightly varied synthesis conditions. It was found that spin-coating on gold surfaces with a functional self-assembled monolayer (SAM) made from carboxylate-terminated 16-mercaptohexadecanoic acid (MHDA) at an elevated equimolar ratio 1 mM yields an equivalent but clearer diffraction pattern, shown in **Figure 5.12**. The equivalence of the two GIWAXS diffractograms (in **Figure 5.2b** and **Figure 5.12**) is shown by comparing their pXRD patterns in **Figure 5.13**. All peak positions line up perfectly and there are no additional peaks in either of the two patterns that would indicated different crystalline phases.

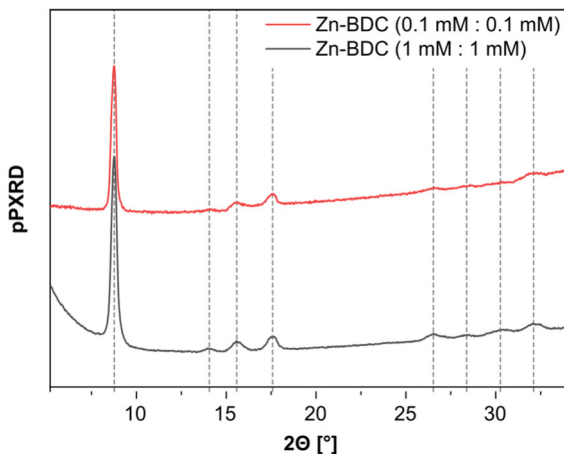


Figure 5.13. pPXRD patterns from two different thin films made from equimolar precursor ratios of 0.1 mM on Si and 1 mM on MHDA Au (from diffractograms in Figure 5.2b and Figure 5.12). The alignment of all observed diffraction peaks indicates the equivalence of both structures. Adapted from Fischer et al. with permission (CC BY 4.0).²³¹

original Cu-BDCKAKSUL (exchanging Cu by Zn atoms, adding hydrogen atoms to ensure charge neutrality and fully unconstrained geometry optimization) and is shown in **Figure 5.14a**. The comparison of its calculated PXRD pattern with the pPXRD of the GIWAXS diffractogram in **Figure 5.14b** displays the exceptional match of peak positions. It shall be noted that the intensity values are not expected to match in this comparison because of the different measurement geometries in GIWAXS and PXRD and a proper correction for that is neither trivial nor needed here. The Zn-BDC MHOH structure consists of thin ZnOH sheets that comprise the carboxylate groups of the BDC on either side which connect neighboring layers. This is the second type of ZnOH sheet discussed in this work, which is, however, fundamentally different from the one inside the LZH. In the LZH, a large substructure is formed by zinc and oxygen atoms in octahedral and tetrahedral configuration, in which most of the Zn atoms have no connection to

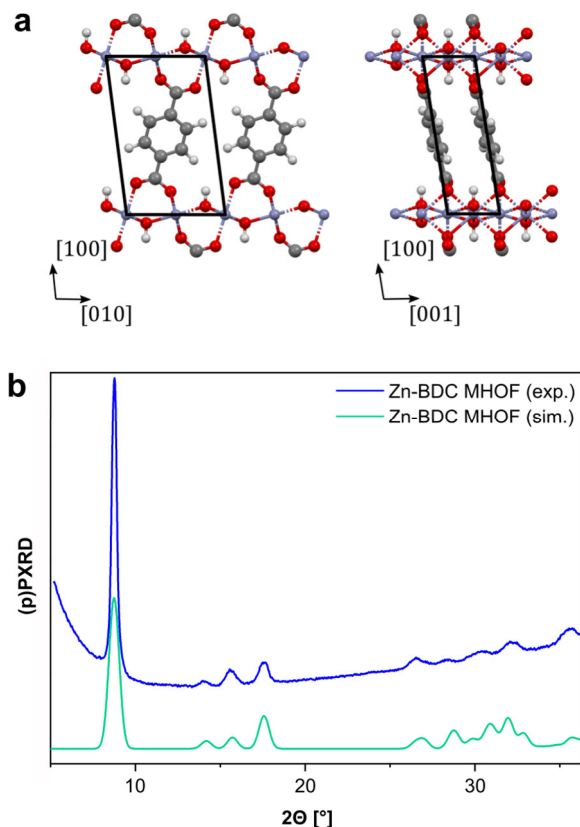


Figure 5.14. Zn-BDC MHOF structural model and (p)PXRD comparison. **a)** Structural model for Zn-BDC MHOF obtained from *ab initio* calculations. BDC bridges ZnOH sheets by direct coordination of carboxylate groups with Zn atoms. **b)** Comparison of experimental pPXRD (generated from GIWAXS diffractogram in Figure 5.12) and simulated PXRD based on the structural model for Zn-BDC MHOF. The very strong similarity between the curves is indication of the real structure matching the simulation. Adapted from Fischer et al. with permission (CC BY 4.0).²³¹

the linker molecules. In contrast, in the MHOF Zn hydroxide sheet, metal and oxygen atoms are located within a single layer in which every Zn atom is bonded to oxygens from linker carboxylates. Reconsidering the molecular structures in **Figure 5.5b** and **Figure 5.14a** should make this very clear.

In the second step for structure identification, the experimental 2D diffraction pattern was compared to simulated ones arising from the Zn-BDC MHOF structure in different preferred orientations. The presence of more than one distinct crystallite orientation is suggested by multiple intensity maxima on the same diffraction ring as apparent in **Figure 5.12**. Three such crystallite orientations could be identified described by the parallel alignment of the (410), (100) and (001) reciprocal lattice planes towards the substrate. These crystallite orientations are illustrated in **Figure 5.15** and the diffraction peaks associated to them inserted by black, red and green diamonds, respectively, in **Figure 5.12**. Evidently, all major experimental intensity maxima are explained by either of the three proposed crystallite orientations. The matching peaks in the simulated pattern are indicated by their Laue indices and labeled additionally by crosses over the diamonds. The agreement of experimental and simulated peak positions clearly verifies the structural hypothesis of an MHOF for the Zn-BDC thin film made from equimolar spin-coating conditions. Interestingly, among the simulated peak positions, there are several that are not backed by an experimental diffraction peak.

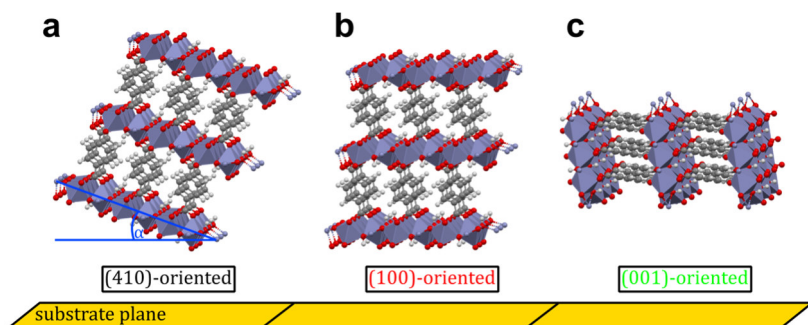


Figure 5.15. Illustration of different postulated Zn-BDC MHOF crystallite orientations derived from the GIWAXS peak positions in Figure 5.12. These orientations are **a)** (410), **b)** (100), **c)** (001), labeling the reciprocal lattice plane parallel to the substrate. In panel a, highlighted in blue, the angle $\alpha \approx 20^\circ$ indicates the tilt of MHOF sheets towards the substrate surface and could be induced by the underlying SAM in the real thin film. Adapted from Fischer et al. with permission (CC BY 4.0).²³¹

Looking more closely, in fact, there seems to be a systematic absence of diffraction peaks with an hkl index of $|h| > 1$ and $k|l| \neq 0$, which could point towards a poor atomic periodicity across multiple MHOF sheets. This observation will be taken up again when discussing a potential structure formation mechanism later on. In passing, it is also noted that the Zn-BDC MHOF 2D diffractogram bears strong resemblance with the data presented by Stassin *et al.* of an isostructural Cu-BDC thin film produced by vapor-phase deposition.¹⁶⁵ As a final remark on the GIWAXS diffractogram analysis, among the three identified orientations, the (001) texture might actually have a rather low contribution as a significant number of its related diffraction peaks lie within the horizon region in the diffractogram. In this region, the intensity maxima might be super-elevated by the Yoneda peak and, hence, overestimated.²³⁰

IRRAS (in ambient air) was also performed on the Zn-BDC MHOF thin film to obtain complementary information on its structure. The acquired spectrum is displayed in **Figure 5.16** and shows a somewhat similar appearance as the LZH film before, due to similar molecular ingredients. For example, this time very sharply resolved peaks in the carboxylate stretching vibration band indicate the presence of the BDC linker inside the structure (antisymmetric: 1581 cm^{-1} , symmetric: $1397, 1408\text{ cm}^{-1}$). This is further supported by several other defined absorption peaks at $662, 1017, 1148, 1500\text{ cm}^{-1}$, corresponding C-H bending and C-C vibrations of the central aromatic ring of the BDC linker and the peak at 753 cm^{-1} related to phenyl ring deformation.^{272,273} However, there are also specific features that distinguish this spectrum from the LZH one besides the much more clean overall appearance. In the OH vibration region, the MHOF IRRA spectrum shows a strong peak at 3606 cm^{-1} . At this position, this peak is typically associated with OH stretching modes that are not involved in OH groups,²⁶⁴ whose presence is suggested within the Zn hydroxide sheets by the structural model. A broad OH-related band centered at

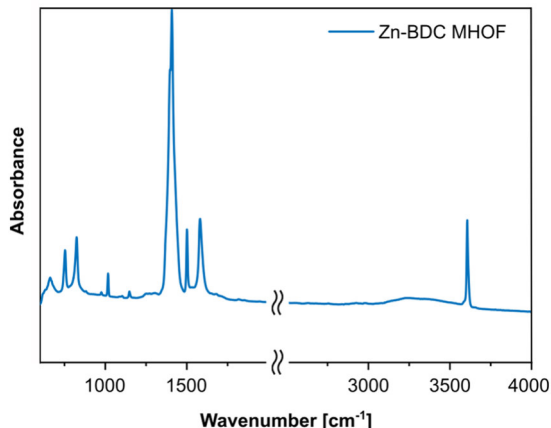


Figure 5.16. Zn-BDC MHOF IRRA spectrum. The prominent peaks around 1400 and 1600 cm^{-1} indicate the presence of carboxylate groups of BDC in the structure, while the one at ~ 3600 points can be related to OH coordinated with Zn atoms. Adapted from Fischer *et al.* with permission (CC BY 4.0).²³¹

3240 cm^{-1} is additionally visible that could be due to some residual ethanol molecules inside the structure or, possibly, defective coordination sites involving non-deprotonated BDC molecules. The observed spectral features agree with the data by Yuan *et al.* on their analog Ni-based materials.²⁷⁴

5.6. Mixed Phases of LZH and MHOF from Zn and BDC

It could be shown that neither for equimolar Zn^{2+} -to-linker ratio nor for a high excess of Zn^{2+} , a SURMOF-2 type structure could be achieved when sequentially spin-coating Zn-BDC. Instead, two different structures could be obtained dependent of the utilized ratio. This provided a stimulus to further probe a broader range of precursor molar ratios. In an attempt to improve thin film anchoring on the surface and thereby facilitate formation of a SURMOF-2 type structure, these samples were grown on carboxylate-terminated Au surfaces functionalized with an MHDA SAM. A range of Zn^{2+} -to-linker molar ratios from 1:10 to 100:1 was tested, thereby keeping the

precursor solution with the higher concentration at 1 mM. The GIWAXS diffractograms of the hereby achieved thin films are given in **Figure 5.17** and **Figure 5.18**.

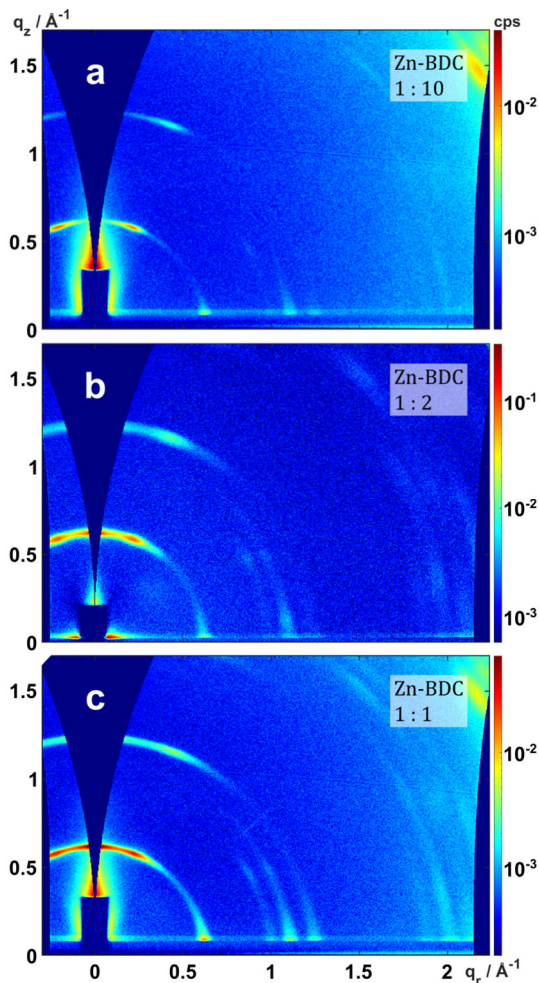


Figure 5.17. GIWAXS diffractograms of Zn-BDC thin films on MHDA Au made from layer-by-layer spin-coated with varying precursor ratios – Part 1. **a) – c)** Diffractograms of structures fabricated with Zn^{2+} -to-linker ratios as indicated in the top right of each panel. For a mild linker excess to equimolar conditions, formation of pure MHOFF is observed. Adapted from Fischer et al. with permission (CC BY 4.0).²³¹

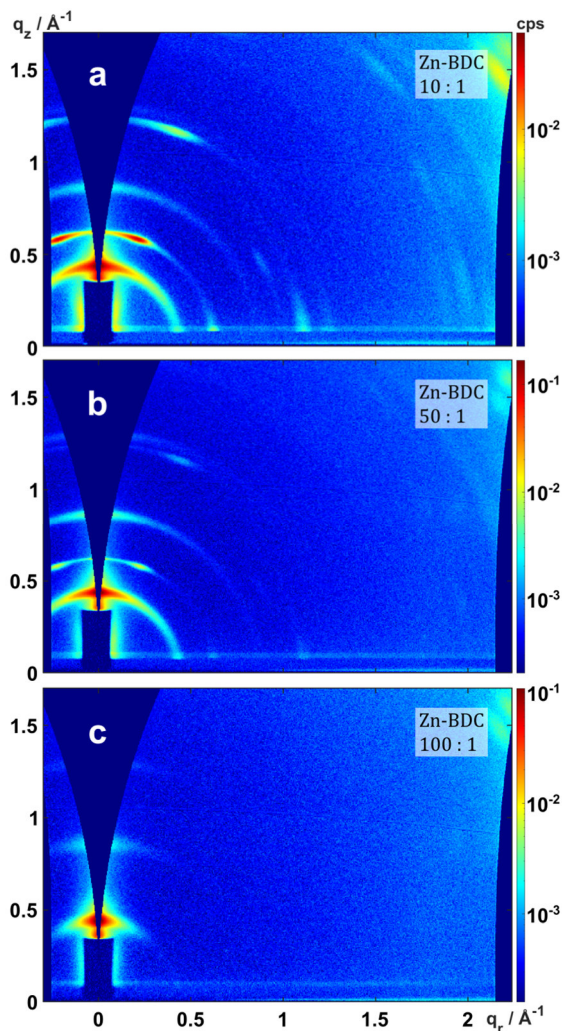


Figure 5.18. GIWAXS diffractograms of Zn-BDC thin films on MHDA Au made from layer-by-layer spin-coated with varying precursor ratios – Part 2. **a) – c)** Diffractograms of structures fabricated with Zn^{2+} -to-linker ratios as indicated in the top right of each panel. For a smaller excess of the metal ion, an intermediate mixed-phase from MHOF and BDC-LZH is formed (10:1 – 50:1). For a strong excess of the metal ion, pure BDC-LZH (100:1) is created. Adapted from Fischer et al. with permission (CC BY 4.0).²³¹

Now having good knowledge of the MHOF and LZH type diffraction patterns, on the first glance already, we can conclude that all thin films within the whole tested range correspond to one of these two structures, and never a SURMOF-2 type structure as in the case of the Cu-BDC. Interestingly however, while the Zn^{2+} -to-linker ratio increases, we observe a gradual progression from a (potentially) pure MHOF phase to (potentially) pure LZH phase with an intermediate type of film in which both structures are present (10:1 and 50:1 in **Figure 5.18a** and **Figure 5.18b**). This is totally in contrast to Cu-BDC structures, which were fabricated for comparison in the same manner at different Cu^{2+} -to-linker ratios (**Figure 5.19**). In this case, the diffraction patterns indicate a structure consistent with literature data on SURMOF-2 (as observed in **Figure 5.2** and **Figure 5.3**) for every

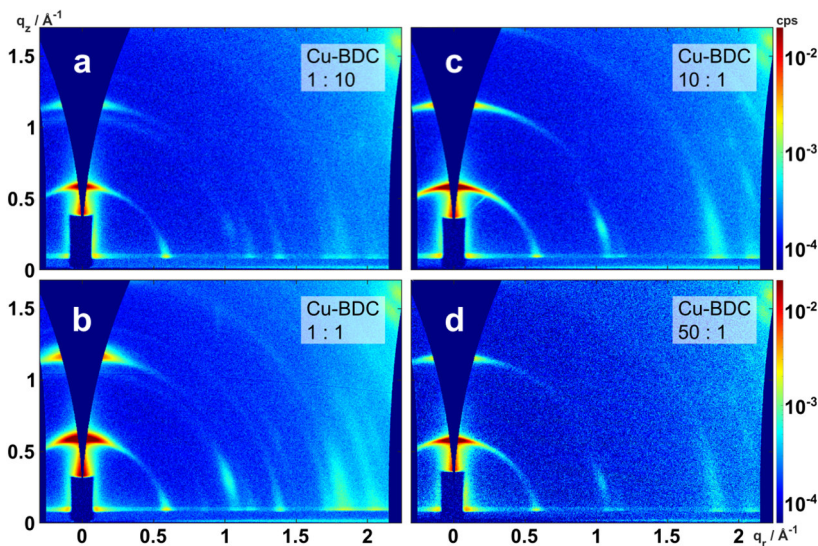


Figure 5.19. GIWAXS diffractograms of Cu-BDC thin films made in reference from layer-by-layer spin-coated with varying precursor ratios on MHDA Au substrates. **a) – d)** Thin film diffractograms resulting from synthesis with precursor ratios as indicated. In contrast to the Zn-based sample series in **Figure 5.17** and **Figure 5.18**, the Cu samples all exhibit the same diffraction pattern, whose peak positions agree with the literature for SURMOF-2 as discussed in **Figure 5.2** and **Figure 5.3**. Adapted from Fischer et al. with permission (CC BY 4.0).²³¹

tested precursor ratio. This provides evidence for the SURMOF-2 type structure being formed by Cu-BDC during layer-by-layer spin-coating for a wide range of metal ion-to-linker ratios which does not apply for Zn.

The IRRA spectra of the whole Zn-BDC sample series, presented in **Figure 5.20**, excellently complement the hypothesis of varying fractions of MHOF and LZH phases being present in the fabricated thin films. After having investigated both types of spectra in detail above already, we can now recognize their individual features in the spectra. At a mild excess of the linker over metal ion to an equimolar ratio, the spectra strongly resemble the MHOF spectrum with sharp peaks at the same locations and the relatively less absorbing OH band centered around 3240 cm^{-1} . Increasing the excess of Zn^{2+} over the linker, the set

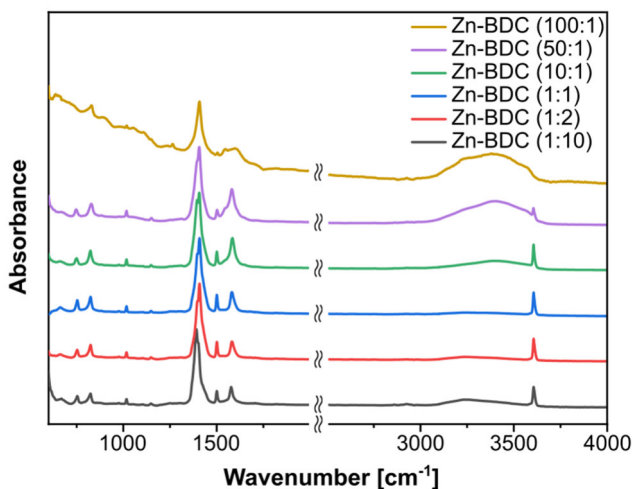


Figure 5.20. IRRA spectra of Zn-BDC thin films made on MHDA Au from layer-by-layer spin-coating with varying precursor ratios. The progression of Zn-BDC thin films made from Zn^{2+} -to-linker ratios of 100:1 to 1:10 (from top to bottom) reveals gradual changes in the absorbance spectrum that correlate with structural changes from LZH to MHOF concluded from the GIWAXS data in Figure 5.17 and Figure 5.18. Adapted from Fischer et al. with permission (CC BY 4.0).²³¹

of defined absorption peaks becomes less and less visible, the carboxylate stretching peaks start to broaden and absorption in the OH band increases while its center shifts to higher wavenumbers. At a ratio of 100:1, the spectrum strongly reminds of the BPDC-LZH spectrum examined earlier in **Figure 5.6a**, as expected for BDC-LZH phase. To give an eye-catching visual impression of the superposition of two distinct IRRA spectra, a composite spectrum from pure LZH phase (100:1, green) and pure MHOF phase (1:1, blue) is produced by simple summation and renormalization in **Figure 5.21**. The resulting artificial spectrum (red) exhibits a high similarity with the real spectrum of a mixed-phase thin film (50:1, black).

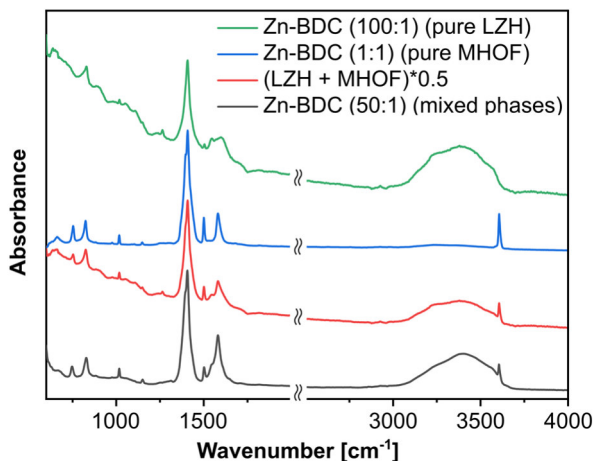


Figure 5.21. Comparison of pure LZH and MHOF Zn-BDC thin film IRRA spectra. Taking the absorbance spectra of pure LZH and MHOF from Figure 5.20, a composite spectrum can be generated by summation and renormalization (red curve). The strong resemblance of this spectrum with the real absorption spectrum of the mixed-phase sample (black curve) provides a qualitative visual indicator of the structural mixing being reflected by the spectral features. Adapted from Fischer et al. with permission (CC BY 4.0).²³¹

5.7. Plausible Structure Formation Mechanism

As an explanation for the formation of the various observed thin film structures, a unified formation mechanism contrary to the common understanding of layer-by-layer spin-coating of MOF structures is proposed. The central aspect of this concept is the conversion of Zn hydroxy acetate basis layers that are generated by spin-casting Zn acetate dihydrate in solution with ethanol. To create a thick enough film of the product of spin-casting the Zn precursor only for characterization, a 1 mM solution was sequentially deposited 40 times (without rinsing cycles). The resulting thin film could be readily examined by GIWAXS, which is shown in **Figure 5.22a**. The observed diffractogram closely resembles the LZH type pattern analyzed above, however, exhibits an extreme confinement around the q_z axis, representing highly oriented, horizontal layers. The peak positions suggest a smaller layer separation than observed before, of ~ 13.6 Å. This distance is a strong pointer towards a Zn hydroxy acetate structure, in which acetate anions together with water molecules are located in between ZnOH slabs.^{236–238,259,275,276} A sketch of this type of structure is given on the left side of **Figure 5.23**. Looking to the literature, this means, apparently, that spin-coating ethanolic solutions of Zn acetate dihydrate leads to a similar material as when employing a sol-gel precursor.²⁷⁷ In the formation process of Zn hydroxy acetate, the different boiling points of ethanol and water could play a major role. In the process of spinning, ethanol evaporates much faster than water, potentially causing the relative amount of water inside the solution droplet to strongly increase.

Furthermore, the overall drying process is tremendously sped-up by the spinning of the substrate. Indication for this aspect being a crucial factor in forming Zn hydroxy acetate is given by comparison to the structure obtained from only drop-casting and natural drying of the Zn precursor solution in **Figure 5.22b**. The GIWAXS diffractogram reveals a totally different pattern of intensity maxima, whose peaks

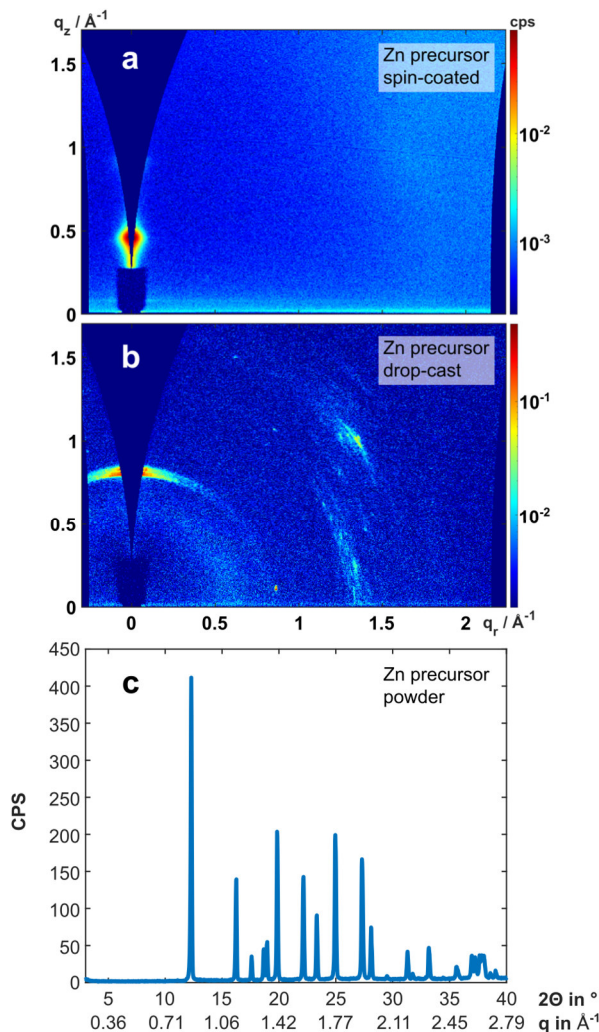


Figure 5.22. GIWAXS and PXRD of Zn acetate dihydrate precursor. GIWAXS diffractograms of **a)** spin-coated thin film, and **b)** drop-cast thin film (no spinning) from a 1 mM ethanol solution. **c)** PXRD of Zn acetate dihydrate powder. The spin-coated thin film diffractogram indicates highly oriented horizontal layers, very similar to the LZHS characterized earlier. The dissimilar diffractograms of the drop-cast thin film and Zn precursor powder point towards a structural transformation happening during substrate spinning. Adapted from Fischer et al. with permission (CC BY 4.0).²³¹

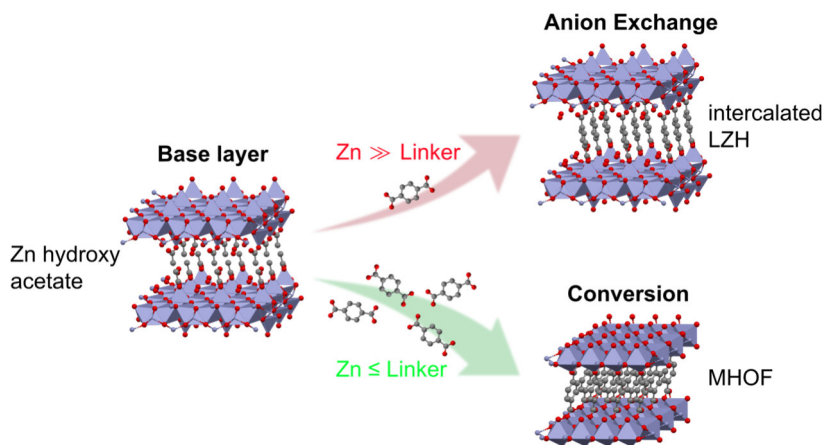


Figure 5.23. Transformation process during layer-by-layer spin-coating as possible explanation for structure formation. Spinning of a Zn acetate dihydrate precursor solution forms a Zn hydroxy acetate basis layer. By adding linker solution in the next deposition step, exemplarily shown with BDC, the Zn^{2+} -to-linker ratio determines which of two types of transformations takes place. Excess Zn^{2+} ions will cause anion exchange generating BDC-LZH, while an equimolar ratio or mild excess of the linker leads to the formation of MHOF. At a mild excess of Zn^{2+} , both processes can happen in parallel. Adapted from Fischer et al. with permission (CC BY 4.0).²³¹

do not match the ones of the spin-cast thin film. For the sake of completeness, also the comparison of the diffraction peak positions of Zn precursor film from spin-casting with the PXRD of the pure precursor in its powder form (**Figure 5.22c**) clearly show that a structural transformation is triggered by the substrate spinning.

Based on these experimental data, the formation of Zn hydroxy acetate within each Zn solution spin-coating cycle is suggested. When the linker solution is added, depending on its concentration, this basis structure can either undergo anion exchange causing the growth of dicarboxylate-intercalated LZH films, or be transformed to an M(H)OF structure. This hypothetical process is depicted in **Figure 5.23**. To delineate this process, based on the detailed investigation of Zn-BDC, approximate reference values can be given: A high Zn^{2+} -to-linker ratio, at $\sim 50:1$ or more, promotes the anionic exchange in the material; at a

ratio of ~1:1 to 1:10 a structural conversion process is triggered; and with a mild excess of Zn^{+2+} (~10:1) both processes can occur in parallel. In case of the shorter BDC linker, the preferred conversion product is a dense MHO structure, while the longer BPDC forms a SURMOF-2 type structure.

A conversion process taking place within each deposition cycle during layer-by-layer spin-coating could be similar to the synthetic process reported by Kim *et al.* growing pillared-layered MOFs on the basis of Cu-Zn hydroxy double salt (HDS) precursor structures.¹²² The Cu-BDC-DABCO MOF thin films obtained by them were described to emerge spontaneously exposing the HDS layer to a linker-pillar solution. Methodically, this is a very similar synthetic approach as the one of this work. Kim *et al.* also discuss the effect of linker solubility on the MOF formation process, which could be a potential determining factor in the layer-by-layer spin-coating process as well.

In the light of the proposed structural formation process, several observational details made earlier shall be reconsidered. Starting with the comparison of BDC-LZH and BPDC-LZH at the bottom of **Figure 5.2**, we could deduce a strong difference in thin film orientation from the two diffractograms. While, in case of BDC, the diffraction pattern confined around the q_z axis signaled a preferred orientation in the form of flat lying layers, the BPDC-based structure was much more poorly oriented. When the thin films are formed from an extremely oriented basis structure of flat-lying Zn hydroxy acetate sheets, it can be readily understood that some of that preferred orientation will be inherited by the resulting materials after anion exchange. Since the BDC linker (7.00 Å) is a geometrically smaller molecule than BPDC, diffusion into the Zn hydroxy acetate interstitial spaces is facilitated, largely preserving the original layered structure when increasing the basal spacing by only ~5 %. In contrast, incorporation of the longer BPDC linkers (11.34 Å) could expand small initial structural defects,

locally breaking the layered material and causing a much more random orientation overall. This trend can be observed to continue in **Figure 5.8** for the even longer linkers L3 (12.16 Å) and L4 (20.75 Å). Hence, it is concluded that geometric effects related to the organic linker size, in general, can affect infiltration of an LZH structure. However, anion exchange is still considered a plausible mechanism, even if the process might occur on a slightly longer time scale as the layer-by-layer approach mitigates reduced diffusion rates by only requiring penetration into a small number of surface layers within each deposition cycle.

Another interesting observation made examining the GIWAXS diffractogram of Zn-BDC MHOF on the MHDA Au surface, was the particular set of preferred orientations of growth and the systematic absence of certain diffraction peaks. Coming from a Zn hydroxy acetate slabs that lie flat on the substrate that is then transformed to an MHOF, the (001) texture is, expectedly, the least likely one out of the three observed ones as it requires a 90° tilt of layers after conversion. This explains the more pronounced diffraction maxima related to the (410) and (100) orientations as these do not necessitate massive crystallite rotations. Thereby, the (100) texture directly adapts the horizontally layered structure of the Zn hydroxy acetate base layer. The (410) orientation is a bit more intriguing as it involves a distinct inclination angle of the ZnOH layers of approximately 20° as indicated in **Figure 5.15a**. Interestingly, the (410) seems to be linked to the MHDA SAM. This orientation producing the distinctive off-axis {100}, {200}, {300} diffraction peaks – labeled in black in **Figure 5.12** that are also visible in every MHOF instance of the Zn-BDC sample series grown on MHDA – is absent in the thin film grown on Si in **Figure 5.2b**. The particular inclination angle of ZnOH sheets in the (410) could be caused by crystallites directly anchored to MHDA molecules thereby adapting the tilt angle of their carbon chains that is ~24° on average according to the literature.²⁷⁸ In the consequence, the

5.8. Thin film PL

In this final section, a change in PL is shown to be an indicator of different Zn-based structure formation that is easily accessible. As a primary example, the PL of the BPDC-LZH thin film exhibits significantly different emission characteristics than the SURMOF-2 type structure. This is illustratively shown by a photo of both thin films under a 254 nm excitation by a UV lamp in **Figure 5.25** and quantitatively by a detailed characterization of the time-integrated and time-resolved PL of the BPDC-based thin films summarized in **Figure 5.26a** and **b**. These measurements were carried out on an FS5 spectrofluorometer. For comparison, the PL spectrum was also acquired for BPDC in ethanol (0.01 mM) and BPDC in powder form. In relation to the BPDC emission in solution, peaking at 332 nm, the thin film emission exhibits a significantly red-shifted spectrum that is comparable to BPDC powder. The PL of the BPDC-LZH thereby being less red-shifted than that of the SURMOF-2 type structure is consistent with the structural characterization that suggests a larger chromophore separation in the LZH, possibly further promoted by the

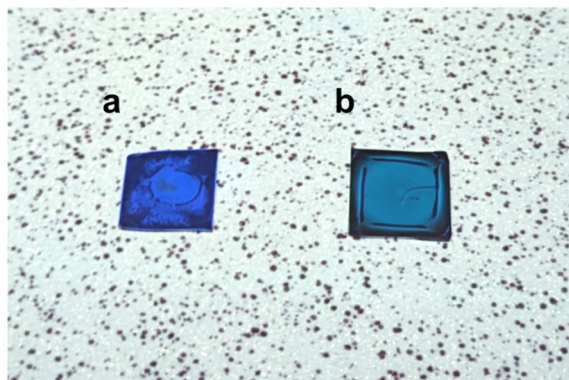


Figure 5.25. Emission from BPDC-based thin films. **a)** BPDC-LZH. **b)** SURMOF-2 type structure. The photo was recorded with 254 nm excitation in an otherwise dark room. The significant difference in emission color serves as a quick indicator of the thin film structure after synthesis. Adapted from Fischer et al. with permission (CC BY 4.0).²³¹

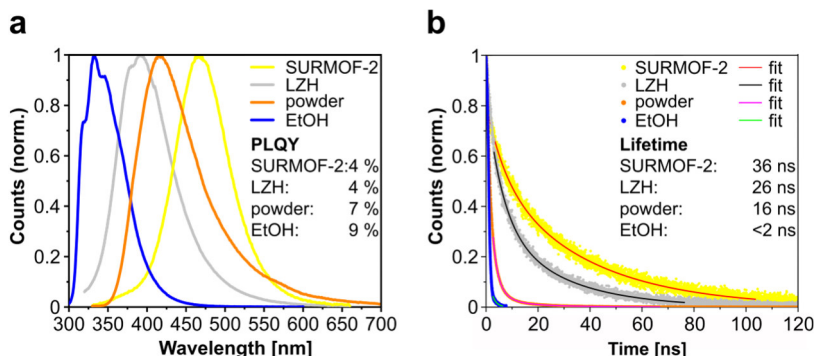


Figure 5.26. PL of BPDC and BPDC-based structures. **a)** Time-integrated PL of BPDC in ethanol solution, powder form, LZH and SURMOF-2 type structure. **b)** Time-resolved PL of the same materials along with (multi-)exponential fits. In small insets, the PLQY and lifetimes of the slow decay components are given. Aggregate states in LZH and SURMOF-2 type structure are assumed due to dense chromophore packing, resulting in an increased excited-state lifetime and a peak emission red-shift comparable to BPDC in its powder form. Adapted from Fischer et al. with permission (CC BY 4.0).²³¹

turbostratic disorder, compared to the SURMOF-2 type structure. Stronger intermolecular interactions in the latter structure are signified by the strongly shifted peak emission at 467 nm in comparison to 391 nm in the case of LZH. BPDC powder is situated in between the thin film materials with a PL maximum at 416 nm. The probability that the thin film luminescence stems from intermolecular states is supported by their time-resolved emission decay profiles not being mono-exponential as is the case for BPDC in solution. The thin film aggregate state lifetime is approximately an order of magnitude longer than the lifetime in solution, whereby the SURMOF-2 type structure exhibits the longest decay time. The PLQY of BPDC in solution and as powder are both higher than the that of LZH and SURMOF-2 type structures. This is a sign of suppressed radiative decay rates in the thin films which can have a long list of potential reasons such as aggregation-induced quenching, inter-chromophoric energy transfer processes, vibrational coupling between the MOF lattice and the linker, etc. Irrespective of the concrete mechanisms, the thin film

PL characteristics clearly indicate the incorporation of the linkers in dense frameworks that are structurally different.

As a side note, a potential red-shift of the thin film emission was evaluated but concluded to be of very minor influence, if present at all. Comparison of the absorbance data revealed no significant absorption above 400 nm for the linker in solution and thin films on Si and, furthermore, the emission spectra red edge's reveal intersection points which should not be the case for major shifts by self-absorption.^{231,279,280} Moreover, if multiple re-emission events occurred inside the thin film, the number of escaping photons should be severely reduced and be reflected in a drastically lower PLQY. This, however, was not observed as well.

Similar PL data obtained on the Zn-BDC series reflect the structural progression from MHOF, to intermediate mixed-phase, and LZH thin films and is presented in **Figure 5.27**. The measurements were conducted using self-assembled PL setup with a fiber-coupled spectrometer and CW 300 nm LED for excitation. The steady-state thin films PL spectra in **Figure 5.27a** are collectively red-shifted by 50 – 60 nm in comparison to the emission of BDC powder peaking at 383 nm, as a result of linkers densely packed inside the structures. The PL peak of the pure MHOF thin film appears to be slightly less red-shifted than the one of pure LZH. However, at the same time the LZH spectrum is significantly broadened in comparison. A possible reason for that can be a less rigid coordination of the linker in the LZH, thereby granting access to a range of vibrational modes (that could also explain the appearance of small shoulder-like features) and shifting the mean emission to a slightly lower energy. Using the pure emission spectra of MHOF and LZH as a basis, the mixed-phase spectra can be recreated with striking accuracy by artificial composite spectra (indicated by black curves). To check for inhomogeneities in the spatial distribution of MHOF and LZH crystallites on the substrate potentially created by the substrate spinning, the PL of a mixed thin

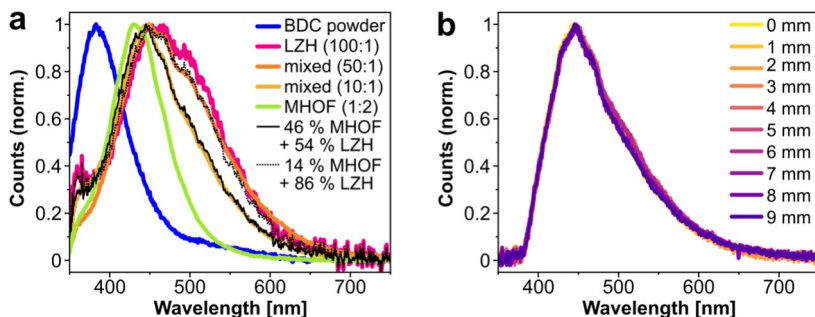


Figure 5.27. PL of BDC-based structures. **a)** Emission of Zn-BDC LZH, MHOF and mixed-phase thin films and BDC powder. The pure MHOF and LZH PL spectra are used to model the mixed film emission, as shown by the two black lines. A red-shift of all thin film emission by approximately 50 – 60 nm with respect to the BDC powder can be observed, informative of the linker incorporation within the metal-organic lattices. The peak PL of pure MHOF, thereby, appears slightly less red-shifted than the pure LZH emission. **b)** Spatial PL scan of Zn-BDC (10:1, mixed-phase) thin film recorded by laterally shifted probing with a microscope objective. Since no variation could be detected, any significant local variation of LZH vs. MHOF grains must be on a smaller scale than the 0.9 μm estimated focal spot size. Adapted from Fischer et al. with permission (CC BY 4.0).²³¹

film was acquired spatially resolved using a microscope objective with an estimated focal spot size of 0.9 μm . Laterally moving the sample, the emission was recorded in 1 mm increments across the whole coated substrate area. The resulting spectra shown in **Figure 5.27b** all exhibit the same shape, indicating no large-scale aggregation of the one or the other type of crystallite across the sample. Any potential local variation of individual grain densities must, hence, be on a smaller length scale than the microscope spot size.

In summary, the significant changes observed in the PL across the different thin films corroborate the previous GIWAXS analysis and provide for an easily observable structural indicator.

5.9. Conclusion

This work has demonstrated that GIWAXS combined with DFT calculations provides for an excellent tool for the determination of

previously unknown metal-organic thin film structures. It was found that the commonly used layer-by-layer spin-coating method utilizing Zn acetate dihydrate in together with various dicarboxylic linkers in ethanolic precursor solution in many cases does not yield a SURMOF-2 structure. For the combination Zn-BPDC, the SURMOF-2 structure only emerges in case of an equimolar precursor ratio. In the case of Zn-BDC, the formation of SURMOF-2 could never be observed. Instead, for a Zn^{2+} -to-BDC ration of smaller or equal to one, an MHOF structure is obtained from spin-coating. For a high excess of Zn^{2+} , for all tested dicarboxylic linkers, intercalated LZH thin films were grown exclusively. Analyzing a sample series of Zn-BDC from a wide range of precursor ratios, it was found that there is an intermediate range, with a mild excess of Zn^{2+} , in which both LZH and MHOF can form in parallel. Strong evidence could be provided for the structural claims by strong agreement between simulated diffraction data based on theoretical model structures and GIWAXS experimental patterns, supported by IR spectral analysis. Investigating the luminescence of the various types of structures obtained, showed differences in emission spectra and excited state lifetimes that reflect the different structural environments in which the organic chromophores are situated. Based on the detailed structural insight acquired, a formation mechanism was suggested differing from the classical understanding of layer-by-layer synthesis. Spin-coating of the Zn acetate dihydrate precursor solution is hypothesized to always lead to an LZH film with intercalated acetic acid molecules forming a basis layer. This basis layer then either undergoes anion exchange maintaining the LZH structure (for high excess of Zn^{2+}), or conversion to a MOF or MHOF (for a sufficient amount of linker molecules) in the subsequent deposition step.

The presented findings point out that careful structural characterization with advanced techniques such as GIWAXS is imperative in the development of metal-organic thin film structures.

The extreme variety of crystalline structures emerging from Zn and dicarboxylic acids that can appear very similar if only evaluated by out-of-plane XRD measurements emphasizes this need. Especially in combination with structural modeling, GIWAXS analysis is an extremely useful technique to verify structural hypotheses of fabricated thin films. The methodology demonstrated can be applied to any other targeted MOF structure which will be of great benefit within the research community contributing to more thorough structural evidence. Furthermore, the demonstration of easily obtained crystalline structures from spin-casting whose structure can be controlled by the molar ratio of utilized precursors provides a low-level access to oriented thin film without the need for involved synthetic protocols. This is a further step towards highly integrated optoelectronic devices based on MOFs or LZH intercalated with functional molecules in the future.

6. PL Turn-on by Flow-mediated Chromophore Realignment in MOFs

This chapter is based on my first-author manuscript in submission “Nanoscale Flow Indicator: Molecular Rotor Realignment Modulates Luminescence in Metal-Organic Framework Thin Films”. Thin film synthesis, XRD, SEM and spectroscopic measurement and analysis thereof, figure design and data presentation were performed by J. C. Fischer (author) as well as the conception of liquid flow-mediated molecular rotation. The co-author T. Zhao provided support in thin film synthesis, characterization measurements and figure creation and conceived the idea of the drop-casting synthesis for oriented thin films. The co-author H. Ji performed calculations to determine the rotational barrier of the rotor linkers. The co-author Busko D. built the setup that was used to measure the PLQY and provided intellectual input. The co-author Y. Li and J. Nyarige provided substrates for the thin film synthesis and intellectual input. The co-authors B. S. Richards and I. A. Howard supervised the project and provided scientific guidance, intellectual input and proof-reading.

6.1. Motivation

MOFs grown as thin films with controlled crystallite orientation are predestined for the use as chemical sensing platforms.^{170,281} There is an extremely wide variety of mechanisms between a MOF and an analyte that can evoke a measurable response (also referred to as host-guest interactions).^{282–284} One of the most versatile types of such interactions for sensing is a change in the luminescent properties of the MOF.^{54,281,285–287} Often these changes originate from luminescence quenching effects due to sorption of an analyte, creating a turn-off sensing event. This technique, however, suffers from the significant drawback that a multitude of effects can lead to a loss signal besides the targeted interaction with the analyte.^{167,281} A turn-on

characteristic, in contrast, would be much more desirable since it allows for a superior signal-to-noise ratio measuring against a dark background and is less prone to false positive results (*e.g.* PL quenching by other effects than the analyte interaction).¹⁶⁷ Such properties are key for integration into applications the capability of real-time sensing.

An intriguing strategy to not only sense the presence of an analyte inside a MOF's pores but also the movement is to incorporate building blocks that allow for molecular motion inside a crystalline solid. Nanoscale motion that has already been demonstrated inside of MOFs includes rotation, shuttling or switching movements.^{178–180,182–184,195} A main criterion in the development of such materials is targeted design of pore geometries to create sufficient open spaces for unhindered molecular motion, to allow access for guest species to enter the network and modify the motion properties.^{186–190} Especially MOF systems that contain rotor molecules have garnered notable interest due to their ability to combine low energetic barriers to rotation with intermolecular interactions. Fast molecular rotation has been realized by using sp^3 - sp^2 or sp^2 - sp hybridized orbital bonds (see **Section 2.2.1** for more details) as rotor axes that, in the case of dipolar rotors, has even allowed for collective reorientation behavior inside a MOF.^{177,188,198,202,288,289} In contrast, rotor axes made from sp^2 - sp^2 exhibit a much higher activation energies for full rotation due to a higher degree of electronic conjugation.^{188,202,288,289} This results in a slower rotation or even stationary conformations. However, such a relative stability of a rotor offers the possibility to reversibly switch it between different states that can be used for sensing.

In this work, a combination of a luminescence change interaction and molecular rotation is demonstrated in the form of a unique luminescent indicator to report solvent flow through oriented MOF crystallites.

6.2. Overview

In this chapter, molecular motion of nanoscopic rotors in response to fluid flow through the pores of a solid MOF is investigated that causes a strong luminescence turn-on effect. The examined layered-pillared MOFs based on Zn, ADC and DABCO materials are produced as thin films employing an easy and novel drop-casting method on a heated substrate that yields structures with a preferred $\langle 001 \rangle$ orientation. This method was shown to also work for the isorecticular MOF with BPY pillars instead of DABCO, however, it does not work for less bulky linkers. As solvent evaporates from the oriented thin films, linkers are collectively driven into an upwards tilted configuration. Spectroscopic studies reveal that the resulting rigidification and mutual alignment of the anthracene units influence their excited state dynamics and emission properties, enhancing exciton transport and altering photoluminescence in terms of intensity, wavelength, and excited state decay behavior. This behavior is unique to solvent molecules with a kinetic diameter small enough to readily diffuse through the MOF pores such as methanol and ethanol. As a proof-of-concept for application of the MOF thin film as a liquid flow indicator, the Zn-ADC-DABCO coating is grown on a molecular sieve. Under UV illumination, the superficial MOF coating indicates solvent release from the sieve after soaking in methanol by a blue glow. In the following, firstly, the fabrication procedure is explained along with reasoning on the growth mechanism automatically yielding $\langle 001 \rangle$ -oriented structures. Secondly, the luminescence turn-on upon solvent evaporation from the MOF pores is investigated, followed by experimental evidence and theoretical modeling for ADC linker rotation taking place in response to solvent flow through the MOF channels. As a last part, the prototypical usage of the MOF thin film as a flow indicator coating is presented.

6.3. <001>-oriented Thin Films by Drop-casting

The pillared layer structure of the Zn-ADC-DABCO MOF exhibits a particularly useful topology considering molecular rotary motion. The DABCO pillars separating Zn-ADC paddle wheel planes allow for substantial free volume that enables the dicarboxylic rotors to rotate or librate without steric hindrance. Commonly, highly oriented pillared layer MOFs are produced in the form of thin films by layer-by-layer growth techniques that involve the alternating exposure of a substrate to separate solutions containing linker and metal precursor (as for example the spin-coating approach discussed in **Chapter 5**).^{121,159,170} This type of fabrication technique can provide precise control over the crystalline layer growth but is also very time-consuming. The drop-casting method utilized here, presents a facile alternative that is much faster and repeatably yields oriented Zn-ADC-DABCO thin films. The procedure involves dropping of a freshly mixed precursor solution based on ethanol that contains Zn acetate dihydrate, hydrochloric acid, ADC and DABCO molecules onto a Si substrate heated to 50 °C. For the full details of the synthesis method, the reader is referred to **Section 3.1.4** in the Methods chapter. This one-step protocol illustrated in **Figure 6.1a** can be repeated multiple times, with intermediate sample rinsing to remove unreacted components, to grow closed layers in the range of 100 nm. The drop-casting synthesis automatically promotes a preferred orientation of growth along the <001> direction which leads to the pillar molecules being vertically aligned on the substrate, as seen in the sketch in **Figure 6.1b**.

Examining the resulting thin films by means of SEM from the top and the side (**Figure 6.2**) reveals horizontally aligned, plate-like crystallites that are intergrown forming a closed layer on the substrate. GIWAXS analysis (**Figure 6.3**) of the samples clearly indicates the preferred <001> orientation by a distinct pattern exhibiting the DABCO-related {002}, {004}, *etc.* diffraction peaks along the q_z axis.

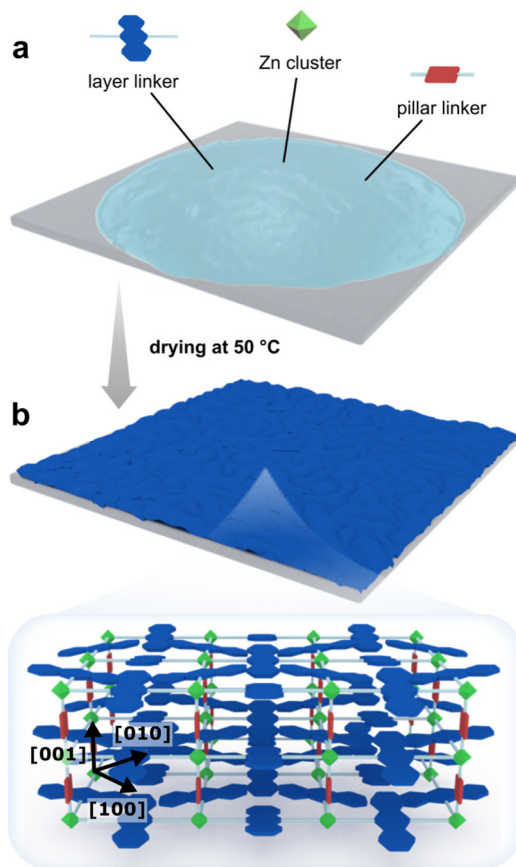


Figure 6.1. Oriented Zn-ADC-DABCO thin films from drop-casting on hot plate. **a)** Droplet of ethanol-based precursor solution on a cleaned Si substrate. **b)** Upon successive ethanol evaporation at 50 °C, a thin film is formed with preferential $\langle 001 \rangle$ -orientation such that the pillar linkers are vertically aligned on the substrate.

This already signals the preferred orientation with vertically aligned pillar molecules. To make it even more clear, the expected diffraction pattern from the Zn-ADC-DABCO MOF in the $\langle 001 \rangle$ orientation, based on a bulk structural model from the literature,²⁹⁰ is shown for comparison by black diamonds. All experimental peaks line up with the simulated ones, highlighted by closed diamonds with their Laue

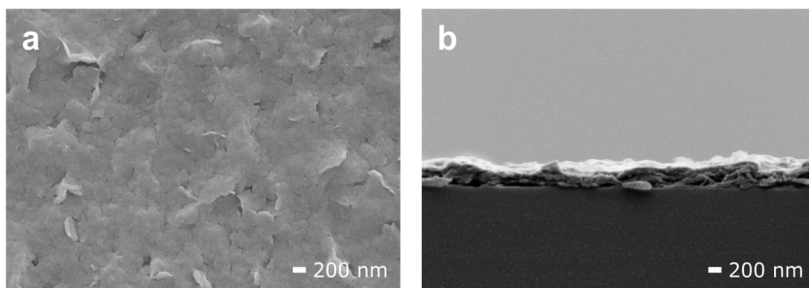


Figure 6.2. SEM images of Zn-ADC-DABCO thin film. **a)** Surface view. **b)** Cross-sectional view. The thin film appears as a closed layer made up of flat-lying, sheet-like crystallites of the order of 200 nm.

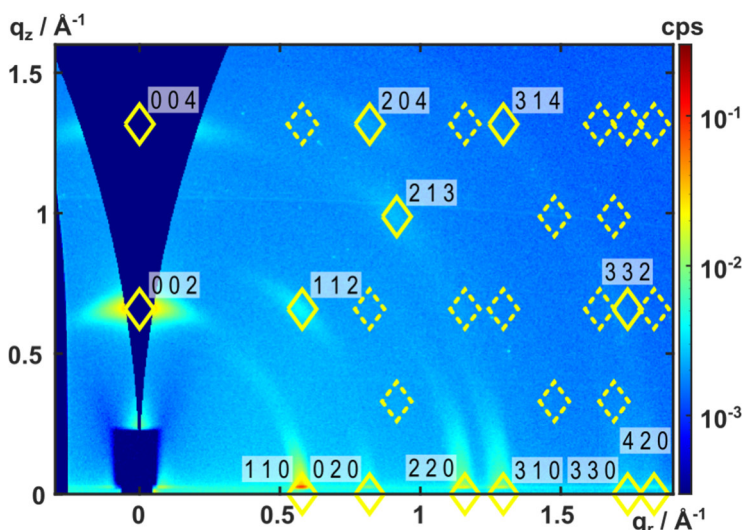


Figure 6.3. GIWAXS diffractogram of Zn-ADC-DABCO thin film in comparison to the expected peak positions (dashed diamonds, solid and labeled diamonds where experiment and simulation coincide) simulated based on bulk structural model data from the literature.²⁹⁰ The measured intensity maxima exhibit a good agreement with the simulated pattern, where observed peaks are labeled with their Laue indices (closed diamonds). The preferred $\langle 001 \rangle$ -orientation can be deduced from the $\{002\}$ diffraction peak aligned with the q_z axis.

index next to them. In order for this synthesis to yield $\langle 001 \rangle$ -oriented thin films, optimal conditions, such as precursor concentrations in the

growth solution and hot plate temperature, needed to be found first. In order to compare and evaluate samples obtained from different sets of parameters, a figure of merit describing orientational quality is needed.

Similar to the thin film texture analysis in **Chapter 4**, the orientational quality of the produced thin films can be quantified by evaluating an azimuthal pole figure. However, in contrast to comparing an oriented fraction of crystallites with a totally randomly oriented portion as previously in **Chapter 4**, we now consider a slightly different case. Here, there is no 3D powder fraction that would be indicated by a ring in the diffractogram. Instead, now the interest lies in evaluating the orientational quality of the crystallite orientation itself. In the 2D diffractogram, the azimuthal width of an intensity maximum reflects on the angular distribution of crystallite alignments around a certain preferred orientation.^{78–80} Hence, the orientational quality will be assessed by measuring the azimuthal full width at half maximum (FWHM) of a Gaussian fit, using the same MATLAB routine as in **Chapter 4** of an individual diffraction maximum. As a reporter, again the highest-intensity off-axis diffraction peak is chosen, which is the {112} peak in the case of the Zn-ADC-DABCO MOF.

As an initial starting point, all precursors were dissolved in ethanol at a concentration of 0.20 mM and a hot plate temperature of 40 °C was chosen. Fixing one of the two parameters, respectively, variation of the other one was tested. These initial screenings are summarized by the GIWAXS diffractograms show in **Figure 6.4** and **Figure 6.5** for samples from different precursor concentrations and **Figure 6.6** and **Figure 6.7** from different temperatures. Starting with the analysis of precursor concentration variation, the initial attempt at 0.20 mM equimolar ratios, fortunately, already yields a preferred orientation signaled by the distinct pattern discussed earlier. Based on the moieties present in the targeted structure ((Zn)₂(ADC)₂DABCO), a smaller amount of DABCO would be suggested also in the precursor

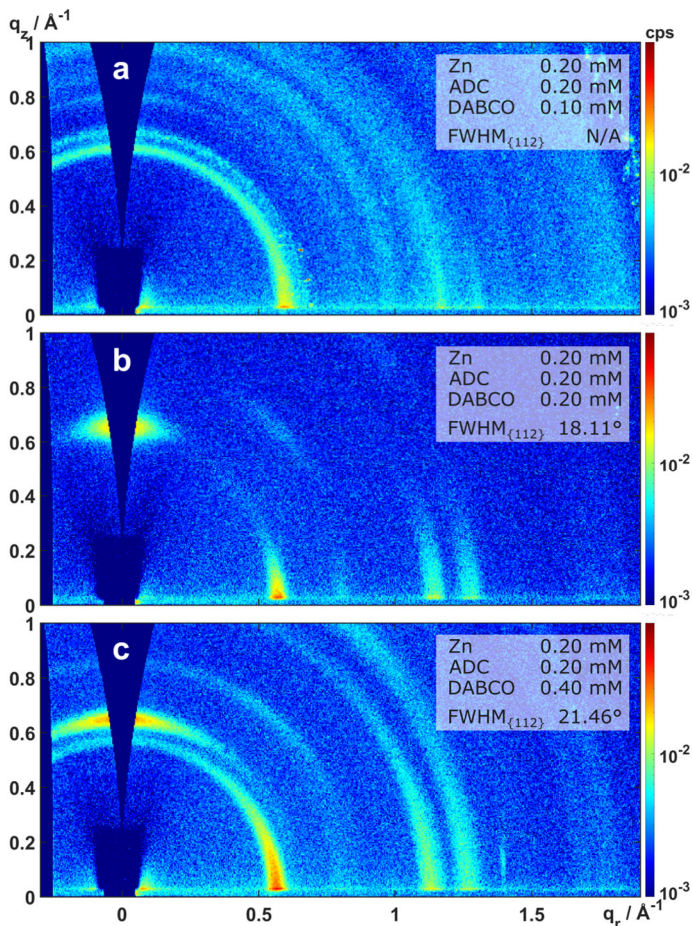


Figure 6.4. GIWAXS diffractograms of Zn-ADC-DABCO thin films synthesized at 40°C with different precursor concentrations – Part 1. **a) – c)** Diffractograms of thin films made from precursor concentrations in the growth solution droplet as indicated with $\{112\}$ FWHM as measure of preferred orientation quality. $\langle 001 \rangle$ -oriented crystal growth is only observed for a narrow region of equimolar precursor concentrations.

solution, the impact of varying its concentration was tested (**Figure 6.4a – c**). Interestingly, both, lower and also higher concentration of DABCO in the precursor solution, exemplified by 0.10 mM in **Figure 6.4a** and 0.40 mM in **Figure 6.4c**, only resulted in much worse results.

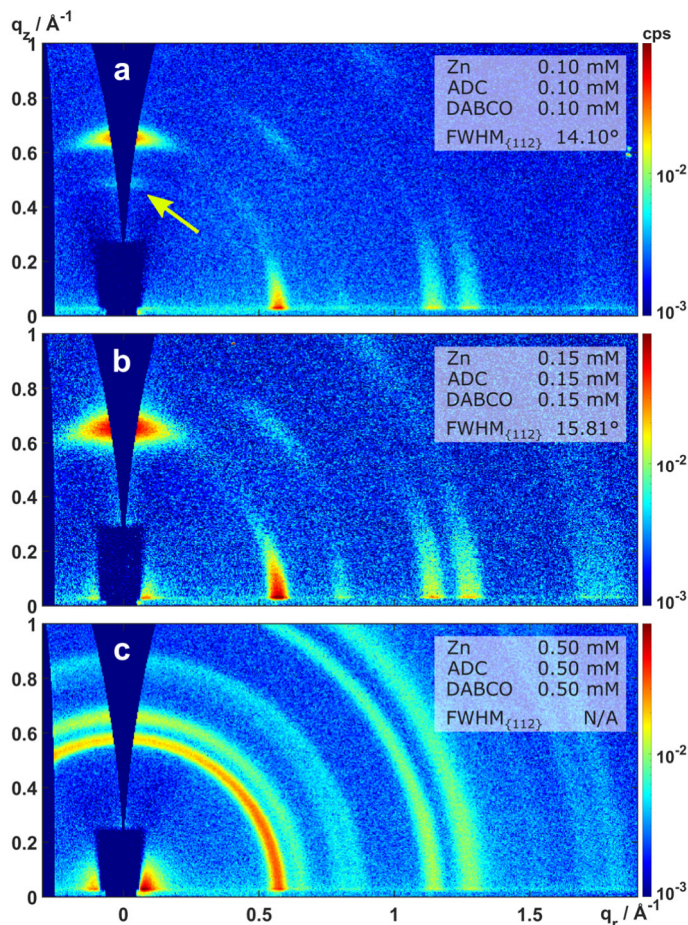


Figure 6.5. GIWAXS diffractograms of Zn-ADC-DABCO thin films synthesized at 40°C with different precursor concentrations – Part 2. **a) – c)** Diffractograms of thin films made from precursor concentrations in the growth solution droplet as indicated with {112} FWHM as measure of preferred orientation quality. <001>-oriented crystal growth is only observed for a narrow region of equimolar precursor concentrations. At 0.10 mM, an additional diffraction peak is observable along the q_z axis (labeled by a red arrow) that is not expected for Zn-ADC-DABCO, potentially indicating an undesired byproduct.

In each case, the distinct diffraction pattern was replaced by diffraction rings signaling a random crystallite orientation.

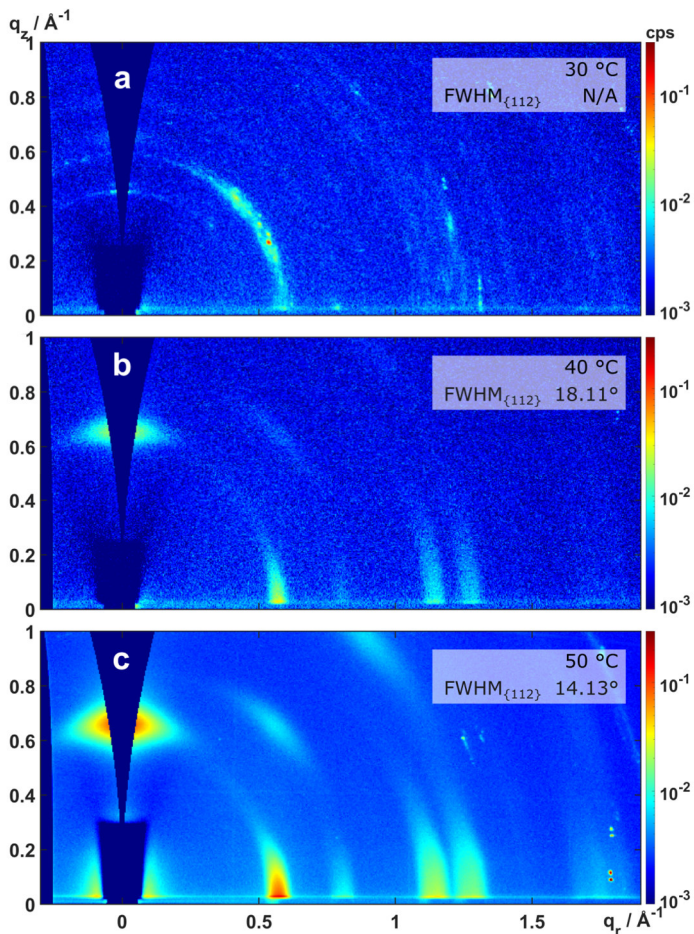


Figure 6.6. GIWAXS diffractograms of Zn-ADC-DABCO thin films synthesized with an equimolar precursor concentration of 0.20 mM at different hot plate temperatures – Part 1. **a) – c)** Diffractograms of thin films fabricated from 30 to 50°C with $\{112\}$ FWHM as measure of preferred orientation quality. At 30°C, no clear layer-pillar MOF diffraction pattern is observed, indicating that the synthesis needs a certain activation temperature.

Subsequently assessing a varied overall concentration level, a lowering (**Figure 6.5a, b**) resulted in improved preferential crystallite orientation, *i.e.* smaller azimuthal FWHM of the $\{112\}$ reporter peak

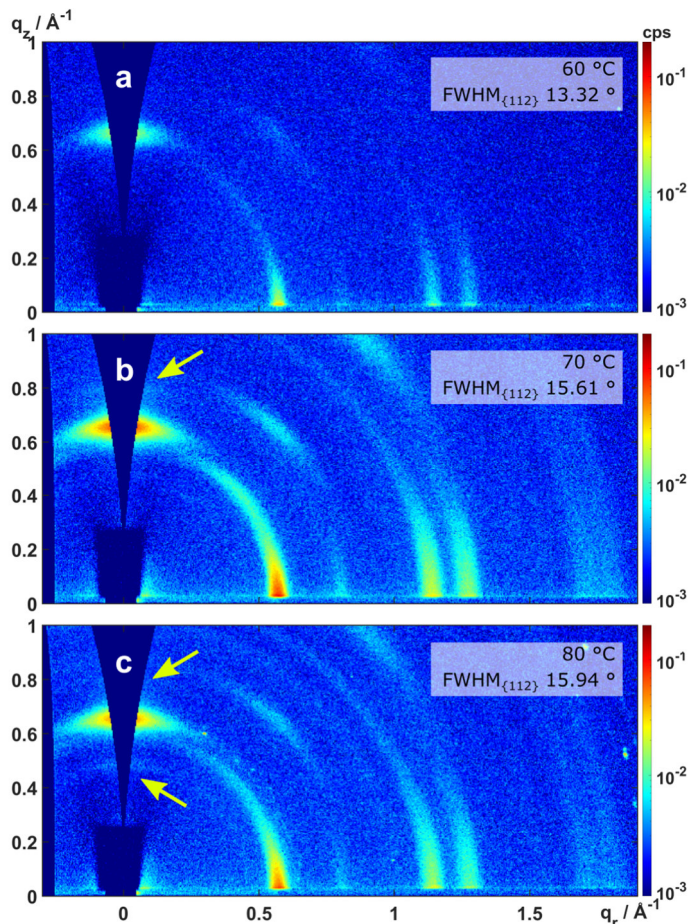


Figure 6.7. GIWAXS diffractograms of Zn-ADC-DABCO thin films synthesized with an equimolar precursor concentration of 0.20 mM at different hot plate temperatures – Part 2. **a) – c)** Diffractograms of thin films fabricated from 60 to 80°C with $\{112\}$ FWHM as measure of preferred orientation quality. Starting at 70°C, additional diffraction peaks become visible along the q_z axis (indicated by yellow arrows) that are unexpected for the Zn-ADC-DABCO structure, hence, suggesting another unwanted synthesis product.

(as indicated in the figure panels). However, paying close attention to the q_z axis in **Figure 6.5a** reveals an additional diffraction peak at ~ 0.5

\AA^{-1} that is not expected from the simulated pattern for Zn-ADC-DABCO (see **Figure 6.3**). Thus, it suggests the formation of another, unwanted crystalline phase in this case. An increase of the concentration level, on the other hand, led to a worsened crystallite orientation to the point where only rings are visible at 0.50 mM (**Figure 6.5c**), without an additional ring at $\sim 0.5 \text{ \AA}^{-1}$.

Moving on to the initial evaluation of the temperature in **Figure 6.6** and **Figure 6.7**, we can see that for a temperature lower than 40 °C (**Figure 6.6a**), no clear Zn-ADC-DABCO diffraction pattern (neither peaks nor rings) is obtained, indicating that a certain activation energy is needed to start the MOF formation process. For higher temperatures, first, there is again an improvement of the average crystallite orientation from 40 to 60 °C (**Figure 6.6b, c** and **Figure 6.7a**). However, starting from 70 °C (**Figure 6.7b, c**), again additional diffraction peaks along the q_z axis become visible pointing towards unwanted reaction side products.

Concluding from these initial synthesis parameter tests, there seems to be an optimum between 40 to 60 °C with an equimolar precursor concentration level around 0.15 mM. For this reason, another more detailed synthesis condition screening was performed in this confined range. The graph in **Figure 6.8** shows the $\{112\}$ FWHM extracted from the GIWAXS diffractograms of the thin films obtained from synthesis at the given concentration and temperature values. The color bar reaches from light green to dark blue, indicating FWHM values of 12.5 to 20.5°. These results indicate that the best synthesis results are achieved at 0.15 mM and 50 °C. All of the following studies were, hence, based on these synthesis conditions. The GIWAXS diffractograms have also been scanned for additional diffraction peaks corresponding to undesired additional crystalline phases as done before. For the following four samples such additional peaks were found: 0.05 mM / 40 °C, 0.10 mM / 40 °C, 0.25 mM / 45 °C, 0.25 mM / 60 °C. All these parameter combinations are located at the

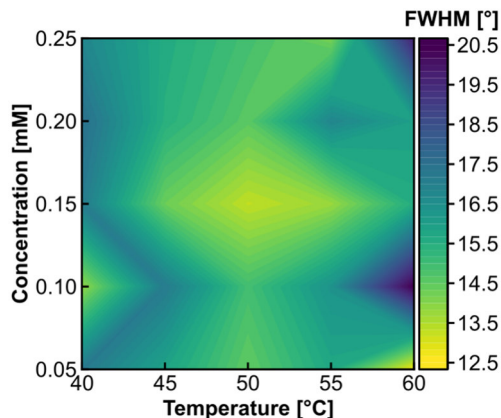


Figure 6.8. Narrow Zn-ADC-DABCO thin film fabrication parameter screening. As a figure of merit for the quality of the thin film orientation, the azimuthal FWHM of the {112} diffraction peak is given color-coded from light green to dark blue in dependence of (equimolar) precursor concentration level and hot plate temperature. The best quality is achieved for a combination of 0.15 mM and 50 °C.

very edges of the tested narrow parameter space and none were found near the optimum.

To gain more insight about the MOF formation process, XRD studies were performed on thin films made from different drop-cast precursor solution volumes, which is presented in **Figure 6.9** to **Figure 6.11**. The PXRD patterns in **Figure 6.9** were obtained on thin films from an increasing amount of $30 \mu\text{L cm}^{-2}$ droplets up to a total maximum of $1672 \mu\text{L}$. We observe a step-wise increase of the {002} diffraction peak and its higher orders the more solution was drop-cast. This is evidence for successive growth of the MOF layer with each deposition cycle. Thereby, the preferred orientation seems to be present from the first deposition on. To verify this observation, we turn to the GIWAXS analysis that is more sensitive to extremely thin layers than PXRD. Thus, in **Figure 6.10** and **Figure 6.11**, GIWAXS diffractograms of 1 to 4 deposition cycle(s) with $82 \mu\text{L cm}^{-2}$ droplet(s) and 1 to 8 deposition cycle(s) with a $10 \mu\text{L cm}^{-2}$ droplet(s) are shown.

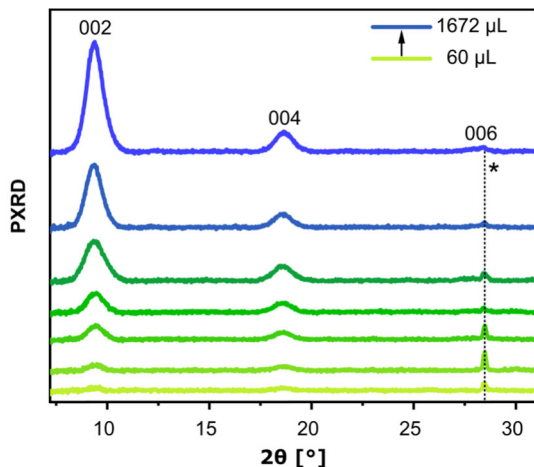


Figure 6.9. PXRD data on droplet-dependent Zn-ADC-DABCO synthesis. Thin films were fabricated with an increasing total drop-cast volume from 60 to 1672 μL applied by 30 $\mu\text{L cm}^{-2}$ droplets. The vertical probing by the Bragg-Brentano measurement reflects the vertical periodicity according to the DABCO pillar spacing and its higher orders, therefore the labelling 002, 004, 006. The step-wise increase in signal intensity confirms successive thin film growth with more and more drop-cast precursor solution. The sharp peak at $\sim 28.5^\circ$ labeled by an asterisk is due to the underlying Si substrate.

These droplet volumes represent the maximum volume that could be drop-cast without flowing off the substrate and the minimum still wetting the whole substrate surface, respectively. These additional results confirm clearly that the preferred $\langle 001 \rangle$ orientation is indeed present from the first deposition cycle onwards since in each case the diffraction pattern matches the one examined in **Figure 6.3**. In case of the larger droplets, additional deposition cycles furthermore seem to enhance the average crystallite orientation, decreasing the $\{112\}$ FWHM from 24.51° to 17.19° . In case of smaller droplets such as the 30 $\mu\text{L cm}^{-2}$ this is not the case. Here the 836 to 1672 μL samples all exhibit similar $\{112\}$ FWHM value of 15.36 , 15.40 and 15.48° . We will interpret this observation a bit later, when discussing a possible MOF formation mechanism. To summarize the most important insights of the drop-cast volume investigation: 1) the preferred MOF orientation

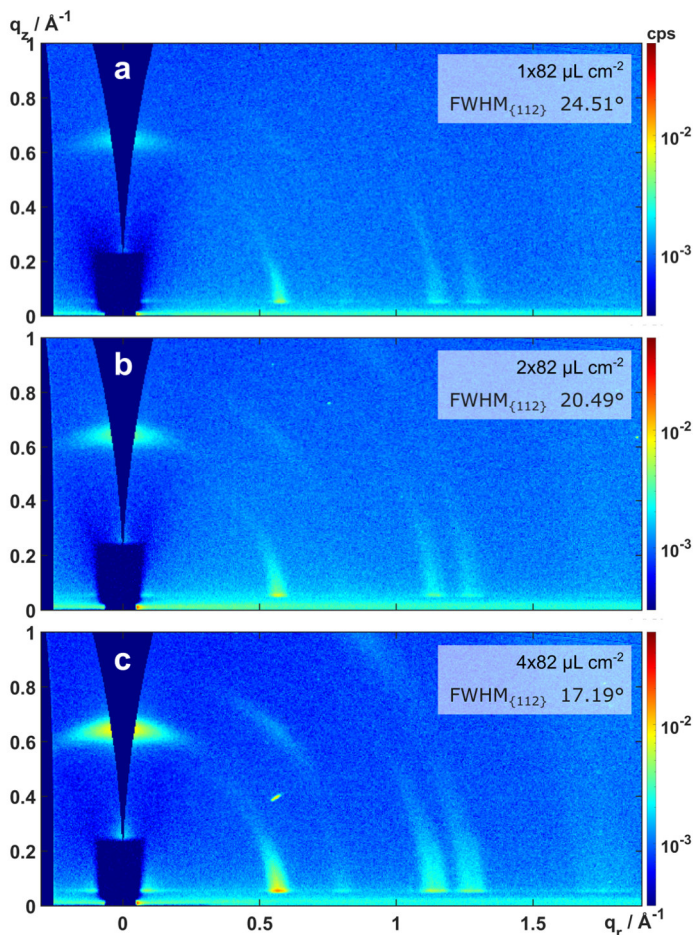


Figure 6.10. GIWAXS diffractograms of droplet-dependent Zn-ADC-DABCO synthesis from large droplets. **a) – c)** Different drop-cast precursor solution volumes as indicated. The Zn-ADC-DABCO-specific diffraction pattern is visible from the droplet deposition on and becomes more intense the more growth solution was applied. This indicates that from the start of the synthesis, crystallites in the $\langle 001 \rangle$ -preferred orientation are grown. To better illustrate the intensification of the scattering intensity, all diffractograms are shown with the same color scale.

is present from the first synthesis step onwards, 2) multiple cycles of deposition lead to step-wise growth of the MOF layer and 3) smaller

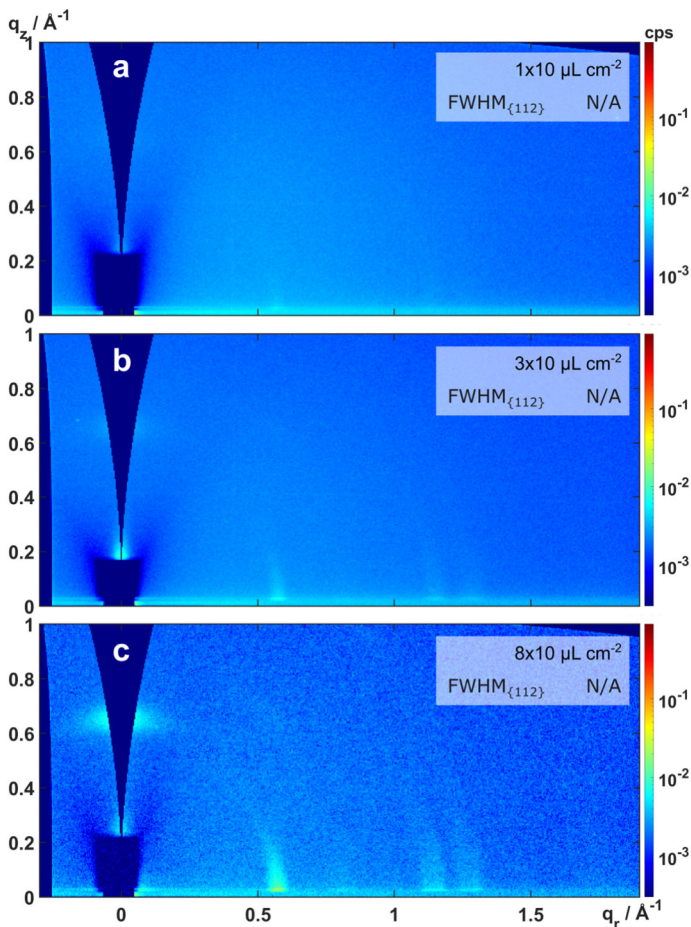


Figure 6.11. GIWAXS diffractograms of droplet-dependent Zn-ADC-DABCO synthesis from small droplets. **a) – c)** Different drop-cast precursor solution volumes as indicated. In a very weak form, even from small droplets, the Zn-ADC-DABCO-specific diffraction pattern is visible with only one deposition cycle. The gradual intensification of the diffraction pattern indicates that from the start of the synthesis, crystallites in the $\langle 001 \rangle$ -preferred orientation are grown. The diffractograms are shown with the same color scale to better track the diffraction intensity increase.

droplet volumes yield slightly better oriented thin films than maximum volumes.

Besides the fabrication of Zn-ADC-DABCO thin films *via* drop-casting that led to the <001>-oriented MOF thin films, also the synthesis of similar layered pillar MOFs was attempted, using the same protocol with the initial 0.20 mM equimolar precursor concentration level, and a hot plate temperature of 50 °C. The GIWAXS diffractograms of the obtained thin films using successively less bulky dicarboxylic ligands NDC (1,4-naphthalenedicarboxylic acid) and BDC are shown in **Figure 6.12** in comparison to the Zn-ADC-DABCO. In contrast to the bulky anthracene-based linker that leads to highly oriented films, NDC and BDC only lead to poorly defined diffraction rings that indicate low crystallinity and absence of a preferred orientation. However, keeping the ADC linker and exchanging the pillar ligand for the longer BPy molecule led to a promising synthesis result, that was slightly refined by reducing the concentration of BPy to 0.05 mM and is displayed in **Figure 6.13**. To provide a visual clue that the observed diffraction maxima match the peak positions expected for Zn-ADC-BPy in <001> orientation, also in this case the simulated pattern based on a literature bulk crystal structure is superimposed as black diamonds.²⁹¹ The observed experimental peaks match the simulated peaks (indicated again by closed diamonds and Laue indices), although the average crystallite orientation is slightly worse than in the case of Zn-ADC-DABCO. Nevertheless, this is a promising result pointing towards a general applicability of the drop-casting synthesis procedure for similar ADC-based layer-pillar MOF structures.

Based on all presented experimental results, a MOF formation mechanism during drop-casting is proposed that is consistent with theories for growth of self-organized MOF thin films with preferred orientation in the literature. As presented by Hupp and co-workers,¹⁵⁴ layered pillar MOF film growth can be initiated from a metal-oxide surface by vertically binding DABCO pillar molecules. Furthermore, the literature provides evidence for the bond between Zn paddle wheels and pillar molecules being prone to attack by substituting water molecules.^{273,292} This bond, however, can be protected by steric

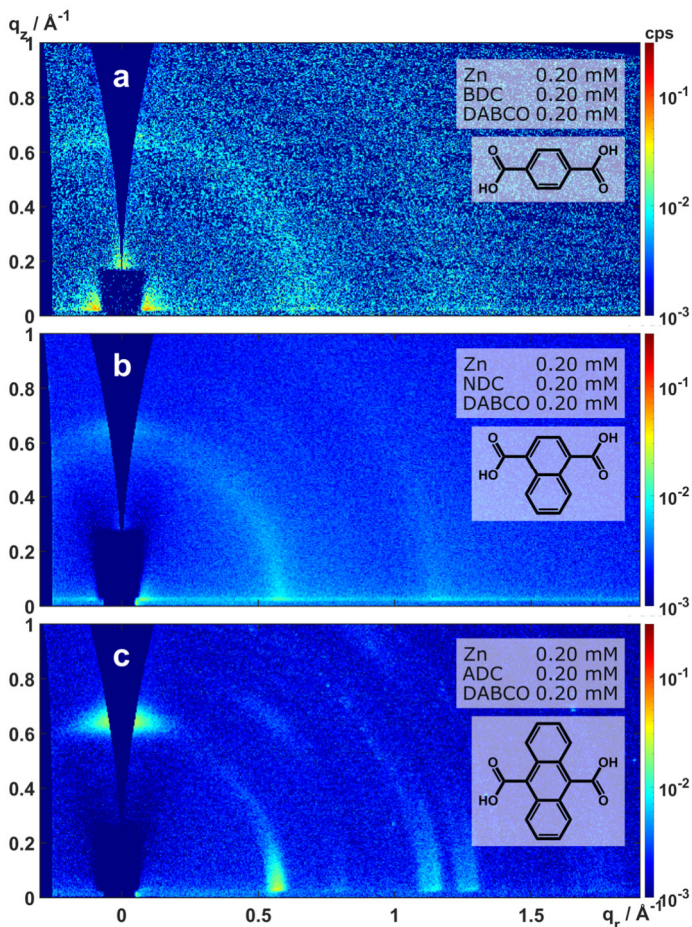


Figure 6.12. GIWAXS diffractograms of drop-cast thin films using different linkers. Thin film fabrication based on Zn, DABCO and **a)** BDC, **b)** NDC, and **c)** ADC has been attempted at 0.20 mM at 50°C. Only synthesis with the bulky ADC ligand yields an oriented structure, while in the other two cases, poorly defined diffraction rings point towards low crystallinity and absence of a preferred orientation.

interaction of surrounding bulky molecules forming the Zn paddle wheel and, thereby, reduce the chance of water molecules replacing DABCO pillars.^{292,293} Based on this concept, the formation of Zn paddle wheels always needs to take place before a stable incorporation of

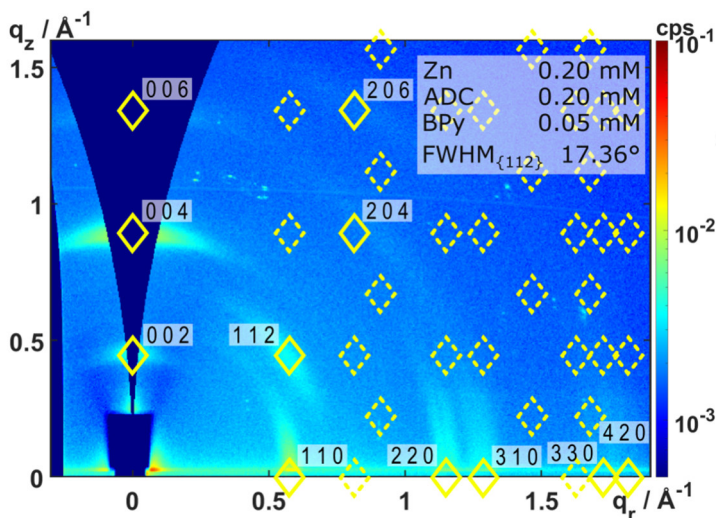


Figure 6.13. GIWAXS diffractogram of drop-cast Zn-ADC-BPy. Synthesis with metal precursor and ADC concentrations of 0.20 mM and BPy at 0.05 mM results in a thin film with a $\langle 001 \rangle$ -orientation comparable to Zn-ADC-DABCO. The experimental diffraction pattern is compared with simulated peak positions (dashed diamonds, solid and labeled diamonds where experiment and simulation coincide) based on a bulk structural model.²⁹¹ Corresponding experimental and calculated peaks are indicated by closed diamonds and crystal plane indexation.

DABCO ligands to form the layered pillar MOF lattice is possible. This means that MOF growth within the Zn-ADC plane must be the fastest which results in the formation of plate-like crystallites. With these concepts in mind, two processes are derived that explain the $\langle 001 \rangle$ -oriented MOF growth which are illustrated in **Figure 6.14**. The first mechanism (**Figure 6.14a**) is surface-initiated crystallization where the MOF grows along the horizontal substrate surface with the pillar molecules pointing vertically upwards as dictated by the DABCO basis layer that forms on the SiO_2 when the precursor solution is applied to the substrate. The second mechanism (**Figure 6.14b**) is crystallization in solution where platelets spontaneously form distributed across the whole solution droplet. The sheet-like crystallites are most likely to land flat on the surface where they can successively intergrow with

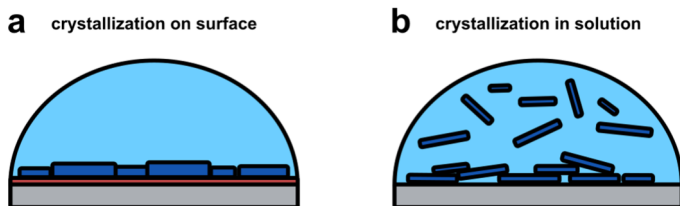


Figure 6.14. Proposed growth mechanisms causing $\langle 001 \rangle$ -preferred crystallite orientation in drop-casting synthesis. Two processes, **a)** crystallization on the substrate surface and **b)** crystallization in solution, are suggested to lead to the preferred thin film orientation in parallel. In the first case, direct anchoring of DABCO molecules on the SiO_2 surface leads to a controlled planar growth of crystallites that are templated to grow with their pillars in vertical alignment due to the DABCO coordination. In the second case, crystallites form in solution in the form of platelets that are most likely land flat on the surface and bind to crystallites already at the ground.

already present crystallites. Further experimental observations made support this hypothesis: Oriented thin films were achieved on different surfaces other than $\text{Si}(\text{O}_2)$ such as TiO_2 , Gd_2O_3 , ZnO , and Ag with very similar average crystallite orientation (as seen in **Figure 6.15**). Oriented thin film synthesis on silver, however, would not be possible if a DABCO surface- anchoring would be the only way for the crystallites to form in this configuration since there is no oxide layer on top of it. Upon close examination, the diffractogram of the sample on silver exhibits the worst broadest deviation of crystallites from the $\langle 001 \rangle$ orientation which would be readily understood considering crystallization in solution. Another result of the proposed growth mechanism is the vertical film make-up consisting of layered crystallites instead of a thick single crystal layer.

This is in fact observed by visual examination of the SEM image shown in **Figure 6.2**. Supporting evidence is also obtained from a further analysis of the PXRD patterns related to increasing precursor solution volumes in **Figure 6.9**. According to the Scherrer equation ($d = K\lambda_{x\text{-ray}}/FWHM \cdot \cos(\theta)$, with the Scherrer constant $K \approx 0.9$, the

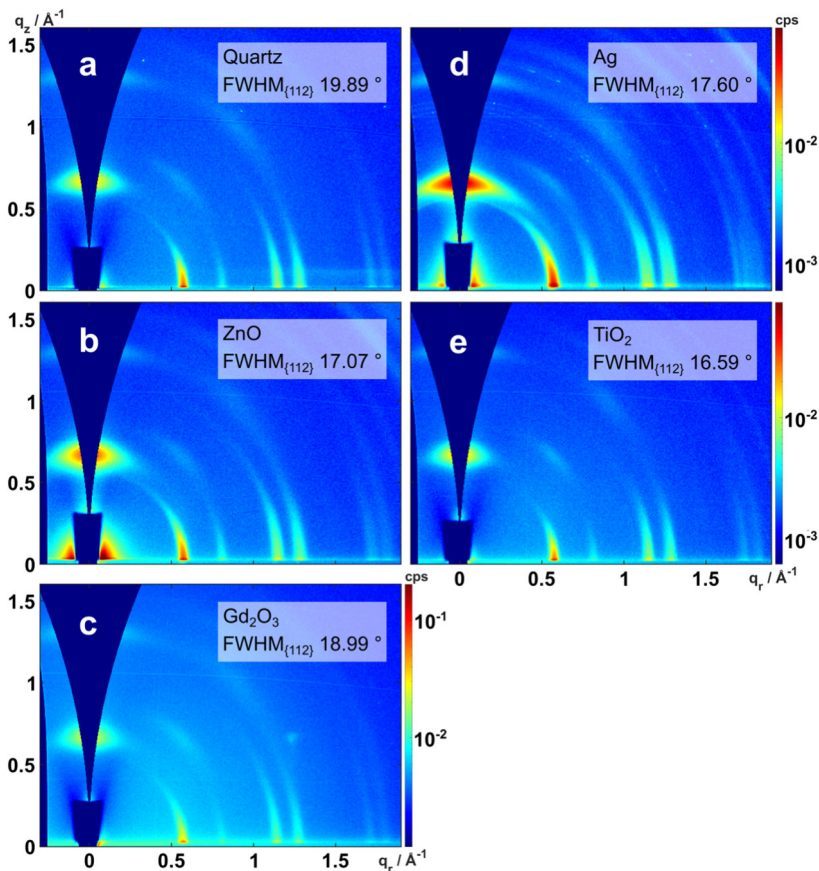


Figure 6.15. GIWAXS diffractograms of Zn-ADC-DABCO grown on different substrates. Among the oxide substrates, TiO_2 shows the best preferred orientation. Interestingly, while the silver sample exhibits a similar $\{112\}$ FWHM, simultaneously, ring-like features are visible in the diffractogram that suggest that a significant portion of crystallites are actually randomly oriented. This points towards a templating effect of DABCO binding to an oxide layer that is not present in case of the silver substrate. Here, we can likely see a sample whose oriented crystallites were only brought into this configuration by the effect of plate-like crystallites randomly falling down from solution and layering flat on the surface for geometric reasons.

wavelength of X-ray photons $\lambda_{X\text{-ray}} \approx 0.154 \text{ nm}$, and the diffraction angle θ),^{294,295} the crystallite thickness d can be estimated based on

the FWHM (in radians) of a Gaussian-shaped PXRD peak. In case of a sequential growth of crystallites with successive deposition cycles, the FWHM becomes smaller with each step, which would translate to an increasing film thickness according to the formula. However, the opposite is the case, as can be seen in the plot in **Figure 6.16** displaying crystallite thickness over drop-cast volume. In fact, this estimated average crystallite thickness goes down and reaches a plateau at approximately 400 μL of drop-cast solution. This behavior can be explained directly based on the two separate growth mechanisms: In the first deposition cycle, DABCO binds to the SiO_2 surface and triggers surface-initiated growth. Simultaneously, a few crystallites form in the solution and fall down. Since the substrate is blank at the beginning, the chance of such a crystallite landing on one that has formed on the ground is rather low. In the following deposition steps, the crystallites already on the surface begin to grow

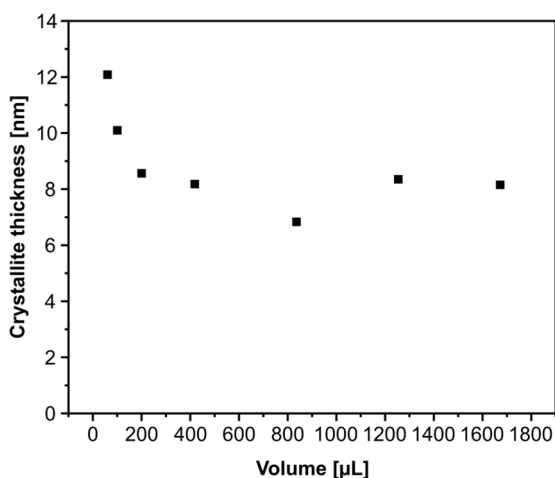


Figure 6.16. Crystallite thickness over drop-cast growth solution volume. The data is based on the Scherrer equation and the FWHM of the first diffraction peak progression of the PXRD patterns in Figure 6.9. After a quick drop at the beginning, the average crystallite thickness approximately stays constant. This can be explained by crystallites formed in solution continuously covering the MOF layer emerging from the substrate surface. Thereby, the growth of substrate-bound crystallites is limited.

larger, but solution-formed crystallites continue to emerge and, with increasing likelihood, might cover the crystallites that have grown larger on the substrate surface. This process effectively limits the maximum thickness crystallites can achieve with more and more deposition cycles and explains the estimated average crystallite thickness reaching a roughly constant value after a certain amount of drop-cast volume in **Figure 6.16**. Interestingly, there seems to be an influence of the droplet volume in this process. Looking back at the comparison of the {112} FWHM after multiple deposition cycles with maximum ($82 \mu\text{L cm}^{-2}$) and medium droplet volumes ($30 \mu\text{L cm}^{-2}$), a successive decrease of the FWHM was noticed in the maximum case and no change in the medium case. In a larger droplet, crystallization in solution becomes more relevant than surface growth which means that crystallites initially deposit much more unordered. In this case, performing multiple deposition steps is beneficial for the average crystallite orientation as a flatter overall crystallite deposition is statistically more likely after a large number of crystallites has fallen down from solution. The two competing formation processes are more balanced for smaller droplets and therefore, repeated (random) deposition of falling crystallites from solution doesn't play such an important role in this case. With this observation being made, it might actually be better to use even lower droplet volumes such as $10 \mu\text{L cm}^{-2}$ or less for each sample synthesis. However, this would make the synthesis much more time consuming and in case of extremely small volumes, also the reaction time (until all ethanol has evaporated) would be significantly reduced. This could also have an influence on the resulting thin film. Therefore, $30 \mu\text{L cm}^{-2}$ was chosen as a balanced practical optimum that reliably yields thin films with satisfyingly high orientational quality in a very short amount of time.

6.4. Luminescence Turn-on During Solvent Evaporation

The ADC linker dissolved in ethanol presents a bright photoluminescence with a fairly high PLQY of ~48 % at 0.1 mM

concentration. This stimulated the investigation of the emissive properties of the linker when incorporated in the layered pillar MOF thin film. However, instead of a comparably strong emission, the MOF only glows barely visible to the naked eye with a PLQY of $\sim 1\%$. The strongly reduced emission in the MOF has been explained by self-quenching due to tight chromophore packing in the past.²⁹⁶ Aiming to activate the MOF PL, the thin films were exposed to various solvents such as *n*-hexane, cyclohexane, toluene, acetone and ethanol. Hereby, an intriguing discovery was made. While none of the tested solvents had any effect on the MOF emission except ethanol, this solvent led to a very strong luminescence turn-on when evaporating from the thin film right before it totally turned dry. To capture and analyze this behavior, the PL was monitored throughout the whole process of applying and evaporating of an ethanol droplet on a Zn-ADC-DABCO thin film. The analysis of this spectroscopic data is summarized in **Figure 6.17** and **Figure 6.18**. We begin the examination by considering the normalized PL intensity averaged from 410 to 430

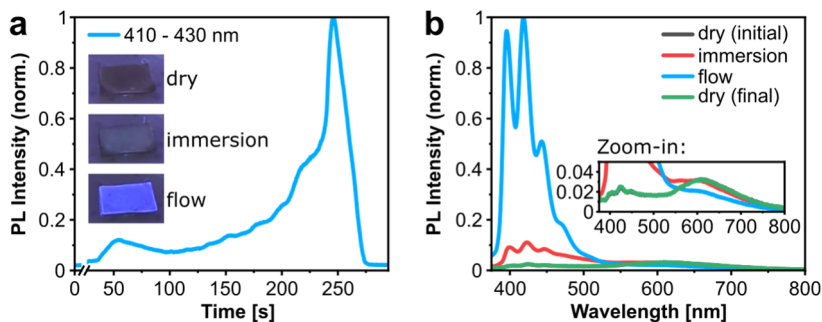


Figure 6.17. PL turn-on effect in Zn-ADC-DABCO during ethanol evaporation. **a)** Normalized PL intensity averaged in the wavelength range from 410 to 430 nm over time. At ~ 6 s, the ethanol droplet was applied with a micropipette (clipped region). The photo insets show the visual appearance of Zn-ADC-DABCO on Si in the different emissive states, depending on ethanol evaporation (“dry” – initial and final states, “immersion” – thin film immersion in the solvent on the substrate, “flow” – evaporation end phase when solvent leaves the MOF pores). **b)** Time-integrated PL spectra according to different solvent evaporation states.

nm in **Figure 6.17a**. Starting and ending the experiment in the dry state, the thin film shows only the minimal baseline luminescence. With the addition of solvent at ~6 s, there is an increase of the PL intensity reaching a rough plateau approximately 10 times higher than when in the dry state, while the solvent droplet still sits on the sample. Towards the final phase of drying, when the solvent is released from inside the MOF pores, the emission level again increases dramatically peaking at roughly a factor of 50 over baseline. This bright emission lasts for a couple of seconds before rapidly dropping back to the default emission of the dry state. Given in **Figure 6.17b** is a comparison of time-integrated spectra extracted from the same measurement by averaging the with PL spectra within the respective solvent evaporation phases.

The complete evolution of the emission spectrum during this process is depicted in **Figure 6.18a** and **Figure 6.18b**, showing the normalized PL intensity based on a logarithmic color scale to provide better insight into the emission changes over time. The three dominant emission peaks in this range closely resemble the PL of ADC monomers measured in ethanol at a concentration of 5×10^{-8} M, displayed in **Figure 6.19a**, and point out the linkers as the major components dominating the MOF luminescence. Interestingly, the positions of local peak emission can be linked to distinct phases during the solvent evaporation experiment. The peak shift can be clearly seen in the zoomed-in version of the spectral evolution in **Figure 6.18b**, focusing on the wavelength range from 380 to 480 nm. The three local peak positions in each individual spectrum are labeled by black dots in both figure panels of **Figure 6.18**. Right after applying the solvent droplet, a first strong blue-shift in all three emission peaks, roughly from 6 to 40 s. The wavelength shift is the strongest in the two highest energy emission components. Similar small differences are found among dry and solvated emission of related MOF structures in the literature that also contain Zn-ADC paddle wheels.^{297,298} Due to

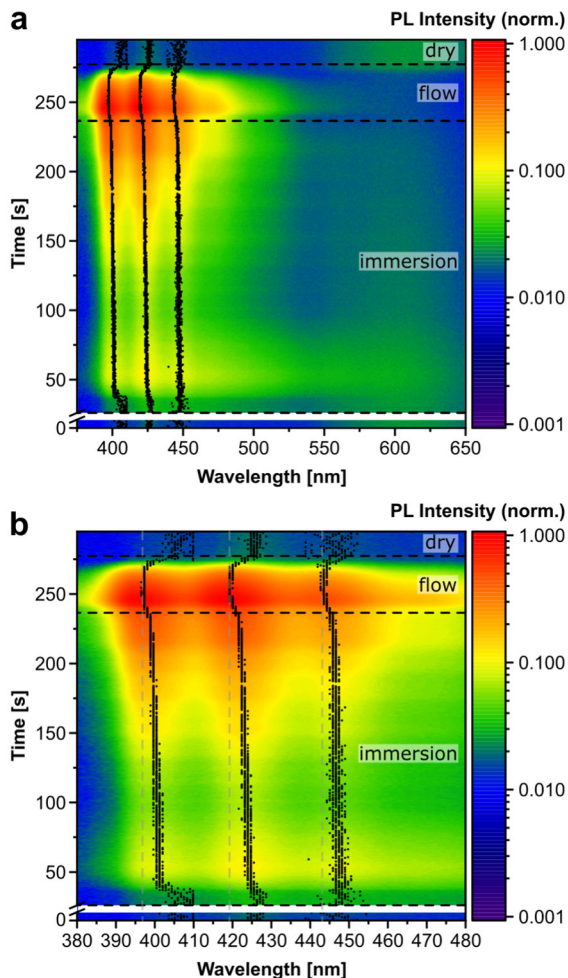


Figure 6.18. PL turn-on effect in Zn-ADC-DABCO during ethanol evaporation. **a)** Full spectral evolution of the thin film PL over time. **b)** Zoomed-in version of the plot in a) to more clearly show peak emission wavelength shifts over time. The normalized PL intensity is depicted by a logarithmic color scale. According to the peak emission shifts, dry, immersion and flow state labels were assigned.

this interaction between ADC and the surrounding solvent molecules flooding the MOF's pores, this emission phase is referred to as "immersion" state in the following. The peak positions then remain

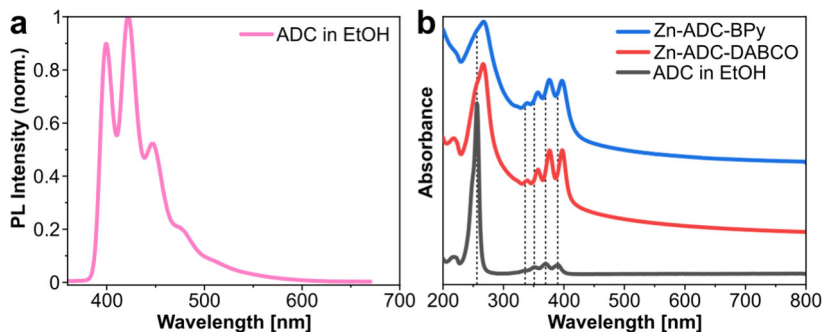


Figure 6.19. ADC emission and absorption. **a)** Emission spectrum of ADC in ethanol at a concentration of 5×10^{-8} M. The clear vibronic structure with producing peaks at 399, 422 and 447 nm are indication of a monomeric emission. **b)** Absorbance spectra of ADC in ethanol at a concentration of 5×10^{-6} M, Zn-ADC-DABCO and Zn-ADC-BPy thin films on quartz. The similarity of pure ADC and MOF absorbance spectra points out the linker as major component determining the thin film absorption. The notable red-shift (visually highlighted by dashed lines indicating the ADC absorbance peak positions) is due to linker coordination with Zn clusters inside the MOFs.

roughly constant, with a very slight further blue-shifting tendency, before a sudden jump at ~ 235 to ~ 250 s occurs in the final evaporation phase coinciding with the spike in PL intensity. This second blue-shift points towards a second effect taking place inside the MOF besides the solvatochromism observed at the beginning of the experiment. As this is the final drying phase when the remaining solvent should be flowing out from the MOF's pores and the thin film turns visibly dry again, this phase is termed "flow" state. At the end of the flow phase, the material quickly reverts back to the dry emission characteristics with the low baseline luminescence intensity and emission peaks at their initial positions.

Besides the emission from individual ADC linkers inside the MOF that show their distinct high-energy emission peaks, another very broad emission can be seen centered around approximately 600 nm that is actually dominating in the initial and final dry states (**Figure 6.17b**). In the literature, the existence of various low-energy emissive states is proposed in dense anthracene-based systems dependent on their

mutual orientation and energetic coupling.^{92–94} Considering different interactions between neighboring ADC linkers in their excited states, a reconfiguration of anthracene units is suggested where adjacent π planes move into a slipped face-to-face configuration. This emissive state is observed increasingly pronounced under prolonged UV illumination of the dry MOF thin film (**Figure 6.20**) which supports the hypothesis of an alternative configuration of linkers being formed in their excited state. Interestingly, this lower-energy emission is suppressed in the flow state (**Figure 6.17b**) and recovers its initial PL intensity level in the final dry state. This gives a first indication of rotational realignment of ADC linkers playing a major role during the PL turn-effect which will be discussed in great detail later on.

The data presented in **Figure 6.17**, **Figure 6.18** and **Figure 6.20** was acquired using a fs-pulsed laser at 343 nm at 20 kHz as excitation as part of a fluence-dependent measurement series that will be discussed in the next section. However, the same behavior was seen when using a CW LED at 300 or 365 nm as excitation source. These have been used, for example, performing additional measurements of

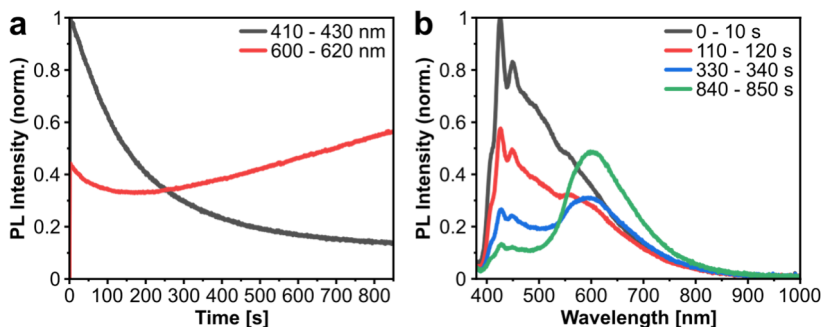


Figure 6.20. Zn-ADC-DABCO dry state PL over time during UV illumination. **a)** Averaged PL intensity over time for higher energy (410 – 430 nm) and lower energy (600 – 620 nm) emission peaks. **b)** PL spectra at different time frames as indicated in the top right. The Zn-ADC-DABCO MOF thin film shows a shift of the dry state emission maximum from ~420 to ~600 nm under prolonged excitation which can point towards an alternative preferred configuration of linkers in the excited state that leads to a lower energy emission.

solvent evaporation (throughout **Figure 6.22**, **Figure 6.24**, **Figure 6.25**) with different experimental conditions varied that will be discussed a bit later.

Corresponding to the similarity between the emission of ADC in solution and the MOF thin film, also their absorption characteristics bear strong resemblance. **Figure 6.19b** shows the absorbance of ADC in ethanol at a concentration of 5×10^{-6} M in comparison to Zn-ADC-DABCO (and also Zn-ADC-BPy) thin films grown on quartz substrates. The similarity of the spectra again supports the conclusion that the ADC linker is the major component determining the optical material properties. The slight red-shift of the thin films' absorbance peaks with respect to the ligand in solution is evidence of the linker coordination inside the MOFs. Absorbance data was also acquired time-resolved during the evaporation of an ethanol droplet applied to the surface of a Zn-ADC-DABCO sample of quartz. Therefore, the whole sample was illuminated by a collimated beam of white light from a De-Ha-lamp in substrate-orthogonal transmission. The resulting data from this measurement is represented in **Figure 6.21** in a similar manner as the PL spectral evolution before. In full correspondence to the thin film PL, the absorbance peaks also shift over time with the same behavior in response to the different solvent evaporation phases. The absolute absorbance values themselves, in this measurement, are not only related to the thin film. Due to the measurement being done in transmission with a wide beam covering the whole sample, the geometric shape of the solvent droplet situated on top of the substrate also influences the amount of light being transmitted through the sample. This leads, for example, to the strong apparent increase of absorbance right after the application of the droplet (red area around ~50 s). The observed fine changes in peak absorption wavelengths over time complement the prior PL analysis and confirms the ADC linker being the critical changing component responsible for the observed effect upon solvent release from the

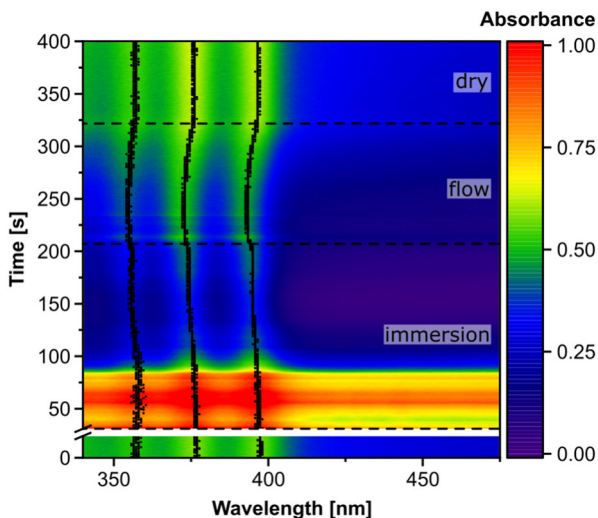


Figure 6.21. Evolution of Zn-ADC-DABCO apparent absorbance during ethanol evaporation. Black dots indicate the local maximum positions over time. Very similar to the behavior of the thin film's PL, the peak absorbance values change depending on the evaporation state of ethanol. The absorbance values themselves are not only due to the changes in thin film absorption but are majorly influenced by the changing (dome-shaped) droplet geometry on the sample in this measurement, for example causing the strong apparent absorbance directly after solvent application (red area).

MOF. The PL turn-on effect during solvent evaporation is very repeatable, evident by **Figure 6.22** showing the PL intensity in dry and flow states over successive cycles of ethanol dropping. Thereby, the MOF's structural properties, including the high level of orientation, stay constant throughout such repeated experiments (**Figure 6.23**). Furthermore, the peak luminescence was observed to be dependent of the applied solvent volume, causing an approximately linear increase of the maximum PL intensity (along with a longer time delay after droplet application) with droplet volume (**Figure 6.24a**). This is suggestive of a connection between the turn-on effect and the number of solvent molecules filling the pores of the MOF thin film. Moreover, as suggested by the earlier test with much bigger solvent molecules such as n-hexane or toluene before, the solvent molecule size is a deciding factor for the luminescence turn-on to occur.

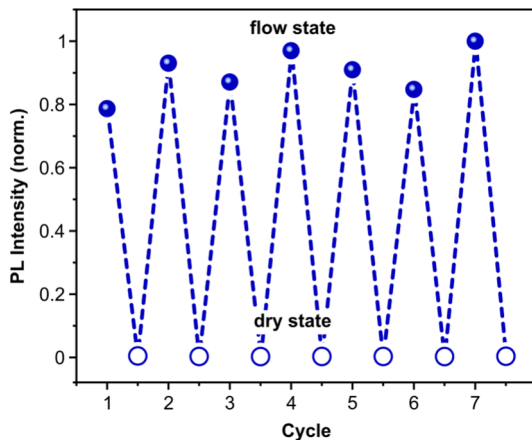


Figure 6.22. PL intensity of Zn-ADC-DABCO in dry state and flow state during ethanol evaporation across successive solvent dropping cycles. The luminescence turn-on effect shows in every iteration.

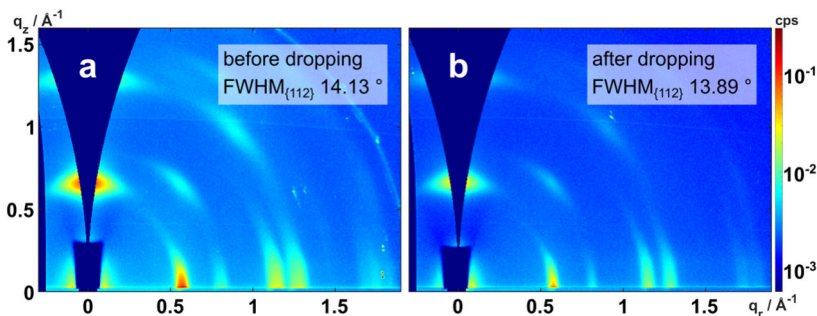


Figure 6.23. GIWAXS diffractograms of Zn-ADC-DABCO thin film before and after ethanol dropping experiments. **a)** Measurement after thin film synthesis, before the ethanol dropping and evaporation experiments. **b)** Measurement after many ethanol dropping and evaporation experiments. The thin film morphology and preferred orientation are not affected by the experiments, resulting in both GIWAXS data showing the same diffraction pattern and very similar {112} FWHM values.

Additional tests with methanol (3.6 Å),²⁹⁹ and isopropanol (4.7 Å),³⁰⁰ which have similar kinetic diameters (given in parenthesis) as ethanol (4.3 Å),²⁹⁹ reveal an identical PL turn-on occurring when using the smaller sized methanol, whereas the bigger isopropanol does not

cause any response (**Figure 6.24b**). These observations further support the idea that the critical mechanism underlying the PL turn-on occurs inside the MOF pores, that can only be effectively entered by sufficiently small solvent molecules. Finally, it is mentioned that the same PL turn-on process was observed in Zn-ADC-BPy using ethanol and methanol as dropped solvents. **Figure 6.25** shows the striking similarity of the isorecticular MOF system based on the

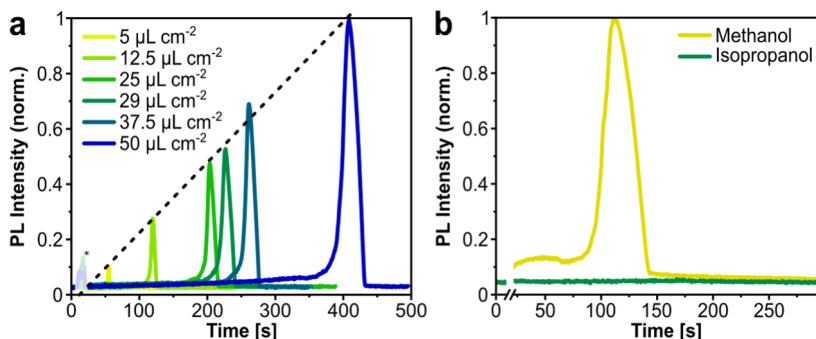


Figure 6.24. PL of Zn-ADC-DABCO during solvent evaporation. **a)** PL intensity over time for different applied volumes of ethanol. The peak intensity increases with applied solvent volume. **b)** PL intensity over time in case of methanol and isopropanol evaporation from the thin film sample. Methanol shows the same PL turn-on as ethanol. Isopropanol, however, does not cause any response.

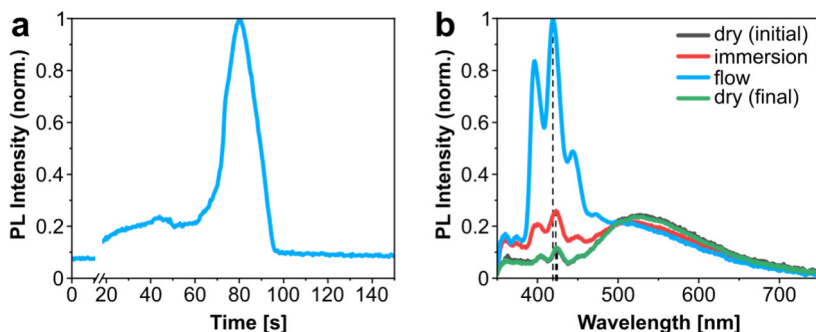


Figure 6.25. PL turn-on effect in Zn-ADC-BPy during methanol evaporation. **a)** PL intensity averaged from 410 to 430 nm over time. **b)** Time-integrated PL spectra according to the different solvent evaporation states. All characteristics of the PL turn-on are similar as in Zn-ADC-DABCO.

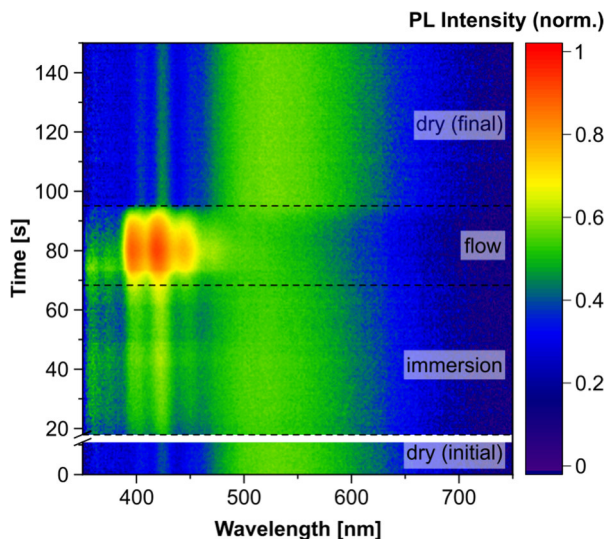


Figure 6.26. Spectral evolution of PL turn-on effect in Zn-ADC-BPy during methanol evaporation. All characteristics are very similar as in Zn-ADC-DABCO.

example using methanol as solvent. In conclusion, all these observations strongly point towards solvent molecules flowing out of the MOF pores, inducing a change in the emissive ADC linker that results in a modulating effect on the films' PL.

6.5. Molecular Rotor Realignment

In the previous section, we deduced that the ADC rotor linkers within the layered pillar MOF thin films govern their photophysical properties. Therefore, a change in the thin films' absorption and emission can be retraced to changes in the organic chromophores and/or their local environments. Considering solvent molecules directionally flowing through the MOF's channels, a potential sticking or dragging interaction between solvent and molecular rotors has been suggested in the literature, that is linked to a notable alteration of the viscosity by the nanoconfinement.^{187,301} Thus, the following interaction between flowing solvent molecules and ADC rotors is

proposed (illustrated in **Figure 6.27**): In the dry state, the ADC rotors are in their default configurations with minimal potential energy. When ethanol is introduced into the system, the solvent molecules diffuse within the pore network filling up the previously empty spaces between the linkers. After all ethanol on top of the thin film has evaporated, the solvent molecules start being released from inside the MOF. This creates a vertical solvent upstream that drags the rotors into a more vertical orientation, increasing their dihedral angles (i.e., the angles between the anthracene plane and the dicarboxylic groups, as indicated in the figure in red) from approximately 90° to close to 180° . Being held in this upwards orientation leads to a rigidification and near parallel alignment of neighboring rotor planes causing the luminescence turn-on. Such an interaction between specific solvents and the MOF could then be readily understood based on the kinetic diameter of the solvent molecules. On the basis of the experiments presented in **Figure 6.24**, the kinetic diameters of methanol and ethanol are small enough to pass the MOF pores while isopropanol is already too bulky. In the following, more experimental evidence for the ADC realignment will be presented and discussed in detail.

An upwards tilt of the ADC rotors was made observable directly by probing the thin films absorption with a substrate orthogonal illumination. With such a measurement configuration, the transition moments of ADC are nearly perpendicularly aligned to the incoming beam due to the $\langle 001 \rangle$ -orientation of MOF crystallites. A collective change of rotor orientation reduces the chromophores' absorption cross-sections and causes a reduction of the thin film absorption. With the thin film situated on a Si substrate, the measurement was conducted in reflection mode. Therefore, the detected signal predominantly consists of light that was transmitted by the MOF layer twice, with a minor contribution of isotropically scattered light from the thin film surface. An increased reflection then translates to a drop

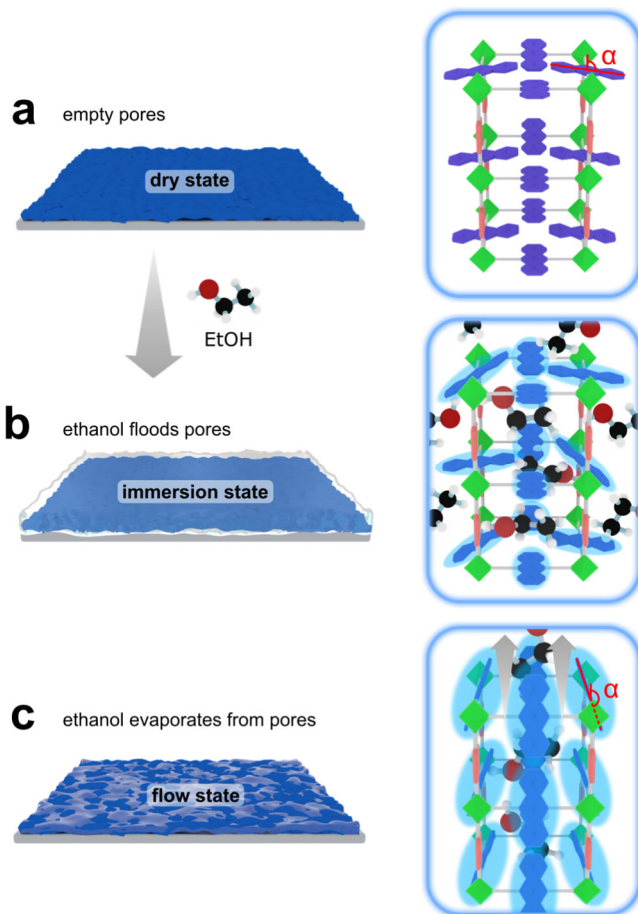


Figure 6.27. ADC rotor alignment by solvent upstream during evaporation from the MOF pores. The MOF is schematically shown in **a)** dry state, **b)** immersion state, and **c)** flow state. In the dry state, the pores of the MOF are empty and the ADC linkers in their default configuration. Upon addition of ethanol, the MOF channels are filled by diffusing solvent molecules. In the final phase of solvent evaporation, the flow state, ethanol leaves the MOF pores. The collective molecular upstream drags the anthracene units into a more vertical configuration increasing the dihedral angle α from $\sim 90^\circ$ to close to 180° , as indicated in red, and causing a strong emission enhancement.

in the thin film's absorption. The experimental reflection data acquired with an FS5 spectrofluorometer at different probe wavelengths and showing the end phase of ethanol evaporation, is presented in **Figure 6.28a**. At 260 and 350 nm, that correspond to anthracene excitations with transition dipole moments along the long and short molecular axis,³⁰² the reflection signal clearly increases right before the thin film turns dry – highly resembling the strong PL turn-on phase observed earlier in **Figure 6.17a**. This behavior precisely matches the expectation expressed above for a collective realignment of anthracene rotors inside the MOF. For 300 and 550 nm probing wavelengths at which the linker absorption is much weaker (**Figure 6.19b**), the reflection modulation before turning dry is reduced to a sudden jump from higher to lower absorption. This matches the characteristic of the pure Si, shown in **Figure 6.28b**, excluding an effect not related to the MOF thin film causing the peak in reflection before total drying.

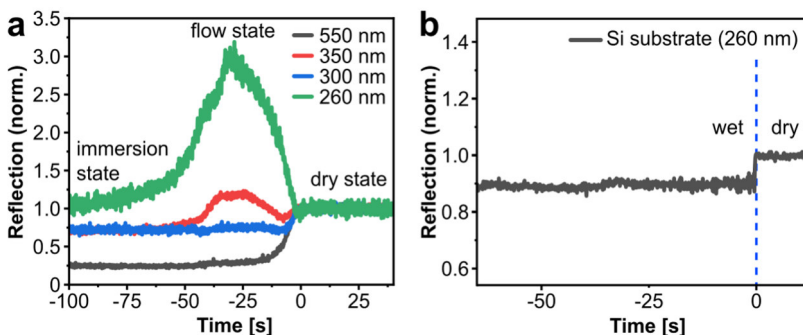


Figure 6.28. Reflection of Zn-ADC-DABCO on Si during ethanol evaporation. **a)** Reflection of Zn-ADC-DABCO thin film on a Si substrate at different wavelengths as indicated. **b)** Reflection of a bare Si substrate for reference. The individual reflection profiles have been normalized to their dry state level and shifted along the time axis such that their transitions to the dry state coincide. For wavelengths which correspond to the longitudinal and transverse transition dipole moments of anthracene (260 and 350 nm), there is a strong reflection increase shows up right before the ethanol has evaporated completely. For wavelengths with low ADC absorption (300 and 550 nm), the reflection signal resembles the bare Si reference measurement.

To assess the possibility for such a proposed rotation of the ADC linkers in a simulation, DFT calculations have been conducted examining the ligand's potential energy in dependence of its dihedral angle by a collaboration partner at the National Center for Nanoscience and Technology, Beijing. The calculations were performed on isolated ADC molecules considering an in-phase rotation of the carboxylic groups as would be given in a MOF environment. The resulting potential energy barrier to rotation over the dihedral angle α is shown in **Figure 6.29a**. As indicated by the small inset in the top right corner, an angle α of 0° (or 180°) would indicate parallel anthracene-carboxylate alignment. The simulation reveals a plateau region for α ranging from approximately 50 to 130° in which the linkers can rotate with almost no change in potential energy. At higher (or lower) angles towards a parallel alignment of anthracene unit and carboxylic groups, however, there is a steep increase towards a barrier to full rotation of $\sim 140 \text{ kJ mol}^{-1}$. These obtained results are in line with values in the literature,³⁰² and indicate that the linker can be easily rotated within a certain range of movement. Based on this model data, a rigidification of the linker in the flow phase is proposed that is caused by torque of upstreaming solvent molecules on the one side and the steeply increasing potential energy barrier on the other side. The consequent suppression of vibrational modes of the linker, reducing non-radiative excited state relaxation,^{100,101,303} is a plausible cause for the luminescence turn-on effect observed in the flow phase. To a lesser but still notable extent, librational modes of the rotors could be impaired in the immersion state by solvent molecules surrounding the ADC rotors, leading to the small luminescence enhancement with respect to the dry state.¹²⁸

Emission enhancement by rigidification of the chromophore is also in line with PLQY data on pure ADC linkers in ethanol at different concentrations. While the linker exhibits a PLQY of 48 % at 10^{-4} M as mentioned earlier, the value drops to 8 % when the concentration is

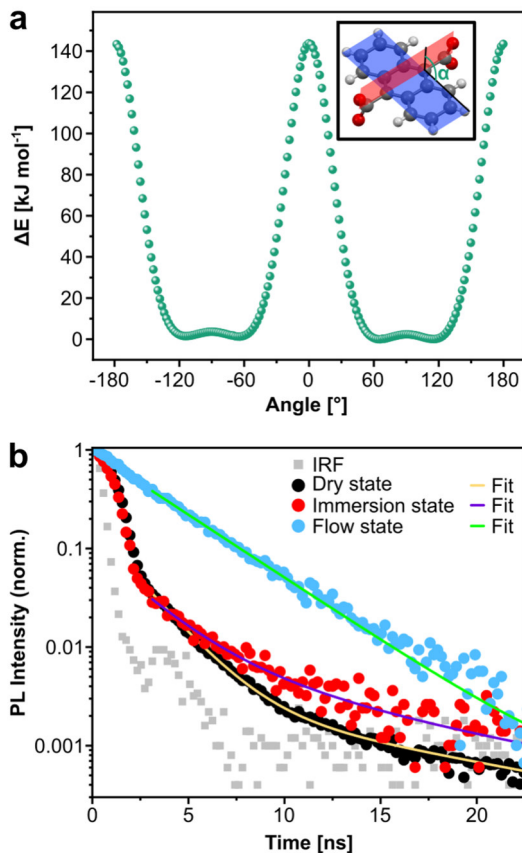


Figure 6.29. Simulated ADC linker rotation and time-resolved Zn-ADC-DABCO PL in different ethanol evaporation states. **a)** Simulated rotational barrier of an isolated ADC rotor over its dihedral angle. A dihedral angle of 0° corresponds to the carboxylic groups and the anthracene axis being parallel, as shown in the rotor sketch. Approaching such parallel alignment, there is a steep increase in the potential energy profile. **b)** PL decay profiles of Zn-ADC-DABCO in different ethanol evaporation phases. The differently colored decay curves correspond to emission states as indicated in the legend. While the MOF in the dry state and immersion state shows a bi-exponential decay profile, this changes to a mono-exponential profile in the flow state.

reduced by 100 times to 10^{-6} M. This observation could be explained by the same rigidification mechanism, this time caused by aggregation

at higher concentration and resulting steric interactions between individual ADC molecules. Therefore, an aggregation-induced emission enhancement of ADC in solution supports a PL turn-on by rigidification of the linker inside the MOF. Based on this concept, the low PLQY of the dry MOF thin film could be an indirect evidence for the sufficiently free pore volume that allows for unhindered librational motion of ADC linkers that entails preferred non-radiative deactivation pathways.

Another experimental indicator of reduced energetic disorder in the flow state supporting this hypothesis is given by time-resolved PL data measured by TCSPC on an FS5 spectrofluorometer. **Figure 6.29b** depicts the PL intensities over time of the Zn-ADC-DABCO emission in different ethanol evaporation phases (with fitted exponential lifetimes given in **Table 6.1**). The PL decay in the dry and immersion state exhibits a bi-exponential characteristic signalling different radiative deactivation channels of the excited fluorophores. This changes in the flow state, where the deactivation mechanism seems to be simplified, only showing a mono-exponential decay profile.

As the measurements of the excited state lifetime in the different evaporation phases was not straight-forward, a more detailed explanation of the procedure is given. In order to record TCSPC data of the MOF thin film in the flow phase and immersion phases, their individual time durations needed to be artificially extended. To keep the sample in the flow state for a longer period of time, after applying an ethanol droplet to the substrate surface, right with the onset of the strong luminescence turn-on, it was covered with a quartz substrate and sealed around the edges by a Teflon band. With the enclosure applied to the thin film at this moment, the solvent molecules have already created the vertical upstreaming channels inside the MOF pores but are hindered from being released at the surface (or at least

Table 6.1. Fitted lifetimes of Zn-ADC-MOF and ADC monomer PL decay. The lifetimes were obtained from mono-exponential (flow state and monomer in solution) and bi-exponential (dry state and immersion state) tail fitting.

ADC emission phase	Short lifetime (weight)	Long lifetime (weight)
MOF dry state	1.89 ns (98 %)	12.63 ns (2 %)
MOF immersion state	2.32 ns (89 %)	8.54 ns (11 %)
MOF flow state	3.39 ns	-

significantly slowed down). With this approach, the thin film could be held in the bright emission phase for several minutes, allowing for the TCSPC measurement to be executed. In a similar manner, the sample was kept for a prolonged time in the immersion phase, by being situated inside a flat-lying, open quartz cuvette (with a ground 1 cm-by-1 cm ground area) notably slowing down evaporation of the solvent from the film.

The separation between neighboring linkers in the flow state is large enough to suppress direct coupling between molecular orbitals. On the other hand, resonant energy transfer among adjacent anthracene units should still be able to occur within the MOF and should be enhanced in case of close to parallelly aligned rotors in the flow state. This has been tested by fluence-dependent PL measurements of Zn-ADC-DABCO MOF comparing the PL peak intensity in the dry state and flow state, shown in **Figure 6.30**. While the dry state PL intensity linearly increases with the exciton density, the flow state PL shows a sublinear profile. This points towards enhanced quenching at higher fluences in the flow state caused by improved exciton mobility leading to exciton-exciton annihilation. The experimental flow state data was fitted based on the one-dimensional exciton diffusion model from Oldenburg *et al.* introduced in **Equation 2.36**,¹⁰³ according to the anisotropic energy transfer between neighboring linkers inside the layer-pillar MOF. This resulted in a fitting parameter $p = L_{1D}R_0^2$ of

$\sim 1.61 \cdot 10^{-18} \text{ cm}^3$. Based on a MOF film thickness of 50 nm, the spectral overlap between Zn-ADC-DABCO absorption and its flow state emission spectra ($2.77 \cdot 10^{-11} \text{ cm}^6 \text{ mol}^{-1}$), and estimated values for refractive index (1.5, based on similar MOFs in the literature)³⁰⁴, orientational factor (1, for parallel anthracene alignment), PLQY (50 %, based on dry state PLQY times PL enhancement factor) an approximate Förster radius of 3.7 nm was estimated according to **Equation 2.31**. Together with the found fitting parameter, this leads to an estimated 1D diffusion length of $\sim 120 \text{ nm}$.

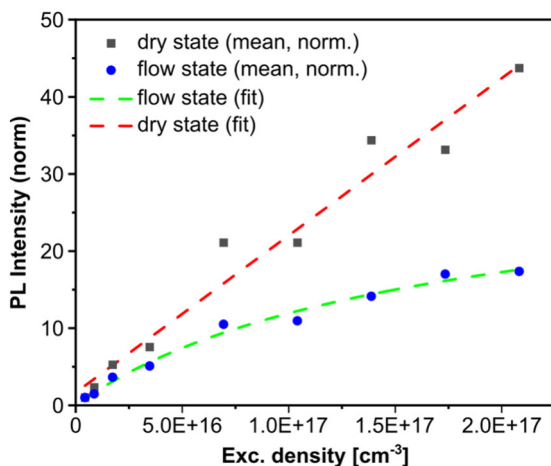


Figure 6.30. Fluence-dependent PL of Zn-ADC-DABCO. PL intensity in dry state (black) and flow state (blue) over exciton density. While the dry state emission scales linearly with the excitation, the flow state shows a sublinear dependence. The sublinear behavior points towards PL quenching by exciton-exciton annihilation that at higher excitation densities that could be explained by an enhanced exciton mobility in the flow state. The PL intensities shown are mean values from three ethanol evaporation experiments done for each exciton density. The presented data points were measured in an upwards and downwards scan of the exc. density, taking every second data check for a potential change over time. In fact, a slight decay of the emission around 430 nm was observed over time. This is in line with the observations shown in Figure 6.20.

The fluence-dependent PL measurements confirm notable differences in excited state mobility between flow state and dry state and thereby support a collective alignment of ADC rotors in the luminescence turn-on phase. In summary, the presented experimental and simulation data strongly support the hypothesis of a rotation of ADC linkers in the flow phase that changes their photoluminescent properties.

6.6. Proof-of-concept Demonstrator

As a final part of this investigation, a prototypical application of the Zn-ADC-DABCO MOF thin film as volatile solvent flow indicator was demonstrated by coating a 4 Å molecular sieve using the drop-casting method. The MOF layer on the surface of the spherical sieve provides an optical indication of methanol evaporation by a blue emission visible by eye, shown in the image series in **Figure 6.31**. Here, the sorption and release of methanol is recorded under a 254 nm lamp. To monitor the luminescence and sorption state, the upper row shows the coated sieve with the room lighting turned on, and the lower row with the lighting switched on. After initial exposure of the sieve to the solvent (at 0 s), a distinct glowing pattern emerges on the sphere's surface in the form of a ring around the sieve that is moving towards the top and then converging into a bright spot at the top. This behavior points towards the emergence preferential flow channels building inside the molecular sieve, similar to the behavior of fluids in other porous materials.^{305,306} The emission at the top persists for several minutes while the sieve appears already dry on the outside (bottom **Figure 6.31f**) before vanishing and thereby indicating the decline of solvent release from the sieve's interior. The proof-of-concept application shows the potential of the MOF thin film as a functional coating that can be applied to a surface for a visual indication of solvent flow in real-time. The potential for a further development into a full flow sensor will be further elucidated in the

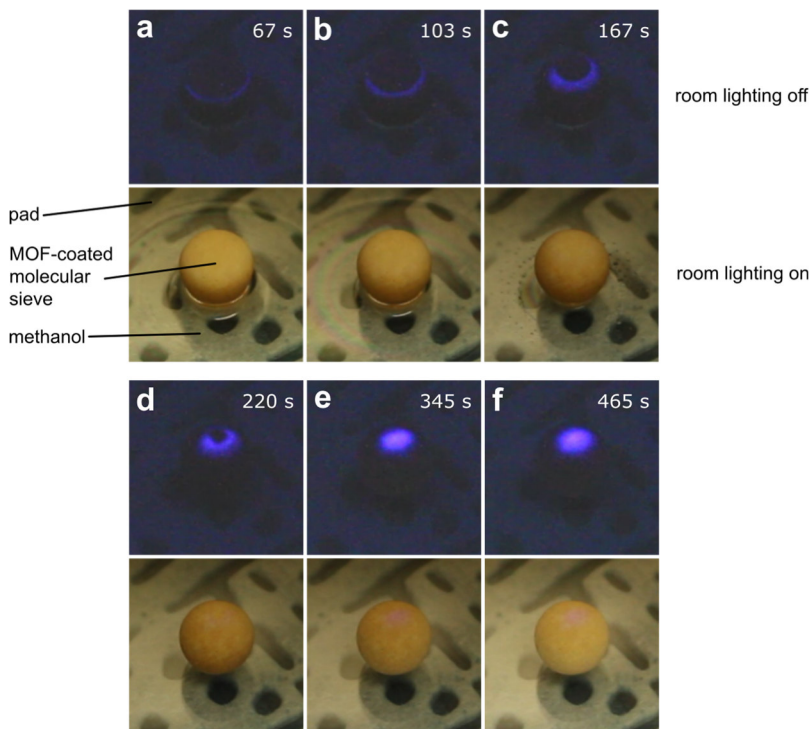


Figure 6.31. Proof-of-concept application for solvent flow indication by Zn-ADC-DABCO coating. **a) – f)** Emission of the MOF coating on a spherical 4 Å molecular sieve during soaking and release of methanol. The coated sieve is situated in a petri dish on an underlying pad and illuminated by a 254 nm lamp. Top and bottom row photos show the same situation with room lighting switched off and on. The time stamps show the time elapsed since the first exposure of the sieve to the solvent. The emissive area migrating towards the top of the sieve reports preferred regions of solvent release. The apical emission stays for several minutes after the sieve appears dry already from the outside and ceases after approximately half an hour.

outlook in **Section 7.2**. In contrast to similar nanoscale flow sensors reported in the literature that are based on integrated field effect transistors,^{307,308} the MOF-based coating does not have the need for electronic parts or a voltage supply and would therefore exhibit a much-reduced complexity of implementation. Furthermore, it does not rely on the use of marker molecules such as, for example,

fluorescent labels inside a liquid that could be used to optically monitor its passage through porous materials. If applied on top of a suitable membrane, the MOF coating could be used to monitor the membrane's performance and identify clogged regions by spatially resolved evaluation of the PL response. Other potential areas of applications for a nanoscale flow sensor coating could be tracking the flow of electrolyte through porous electrodes in battery or fuel cell development or optimizing heat management in microporous cooling systems.

6.7. Conclusion

In the final results chapter of the thesis, a simple drop-casting method to generate a Zn-ADC-DABCO layer-pillar MOF thin film with preferred orientation that holds chromophores capable of rotational motion inside the lattice. Guided by GIWAXS-based structural analysis, the influence from varying diverse synthesis parameters on the average orientation of crystallites was tested which allowed the determination of synthetic conditions yielding the lowest angular deviation of crystallites from the targeted orientation. The best results were achieved for a 0.15 mM concentration of all precursors in a common growth solution that is dropped onto a substrate heated to a mild elevated temperature of 50 °C. The preferential crystallite orientation along the <001> crystal lattice direction normal to the substrate plane was shown to be present on multiple different surfaces showing the wide applicability of the synthesis approach. Based on these results, a two-part thin film formation mechanism was suggested comprising surface-initiated crystallite growth and integration of sedimented crystal platelets forming inside the growth solution droplet. In addition to Zn-ADC-DABCO, the same synthesis was demonstrated to also yield oriented thin films in case of the isorecticular BPy-based MOF. In these fabricated thin film materials containing luminescent molecular rotors, a remarkable PL turn-on effect was discovered during the evaporation of solvents from the

porous structures visibly enhancing the emission by a factor of ~50 times. Detailed examination of the changing optical properties during this process including absorption and excited state dynamics provided experimental evidence of a collective change of the rotational state of ADC inside the MOF triggered by the volatile flow of solvent leaving its pores. In a proof-of-concept application, a Zn-ADC-DABCO MOF coating enabled the visual indication of methanol release from a molecular sieve in real-time. This new type of method utilizing dynamic realignment of movable linkers in MOFs to report solvent transport will pave the way for new nanoscale sensing applications in the future.

7. Conclusion and Outlook

7.1. Conclusion

This thesis demonstrated how detailed structural characterization of MOF thin films on a laboratory-scale using GIWAXS can be achieved and how this can majorly improve 1) quality of synthesis outcome, 2) leverage understanding of structural formation mechanisms, and 3) development of new fabrication routes. This was shown on specific systems like UiO and Zn-based stacked layer MOFs thin films created from different synthesis methods. Moreover, a novel effect in a layer-pillar MOF holding luminescent rotor linkers was presented that leads to a significant modulation of the thin film PL triggered by molecular rotation in response to directional solvent flow inside the pores.

In the first results part (**Chapter 4**), a workflow for GIWAXS measurements in a laboratory environment was presented that allowed for the quantitative analysis of oriented vs. non-oriented crystallite moieties in MOF thin films. Using this technique, UiO thin films created using a vapor-assisted conversion method from the literatures were analyzed. Probing the obtained structures as a whole and also with depth-resolution allowed to derive the structural make-up, often showing a unoriented 3D powder structure on top of an oriented 2D powder bottom layer. These insights pointing towards increased homogeneous nucleation towards the end of the thin film formation allowed to adjust synthetic conditions aiming to prevent such effects. This enabled an improvement of the fraction of crystallites in the desired 2D texture from 4 % to 95 %. By applying the synthesis procedure successively with an oriented UiO-66 bottom layer serving as a substrate for a UiO-67 top layer a UiO heterostructure was achieved. Depth-dependent GIWAXS analysis to quantify crystallite fractions confirmed the formation of a multilayer structure with a high percentage of crystallites with the 2D powder

Conclusion and Outlook

texture in bottom (83 %) and top layer (> 94 %). This showcase of GIWAXS-guided synthesis adaptation is anticipated to stimulate the more wide-spread use of this approach to optimize fabrication protocols leading the way to new standards in MOF thin film production.

After demonstrating the quantification of different textures inside one type of thin film, the second results part (**Chapter 5**) focusses on the identification of unknown crystalline thin films including multiple phases in one thin film. Target of the investigation were Zn-based metal-organic thin films created by layer-by-layer spin-coating that deviate in part strongly from analogously produced Cu-based structures. Utilizing a combined approach of a detailed experimental characterization by means of GIWAXS and density functional theory calculations to arrive at structural models. With this technique multiple different types of structures could be identified, all emerging from layer-by-layer spin-coating of a Zn precursor and dicarboxylic linkers. Comparing the recorded two-dimensional diffraction patterns of all obtained structures readily points towards a major impact of the molar ratio of Zn ion to linker utilized for spin-coating precursor solutions. For an equimolar ratio, only in the case of the BPDC linker, the formation of the expected SURMOF-2 type structure was confirmed matching its Cu-analog. In the case of BDC, a different metal-hydroxide organic framework was formed. Spin-coating with a high excess of Zn^{2+} ions over the linker, always results in LZH structures that hold dicarboxylic linkers as pillars in between zinc hydroxide sheets. This was also confirmed by testing additional ligand molecules longer than BDC or BPDC. Especially the Zn-BDC structures appear very similar in out-of-plane diffraction to the initially expected SURMOF-2 and, therefore, pose the potential threat of misinterpretation if not characterized carefully. Examining further Zn^{2+} -to-BDC ratios for the spin-coating synthesis, the formation of mixed phase thin films was observed. These were clearly evident by

superimposed two-dimensional diffraction patterns containing the features of MHOF and LZH crystal phases and also additionally confirmed by analysis of their IRRA spectra. In a greater context, this establishes the clear possibility of dual product synthetic outcome from layer-by-layer spin-coating that needs to be considered in general when interpreting such thin film diffraction data. The structural findings presented in this results part pointed towards a new understanding of the structure formation process in the layer-by-layer spin-coating technique using Zn acetate dihydrate as a metal precursor. The new interpretation involves the formation of Zn hydroxy acetate basis layer in each metal deposition step which is then transformed into different structures depending on the relative amount of linker added in the following spin-coating step. Finally, this chapter showcased how chromophores situated in different structural environments notably change their photoluminescent properties, in the case of bi-phasic thin films even reflecting different fractions of the two different crystalline components. Based on these examples, thin film photoluminescence could even be used to provide quick structural feedback immediately after synthesis visible by eye.

Making use of the earlier established GIWAXS measurement and analysis workflow, the final results part (**Chapter 6**) deals with an oriented MOF thin film based on Zn, ADC and DABCO in which the chromophore can perform unhindered rotational motion. To produce the layer-pillar MOF architecture, a simple one-step drop-casting method was developed. Synthesis optimization was performed with a GIWAXS-based figure-of-merit using a similar approach as in the earlier case to determine different shares of textures in UiO thin films – this time to evaluate the average quality of a desired texture probing the angular deviation of crystallites from the perfect targeted orientation. Based on these values, the influence of different synthetic conditions could be determined and optimized, showing that highest quality thin films are obtained for 0.15 mM concentration

Conclusion and Outlook

for all precursors contained in growth solution droplet applied to a substrate heated to 50 °C. Based on the insights gained from the structural characterization under many different synthesis conditions, an oriented thin film formation mechanism was concluded that comprises a mixture of surface-initiated layer growth and integration of crystallite platelets forming throughout the growth solution droplet volume. A somewhat general applicability of this drop-casting approach was hinted at by achieving similar results when exchanging the pillar molecule DABCO for the longer BPy. Investigating the thin film luminescence during the evaporation of solvent from their pore channels, in both DABCO- and BPy-based systems a remarkable luminescence turn-on effect was discovered. Right before the thin films turn completely dry, their emission is enhanced ~50 times, leading to a uniform glow visible by eye. By detailed studying of the changing optical properties during the different phases of solvent evaporation, the luminescence turn-on effect could be ascribed to the collective upwards rotation of anthracene units in response to the solvent upstream through the MOF's pores. This effect never reported before has the potential to open a new class of future nanoscale devices to report liquid flow.

To summarize, this thesis aimed to contribute to central aspects in the development of new MOF thin film materials. The demonstrated lab-scale GIWAXS measurement and analysis procedures has proven helpful to improve structural understanding of fabricated materials on a day-to-day basis. Utilizing this technique led to optimization of synthetic protocols involving many different fabrication methods for higher quality MOF thin films. Previously not understood differences of Zn-based structures expected to resemble their Cu-based analogs have been recognized and identified using a synergistic approach of GIWAXS analysis and theoretical modeling. Finally, a highly novel application of molecular rotors inside a pillar-layer has been identified and demonstrated.

7.2. Outlook

To provide some guidance towards further developments building on top of the topics dealt with in this thesis, proceeding thoughts are given below grouped by different research directions:

Integrated flow sensors

The discovery of a solvent flow indication mechanism provides an exciting foundation for the future development for sensing devices. In order to further develop the molecular system into a full sensor, typical technical requirements need to be met such as linearity, accuracy, sensitivity, limit of detection or stability. In the following, these criteria and possible ways of how to meet them shall be discussed. To test the linearity and accuracy of the MOF coating's photoluminescent signal in response to a varying amount of solvent volume streaming through its pores, the experiments done already based on different applied solvent volumes can be developed further. Using a highly sensitive balance such as a quartz crystal microbalance to monitor the mass of solvent evaporating from the MOF while simultaneously recording the PL of the thin film would allow to investigate the direct relation between leaving solvent volume and PL response. This can be developed even further if the QCM system is operated at different temperatures, providing information about the influence of evaporation speed and, therewith, solvent flow rate. Since the flow indication mechanism is currently understood as a gate-opening effect that either can or cannot be triggered, a linearly changing response towards different volumes of solvent moving through the MOFs pores would be understood as a simultaneous flow through an increasing number of pore channels. Another approach in the current development would be the integration of the MOF coating on top of membranes, equipping them with the ability to report fluid passage in real-time. In this scenario, ideally, the pore structure of the membrane should be matched in size with the one of the MOF coating

Conclusion and Outlook

to allow for a liquid flow of similar scale through both layers. By controlling the flow through the membrane in a microfluidic measurement setup, the sensitivity and the limit of detection of the flow sensing could be measured. The current physical understanding would suggest the need for a certain minimum pressure that needs to be applied for the solvent molecules to force open the chromophore gates which would then dictate the detection limit of a minimal flow. The sensitivity then depends on the number of parallel opened MOF pore channels in response to variations in the flow rate. By operating such a microfluidic system for multiple cycles and over extended periods of time, finally, the stability of the sensor coating can be tested. Development beyond these considerations can then involve, for example, investigating and enhancing the long-term stability which could be approached by introducing a mixture of different metal ions in the SBUs such as Zn and Cu. Another opportunity is the adjustment of flow channel dimensions in the MOF to generate flow indicator/sensor coatings tailored to different molecular kinetic diameters. This would necessitate the incorporation of rotor linkers of different length. Linkers worth exploring for that matter would be for example diphenyl anthracene- or diphenyl pentacene-based dicarboxylic acids, as depicted in **Figure 7.1a** and **Figure 7.1b**.

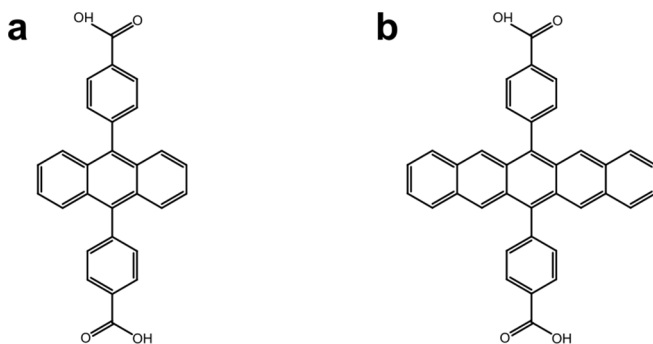


Figure 7.1. Longer rotor linkers for increased pore dimensions in the MOF system. **a)** Diphenyl anthracene-dicarboxylic acid. **b)** Diphenyl pentacene-dicarboxylic acid.

UiO multilayer sensors

The demonstration of textured UiO heterostructures is a promising step towards multilayer sensing architectures. Stacked sensor architectures with multiple active levels open up a multitude of advanced applications: Different linkers within different layers offer multifunctionality offering the possibility to probe for various analytes at the same time. Utilizing gradually changing scales of porosity by incorporation of differently sized linkers can thereby lead to a selective pre-filtration whereby outer layers can prevent certain molecules from interfering with detection events taking place at deeper layers. An advanced potential optical application could be the amplification of a photoluminescent sensing signal created at the bottom layer of a MOF multilayer structure that is then amplified by the layers above. This could be an approach to enhance analyte detection limits. One possible implementation of an amplification mechanism could be the usage of stimulated emission cascades with high PLQY reporter linkers used in the top layers. As immediate next steps towards such future applications based on UiO heterostructures, there are two major challenges that need to be solved. The first challenge is to realize the creation of double-layer structures with arbitrary combinations of dicarboxylic linkers to allow for a later adjustment of the sensor stack to any desired functionality by using dicarboxylic linker with specialized side groups. This can involve for example linkers containing certain functional groups influencing the photophysical properties of the UiO MOF or that can be used, for example, as catalytic sites. Here, one approach could be the direct synthesis of MOF layers already containing the desired linkers. Another possibility could be the post-synthetic exchange of linkers.^{309,310} If such a growth procedure is pursued, two questions become important: Firstly, whether the exchange of longer ligands for example located in the top layer would also affect the bottom layer containing smaller ligands; secondly, whether a ligand exchange can

Conclusion and Outlook

be performed without a loss of thin film texture. The second major challenge would be the realization of more complex heterostructures including three or more layers. Hereby, an investigation is relevant on which types of different underlying (crystalline) substrates growth of UiO layers on top is possible to achieve.

Functional LZH thin films

The ability to rapidly generate thin films of LZHs holding various dicarboxylic anions provides a versatile platform for functional coatings besides MOFs. Thereby, LZH thin films can exhibit unique benefits over MOFs such as enhanced longevity due to a certain structural flexibility without total loss of structure (as shown by the dehydration experiment) and therefore potentially higher resistance to mechanical stress. Furthermore, LZH have improved chemical stability against environmental moisture which is an often-occurring issue for MOFs. Two properties of LZH materials are especially interesting regarding their functional versatility. This thesis has shown that luminescent chromophores incorporated in LZH structures retain their emissive behavior (even though it is altered with respect to the isolated ligand) without being quenched. The second interesting finding is the soaking of water from ambient air and integration into the molecular structure. This means that the material is capable of sorption of molecules from the surrounding atmosphere. Exploiting this property, incorporation of specialized organic ligands that respond to the presence of certain atmospheric molecules inside the structure with a change of their emission spectrum can facilitate a luminescent sensor coating. Another potential application are thin films with designer absorption properties. Layer-by-layer deposition can thereby conveniently control the film thickness and intercalation of specifically chosen linker molecules or even combinations of several linker molecules with the same length determine the resulting absorption spectrum. Well suited for testing such an application

would be the usage of aromatic dicarboxylic acids with different levels of conjugation (such as BDC, NDC, ADC for example), or different types of porphyrin-based carboxylic acids, which have a common length but different optical properties.^{246,248} An important question to solve in the future thereby is whether the high orientation of the initial zinc hydroxy acetate basis can be retained, as was observed in the case of the small BDC linkers, also for longer or more bulky linker molecules. A useful linker with intermediate dimensions to start such a detailed investigation could be the 2,6-NDC molecule.

MOF thin film formation mechanisms

A topic that is essential for the rapid development and any new MOF thin film architecture is a sound understanding of structure formation mechanisms. The conclusion drawn in this thesis that layer-by-layer spin-coating based on Zn acetate dihydrate as a metal precursor creates Zn hydroxy acetate films, poses the question whether the same type of basis layers could also be formed in similar deposition techniques such as spray-coating or dip-coating. The potential formation of a basis layer that is converted successively instead of metal SBU seeding is important to clarify in order to control and optimize the growth of thin films, for example in terms of uniform thickness, texture and prevention of island-growth. A further question is then, whether the same applies when performing a Cu-based synthesis. In addition to GIWAXS analysis, techniques such as locally resolved IR spectroscopy could provide useful insights to improve understanding of structure formation mechanisms.³¹¹ Moreover, the simple drop-casting synthesis in ambient conditions demonstrated for ADC-containing layer-pillar MOFs would be very attractive to adapt also to architectures containing different ligands. Initial tests performed with less bulky linkers in the form of BDC and NDC did not yield comparable results, supporting the hypothesis that steric protection of the Zn-pillar bond from water is essential for the thin

Conclusion and Outlook

film formation. Drop-casting synthesis under anhydrous conditions would be a reasonable direction worth investigating.

8. References

1. Hoskins, B. F. & Robson, R. Infinite Polymeric Frameworks Consisting of Three Dimensionally Linked Rod-like Segments. *J. Am. Chem. Soc.* **111**, 5962–5964 (1989).
2. Hoskins, B. F. & Robson, R. Design and Construction of a New Class of Scaffolding-like Materials Comprising Infinite Polymeric Frameworks of 3D-Linked Molecular Rods. A Reappraisal of the $\text{Zn}(\text{CN})_2$ and $\text{Cd}(\text{CN})_2$ Structures and the Synthesis and Structure of the Diamond-Related Framework. *J. Am. Chem. Soc.* **112**, 1546–1554 (1990).
3. O. M. Yaghi, Guangming Li & Hailian Li. Selective binding and removal of guests in a microporous metal-organic framework. *Nature* **378**, 703–706 (1995).
4. Kondo, M., Yoshitomi, T., Seki, K., Matsuzaka, H. & Kitagawa, S. Three-Dimensional Framework with Channeling Cavities for Small Molecules: $\{[\text{M}_2(4,4'\text{-bpy})_3(\text{NO}_3)_4] \cdot x\text{H}_2\text{O}\}_n$ ($\text{M} = \text{Co}, \text{Ni}, \text{Zn}$). *Angew. Chemie (International Ed. English)* **36**, 1725–1727 (1997).
5. Livage, C., Egger, C. & Férey, G. Hybrid open networks (MIL 16): Synthesis, crystal structure, and ferrimagnetism of $\text{Co}_4(\text{OH})_2(\text{H}_2\text{O})_2(\text{C}_4\text{H}_4\text{O}_4)_3 \cdot 2\text{H}_2\text{O}$, a new layered cobalt(II) carboxylate with 14-membered ring channels. *Chem. Mater.* **11**, 1546–1550 (1999).
6. The Cambridge Crystallographic Data Centre. How many MOFs are there in the CSD?
<https://www.ccdc.cam.ac.uk/support-and-resources/support/case/?caseid=46cf9882-92de-ed11-96a2-00505695c114> (2024).
7. Holst, J. R. & Cooper, A. I. Ultrahigh surface area in porous solids. *Adv. Mater.* **22**, 5212–5216 (2010).

References

8. Farha, O. K., Eryazici, I., Jeong, N. C., Hauser, B. G., Wilmer, C. E., Sarjeant, A. A., Snurr, R. Q., Nguyen, S. T., Yazaydin, A. Ö. & Hupp, J. T. Metal-organic framework materials with ultrahigh surface areas: Is the sky the limit? *J. Am. Chem. Soc.* **134**, 15016–15021 (2012).
9. Hönicke, I. M., Senkovska, I., Bon, V., Baburin, I. A., Bönisch, N., Raschke, S., Evans, J. D. & Kaskel, S. Balancing Mechanical Stability and Ultrahigh Porosity in Crystalline Framework Materials. *Angew. Chemie - Int. Ed.* **57**, 13780–13783 (2018).
10. Chen, Z., Kirlikovali, K. O., Idrees, K. B., Wasson, M. C. & Farha, O. K. Porous materials for hydrogen storage. *Chem* **8**, 693–716 (2022).
11. Nazir, G., Rehman, A., Hussain, S., Aftab, S., Heo, K., Ikram, M., Patil, S. A. & Aizaz Ud Din, M. Recent Advances and Reliable Assessment of Solid-State Materials for Hydrogen Storage: A Step Forward toward a Sustainable H₂ Economy. *Adv. Sustain. Syst.* **6**, 1–34 (2022).
12. Tao, Y. R. & Xu, H. J. A critical review on potential applications of Metal-Organic frameworks (MOFs) in adsorptive carbon capture technologies. *Appl. Therm. Eng.* **236**, (2024).
13. Trickett, C. A., Helal, A., Al-Maythalony, B. A., Yamani, Z. H., Cordova, K. E. & Yaghi, O. M. The chemistry of metal-organic frameworks for CO₂ capture, regeneration and conversion. *Nat. Rev. Mater.* **2**, 1–16 (2017).
14. Sutton, A. L., Mardel, J. I. & Hill, M. R. Metal-Organic Frameworks (MOFs) As Hydrogen Storage Materials At Near-Ambient Temperature. *Chem. - A Eur. J.* **202400717**, 1–11 (2024).
15. Sengupta, D., Melix, P., Bose, S., Duncan, J., Wang, X., Mian, M. R., Kirlikovali, K. O., Joodaki, F., Islamoglu, T., Yildirim, T., Snurr, R. Q. & Farha, O. K. Air-Stable Cu(I) Metal-Organic

- Framework for Hydrogen Storage. *J. Am. Chem. Soc.* **145**, 20492–20502 (2023).
16. Demir, H., Aksu, G. O., Gulbalkan, H. C. & Keskin, S. MOF Membranes for CO₂ Capture: Past, Present and Future. *Carbon Capture Sci. Technol.* **2**, 100026 (2022).
 17. Ding, M., Flaig, R. W., Jiang, H. L. & Yaghi, O. M. Carbon capture and conversion using metal-organic frameworks and MOF-based materials. *Chem. Soc. Rev.* **48**, 2783–2828 (2019).
 18. Xiang, S., He, Y., Zhang, Z., Wu, H., Zhou, W., Krishna, R. & Chen, B. Microporous metal-organic framework with potential for carbon dioxide capture at ambient conditions. *Nat. Commun.* **3**, (2012).
 19. Caskey, S. R., Wong-Foy, A. G. & Matzger, A. J. Dramatic tuning of carbon dioxide uptake via metal substitution in a coordination polymer with cylindrical pores. *J. Am. Chem. Soc.* **130**, 10870–10871 (2008).
 20. Banerjee, R., Furukawa, H., Britt, D., Knobler, C., O’Keeffe, M. & Yaghi, O. M. Control of pore size and functionality in isorecticular zeolitic imidazolate frameworks and their carbon dioxide selective capture properties. *J. Am. Chem. Soc.* **131**, 3875–3877 (2009).
 21. Lin, J. Bin, Nguyen, T. T. T., Vaidhyanathan, R., Burner, J., Taylor, J. M., Durekova, H., Akhtar, F., Mah, R. K., Ghaffari-Nik, O., Marx, S., Fylstra, N., Iremonger, S. S., Dawson, K. W., Sarkar, P., Hovington, P., Rajendran, A., Woo, T. K. & Shimizu, G. K. H. A scalable metal-organic framework as a durable physisorbent for carbon dioxide capture. *Science (80-.).* **374**, 1464–1469 (2021).
 22. Hanikel, N., Prévot, M. S. & Yaghi, O. M. MOF water harvesters. *Nat. Nanotechnol.* **15**, 348–355 (2020).
 23. Kim, H., Yang, S., Rao, S. R., Narayanan, S., Kapustin, E. A.,

References

- Furukawa, H., Umans, A. S., Yaghi, O. M. & Wang, E. N. Water harvesting from air with metal-organic frameworks powered by natural sunlight. *Science* (80-.). **356**, 430–434 (2017).
24. Fuchs, A., Knechtel, F., Wang, H., Ji, Z., Wuttke, S., Yaghi, O. M. & Ploetz, E. Water Harvesting at the Single-Crystal Level. *J. Am. Chem. Soc.* **145**, 14324–14334 (2023).
25. Fu, Z. & Xu, G. Crystalline, Highly Oriented MOF Thin Film: the Fabrication and Application. *Chem. Rec.* **17**, 518–534 (2017).
26. Liu, X., Demir, N. K., Wu, Z. & Li, K. Highly Water-Stable Zirconium Metal-Organic Framework UiO-66 Membranes Supported on Alumina Hollow Fibers for Desalination. *J. Am. Chem. Soc.* **137**, 6999–7002 (2015).
27. Sorribas, S., Gorgojo, P., Téllez, C., Coronas, J. & Livingston, A. G. High flux thin film nanocomposite membranes based on metal-organic frameworks for organic solvent nanofiltration. *J. Am. Chem. Soc.* **135**, 15201–15208 (2013).
28. Li, Y. S., Bux, H., Feldhoff, A., Li, G. N., Yang, W. S. & Caro, J. Controllable synthesis of metal-organic frameworks: From MOF nanorods to oriented MOF membranes. *Adv. Mater.* **22**, 3322–3326 (2010).
29. Liu, J. & Wöll, C. Surface-supported metal-organic framework thin films: Fabrication methods, applications, and challenges. *Chem. Soc. Rev.* **46**, 5730–5770 (2017).
30. Wang, S. & Wang, X. Multifunctional Metal-Organic Frameworks for Photocatalysis. *Small* **11**, 3097–3112 (2015).
31. Zhang, L., Cui, P., Yang, H., Chen, J., Xiao, F., Guo, Y., Liu, Y., Zhang, W., Huo, F. & Liu, B. Metal-organic frameworks as promising photosensitizers for photoelectrochemical water splitting. *Adv. Sci.* **3**, 1–6 (2015).
32. Ye, L., Liu, J., Gao, Y., Gong, C., Addicoat, M., Heine, T., Wöll,

- C. & Sun, L. Highly oriented MOF thin film-based electrocatalytic device for the reduction of CO₂ to CO exhibiting high faradaic efficiency. *J. Mater. Chem. A* **4**, 15320–15326 (2016).
33. Bi, S., Banda, H., Chen, M., Niu, L., Chen, M., Wu, T., Wang, J., Wang, R., Feng, J., Chen, T., Dincă, M., Kornyshev, A. A. & Feng, G. Molecular understanding of charge storage and charging dynamics in supercapacitors with MOF electrodes and ionic liquid electrolytes. *Nat. Mater.* **19**, 552–558 (2020).
34. Ye, Z., Jiang, Y., Li, L., Wu, F. & Chen, R. *Rational Design of MOF-Based Materials for Next-Generation Rechargeable Batteries. Nano-Micro Letters* vol. 13 (2021).
35. Liu, J. & Wöll, C. Surface-supported metal-organic framework thin films: Fabrication methods, applications, and challenges. *Chem. Soc. Rev.* **46**, 5730–5770 (2017).
36. Wang, L., Han, Y., Feng, X., Zhou, J., Qi, P. & Wang, B. Metal-organic frameworks for energy storage: Batteries and supercapacitors. *Coord. Chem. Rev.* **307**, 361–381 (2016).
37. Sheberla, D., Bachman, J. C., Elias, J. S., Sun, C. J., Shao-Horn, Y. & Dincă, M. Conductive MOF electrodes for stable supercapacitors with high areal capacitance. *Nat. Mater.* **16**, 220–224 (2017).
38. Nam, K. W., Park, S. S., dos Reis, R., Dravid, V. P., Kim, H., Mirkin, C. A. & Stoddart, J. F. Conductive 2D metal-organic framework for high-performance cathodes in aqueous rechargeable zinc batteries. *Nat. Commun.* **10**, 1–10 (2019).
39. Chueh, C. C., Chen, C. I., Su, Y. A., Konnerth, H., Gu, Y. J., Kung, C. W. & Wu, K. C. W. Harnessing MOF materials in photovoltaic devices: Recent advances, challenges, and perspectives. *J. Mater. Chem. A* **7**, 17079–17095 (2019).
40. Ryu, U. J., Jee, S., Park, J. S., Han, I. K., Lee, J. H., Park, M. &

References

- Choi, K. M. Nanocrystalline Titanium Metal-Organic Frameworks for Highly Efficient and Flexible Perovskite Solar Cells. *ACS Nano* **12**, 4968–4975 (2018).
41. Lee, J., Tsvetkov, N., Shin, S. R. & Kang, J. K. Fast Charge Transfer and High Stability via Hybridization of Hygroscopic Cu-BTC Metal-Organic Framework Nanocrystals with a Light-Absorbing Layer for Perovskite Solar Cells. *ACS Appl. Mater. Interfaces* **14**, 35495–35503 (2022).
42. Vinogradov, A. V., Zaahe-Hertling, H., Hey-Hawkins, E., Agafonov, A. V., Seisenbaeva, G. A., Kessler, V. G. & Vinogradov, V. V. The first depleted heterojunction TiO₂–MOF-based solar cell. *Chem. Commun.* **50**, 10210–10213 (2014).
43. Hou, X., Pan, L., Huang, S., Wei, O. Y. & Chen, X. Enhanced Efficiency and stability of Perovskite Solar Cells using Porous Hierarchical TiO₂ Nanostructures of Scattered Distribution as Scaffold. *Electrochim. Acta* **236**, 351–358 (2017).
44. Lee, C. C., Chen, C. I., Liao, Y. Te, Wu, K. C. W. & Chueh, C. C. Enhancing Efficiency and Stability of Photovoltaic Cells by Using Perovskite/Zr-MOF Heterojunction Including Bilayer and Hybrid Structures. *Adv. Sci.* **6**, (2019).
45. Chang, T. H., Kung, C. W., Chen, H. W., Huang, T. Y., Kao, S. Y., Lu, H. C., Lee, M. H., Boopathi, K. M., Chu, C. W. & Ho, K. C. Planar Heterojunction Perovskite Solar Cells Incorporating Metal-Organic Framework Nanocrystals. *Adv. Mater.* **27**, 7229–7235 (2015).
46. Arora, H., Dong, R., Venanzi, T., Zscharschuch, J., Schneider, H., Helm, M., Feng, X., Cánovas, E. & Erbe, A. Demonstration of a Broadband Photodetector Based on a Two-Dimensional Metal–Organic Framework. *Adv. Mater.* **32**, (2020).
47. Tian, Y. B., Vankova, N., Weidler, P., Kuc, A., Heine, T., Wöll,

- C., Gu, Z. G. & Zhang, J. Oriented Growth of In-Oxo Chain Based Metal-Porphyrin Framework Thin Film for High-Sensitive Photodetector. *Adv. Sci.* **8**, 1–8 (2021).
48. Tang, Y., Wu, H., Cao, W., Cui, Y. & Qian, G. Luminescent Metal–Organic Frameworks for White LEDs. *Adv. Opt. Mater.* **9**, 1–14 (2021).
49. Sun, C. Y., Wang, X. L., Zhang, X., Qin, C., Li, P., Su, Z. M., Zhu, D. X., Shan, G. G., Shao, K. Z., Wu, H. & Li, J. Efficient and tunable white-light emission of metal-organic frameworks by iridium-complex encapsulation. *Nat. Commun.* **4**, 1–8 (2013).
50. Lustig, W. P., Shen, Z., Teat, S. J., Javed, N., Velasco, E., O’Carroll, D. M. & Li, J. Rational design of a high-efficiency, multivariate metal-organic framework phosphor for white led bulbs. *Chem. Sci.* **11**, 1814–1824 (2020).
51. Müller-Buschbaum, K., Beuerle, F. & Feldmann, C. MOF based luminescence tuning and chemical/physical sensing. *Microporous Mesoporous Mater.* **216**, 171–199 (2015).
52. Liu, Y., Xie, X. Y., Cheng, C., Shao, Z. S. & Wang, H. S. Strategies to fabricate metal-organic framework (MOF)-based luminescent sensing platforms. *J. Mater. Chem. C* **7**, 10743–10763 (2019).
53. Liao, Z., Xia, T., Yu, E. & Cui, Y. Luminescent metal–organic framework thin films: From preparation to biomedical sensing applications. *Crystals* **8**, (2018).
54. Hu, Z., Deibert, B. J. & Li, J. Luminescent metal-organic frameworks for chemical sensing and explosive detection. *Chem. Soc. Rev.* **43**, 5815–5840 (2014).
55. Yuan, H., Li, N., Fan, W., Cai, H. & Zhao, D. Metal-Organic Framework Based Gas Sensors. *Adv. Sci.* **9**, 1–27 (2022).
56. Haldar, R., Jakoby, M., Mazel, A., Zhang, Q., Welle, A.,

References

- Mohamed, T., Krolla, P., Wenzel, W., Diring, S., Odobel, F., Richards, B. S., Howard, I. A. & Wöll, C. Anisotropic energy transfer in crystalline chromophore assemblies. *Nat. Commun.* **9**, 1–8 (2018).
57. Nefedov, A., Haldar, R., Xu, Z., Kühner, H., Hofmann, D., Goll, D., Sapotta, B., Hecht, S., Krstić, M., Rockstuhl, C., Wenzel, W., Bräse, S., Tegeder, P., Zojer, E. & Wöll, C. Avoiding the Center-Symmetry Trap: Programmed Assembly of Dipolar Precursors into Porous, Crystalline Molecular Thin Films. *Adv. Mater.* **33**, 1–6 (2021).
58. Wan, R., Mankus, D., Lee, W. S., Lytton-Jean, A. K. R., Tisdale, W. A. & Dinca, M. Dipole-dependent waveguiding in an anisotropic metal-organic framework. *J. Am. Chem. Soc.* **145**, 19042–19048 (2023).
59. Patwardhan, S., Jin, S., Son, H. J. & Schatz, G. C. Ultrafast energy migration in porphyrin-based Metal Organic Frameworks (MOFs). *Mater. Res. Soc. Symp. Proc.* **1539**, 22–27 (2013).
60. Li, S., Chen, Z., Yang, F. & Yue, W. Emerging two-dimensional materials for analytical lab-on-chip platforms: A review of electrochemical and optical biosensor. *Microchem. J.* **194**, 109247 (2023).
61. Mansour, F. R., Hammad, S. F., Abdallah, I. A., Bedair, A., Abdelhameed, R. M. & Locatelli, M. Applications of metal organic frameworks in point of care testing. *TrAC - Trends Anal. Chem.* **172**, 117596 (2024).
62. Theyagarajan, K. & Kim, Y. J. Metal Organic Frameworks Based Wearable and Point-of-Care Electrochemical Sensors for Healthcare Monitoring. *Biosensors* **14**, (2024).
63. Zuliani, A., Khair, N. & Carrillo-Carrión, C. Recent progress of metal–organic frameworks as sensors in (bio)analytical fields:

- towards real-world applications. *Anal. Bioanal. Chem.* **415**, 2005–2023 (2023).
64. Tsai, H., Shrestha, S., Vilá, R. A., Huang, W., Liu, C., Hou, C. H., Huang, H. H., Wen, X., Li, M., Wiederrecht, G., Cui, Y., Cotlet, M., Zhang, X., Ma, X. & Nie, W. Bright and stable light-emitting diodes made with perovskite nanocrystals stabilized in metal–organic frameworks. *Nat. Photonics* **15**, 843–849 (2021).
65. Begum, S., Hassan, Z., Bräse, S., Wöll, C. & Tsotsalas, M. Metal-Organic Framework-Templated Biomaterials: Recent Progress in Synthesis, Functionalization, and Applications. *Acc. Chem. Res.* **52**, 1598–1610 (2019).
66. Birkholz, M. *Thin Film Analysis by X-Ray Scattering*. (WILEY-VCH Verlag GmbH & Co. KGaA, 2006).
67. He, B. B. *Two-dimensional X-ray Diffraction*. (John Wiley and Sons Inc, 2018).
68. Als-Nielsen, J. & McMorrow, D. *Elements of modern X-ray physics*. (Wiley, a John Wiley & Sons, Ltd. Publication, 2011).
69. Werzer, O., Kowarik, S., Gasser, F., Jiang, Z., Strzalka, J., Nicklin, C. & Resel, R. X-ray diffraction under grazing incidence conditions. *Nat. Rev. Methods Prim.* **4**, (2024).
70. Kavita, S., Alagusoundarya, M., Ramakrishna, V. V., Suresh, V., Bhatt, P., Srimathi, P., Archana, R., Kar, D., Thomas, T. & Gopalan, R. On the table-like magnetocaloric effect, microstructure and mechanical properties of $\text{La}_{0.9}\text{Fe}_{11.6}\text{Si}_{1.4}$ system. *J. Alloys Compd.* **895**, 162597 (2022).
71. Valenzano, L., Civalieri, B., Chavan, S., Bordiga, S., Nilsen, M. H., Jakobsen, S., Lillerud, K. P. & Lamberti, C. Disclosing the complex structure of UiO-66 metal organic framework: A synergic combination of experiment and theory. *Chem. Mater.* **23**, 1700–1718 (2011).

References

72. Fischer, J. C., Li, C., Hamer, S., Heinke, L., Herges, R., Richards, B. S. & Howard, I. A. GIWAXS Characterization of Metal–Organic Framework Thin Films and Heterostructures: Quantifying Structure and Orientation. *Adv. Mater. Interfaces* **10**, (2023).
73. Jiang, Z. GIXSGUI: A MATLAB toolbox for grazing-incidence X-ray scattering data visualization and reduction, and indexing of buried three-dimensional periodic nanostructured films. *J. Appl. Crystallogr.* **48**, 917–926 (2015).
74. Shao, S., Dong, J., Duim, H., ten Brink, G. H., Blake, G. R., Portale, G. & Loi, M. A. Enhancing the crystallinity and perfecting the orientation of formamidinium tin iodide for highly efficient Sn-based perovskite solar cells. *Nano Energy* **60**, 810–816 (2019).
75. Savikhin, V., Steinrück, H. G., Liang, R. Z., Collins, B. A., Oosterhout, S. D., Beaujuge, P. M. & Toney, M. F. GIWAXS-SIIRkit: Scattering intensity, indexing and refraction calculation toolkit for grazing-incidence wide-angle X-ray scattering of organic materials. *J. Appl. Crystallogr.* **53**, 1108–1129 (2020).
76. Schrode, B., Pachmayer, S., Dohr, M., Röthel, C., Domke, J., Fritz, T., Resel, R. & Werzer, O. GIDVis: a comprehensive software tool for geometry-independent grazing-incidence X-ray diffraction data analysis and pole-figure calculations. *J. Appl. Crystallogr.* **52**, 683–689 (2019).
77. Steele, J. A., Solano, E., Hardy, D., Dayton, D., Ladd, D., White, K., Chen, P., Hou, J., Huang, H., Saha, R. A., Wang, L., Gao, F., Hofkens, J., Roelofs, M. B. J., Chernyshov, D. & Toney, M. F. How to GIWAXS: Grazing Incidence Wide Angle X-Ray Scattering Applied to Metal Halide Perovskite Thin Films. *Adv. Energy Mater.* **2300760**, (2023).
78. Ogle, J., Powell, D., Amerling, E., Smilgies, D. M. & Whittaker-

- Brooks, L. Quantifying multiple crystallite orientations and crystal heterogeneities in complex thin film materials. *CrystEngComm* **21**, 5707–5720 (2019).
79. Mahmood, A. & Wang, J. L. A Review of Grazing Incidence Small- and Wide-Angle X-Ray Scattering Techniques for Exploring the Film Morphology of Organic Solar Cells. *Sol. RRL* **4**, (2020).
80. Rivnay, J., Mannsfeld, S. C. B., Miller, C. E., Salleo, A. & Toney, M. F. Quantitative determination of organic semiconductor microstructure from the molecular to device scale. *Chem. Rev.* **112**, 5488–5519 (2012).
81. Hammond, M. R., Kline, R. J., Herzog, A. A., Richter, L. J., Germack, D. S., Ro, H. W., Soles, C. L., Fischer, D. A., Xu, T., Yu, L., Toney, M. F. & DeLongchamp, D. M. Molecular order in high-efficiency polymer/fullerene bulk heterojunction solar cells. *ACS Nano* **5**, 8248–8257 (2011).
82. Roe, R.-J. *Methods of X-Ray and Neutron Scattering in Polymer Science*. (Oxford Univ. Press, 2000).
83. Allen, J. E., Yager, K. G., Hlaing, H., Nam, C. Y., Ocko, B. M. & Black, C. T. Enhanced charge collection in confined bulk heterojunction organic solar cells. *Appl. Phys. Lett.* **99**, 163301 (2011).
84. Johnston, D. E., Yager, K. G., Hlaing, H., Lu, X., Ocko, B. M. & Black, C. T. Nanostructured Surfaces Frustrate Polymer Semiconductor Molecular Orientation. *ACS Nano* **8**, 243–249 (2014).
85. Cavka, J. H., Jakobsen, S., Olsbye, U., Guillou, N., Lamberti, C., Bordiga, S. & Lillerud, K. P. A new zirconium inorganic building brick forming metal organic frameworks with exceptional stability. *J. Am. Chem. Soc.* **130**, 13850–13851 (2008).
86. Zhao, Y., Zeng, H., Zhu, X. W., Lu, W. & Li, D. Metal-organic

References

- frameworks as photoluminescent biosensing platforms: Mechanisms and applications. *Chem. Soc. Rev.* **50**, 4484–4513 (2021).
87. Lin, R. B., Liu, S. Y., Ye, J. W., Li, X. Y. & Zhang, J. P. Photoluminescent metal–organic frameworks for gas sensing. *Adv. Sci.* **3**, 1–20 (2016).
88. Köhler, A. & Bässler, H. *Electronic Processes in Organic Semiconductors*. (WILEY-VCH Verlag GmbH & Co. KGaA, 2015).
89. Valeur, B. & Berberan-Santos, M. N. *Molecular Fluorescence: Principles and Applications*. (Wiley-VCH Verlag & Co. KGaA, 2012).
90. Atkins, P. & Friedman, R. *Molecular Quantum Mechanics*. (Oxford University Press Inc., 2011).
91. Birks, J. B. *Photophysics of aromatic molecules*. (Wiley-Interscience, 1970).
92. Garci, A., Beldjoudi, Y., Kodaimati, M. S., Hornick, J. E., Nguyen, M. T., Cetin, M. M., Stern, C. L., Roy, I., Weiss, E. A. & Stoddart, J. F. Mechanical-Bond-Induced Exciplex Fluorescence in an Anthracene-Based Homo[2]catenane. *J. Am. Chem. Soc.* **142**, 7956–7967 (2020).
93. Erdemir, S. & Kocyigit, O. Anthracene excimer-based “turn on” fluorescent sensor for Cr³⁺ and Fe³⁺ ions: Its application to living cells. *Talanta* **158**, 63–69 (2016).
94. Hinoue, T., Shigenoi, Y., Sugino, M., Mizobe, Y., Hisaki, I., Miyata, M. & Tohnai, N. Regulation of π -stacked anthracene arrangement for fluorescence modulation of organic solid from monomer to excited oligomer emission. *Chem. - A Eur. J.* **18**, 4634–4643 (2012).
95. Dreuw, A., Plötner, J., Lorenz, L., Wachtveitl, J., Djanhan, J. E.,

- Brüning, J., Metz, T., Bolte, M. & Schmidt, M. U. Molecular mechanism of the solid-state fluorescence behavior of the organic pigment yellow 101 and its derivatives. *Angew. Chemie - Int. Ed.* **44**, 7783–7786 (2005).
96. Varghese, S. & Das, S. Role of molecular packing in determining solid-state optical properties of π -conjugated materials. *J. Phys. Chem. Lett.* **2**, 863–873 (2011).
97. Hong, Y., Lam, J. W. Y. & Tang, B. Z. Aggregation-induced emission. *Chem. Soc. Rev.* **40**, 5361–5388 (2011).
98. Tang, B. Z., Zhan, X., Yu, G., Sze Lee, P. P., Liu, Y. & Zhu, D. Efficient blue emission from siloles. *J. Mater. Chem.* **11**, 2974–2978 (2001).
99. Luo, J., Xie, Z., Xie, Z., Lam, J. W. Y., Cheng, L., Chen, H., Qiu, C., Kwok, H. S., Zhan, X., Liu, Y., Zhu, D. & Tang, B. Z. Aggregation-induced emission of 1-methyl-1,2,3,4,5-pentaphenylsilole. *Chem. Commun.* **18**, 1740–1741 (2001).
100. Shustova, N. B., McCarthy, B. D. & Dincă, M. Turn-on fluorescence in tetraphenylethylene-based metal-organic frameworks: An alternative to aggregation-induced emission. *J. Am. Chem. Soc.* **133**, 20126–20129 (2011).
101. Shustova, N. B., Ong, T. C., Cozzolino, A. F., Michaelis, V. K., Griffin, R. G. & Dincă, M. Phenyl ring dynamics in a tetraphenylethylene-bridged metal-organic framework: Implications for the mechanism of aggregation-induced emission. *J. Am. Chem. Soc.* **134**, 15061–15070 (2012).
102. Yadav, L. D. S. *Organic Spectroscopy*. (Springer Science+Business Media Dordrecht, 2005). doi:10.1007/978-1-4020-2575-4.
103. Oldenburg, M., Turshatov, A., Busko, D., Jakoby, M., Haldar, R., Chen, K., Emandi, G., Senge, M. O., Wöll, C., Hodgkiss, J. M., Richards, B. S. & Howard, I. A. Enhancing the

References

- photoluminescence of surface anchored metal-organic frameworks: Mixed linkers and efficient acceptors. *Phys. Chem. Chem. Phys.* **20**, 11564–11576 (2018).
104. Tamai, Y., Ohkita, H., Bente, H. & Ito, S. Exciton Diffusion in Conjugated Polymers: From Fundamental Understanding to Improvement in Photovoltaic Conversion Efficiency. *J. Phys. Chem. Lett.* **6**, 3417–3428 (2015).
 105. Lunt, R. R., Giebink, N. C., Belak, A. A., Benziger, J. B. & Forrest, S. R. Exciton diffusion lengths of organic semiconductor thin films measured by spectrally resolved photoluminescence quenching. *J. Appl. Phys.* **105**, (2009).
 106. Mikhnenko, O. V., Azimi, H., Scharber, M., Morana, M., Blom, P. W. M. & Loi, M. A. Exciton diffusion length in narrow bandgap polymers. *Energy Environ. Sci.* **5**, 6960–6965 (2012).
 107. Yost, S. R., Hontz, E., Yeganeh, S. & Van Voorhis, T. Triplet vs singlet energy transfer in organic semiconductors: The tortoise and the hare. *J. Phys. Chem. C* **116**, 17369–17377 (2012).
 108. Chen, Z., Mian, M. R., Lee, S. J., Chen, H., Zhang, X., Kirlikovali, K. O., Shulda, S., Melix, P., Rosen, A. S., Parilla, P. A., Gennett, T., Snurr, R. Q., Islamoglu, T., Yildirim, T. & Farha, O. K. Fine-tuning a robust metal-organic framework toward enhanced clean energy gas storage. *J. Am. Chem. Soc.* **143**, 18838–18843 (2021).
 109. Liu, G., Chernikova, V., Liu, Y., Zhang, K., Belmabkhout, Y., Shekhah, O., Zhang, C., Yi, S., Eddaoudi, M. & Koros, W. J. Mixed matrix formulations with MOF molecular sieving for key energy-intensive separations. *Nat. Mater.* **17**, 283–289 (2018).
 110. Zhou, S., Shekhah, O., Ramírez, A., Lyu, P., Abou-Hamad, E., Jia, J., Li, J., Bhatt, P. M., Huang, Z., Jiang, H., Jin, T., Maurin,

- G., Gascon, J. & Eddaoudi, M. Asymmetric pore windows in MOF membranes for natural gas valorization. *Nature* **606**, 706–712 (2022).
111. An, B., Li, Z., Song, Y., Zhang, J., Zeng, L., Wang, C. & Lin, W. Cooperative copper centres in a metal–organic framework for selective conversion of CO₂ to ethanol. *Nat. Catal.* **2**, 709–717 (2019).
112. Wang, T., Gao, L., Hou, J., Herou, S. J. A., Griffiths, J. T., Li, W., Dong, J., Gao, S., Titirici, M. M., Kumar, R. V., Cheetham, A. K., Bao, X., Fu, Q. & Smoukov, S. K. Rational approach to guest confinement inside MOF cavities for low-temperature catalysis. *Nat. Commun.* **10**, 1–9 (2019).
113. Dong, R., Han, P., Arora, H., Ballabio, M., Karakus, M., Zhang, Z., Shekhar, C., Adler, P., Petkov, P. S., Erbe, A., Mannsfeld, S. C. B., Felsner, C., Heine, T., Bonn, M., Feng, X. & Cánovas, E. High-mobility band-like charge transport in a semiconducting two-dimensional metal–organic framework. *Nat. Mater.* **17**, 1027–1032 (2018).
114. Liu, Y., Wei, Y., Liu, M., Bai, Y., Liu, G., Wang, X., Shang, S., Gao, W., Du, C., Chen, J. & Liu, Y. Two-Dimensional Metal–Organic Framework Film for Realizing Optoelectronic Synaptic Plasticity. *Angew. Chemie - Int. Ed.* **60**, 17440–17445 (2021).
115. Li, X., Yu, J., Gosztola, D. J., Fry, H. C. & Deria, P. Wavelength-Dependent Energy and Charge Transfer in MOF: A Step toward Artificial Porous Light-Harvesting System. *J. Am. Chem. Soc.* **141**, 16849–16857 (2019).
116. Shi, X. M., Wang, Z., Chen, M. H., Wu, Q. Q., Chen, F. Z., Fan, G. C. & Zhao, W. W. Highly Light-Harvesting MOF-on-MOF Heterostructure: Cascading Functionality to Flexible Photogating of Organic Photoelectrochemical Transistor and Bienzyme Cascade Detection. *Anal. Chem.* **96**, 3679–3685 (2024).

References

117. Eddaoudi, M., Moler, D. B., Li, H., Chen, B., Reineke, T. M., O’Keeffe, M. & Yaghi, O. M. Modular chemistry: Secondary building units as a basis for the design of highly porous and robust metal-organic carboxylate frameworks. *Acc. Chem. Res.* **34**, 319–330 (2001).
118. Hailian, L., Mohamed, E., M, O. & O, M. Y. Design and synthesis of an exceptionally stable and highly porous metal-organic framework. *Nature* **402**, 276–279 (1999).
119. Eddaoudi, M., Kim, J., Rosi, N., Vodak, D., Wachter, J., O’Keeffe, M. & Yaghi, O. M. Systematic design of pore size and functionality in isorecticular MOFs and their application in methane storage. *Science (80-.).* **295**, 469–472 (2002).
120. Eddaoudi, M., Li, H. & Yaghi, O. M. Highly porous and stable metal-organic frameworks: Structure design and sorption properties. *J. Am. Chem. Soc.* **122**, 1391–1397 (2000).
121. McCarthy, B. D., Liseev, T., Beiler, A. M., Materna, K. L. & Ott, S. Facile Orientational Control of M2L2P SURMOFs on <100> Silicon Substrates and Growth Mechanism Insights for Defective MOFs. *ACS Appl. Mater. Interfaces* **11**, 38294–38302 (2019).
122. Kim, K. J., Ellis, J. E., Howard, B. H. & Ohodnicki, P. R. Centimeter-Scale Pillared-Layer Metal-Organic Framework Thin Films Mediated by Hydroxy Double Salt Intermediates for CO2Sensor Applications. *ACS Appl. Mater. Interfaces* **13**, 2062–2071 (2021).
123. Chui, S. S. Y., Lo, S. M. F., Charmant, J. P. H., Orpen, A. G. & Williams, I. D. A chemically functionalizable nanoporous material [Cu₃(TMA)₂(H₂O)₃](n). *Science (80-.).* **283**, 1148–1150 (1999).
124. Hobday, C. L., Marshall, R. J., Murphie, C. F., Sotelo, J., Richards, T., Allan, D. R., Düren, T., Coudert, F. X., Forgan, R.

- S., Morrison, C. A., Moggach, S. A. & Bennett, T. D. A computational and experimental approach linking disorder, high-pressure behavior, and mechanical properties in UiO frameworks. *Angew. Chemie - Int. Ed.* **55**, 2401–2405 (2016).
125. Bambalaza, S. E., Langmi, H. W., Mokaya, R., Musyoka, N. M., Ren, J. & Khotseng, L. E. Compaction of a zirconium metal-organic framework (UiO-66) for high density hydrogen storage applications. *J. Mater. Chem. A* **6**, 23569–23577 (2018).
126. Kalmutzki, M. J., Hanikel, N. & Yaghi, O. M. Secondary building units as the turning point in the development of the reticular chemistry of MOFs. *Sci. Adv.* **4**, 1–16 (2018).
127. Bhunia, M. K., Hughes, J. T., Fetting, J. C. & Navrotsky, A. Thermochemistry of paddle wheel MOFs: Cu-HKUST-1 and Zn-HKUST-1. *Langmuir* **29**, 8140–8145 (2013).
128. Mahdian, S., Naimi-Jamal, M. R. & Panahi, L. Activity of M₂(BDC)₂(DABCO) (M= Co, Ni, Cu and Zn) Metal-Organic Frameworks Prepared via Ball-Milling Solvent-Free Method in Acylation of Alcohols, Amines and Aldehydes. *ChemistrySelect* **3**, 11223–11229 (2018).
129. Yuan, S., Qin, J. S., Lollar, C. T. & Zhou, H. C. Stable Metal-Organic Frameworks with Group 4 Metals: Current Status and Trends. *ACS Cent. Sci.* **4**, 440–450 (2018).
130. Marshall, R. J., Hobday, C. L., Murphie, C. F., Griffin, S. L., Morrison, C. A., Moggach, S. A. & Forgan, R. S. Amino acids as highly efficient modulators for single crystals of zirconium and hafnium metal-organic frameworks. *J. Mater. Chem. A* **4**, 6955–6963 (2016).
131. Adams, M., Kozłowska, M., Baroni, N., Oldenburg, M., Ma, R., Busko, D., Turshatov, A., Emandi, G., Senge, M. O., Haldar, R., Wöll, C., Nienhaus, G. U., Richards, B. S. & Howard, I. A.

References

- Highly Efficient One-Dimensional Triplet Exciton Transport in a Palladium-Porphyrin-Based Surface-Anchored Metal-Organic Framework. *ACS Appl. Mater. Interfaces* **11**, 15688–15697 (2019).
132. Arslan, H. K., Shekhah, O., Wieland, D. C. F., Paulus, M., Sternemann, C., Schroer, M. A., Tiemeyer, S., Tolan, M., Fischer, R. A. & Wöll, C. Intercalation in layered metal-organic frameworks: Reversible inclusion of an extended π -system. *J. Am. Chem. Soc.* **133**, 8158–8161 (2011).
133. Liu, B., Tu, M., Zacher, D. & Fischer, R. A. Multi variant surface mounted metal-organic frameworks. *Adv. Funct. Mater.* **23**, 3790–3798 (2013).
134. Chai, L., Pan, J., Hu, Y., Qian, J. & Hong, M. Rational Design and Growth of MOF-on-MOF Heterostructures. *Small* vol. 17 2100607 at <https://doi.org/10.1002/sml.202100607> (2021).
135. Shekhah, O., Hirai, K., Wang, H., Uehara, H., Kondo, M., Diring, S., Zacher, D., Fischer, R. A., Sakata, O., Kitagawa, S., Furukawa, S. & Wöll, C. MOF-on-MOF heteroepitaxy: Perfectly oriented $[\text{Zn}_2(\text{ndc})_2(\text{dabco})]_n$ grown on $[\text{Cu}_2(\text{ndc})_2(\text{dabco})]_n$ thin films. *Dalt. Trans.* **40**, 4954–4958 (2011).
136. Ikigaki, K., Okada, K., Tokudome, Y., Toyao, T., Falcaro, P., Doonan, C. J. & Takahashi, M. MOF-on-MOF: Oriented Growth of Multiple Layered Thin Films of Metal–Organic Frameworks. *Angew. Chemie - Int. Ed.* **58**, 6886–6890 (2019).
137. Wang, Z., Liu, J., Lukose, B., Gu, Z., Weidler, P. G., Gliemann, H., Heine, T. & Wöll, C. Nanoporous designer solids with huge lattice constant gradients: Multiheteroepitaxy of metal-organic frameworks. *Nano Lett.* **14**, 1526–1529 (2014).
138. Oldenburg, M., Turshatov, A., Busko, D., Wollgarten, S., Adams, M., Baroni, N., Welle, A., Redel, E., Wöll, C., Richards, B. S. & Howard, I. A. Photon Upconversion at Crystalline

- Organic–Organic Heterojunctions. *Adv. Mater.* **28**, 8477–8482 (2016).
139. Zhao, T., Taghizade, N., Fischer, J. C., Richards, B. S. & Howard, I. A. [001]-Oriented heteroepitaxy for fabricating emissive surface mounted metal-organic frameworks. *J. Mater. Chem. C* **12**, 5496–5505 (2024).
140. Haldar, R., Batra, K., Marschner, S. M., Kuc, A. B., Zahn, S., Fischer, R. A., Bräse, S., Heine, T. & Wöll, C. Bridging the Green Gap: Metal–Organic Framework Heteromultilayers Assembled from Porphyrinic Linkers Identified by Using Computational Screening. *Chem. - A Eur. J.* **25**, 7847–7851 (2019).
141. Haldar, R. & Wöll, C. Hierarchical assemblies of molecular frameworks—MOF-on-MOF epitaxial heterostructures. *Nano Res.* **14**, 355–368 (2021).
142. Maity, T., Malik, P., Bawari, S., Ghosh, S., Mondal, J. & Haldar, R. Chemically routed interpore molecular diffusion in metal-organic framework thin films. *Nat. Commun.* **14**, 1–8 (2023).
143. Jiang, S., Jelfs, K. E., Holden, D., Hasell, T., Chong, S. Y., Haranczyk, M., Trewin, A. & Cooper, A. I. Molecular dynamics simulations of gas selectivity in amorphous porous molecular solids. *J. Am. Chem. Soc.* **135**, 17818–17830 (2013).
144. Qian, Q., Asinger, P. A., Lee, M. J., Han, G., Mizrahi Rodriguez, K., Lin, S., Benedetti, F. M., Wu, A. X., Chi, W. S. & Smith, Z. P. MOF-Based Membranes for Gas Separations. *Chem. Rev.* **120**, 8161–8266 (2020).
145. Qin, Y., Han, X., Li, Y., Han, A., Liu, W., Xu, H. & Liu, J. Hollow Mesoporous Metal-Organic Frameworks with Enhanced Diffusion for Highly Efficient Catalysis. *ACS Catal.* **10**, 5973–5978 (2020).
146. Saha, R. & Gomez Garcia, C. J. Extrinsicly conducting MOFs:

References

- guest-promoted enhancement of electrical conductivity, thin film fabrication and applications. *Chem. Soc. Rev.* (2024) doi:10.1039/d4cs00141a.
147. Zojer, E. & Winkler, C. Maximizing the Carrier Mobilities of Metal-Organic Frameworks Comprising Stacked Pentacene Units. *J. Phys. Chem. Lett.* **12**, 7002–7009 (2021).
 148. Gu, C., Zhang, H., Yu, J., Shen, Q., Luo, G., Chen, X., Xue, P., Wang, Z. & Hu, J. Assembled Exciton Dynamics in Porphyrin Metal-Organic Framework Nanofilms. *Nano Lett.* **21**, 1102–1107 (2021).
 149. Chen, D.-H., Gliemann, H. & Wöll, C. Layer-by-layer assembly of metal-organic framework thin films: Fabrication and advanced applications. *Chem. Phys. Rev.* **4**, (2023).
 150. Tham, H. M., Japip, S., Hua, D. & Chung, T. S. Green Layer-by-Layer Method for the Preparation of Polyacrylonitrile-Supported Zinc Benzene-1,4-dicarboxylic Acid Membranes. *ChemSusChem* **11**, 2612–2619 (2018).
 151. So, M. C., Jin, S., Son, H. J., Wiederrecht, G. P., Farha, O. K. & Hupp, J. T. Layer-by-layer fabrication of oriented porous thin films based on porphyrin-containing metal-organic frameworks. *J. Am. Chem. Soc.* **135**, 15698–15701 (2013).
 152. Zheng, R., Fu, Z. H., Deng, W. H., Wen, Y., Wu, A. Q., Ye, X. L. & Xu, G. The Growth Mechanism of a Conductive MOF Thin Film in Spray-based Layer-by-layer Liquid Phase Epitaxy. *Angew. Chemie - Int. Ed.* **61**, (2022).
 153. Zhuang, J. L., Kind, M., Grytz, C. M., Farr, F., Diefenbach, M., Tussupbayev, S., Holthausen, M. C. & Terfort, A. Insight into the Oriented Growth of Surface-Attached Metal-Organic Frameworks: Surface Functionality, Deposition Temperature, and First Layer Order. *J. Am. Chem. Soc.* **137**, 8237–8243 (2015).

154. Goswami, S., Rimoldi, M., Anderson, R., Lee, C., Li, X., Li, A., Deria, P., Chen, L. X., Schaller, R. D., Gómez-Gualdrón, D. A., Farha, O. K. & Hupp, J. T. Toward Ideal Metal-Organic Framework Thin-Film Growth via Automated Layer-by-Layer Deposition: Examples Based on Perylene Diimide Linkers. *Chem. Mater.* **34**, 9446–9454 (2022).
155. Chernikova, V., Shekhah, O. & Eddaoudi, M. Advanced Fabrication Method for the Preparation of MOF Thin Films: Liquid-Phase Epitaxy Approach Meets Spin Coating Method. *ACS Appl. Mater. Interfaces* **8**, 20459–20464 (2016).
156. Yang, X. X., Li, C., Chen, S. M., Gu, Z. G. & Zhang, J. Layer by Layer Spraying Fabrication of Aggregation-Induced Emission Metal-Organic Frameworks Thin Film. *Chem. - A Eur. J.* **202400350**, 1–4 (2024).
157. Pilz, L., Natzeck, C., Wohlgemuth, J., Scheuermann, N., Weidler, P. G., Wagner, I., Wöll, C. & Tsotsalas, M. Fully Automated Optimization of Robot-Based MOF Thin Film Growth via Machine Learning Approaches. *Adv. Mater. Interfaces* **10**, (2023).
158. Thissen, P., Wohlgemuth, J., Weidler, P., Smilgies, D., Heinke, L., Schewe, N., Koenig, M., Krolla, P. & Wöll, C. Elimination of Domain Boundaries Accelerates Diffusion in MOFs by an Order of Magnitude: Monolithic Metal-Organic Framework Thin Films Epitaxially Grown on Si(111) Substrates. *Adv. Funct. Mater.* **2301535**, 1–8 (2023).
159. Zhuang, J., Friedel, J. & Terfort, A. The oriented and patterned growth of fluorescent metal-organic frameworks onto functionalized surfaces. *Beilstein J. Nanotechnol.* **3**, 570–578 (2012).
160. Wang, Z., Rodewald, K., Medishetty, R., Rieger, B. & Fischer, R. A. Control of Water Content for Enhancing the Quality of Copper Paddle-Wheel-Based Metal-Organic Framework Thin

References

- Films Grown by Layer-by-Layer Liquid-Phase Epitaxy. *Cryst. Growth Des.* **18**, 7451–7459 (2018).
161. Haldar, R., Heinke, L. & Wöll, C. Advanced Photoresponsive Materials Using the Metal–Organic Framework Approach. *Adv. Mater.* **32**, (2020).
 162. Virmani, E., Rotter, J. M., Mähringer, A., Von Zons, T., Godt, A., Bein, T., Wuttke, S. & Medina, D. D. On-Surface Synthesis of Highly Oriented Thin Metal-Organic Framework Films through Vapor-Assisted Conversion. *J. Am. Chem. Soc.* **140**, 4812–4819 (2018).
 163. Jin, C., Liu, S., Chen, X., Li, Y., Caro, J. & Huang, A. Oriented growth of large-area metal-organic framework ZIF-8 membrane for hydrogen separation. *J. Memb. Sci.* **711**, 123163 (2024).
 164. Falcaro, P., Okada, K., Hara, T., Ikigaki, K., Tokudome, Y., Thornton, A. W., Hill, A. J., Williams, T., Doonan, C. & Takahashi, M. Centimetre-scale micropore alignment in oriented polycrystalline metal-organic framework films via heteroepitaxial growth. *Nat. Mater.* **16**, 342–348 (2017).
 165. Stassin, T., Rodríguez-Hermida, S., Schrode, B., Cruz, A. J., Carraro, F., Kravchenko, D., Creemers, V., Stassen, I., Hauffman, T., De Vos, D., Falcaro, P., Resel, R. & Ameloot, R. Vapour-phase deposition of oriented copper dicarboxylate metal-organic framework thin films. *Chem. Commun.* **55**, 10056–10059 (2019).
 166. Allendorf, M. D., Bauer, C. A., Bhakta, R. K. & Houk, R. J. T. Luminescent metal-organic frameworks. *Chem. Soc. Rev.* **38**, 1330–1352 (2009).
 167. Pal, T. K. Metal-organic framework (MOF)-based fluorescence “turn-on” sensors. *Mater. Chem. Front.* **7**, 405–441 (2022).
 168. Stavila, V., Talin, A. A. & Allendorf, M. D. MOF-based

- electronic and opto-electronic devices. *Chem. Soc. Rev.* **43**, 5994–6010 (2014).
169. Song, H. I., Bae, J., Lee, E. J., Kirlikovali, K. O., Farha, O. K. & Jeong, N. C. Vibrational Paddlewheel Cu-Cu Node in Metal-Organic Frameworks: Probe of Nonradiative Relaxation. *J. Phys. Chem. C* **124**, 13187–13195 (2020).
170. Ellis, J. E., Crawford, S. E. & Kim, K. J. Metal-organic framework thin films as versatile chemical sensing materials. *Mater. Adv.* **2**, 6169–6196 (2021).
171. Ji, G., Liu, J., Gao, X., Sun, W., Wang, J., Zhao, S. & Liu, Z. A luminescent lanthanide MOF for selectively and ultra-high sensitively detecting Pb²⁺ ions in aqueous solution. *J. Mater. Chem. A* **5**, 10200–10205 (2017).
172. Chen, W., Fan, R., Fan, J., Liu, H., Sun, T., Wang, P. & Yang, Y. Lanthanide Coordination Polymer-Based Composite Films for Selective and Highly Sensitive Detection of Cr^{2O72-} in Aqueous Media. *Inorg. Chem.* (2019) doi:10.1021/acs.inorgchem.9b01841.
173. Ma, W. P. & Yan, B. Lanthanide functionalized MOF thin films as effective luminescent materials and chemical sensors for ammonia. *Dalt. Trans.* **49**, 15663–15671 (2020).
174. Olorunyomi, J. F., Sadiq, M. M., Batten, M., Konstas, K., Chen, D., Doherty, C. M. & Caruso, R. A. Advancing Metal-Organic Frameworks toward Smart Sensing: Enhanced Fluorescence by a Photonic Metal-Organic Framework for Organic Vapor Sensing. *Adv. Opt. Mater.* **8**, 1–11 (2020).
175. Perego, J., Bracco, S., Negroni, M., Bezuidenhout, C. X., Prando, G., Carretta, P., Comotti, A. & Sozzani, P. Fast motion of molecular rotors in metal–organic framework struts at very low temperatures. *Nat. Chem.* **12**, 845–851 (2020).
176. Horike, S., Matsuda, R., Tanaka, D., Matsubara, S., Mizuno,

References

- M., Endo, K. & Kitagawa, S. Dynamic motion of building blocks in porous coordination polymers. *Angew. Chemie - Int. Ed.* **45**, 7226–7230 (2006).
177. Su, Y. S., Lamb, E. S., Liepuoniute, I., Chronister, A., Stanton, A. L., Guzman, P., Pérez-Estrada, S., Chang, T. Y., Houk, K. N., Garcia-Garibay, M. A. & Brown, S. E. Dipolar order in an amphidynamic crystalline metal–organic framework through reorienting linkers. *Nat. Chem.* **13**, 278–283 (2021).
178. Feng, L., Qiu, Y., Guo, Q. H., Chen, Z., Seale, J. S. W., He, K., Wu, H., Feng, Y., Farha, O. K., Dean Astumian, R. & Fraser Stoddart, J. Active mechanisorption driven by pumping cassettes. *Science (80-.).* **374**, 1215–1221 (2021).
179. Zhu, K., O’Keefe, C. A., Vukotic, V. N., Schurko, R. W. & Loeb, S. J. A molecular shuttle that operates inside a metal-organic framework. *Nat. Chem.* **7**, 514–519 (2015).
180. Danowski, W., Castiglioni, F., Sardjan, A. S., Krause, S., Pfeifer, L., Roke, D., Comotti, A., Browne, W. R. & Feringa, B. L. Visible-light-driven rotation of molecular motors in a dual-function metal-organic framework enabled by energy transfer. *J. Am. Chem. Soc.* **142**, 9048–9056 (2020).
181. Bigdeli, F., Lollar, C. T., Morsali, A. & Zhou, H. C. Switching in Metal–Organic Frameworks. *Angew. Chemie - Int. Ed.* **59**, 4652–4669 (2020).
182. Danowski, W., van Leeuwen, T., Abdollahzadeh, S., Roke, D., Browne, W. R., Wezenberg, S. J. & Feringa, B. L. Unidirectional rotary motion in a metal–organic framework. *Nat. Nanotechnol.* **14**, 488–494 (2019).
183. Chen, Q., Sun, J., Li, P., Hod, I., Moghadam, P. Z., Kean, Z. S., Snurr, R. Q., Hupp, J. T., Farha, O. K. & Stoddart, J. F. A Redox-Active Bistable Molecular Switch Mounted inside a Metal-Organic Framework. *J. Am. Chem. Soc.* **138**, 14242–14245

- (2016).
184. Castiglioni, F., Danowski, W., Perego, J., Leung, F. K. C., Sozzani, P., Bracco, S., Wezenberg, S. J., Comotti, A. & Feringa, B. L. Modulation of porosity in a solid material enabled by bulk photoisomerization of an overcrowded alkene. *Nat. Chem.* **12**, 595–602 (2020).
185. Wilson, G. R., Park, K. C., Thaggard, G. C., Martin, C. R., Hill, A. R., Haimerl, J., Lim, J., Maldeni Kankanamalage, B. K. P., Yarbrough, B. J., Forrester, K. L., Fischer, R. A., Pellechia, P. J., Smith, M. D., Garashchuk, S. & Shustova, N. B. Cooperative and Orthogonal Switching in the Solid State Enabled by Metal-Organic Framework Confinement Leading to a Thermo-Photochromic Platform. *Angew. Chemie - Int. Ed.* **62**, (2023).
186. Gonzalez-Nelson, A., Mula, S., Šimėnas, M., Balčiūnas, S., Altenhof, A. R., Vojvodin, C. S., Canossa, S., Banys, J. R., Schurko, R. W., Coudert, F. X. & Van Der Veen, M. A. Emergence of Coupled Rotor Dynamics in Metal-Organic Frameworks via Tuned Steric Interactions. *J. Am. Chem. Soc.* **143**, 12053–12062 (2021).
187. Jiang, X., Duan, H. B., Khan, S. I. & Garcia-Garibay, M. A. Diffusion-controlled rotation of triptycene in a metal-organic framework (MOF) sheds light on the viscosity of MOF-confined solvent. *ACS Cent. Sci.* **2**, 608–613 (2016).
188. Perego, J., Bracco, S., Negroni, M., Bezuidenhout, C. X., Prando, G., Carretta, P., Comotti, A. & Sozzani, P. Fast motion of molecular rotors in metal-organic framework struts at very low temperatures. *Nat. Chem.* (2020) doi:10.1038/s41557-020-0495-3.
189. Perego, J., Bezuidenhout, C. X., Bracco, S., Prando, G., Marchiò, L., Negroni, M., Carretta, P., Sozzani, P. & Comotti, A. Cascade Dynamics of Multiple Molecular Rotors in a MOF: Benchmark Mobility at a Few Kelvins and Dynamics Control

References

- by CO₂. *J. Am. Chem. Soc.* **143**, 13082–13090 (2021).
190. Wilson, B. H., Vojvodin, C. S., Gholami, G., Abdulla, L. M., O’Keefe, C. A., Schurko, R. W. & Loeb, S. J. Precise Spatial Arrangement and Interaction between Two Different Mobile Components in a Metal-Organic Framework. *Chem* **7**, 202–211 (2021).
191. Heinke, L., Cakici, M., Dommaschk, M., Grosjean, S., Herges, R., Bräse, S. & Wöll, C. Photoswitching in two-component surface-mounted metal-organic frameworks: Optically triggered release from a molecular container. *ACS Nano* **8**, 1463–1467 (2014).
192. Kanj, A. B., Bürck, J., Grosjean, S., Bräse, S. & Heinke, L. Switching the enantioselectivity of nanoporous host materials by light. *Chem. Commun.* **55**, 8776–8779 (2019).
193. Dürholt, J. P., Jahromi, B. F. & Schmid, R. Tuning the Electric Field Response of MOFs by Rotatable Dipolar Linkers. *ACS Cent. Sci.* **5**, 1440–1448 (2019).
194. Martinez-Bulit, P., Stirk, A. J. & Loeb, S. J. Rotors, Motors, and Machines Inside Metal–Organic Frameworks. *Trends Chem.* **1**, 588–600 (2019).
195. Thaggard, G. C. *et al.* Breaking the photoswitch speed limit. *Nat. Commun.* **14**, 1–12 (2023).
196. Winston, E. B., Lowell, P. J., Vacek, J., Chocholoušová, J., Michl, J. & Price, J. C. Dipolar molecular rotors in the metal-organic framework crystal IRMOF-2. *Phys. Chem. Chem. Phys.* **10**, 5188–5191 (2008).
197. Jellen, M. J., Jiang, X., Benders, S., Adams, A. & Garcia-Garibay, M. A. Slip/Stick Viscosity Models of Nanoconfined Liquids: Solvent-Dependent Rotation in Metal–Organic Frameworks. *J. Org. Chem.* (2021) doi:10.1021/acs.joc.1c02218.

198. Perego, J., Bezuidenhout, C. X., Bracco, S., Piva, S., Prando, G., Aloisi, C., Carretta, P., Kaleta, J., Le, T. P., Sozzani, P., Daolio, A. & Comotti, A. Benchmark Dynamics of Dipolar Molecular Rotors in Fluorinated Metal-Organic Frameworks. *Angew. Chemie - Int. Ed.* **62**, (2023).
199. Comotti, A., Bracco, S. & Sozzani, P. Molecular Rotors Built in Porous Materials. *Acc. Chem. Res.* **49**, 1701–1710 (2016).
200. Liu, Z., Wang, Y. & Garcia-Garibay, M. A. Rotational Dynamics of an Amphidynamic Zirconium Metal-Organic Framework Determined by Dielectric Spectroscopy. *J. Phys. Chem. Lett.* **12**, 5644–5648 (2021).
201. Dong, J. *et al.* Aggregation-Induced Emission-Responsive Metal-Organic Frameworks. *Chem. Mater.* **32**, 6706–6720 (2020).
202. Feng, L., Astumian, R. D. & Stoddart, J. F. Controlling dynamics in extended molecular frameworks. *Nat. Rev. Chem.* **6**, 705–725 (2022).
203. Liu, X., Kozłowska, M., Okkali, T., Wagner, D., Higashino, T., Brenner-Weiß, G., Marschner, S. M., Fu, Z., Zhang, Q., Imahori, H., Bräse, S., Wenzel, W., Wöll, C. & Heinke, L. Photoconductivity in Metal–Organic Framework (MOF) Thin Films. *Angew. Chemie - Int. Ed.* **58**, 9590–9595 (2019).
204. Saito, K., Xu, T. & Ishikita, H. Correlation between C•O Stretching Vibrational Frequency and p KaShift of Carboxylic Acids. *J. Phys. Chem. B* **126**, 4999–5006 (2022).
205. Fleming, I. & Williams, D. *Spectroscopic Methods in Organic Chemistry*. (Springer Cham, 2019). doi:10.1007/978-3-030-18252-6.
206. Hasegawa, T. *Quantitative Infrared Spectroscopy for Understanding of a Condensed Matter*. (Springer Japan, 2017). doi:10.1007/978-4-431-56493-5.

References

207. Parson, W. W. *Modern Optical Spectroscopy*. (Springer Berlin Heidelberg, 2009). doi:10.1007/978-3-540-37542-5.
208. Saleh, B. E. A. & Teich, M. C. *Fundamentals of Photonics*. (John Wiley and Sons Inc, 2019).
209. Giusfredi, G. *Physical Optics*. (Springer Cham, 2019). doi:10.1007/978-3-030-25279-3.
210. de Mello, J. C., Wittmann, H. F. & Friend, R. H. An Improved Experimental Determination of External Photoluminescence Quantum Efficiency. *Adv. Mater.* **9**, 230–232 (1997).
211. Zheng, Y., Sun, F. Z., Han, X., Xu, J. & Bu, X. H. Recent Progress in 2D Metal–Organic Frameworks for Optical Applications. *Adv. Opt. Mater.* **8**, 1–17 (2020).
212. Howarth, A. J., Peters, A. W., Vermeulen, N. A., Wang, T. C., Hupp, J. T. & Farha, O. K. Best practices for the synthesis, activation, and characterization of metal–organic frameworks. *Chem. Mater.* **29**, 26–39 (2017).
213. Li, C., Chandresh, A., Zhang, Z., Moulai, S. & Heinke, L. Stability and Degradation of Metal–Organic-Framework Films under Ambient Air Explored by Uptake and Diffusion Experiments. *Adv. Mater. Interfaces* **9**, (2022).
214. Feng, J. F., Liu, T. F., Shi, J., Gao, S. Y. & Cao, R. Dual-Emitting UiO-66(Zr&Eu) Metal–Organic Framework Films for Ratiometric Temperature Sensing. *ACS Appl. Mater. Interfaces* **10**, 20854–20861 (2018).
215. Zhai, Z., Zhang, X., Wang, J., Li, H., Sun, Y., Hao, X., Qin, Y., Niu, B. & Li, C. Washable and flexible gas sensor based on UiO-66-NH₂ nanofibers membrane for highly detecting SO₂. *Chem. Eng. J.* **428**, 131720 (2022).
216. Wang, Q., Zhang, X., Chai, X., Wang, T., Cao, T., Li, Y., Zhang, L., Fan, F., Fu, Y. & Qi, W. An Electrochemical Sensor for

- H₂O₂Based on Au Nanoparticles Embedded in UiO-66 Metal-Organic Framework Films. *ACS Appl. Nano Mater.* **4**, 6103–6110 (2021).
217. Chang, C. Y., Wu, K. H., Chang, C. Y., Guo, R. F., Li, G. L. & Wang, C. Y. Enhanced performance and stability of low-bandgap mixed lead-tin halide perovskite photovoltaic solar cells and photodetectors via defect passivation with UiO-66-NH₂ metal-organic frameworks and interfacial engineering. *Mol. Syst. Des. Eng.* **7**, 1073–1084 (2022).
218. Melillo, A., García-Aboal, R., Navalón, S., Atienzar, P., Ferrer, B., Álvaro, M. & García, H. Photoactive Zr and Ti Metal-Organic-Frameworks for Solid-State Solar Cells. *ChemPhysChem* **22**, 842–848 (2021).
219. Wang, C., Xie, Z., Dekrafft, K. E. & Lin, W. Doping metal-organic frameworks for water oxidation, carbon dioxide reduction, and organic photocatalysis. *J. Am. Chem. Soc.* **133**, 13445–13454 (2011).
220. Feng, X., Jena, H. S., Krishnaraj, C., Leus, K., Wang, G., Chen, H., Jia, C. & Van Der Voort, P. Generating Catalytic Sites in UiO-66 through Defect Engineering. *ACS Appl. Mater. Interfaces* **13**, 60715–60735 (2021).
221. Bachinin, S. V., Lubimova, A., Povarov, S. A., Zubok, D., Okoneshnikova, E., Kulakova, A. N., Rzhetskiy, S. S. & Milichko, V. A. Memristive behavior of UiO-66 metal-organic framework single crystal. *Photonics Nanostructures - Fundam. Appl.* **58**, 101206 (2024).
222. Xu, Z., Li, Y., Xia, Y., Shi, C., Chen, S., Ma, C., Zhang, C. & Li, Y. Organic Frameworks Memristor: An Emerging Candidate for Data Storage, Artificial Synapse, and Neuromorphic Device. *Adv. Funct. Mater.* **34**, 1–22 (2024).
223. Villajos, J. A. Experimental Volumetric Hydrogen Uptake

References

- Determination at 77 K of Commercially Available Metal-Organic Framework Materials. *C - J. Carbon Res.* **8**, 5 (2022).
224. Ingerle, D. Glancing Incidence X-ray Analysis (GIXA) X-ray Tools.
<https://gixa.ati.tuwien.ac.at/tools/penetrationdepth.xhtml>.
225. Henke, B. L., Gullikson, E. M. & Davis, J. C. X-ray interactions: Photoabsorption, scattering, transmission, and reflection at $E = 50\text{--}30,000$ eV, $Z = 1\text{--}92$. *Atomic Data and Nuclear Data Tables* vol. 54 181–342 at
<https://doi.org/10.1006/adnd.1993.1013> (1993).
226. Sun, Y., Yao, Q., Xing, W., Jiang, H., Li, Y., Xiong, W., Zhu, W. & Zheng, Y. Residual Strain Evolution Induced by Crystallization Kinetics During Anti-Solvent Spin Coating in Organic–Inorganic Hybrid Perovskite. *Adv. Sci.* **10**, 1–13 (2023).
227. Lee, J. W., Tan, S., Han, T. H., Wang, R., Zhang, L., Park, C., Yoon, M., Choi, C., Xu, M., Liao, M. E., Lee, S. J., Nuryyeva, S., Zhu, C., Huynh, K., Goorsky, M. S., Huang, Y., Pan, X. & Yang, Y. Solid-phase hetero epitaxial growth of α -phase formamidinium perovskite. *Nat. Commun.* **11**, 1–11 (2020).
228. Baker, J. L., Jimison, L. H., Mannsfeld, S., Volkman, S., Yin, S., Subramanian, V., Salleo, A., Alivisatos, A. P. & Toney, M. F. Quantification of thin film crystallographic orientation using X-ray diffraction with an area detector. *Langmuir* **26**, 9146–9151 (2010).
229. Jimison, L. H., Salleo, A., Chabinyc, M. L., Bernstein, D. P. & Toney, M. F. Correlating the microstructure of thin films of poly[5,5-bis(3-dodecyl-2-thienyl)-2,2-bithiophene] with charge transport: Effect of dielectric surface energy and thermal annealing. *Phys. Rev. B - Condens. Matter Mater. Phys.* **78**, 125319 (1–18) (2008).
230. Yoneda, Y. Anomalous surface reflection of X rays. *Phys. Rev.*

- 131**, 2010–2013 (1963).
231. Fischer, J. C., Steentjes, R., Chen, D.-H., Richards, B. S., Zojer, E., Wöll, C. & Howard, I. A. Determining Structures of Layer-by-Layer Spin-Coated Zinc Dicarboxylate-Based Metal-Organic Thin Films. *Chem. – A Eur. J.* **202400565**, 26–29 (2024).
232. Windischbacher, A., Steiner, L., Haldar, R., Wöll, C., Zojer, E. & Kelterer, A. M. Exciton coupling and conformational changes impacting the excited state properties of metal organic frameworks. *Molecules* **25**, (2020).
233. Baroni, N., Turshatov, A., Adams, M., Dolgoplova, E. A., Schliske, S., Hernandez-Sosa, G., Wöll, C., Shustova, N. B., Richards, B. S. & Howard, I. A. Inkjet-Printed Photoluminescent Patterns of Aggregation-Induced-Emission Chromophores on Surface-Anchored Metal-Organic Frameworks. *ACS Appl. Mater. Interfaces* **10**, 25754–25762 (2018).
234. Liu, J., Lukose, B., Shekhah, O., Arslan, H. K., Weidler, P., Gliemann, H., Bräse, S., Grosjean, S., Godt, A., Feng, X., Müllen, K., Magdau, I. B., Heine, T. & Wöll, C. A novel series of isorecticular metal organic frameworks: Realizing metastable structures by liquid phase epitaxy. *Sci. Rep.* **2**, 1–5 (2012).
235. Friedländer, S., Liu, J., Addicoat, M., Petkov, P., Vankova, N., Rüger, R., Kuc, A., Guo, W., Zhou, W., Lukose, B., Wang, Z., Weidler, P. G., Pöppel, A., Ziese, M., Heine, T. & Wöll, C. Linear Chains of Magnetic Ions Stacked with Variable Distance: Ferromagnetic Ordering with a Curie Temperature above 20 K. *Angew. Chemie - Int. Ed.* **55**, 12683–12687 (2016).
236. Hosono, E., Fujihara, S., Kimura, T. & Imai, H. Growth of layered basic zinc acetate in methanolic solutions and its pyrolytic transformation into porous zinc oxide films. *J. Colloid Interface Sci.* **272**, 391–398 (2004).

References

237. Biswick, T., Jones, W., Pacuła, A., Serwicka, E. & Podobinski, J. Evidence for the formation of anhydrous zinc acetate and acetic anhydride during the thermal degradation of zinc hydroxy acetate, $\text{Zn}_5(\text{OH})_8(\text{CH}_3\text{CO}_2)_2 \cdot 4\text{H}_2\text{O}$ to ZnO. *Solid State Sci.* **11**, 330–335 (2009).
238. Schlur, L., Carton, A. & Pourroy, G. A new zinc hydroxy acetate hydrogen carbonate lamellar phase for growing large and clean ZnO nanorod arrays. *Chem. Commun.* **51**, 3367–3370 (2015).
239. Nakagaki, S., Machado, G. S., Stival, J. F., Henrique dos Santos, E., Silva, G. M. & Wypych, F. Natural and synthetic layered hydroxide salts (LHS): Recent advances and application perspectives emphasizing catalysis. *Prog. Solid State Chem.* **64**, (2021).
240. Arizaga, G. G. C., Satyanarayana, K. G. & Wypych, F. Layered hydroxide salts: Synthesis, properties and potential applications. *Solid State Ionics* **178**, 1143–1162 (2007).
241. Morioka, H., Tagaya, H., Karasu, M., Kadokawa, J. I. & Chiba, K. Preparation of hydroxy double salts exchanged by organic compounds. *J. Mater. Res.* **13**, 848–851 (1998).
242. Newman, S. P. & Jones, W. Comparative Study of Some Layered Hydroxide Salts Containing Exchangeable Interlayer Anions. *J. Solid State Chem.* **148**, 26–40 (1999).
243. Ramli, M., Hussein, M. Z. & Yusoff, K. Preparation and characterization of an anti-inflammatory agent based on a zinc-layered hydroxide-salicylate nanohybrid and its effect on viability of Vero-3 cells. *Int. J. Nanomedicine* **8**, 297–306 (2013).
244. Abdul Latip, A. F., Hussein, M. Z., Stanslas, J., Wong, C. C. & Adnan, R. Release behavior and toxicity profiles towards A549 cell lines of ciprofloxacin from its layered zinc hydroxide

- intercalation compound. *Chem. Cent. J.* **7**, 1–11 (2013).
245. Liu, J., Zhang, X. & Zhang, Y. Preparation and release behavior of chlorpyrifos adsorbed into layered zinc hydroxide nitrate intercalated with dodecylbenzenesulfonate. *ACS Appl. Mater. Interfaces* **7**, 11180–11188 (2015).
 246. Demel, J., Kubát, P., Jirka, I., Kovář, P., Pospíšil, M. & Lang, K. Inorganic-organic hybrid materials: Layered zinc hydroxide salts with intercalated porphyrin sensitizers. *J. Phys. Chem. C* **114**, 16321–16328 (2010).
 247. Cursino, A. C. T., Rives, V., Arizaga, G. G. C., Trujillano, R. & Wypych, F. Rare earth and zinc layered hydroxide salts intercalated with the 2-aminobenzoate anion as organic luminescent sensitizer. *Mater. Res. Bull.* **70**, 336–342 (2015).
 248. Cursino, A. C. T., Gardolinski, J. E. F. da C. & Wypych, F. Intercalation of anionic organic ultraviolet ray absorbers into layered zinc hydroxide nitrate. *J. Colloid Interface Sci.* **347**, 49–55 (2010).
 249. Pradhan, D. & Leung, K. T. Controlled growth of two-dimensional and one-dimensional ZnO nanostructures on indium tin oxide coated glass by direct electrodeposition. *Langmuir* **24**, 9707–9716 (2008).
 250. Qiu, J., Guo, M. & Wang, X. Electrodeposition of hierarchical ZnO nanorod-nanosheet structures and their applications in dye-sensitized solar cells. *ACS Appl. Mater. Interfaces* **3**, 2358–2367 (2011).
 251. Emin, S., Fanetti, M., Abdi, F. F., Lisjak, D., Valant, M., Van De Krol, R. & Dam, B. Photoelectrochemical properties of cadmium chalcogenide-sensitized textured porous zinc oxide plate electrodes. *ACS Appl. Mater. Interfaces* **5**, 1113–1121 (2013).
 252. Xu, F., Dai, M., Lu, Y. & Sun, L. Hierarchical ZnO nanowire-

References

- nanosheet architectures for high power conversion efficiency in dye-sensitized solar cells. *J. Phys. Chem. C* **114**, 2776–2782 (2010).
253. Chen, H., Zhu, L., Liu, H. & Li, W. Zn₅(OH)8Cl₂·H₂O-based quantum dots-sensitized solar cells: A common corrosion product enhances the performance of photoelectrochemical cells. *Electrochim. Acta* **105**, 289–298 (2013).
254. Haldar, R., Kozłowska, M., Ganschow, M., Ghosh, S., Jakoby, M., Chen, H., Ghalami, F., Xie, W., Heidrich, S., Tsutsui, Y., Freudenberg, J., Seki, S., Howard, I. A., Richards, B. S., Bunz, U. H. F., Elstner, M., Wenzel, W. & Wöll, C. Interplay of structural dynamics and electronic effects in an engineered assembly of pentacene in a metal-organic framework. *Chem. Sci.* **12**, 4477–4483 (2021).
255. Shekhah, O. Layer-by-layer method for the synthesis and growth of surface mounted metal-organic frameworks (SURMOFS). *Materials (Basel)*. **3**, 1302–1315 (2010).
256. Zacher, D., Yussenko, K., Bétard, A., Henke, S., Molon, M., Ladnorg, T., Shekhah, O., Schüpbach, B., Dea Losa Arcos, T., Krasnopolski, M., Meilikhov, M., Winter, J., Terfort, A., Wöll, C. & Fischer, R. A. Liquid-phase epitaxy of multicomponent layer-based porous coordination polymer thin films of [M(L)(P)0.5] type: Importance of deposition sequence on the oriented growth. *Chem. - A Eur. J.* **17**, 1448–1455 (2011).
257. Li, Q., Gies, J., Yu, X. J., Gu, Y., Terfort, A. & Kind, M. Concentration-Dependent Seeding as a Strategy for Fabrication of Densely Packed Surface-Mounted Metal–Organic Frameworks (SURMOF) Layers. *Chem. - A Eur. J.* **26**, 5185–5189 (2020).
258. Liu, J., Lukose, B., Shekhah, O., Arslan, H. K., Weidler, P., Gliemann, H., Bräse, S., Grosjean, S., Godt, A., Feng, X., Müllen, K., Magdau, I. B., Heine, T. & Wöll, C. A novel series of

- isorecticular metal organic frameworks: Realizing metastable structures by liquid phase epitaxy. *Sci. Rep.* **2**, 2–6 (2012).
259. Moezzi, A., Cortie, M. B., Shimmon, R. & McDonagh, A. M. On the reactivity of zinc hydroxide acetate dihydrate in ethanol. *Eur. J. Inorg. Chem.* 5133–5137 (2013) doi:10.1002/ejic.201300650.
260. Leung, A. H. M., Pike, S. D., Clancy, A. J., Yau, H. C., Lee, W. J., Orchard, K. L., Shaffer, M. S. P. & Williams, C. K. Layered zinc hydroxide monolayers by hydrolysis of organozincs. *Chem. Sci.* **9**, 2135–2146 (2018).
261. Said, S. A., Roberts, C. S., Lee, J. K., Shaffer, M. S. P. & Williams, C. K. Direct Organometallic Synthesis of Carboxylate Intercalated Layered Zinc Hydroxides for Fully Exfoliated Functional Nanosheets. *Adv. Funct. Mater.* **31**, (2021).
262. Kurmoo, M., Kumagai, H., Hughes, S. M. & Kepert, C. J. Reversible Guest Exchange and Ferrimagnetism ($T_c = 60.5$ K) in a Porous Cobalt(II)-Hydroxide Layer Structure Pillared with trans-1,4-Cyclohexanedicarboxylate. *Inorg. Chem.* **42**, 6709–6722 (2003).
263. Poul, L., Jouini, N. & Fievet, F. Layered hydroxide metal acetates (metal = zinc, cobalt, and nickel): Elaboration via hydrolysis in polyol medium and comparative study. *Chem. Mater.* **12**, 3123–3132 (2000).
264. Lutz, H. D. Hydroxide ions in condensed materials – Correlation of spectroscopic and structural data. in *Coordination Chemistry* 85–103 (Springer Berlin Heidelberg, 1995). doi:10.1007/BFb0036823.
265. Hussein, M. Z. bin, Ghotbi, M. Y., Yahaya, A. H. & Abd Rahman, M. Z. Synthesis and characterization of (zinc-layered-gallate) nanohybrid using structural memory effect. *Mater. Chem. Phys.* **113**, 491–496 (2009).

References

266. Gordeeva, A., Hsu, Y. J., Jenei, I. Z., Brant Carvalho, P. H. B., Simak, S. I., Andersson, O. & Häussermann, U. Layered Zinc Hydroxide Dihydrate, $\text{Zn}_5(\text{OH})_{10} \cdot 2\text{H}_2\text{O}$, from Hydrothermal Conversion of $\epsilon\text{-Zn}(\text{OH})_2$ at Gigapascal Pressures and its Transformation to Nanocrystalline ZnO. *ACS Omega* **5**, 17617–17627 (2020).
267. Hesse, M., Meier, H. & Zeeh, B. *Spectroscopic Methods in Organic Chemistry*. (Georg Thieme Verlag KG, 2008).
268. Kumagai, H., Akita-Tanaka, M., Inoue, K. & Kurmoo, M. Hydrothermal synthesis and characterization of a new 3D-network containing the versatile cis, cis-cyclohexane-1,3,5-tricarboxylate. *J. Mater. Chem.* **11**, 2147–2152 (2001).
269. Hamer, S., Röhricht, F., Jakoby, M., Howard, I. A., Zhang, X., Näther, C. & Herges, R. Synthesis of dipolar molecular rotors as linkers for metal-organic frameworks. *Beilstein J. Org. Chem.* **15**, 1331–1338 (2019).
270. Marshall, R. J., Kalinovsky, Y., Griffin, S. L., Wilson, C., Blight, B. A. & Forgan, R. S. Functional Versatility of a Series of Zr Metal-Organic Frameworks Probed by Solid-State Photoluminescence Spectroscopy. *J. Am. Chem. Soc.* **139**, 6253–6260 (2017).
271. Abdelouhab, S., François, M., Elkaim, E. & Rabu, P. Ab initio crystal structure of copper(II) hydroxy-terephthalate by synchrotron powder diffraction and magnetic properties. *Solid State Sci.* **7**, 227–232 (2005).
272. Inoue, S. & Fujihara, S. Liquid-liquid biphasic synthesis of layered zinc hydroxides intercalated with long-chain carboxylate ions and their conversion into ZnO nanostructures. *Inorg. Chem.* **50**, 3605–3612 (2011).
273. Tan, K., Nijem, N., Canepa, P., Gong, Q., Li, J., Thonhauser, T. & Chabal, Y. J. Stability and hydrolyzation of metal organic

- frameworks with paddle-wheel SBUs upon hydration. *Chem. Mater.* **24**, 3153–3167 (2012).
274. Yuan, S., Peng, J., Cai, B., Huang, Z., Garcia-Esparza, A. T., Sokaras, D., Zhang, Y., Giordano, L., Akkiraju, K., Zhu, Y. G., Hübner, R., Zou, X., Román-Leshkov, Y. & Shao-Horn, Y. Tunable metal hydroxide–organic frameworks for catalysing oxygen evolution. *Nat. Mater.* **21**, 673–680 (2022).
275. Rajamathi, J. T., Raviraj, N. H., Ahmed, M. F. & Rajamathi, M. Hexacyanoferrate-intercalated nickel zinc hydroxy double salts. *Solid State Sci.* **11**, 2080–2085 (2009).
276. Kawai, A., Sugahara, Y., Park, I. Y., Kuroda, K. & Kato, C. Preparation of zinc oxide powders from 2-dimensional hydroxy-zinc complexes of basic zinc acetate, chloride, and nitrate, *Ceram. Trans.* 1991, 22, 75. *Ceram. Trans.* **22**, 75–80 (1991).
277. Miller, J. B., Hsieh, H. J., Howard, B. H. & Broitman, E. Microstructural evolution of sol-gel derived ZnO thin films. *Thin Solid Films* **518**, 6792–6798 (2010).
278. Arnold, R., Azzam, W., Terfort, A. & Wöll, C. Preparation, modification, and crystallinity of aliphatic and aromatic carboxylic acid terminated self-assembled monolayers. *Langmuir* **18**, 3980–3992 (2002).
279. Ahn, T. S., Al-Kaysi, R. O., Müller, A. M., Wentz, K. M. & Bardeen, C. J. Self-absorption correction for solid-state photoluminescence quantum yields obtained from integrating sphere measurements. *Rev. Sci. Instrum.* **78**, (2007).
280. Wilson, L. R. & Richards, B. S. Measurement method for photoluminescent quantum yields of fluorescent organic dyes in polymethyl methacrylate for luminescent solar concentrators. *Appl. Opt.* **48**, 212–220 (2009).

References

281. Kreno, L. E., Leong, K., Farha, O. K., Allendorf, M., Van Duyne, R. P. & Hupp, J. T. Metal-organic framework materials as chemical sensors. *Chem. Rev.* **112**, 1105–1125 (2012).
282. Yanai, N., Kitayama, K., Hijikata, Y., Sato, H., Matsuda, R., Kubota, Y., Takata, M., Mizuno, M., Uemura, T. & Kitagawa, S. Gas detection by structural variations of fluorescent guest molecules in a flexible porous coordination polymer. *Nat. Mater.* **10**, 787–793 (2011).
283. Wang, Z., Huang, Y., Xu, K., Zhong, Y., He, C., Jiang, L., Sun, J., Rao, Z., Zhu, J., Huang, J., Xiao, F., Liu, H. & Xia, B. Y. Natural oxidase-mimicking copper-organic frameworks for targeted identification of ascorbate in sensitive sweat sensing. *Nat. Commun.* **14**, 1–9 (2023).
284. Freund, P., Senkovska, I. & Kaskel, S. Switchable Conductive MOF-Nanocarbon Composite Coatings as Threshold Sensing Architectures. *ACS Appl. Mater. Interfaces* **9**, 43782–43789 (2017).
285. Lustig, W. P., Mukherjee, S., Rudd, N. D., Desai, A. V., Li, J. & Ghosh, S. K. Metal-organic frameworks: Functional luminescent and photonic materials for sensing applications. *Chem. Soc. Rev.* **46**, 3242–3285 (2017).
286. Takashima, Y., Martínez, V. M., Furukawa, S., Kondo, M., Shimomura, S., Uehara, H., Nakahama, M., Sugimoto, K. & Kitagawa, S. Molecular decoding using luminescence from an entangled porous framework. *Nat. Commun.* **2**, (2011).
287. Chen, L., Ye, J. W., Wang, H. P., Pan, M., Yin, S. Y., Wei, Z. W., Zhang, L. Y., Wu, K., Fan, Y. N. & Su, C. Y. Ultrafast water sensing and thermal imaging by a metal-organic framework with switchable luminescence. *Nat. Commun.* **8**, 1–10 (2017).
288. Gonzalez-Nelson, A., Coudert, F. X. & van der Veen, M. A. Rotational dynamics of linkers in metal–organic frameworks.

- Nanomaterials* vol. 9 at <https://doi.org/10.3390/nano9030330> (2019).
289. Vogelsberg, C. S., Uribe-Romo, F. J., Lipton, A. S., Yang, S., Hou, K. N., Brown, S. & Garcia-Garibay, M. A. Ultrafast rotation in an amphidynamic crystalline metal organic framework. *Proc. Natl. Acad. Sci. U. S. A.* **114**, 13613–13618 (2017).
 290. Hirai, K., Furukawa, S., Kondo, M., Uehara, H., Sakata, O. & Kitagawa, S. Sequential functionalization of porous coordination polymer crystals. *Angew. Chemie - Int. Ed.* **50**, 8057–8061 (2011).
 291. Gao, Q., Xie, Y. B., Li, J. R., Yuan, D. Q., Yakovenko, A. A., Sun, J. H. & Zhou, H. C. Tuning the formations of metal-organic frameworks by modification of ratio of reactant, acidity of reaction system, and use of a secondary ligand. *Cryst. Growth Des.* **12**, 281–288 (2012).
 292. Tan, K., Nijem, N., Gao, Y., Zuluaga, S., Li, J., Thonhauser, T. & Chabal, Y. J. Water interactions in metal organic frameworks. *CrystEngComm* **17**, 247–260 (2015).
 293. Jasuja, H., Huang, Y. G. & Walton, K. S. Adjusting the stability of metal-organic frameworks under humid conditions by ligand functionalization. *Langmuir* **28**, 16874–16880 (2012).
 294. Holzwarth, U. & Gibson, N. The Scherrer equation versus the ‘Debye-Scherrer equation’. *Nat. Nanotechnol.* **6**, 534 (2011).
 295. Scherrer, P. Abschätzungen von Charaktersummen, Einheit und Klassenzahlen. *Göttinger Nachrichten Gesell* **2**, 98–100 (1918).
 296. Tanaka, D., Horike, S., Kitagawa, S., Ohba, M., Hasegawa, M., Ozawa, Y. & Toriumi, K. Anthracene array-type porous coordination polymer with host-guest charge transfer interactions in excited states. *Chem. Commun.* **i**, 3142–3144

References

- (2007).
297. Li, Q., Zhang, Q., Xue, Z. Z., Hu, J. X. & Wang, G. M. Photoactive Anthracene-9,10-dicarboxylic Acid for Tuning of Photochromism in the Cd/Zn Coordination Polymers. *Inorg. Chem.* **61**, 10792–10800 (2022).
 298. Sikdar, N., Hazra, A., Samanta, D., Haldar, R. & Maji, T. K. Guest-Responsive Reversible Electron Transfer in a Crystalline Porous Framework Supported by a Dynamic Building Node. *Angew. Chemie* **132**, 18637–18642 (2020).
 299. Tang, Y., Dubbeldam, D. & Tanase, S. Water-Ethanol and Methanol-Ethanol Separations Using in Situ Confined Polymer Chains in a Metal-Organic Framework. *ACS Appl. Mater. Interfaces* **11**, 41383–41393 (2019).
 300. Sawamura, K. I., Furuhata, T., Sekine, Y., Kikuchi, E., Subramanian, B. & Matsukata, M. Zeolite Membrane for Dehydration of Isopropylalcohol-Water Mixture by Vapor Permeation. *ACS Appl. Mater. Interfaces* **7**, 13728–13730 (2015).
 301. Jellen, M. J., Jiang, X., Benders, S., Adams, A. & Garcia-Garibay, M. A. Slip/Stick Viscosity Models of Nanoconfined Liquids: Solvent-Dependent Rotation in Metal-Organic Frameworks. *J. Org. Chem.* **87**, 1780–1790 (2022).
 302. Rowe, J. M., Hay, J. M., Maza, W. A., Chapleski, R. C., Soderstrom, E., Troya, D. & Morris, A. J. Systematic investigation of the excited-state properties of anthracene-dicarboxylic acids. *J. Photochem. Photobiol. A Chem.* **337**, 207–215 (2017).
 303. Lustig, W. P., Teat, S. J. & Li, J. Improving LMOF luminescence quantum yield through guest-mediated rigidification. *J. Mater. Chem. C* **7**, 14739–14744 (2019).
 304. Tao, C., Wang, J. & Chen, R. Metal Organic Frameworks-Based

- Optical Thin Films. in *Multilayer Thin Films-Versatile Applications for Materials Engineering* (ed. Basu, S.) (IntechOpen, 2020). doi:10.5772/intechopen.86290.
305. Liu, J., Ju, Y., Zhang, Y. & Gong, W. Preferential Paths of Air-water Two-phase Flow in Porous Structures with Special Consideration of Channel Thickness Effects. *Sci. Rep.* **9**, 1–13 (2019).
 306. Siena, M., Iliev, O., Prill, T., Riva, M. & Guadagnini, A. Identification of Channeling in Pore-Scale Flows. *Geophys. Res. Lett.* **46**, 3270–3278 (2019).
 307. Bourlon, B., Wong, J., Mikó, C., Forró, L. & Bockrath, M. A nanoscale probe for fluidic and ionic transport. *Nat. Nanotechnol.* **2**, 104–107 (2007).
 308. Son, B. H., Park, J. Y., Lee, S. & Ahn, Y. H. Suspended single-walled carbon nanotube fluidic sensors. *Nanoscale* **7**, 15421–15426 (2015).
 309. Chen, X. H., Wei, Q., Hong, J. D., Xu, R. & Zhou, T. H. Bifunctional metal–organic frameworks toward photocatalytic CO₂ reduction by post-synthetic ligand exchange. *Rare Met.* **38**, 413–419 (2019).
 310. Feng, L., Yuan, S., Qin, J. S., Wang, Y., Kirchon, A., Qiu, D., Cheng, L., Madrahimov, S. T. & Zhou, H. C. Lattice Expansion and Contraction in Metal-Organic Frameworks by Sequential Linker Reinstallation. *Matter* **1**, 156–167 (2019).
 311. Delen, G., Ristanović, Z., Mandemaker, L. D. B. & Weckhuysen, B. M. Mechanistic Insights into Growth of Surface-Mounted Metal-Organic Framework Films Resolved by Infrared (Nano-) Spectroscopy. *Chem. - A Eur. J.* **24**, 187–195 (2018).